From the Institute of Signal Processing
of the University of Lübeck
Director: Prof. Dr. Alfred Mertins

Towards Closed Loop Deep Brain Stimulation
An Integrated Approach for Neural Recording and Microstimulation

Dissertation
for Fullfillment of
Requirements
for the Doctoral Degree
of the University of Lübeck

from the Department of Computer Sciences/Engineering

Submitted by

Susanne Löffler
from Sonneberg

Lübeck 2012

First referee: Prof. Dr. rer. nat. Ulrich G. Hofmann

Second referee: Prof. Dr. med. Andreas Moser

Date of oral examination: 24 May 2012

Approved for printing: Lübeck, 30 May 2012

“Flying is learning how to throw yourself to the ground and miss.”

— Douglas Adams

DECLARATION

I hereby declare, that this thesis is my own work and effort and that it has not been submitted anywhere for any award. Where other sources of information have been used, they have been acknowledged.

Lübeck, March 2012

Susanne Löffler

ABSTRACT

Deep brain stimulation with high frequencies around 130 Hz has been established as an effective treatment for parkinsonian motor symptoms and is studied as a promising technique for the therapy of other motoric- and psychomotoric syndroms.

Common systems administer cathodic stimulation pulses with rectangular waveform, frequencies around 130 Hz and unmodulated stimulus amplitude, independent from neuronal feedback. Partly severe side effects due to distortion of surrounding tissue and disruption of neuronal network activity are reported. Thus, there is need for highly customizable systems that administer feedback-controlled *deep brain stimulation* affecting the tissue around the electrode as little as possible. The first step towards the use of such closed-loop systems for *deep brain stimulation* are electrodes that can be used to deliver functional electrical stimulation, and to record neuronal signals, that allow to determine pathological network activity as to provide feedback for neuronal stimulation.

Here, two candidates of bimodal recording and stimulation probes are evaluated. The performance of a stiff metal *Linear Array Probe* is compared to a flexible polyimide based *Flexible Array Probe*. The probes were characterized using *Impedance spectroscopy* along with an equivalent circuit model. The *voltage response* of the probes was determined in the acute stage, right after implantation, and in the chronic stage, after four weeks of implantation. *neuronavigation* was used to characterize the probes' performance at recording neuronal discharge in certain brain areas. In hemiparkinsonian rats with partial lesions of the dopaminergic nigrostriatal projections, subthalamic *high frequency microstimulation* was applied, and the electrophysiological neuronal response was determined.

Increased firing of subthalamic neurons was determined in hemiparkinsonian animals and *high frequency micostimulation* was shown to induce *infraslow oscillations* which could be used as parameters for feedback-controlled neuronal stimulation. Further, it was established, that the effect of subthalamic *high frequency microstimulation* is not due to bulk excitation or inhibition of neuronal tissue, but specifically addressed certain neuronal elements.

ZUSAMMENFASSUNG

Die Tiefenhirnstimulation mit Frequenzen um 130 Hz hat sich bewährt als eine Methode zur Behandlung der motorischen Symptome der Parkinson Erkrankung. Heute untersucht man, ob mit Hilfe der bekannten Technik auch andere Krankheiten behandelt werden können, bei denen die Patienten motorische- oder psychomotorische Symptome zeigen. Übliche Systeme vermitteln kathodische Stimulation in Form von Rechteckpulsen mit Frequenzen um 130 Hz und unmodulierter Amplitude, und sind unabhängig von neuronalen Signalen, die als Antwort auf die Stimulation aufgefasst werden können. Durch Gewebeveränderungen um die Elektrode und Störung von neuronaler Netzwerkaktivität kommt es aber teilweise zu schweren Nebenerscheinungen. In Zukunft wird man Systeme brauchen, die es ermöglichen, die Stimulation genau anzupassen, so dass möglichst wenig neuronales Gewebe beeinflusst wird. Ausserdem werden Systeme entwickelt, die auf die neuronale Antwort zur Stimulation reagieren, also bedarfsabhängig stimulieren. Der erste Schritt hin Systemen, die bedarfsabhängige Tiefenhirnstimulation erlauben, sind Elektroden, die benutzt werden können, funktionelle elektrische Stimulation zu vermitteln, und zur selben Zeit neuronale Signale aufnehmen können, die es erlauben, pathologische Netzwerkaktivität festzustellen, die als Parameter für die Antwort auf elektrische Stimulation dienen könnten.

In der vorliegenden Arbeit wurden zwei Kandidaten für bimodale elektrische Stimulation und Aufnahme neuronaler Signale getestet. Eine starre Sonde mit linearer Anordnung von Ableitekontakten entlang des Schafts und einem einzelnen Stimulationskontakt an der Spitze wurde verglichen mit einer flexiblen Sonde auf Polyimidbasis, die mit Mikrotechnischen Methoden hergestellt wurde. Die Sonden wurde untersucht mit Hilfe von Impedanzspektroskopie und einem geeigneten Modell der elektrischen Bestandteile. Der Spannungsabfall an der Elektrode wurde im akuten Zustand, kurz nach implantation, und im chronischen Zustand, vier Wochen nach Implantation, untersucht. Während der Implantation der Sonden wurde deren Eignung zur Neuronavigation untersucht, also ob man anhand der gemessenen Signale feststellen kann, in welcher Region des Gehirns man sich befindet. Im Tiermodell der Ratte mit einer unilateralen läsion der dopaminergen nigrostriatalen Projektionsneurone durch 6-Hydroxydopamin wurde subthalamische elektrische Hochfrequenzstimulation angewendet und die neuronale Antwort auf die Stimulation gemessen.

Es wurde festgestellt, dass die Aktivität der Neurone im subthalamischen Nucleus erhöht ist, in Tieren mit einer unilateralen Läsion. Weiterhin wurde gezeigt, dass elektrische Hochfrequenzstimulation, sehr langsame Oszillationen neuronaler Aktivität verursacht, die als Parameter für bedarfsgerechte neuronale Stimulation dienen könnten. Ausserdem wurden weitere Hinweise gefunden, dass der Effekt der subthalamischen elektrischen

Hochfrequenzstimulation nicht ungezielte Aktivierung oder Inhibition von neuronaler Elemente darstellt, sondern, dass bestimmte neuronale Elemente spezifisch adressiert werden.

Journal Articles & Submitted Manuscripts

Löffler, S., Füllgraf, H., Hofmann, U. G., Moser, A. N-Methyl-D-Aspartate Receptor Activation Modulates the Local Effect of Electrical High Frequency Stimulation in the Rat Caudate Nucleus, **under review**

Löffler, S., Gasca, F., Richter, L., Leipscher, U., Trillenberg, P., Moser, A. The Effect of Repetitive Transcranial Magnetic Stimulation on Monoamine Outflow in the Nucleus Accumbens Shell in Freely Moving Rats. **submitted to J Neuropharmacol**

Xie, Y., Bonin, T., **Löffler, S.**, G. Hüttmann, V. Tronnier, U.G. Hofmann. Imaging in Vivo Rat Brain Morphology Along Coronal Trajectory with Fiber Optical Coherence Tomography. **submitted to J Biophotonics**

Persson, K. M., Karlsson, R., Svennersten, K., **Löffler, S.**, Jager, E. W. H., Richter-Dahlfors, A., Konradsson, P., Berggren, M. Electronic Control of Cell Detachment Using a Self-Doped Conducting Polymer. **Adv Mat, 23(38), 4403-4408, 2011**

Hiller, A., **Löffler, S.**, Haupt, K., Litza, M., Hofmann, U.G., Moser, A. Electrical high frequency stimulation of the caudate nucleus induces local GABA outflow in freely moving rats. **J Neurosci Methods, 159, 286-290, 2007**

Conference Articles

Krapohl, D., **Löffler, S.**, Moser, A., Hofmann, U.G. Microstimulation in The Brain - Does Microdialysis Influence the Activated Volume of Tissue? Proceedings of the COMSOL Multiphysics User's Conference, Milan, Italy, October 11-14th, 2009

Hammad, S., **Löffler, S.**, Mankodiya, K., Krapohl, D., Pohl, M., Moser, A., Tronnier, V., Hofmann, U.G. Niotrode Array for Rodent Brain Recording Electrical testing. **Biomedizinische Technik, Rostock, 2010**

Xie, Y., Bonin, T., **Löffler, S.**, Hüttmann, G., Tronnier, V., Hofmann, U.G. Fiber spectral domain optical coherence tomography for in vivo rat brain imaging. **SPIE Photonics Europe (EPE10), Brussels, 2010**

Löffler, S., Vogt, S., Hofmann, U. G., Moser, A. Striatal microstimulation in awake animals depends on NMDA receptor activity. **Biomedical Engineering, 53(S1), 241-243, 2008**

Richter, A., **Löffler, S.**, Moser, A., Kruse, C., Danner, S. Bioprobes sheathed with adult stem cells for improvement of tissue reaction during chronic imlantation. **3rd International Symposium On Interface Biology of Implants, Rostock, May 17-19th, 2009**

Löffler, S., Ramrath, L., Hofmann, U.G., Schweikard, A., Moser, A. Robot assisted stereotaxic targeting for STN DBS in the rat brain. **52. Wissenschaftliche Jahrestagung der Deutschen Gesellschaft für Klinische Neurophysiologie und Funktionelle Bildgebung, Magdeburg, April 10-12th, 2008**

Löffler, S., Hofmann, U.G., Moser, A. NMDA receptor modulation affects HFS induced GABA outflow. **Ligand Gated Ion Channels - 18th Neuropharmacology Conference in association with IUPHAR, Washington DC, USA, November 12-14th, 2008**

Ramrath, L., Pohl, M., **Löffler, S.**, Mankodiya, K., Xie, Y., Hofmann, U.G., Schweikard, A. Single fibre Optical Coherence Tomography for Brain Imaging - A preliminary in vitro study. **Proceedings der 7. Jahrestagung der Deutschen Gesellschaft für Computer- und Roboterassistierte Chirurgie, Leipzig, September 24-26th, 2008**

Ramrath, L., Hofmann, U.G., Bonsanto, M.M., Tronnier, V., **Löffler, S.**, Moser, A., Schweikard, A. Robotic Framework for Small Animal Stereotaxy. **FENS Abstr., 4, 096.20, 2008**

Löffler, S., Hiller, A., Fuellgraf, H., Moser, A. NMDA agonist RS-TG attenuates high frequency stimulation induced increase of local GABA outflow in the caudate nucleus of freely moving rats. **Molecular Life Sciences - Herbsttagung der Gesellschaft für Biochemie und Molekul a biologie, Hamburg, September 16-19th, 2007**

Löffler, S., Hiller, A., Haupt, K., Litza, M., Hofmann, U.G., Moser, A. In vivo Rattenmodell zur Bestimmung der Neurotransmitter GABA und Glutamat bei Hochfrequenzstimulation. **Aktuelle Neurologie, 32, S4, 2005**

CONTENTS

Declaration v

Abstract vii

Zusammenfassung ix

Publications & Manuscripts xi

Contents xiii

1 Introduction 1
- 1.1 Electrical Activity in the Brain . . . 1
  - 1.1.1 Action Potential . . . 2
  - 1.1.2 Synaptic & Dendritic Integration . . . 4
- 1.2 Interfacing the Brain . . . 5
  - 1.2.1 Recording of Neuronal Activity . . . 6
  - 1.2.2 Intracerebral Electrical Stimulation . . . 9
- 1.3 Electrode Characterization . . . 11
  - 1.3.1 Impedance Spectroscopy . . . 11
  - 1.3.2 Voltage Response . . . 13
- 1.4 Neuronavigation . . . 14
  - 1.4.1 Targeting the Subthalamic Nucleus . . . 14
- 1.5 Deep Brain Stimulation . . . 15
  - 1.5.1 Mechanism of Action . . . 16
  - 1.5.2 Approved Equipment for Deep Brain Stimulation . . . 17
  - 1.5.3 New Approaches to Deep Brain Stimulation . . . 19
  - 1.5.4 Animal Models of Parkinson's Disease . . . 21
- 1.6 Aim of the Current Work . . . 23

2 Materials and Methods 27
- 2.1 Probes for Neural Recording and Stimulation . . . 27
  - 2.1.1 Linear Array Probes . . . 27
  - 2.1.2 Flexible Array Probes . . . 28
  - 2.1.3 Connection to Commercial Hardware . . . 29
- 2.2 Hardware . . . 30
  - 2.2.1 Stimulation Hardware . . . 30
  - 2.2.2 Recording Hardware . . . 30
- 2.3 Impedance Spectroscopy . . . 31
- 2.4 Chronic Experiments . . . 32
  - 2.4.1 Animals . . . 32
  - 2.4.2 Surgical Procedure . . . 32
  - 2.4.3 Probe Insertion & Neuronavigation . . . 35

2.4.4 Probe Implantation . . . 38
2.4.5 Lesioning Procedure & Sham Treatment . . . 39
2.4.6 Microstimulation and Recording Freely Behaving Animals . . . 41
2.5 Data Analysis . . . 45
2.5.1 Groups & Parameters . . . 45
2.5.2 Signal Processing . . . 47
2.5.3 Edge Detection . . . 47
2.5.4 Wavetrain Derived Parameters . . . 48
2.5.5 Spike Detection & Clustering . . . 49
2.5.6 Spike Event Analysis . . . 50

3 Results **53**
3.1 Probe Characterization . . . 53
3.1.1 Linear Array Probe Impedance Spectra . . . 53
3.1.2 Flexible Array Probe Impedance Spectra . . . 55
3.2 Neuronavigation . . . 58
3.2.1 Wavetrain Appearance . . . 58
3.2.2 Mean Spike Shapes . . . 58
3.2.3 Wavetrain Based Parameters . . . 60
3.2.4 Spike Based Parameters . . . 63
3.3 Voltage Response . . . 66
3.4 Basal Neuronal Activity . . . 69
3.5 Rotational Behaviour . . . 70
3.5.1 Apomorphine Induced Rotational Behaviour . . . 70
3.5.2 Rotational Behaviour Induced by Subthalamic High-frequency Microstimulation . . . 71
3.6 Network Response to High-frequency Microstimulation . . . 72
3.6.1 Signature Curves of Neuronal Activity . . . 73
3.6.2 Averaged Network Response . . . 75
3.7 Single Unit Response to High-frequency Microstimulation . . . 79
3.7.1 Single Unit Activity at Implanted Linear Array Probes 82
3.7.2 Single Unit Activity at Implanted Flexible Array Probes 84

4 Discussion **89**

Bibliography **113**

Acknowledgements **143**

List of Figures **145**

List of Tables **147**

List of Listings **149**

List of Abbreviations **151**

A Curriculum Vitae **A-1**

B LCR Meter **B-1**

C TDT Export **C-1**

D Data Processing **D-1**

E Protocols **E-1**

1

INTRODUCTION

1.1 *Electrical Activity in the Brain*

The *central nervous system* was first described by the roman physician Galen. He saw the spinal cord as an extension to the brain carrying sensation to the limbs. He believed that nerves controlled the actions of muscles in the limbs and that the two principal functions of the nervous system were sensation and motion. Further, he reasoned that nerves must act as a medium for the *"animal spirit"* circulating through the body. In 1762 Galvani explained that the *"animal spirit"* was electricity conducted by the nervous system. By doing so, he created the concept of *bioelectricity* (López-Muñoz & Alamo 2009).

Soon, it became clear that a two-way communication with the central nervous system is possible in terms of electrical stimulation and electrophysiological recording. Fritsch & Hitzig contributed the first topographic studies of the motor cortex by measuring the muscular response to electrical cortical stimulation (Fritsch & Hitzig 2009). These experiments eventually lead to the creation of the first somatosensory map known as *homunculus* by Wilder Penfield (Penfield & Boldrey 1937). At the same time, the first human *electroencephalogram* was measured which enabled the detection of somatosensory evoked potentials (Dawson 1947, Haas 2003).

At a deeper level, the electrical properties of the nerve cell were explored. Matteucci discovered that electrical energy is stored in the nerve cell in form of a potential across the membrane. Du Bois-Reymond measured neural discharge and called it *action potential* (Pearce 2001). A fundamental contribution was made by Hodgkin & Huxley in the 1950s. Studying the giant squid axon, they characterized the neural *action potential* and described the flow of ionic currents across the neural membrane (Hodgkin & Huxley 1952). Together with the almost concurrent description of the Na^+/K^+*-ATPase* (Skou 1957) and the concept of *transmembrane ion channels* a good understanding of the process of neuronal electrical activity on the single cell level emerged.

Today, we can modify the activity of almost every transmembrane ion channel specifically and are still surprised about the variety of implications such an action can cause. We can listen to hundreds of neurons at the same time, and still not fully understand how they interact. We can implant electrodes into the brain that help severely impaired patients to move again. And, still, do not know why it works. Electrical stimulation in the brain is extremely complex since we do not know about the fundamental mechanism and have no means to make simplifying assumptions. Thus, when looking at electrical stimulation and recording in the brain it is always necessary to go back and look at the *action potential* as the fundamental unit of *bioelecticity*.

1.1.1 *Action Potential*

The *action potential* is a summation of the ionic currents flowing across the neuronal membrane. Ions can pass the membrane in three different ways. They are actively transported against a concentration gradient, flow through ion-specific and regulated *ion channels*, or leak through in small amounts. The main player in the active transport is the *Na^+/K^+-ATPase* pumping 1.5 times more sodium ions out of the cell than potassium ions into the cell generating a *resting potential* across the cell membrane which is negative at the *inner leaflet*. *Ion channels*, important for *action potential* generation, are *voltage-gated sodium* and *potassium channels* (Na_v and K_v). Currents, flowing across the membrane, give the *action potential* its characterisitc shape (see figure 1.1).

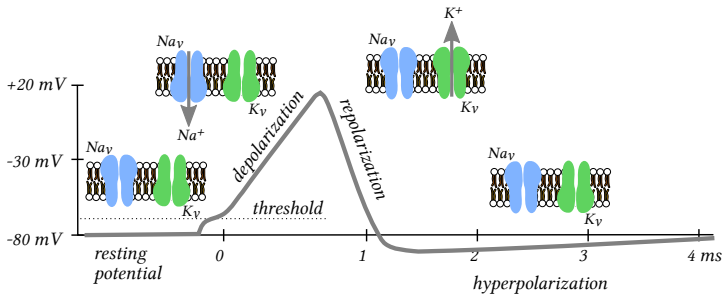

Figure 1.1: An action potential generated by ionic currents flowing across the cell membrane.

Ionic gradients create a *resting potential* of about - 80 mV across the neuronal membrane. When the neuronal membrane is depolarized to a certain threshold, *voltage-gated sodium channels* open. This leads to even more *depolarization* since sodium ions rush into the cell until *voltage-gated sodium channels* close and the *voltage-gated potassium channels* open. This leads to *repolarization* since potassium ions will flow out until the *voltage-gated potassium channels* close again when the *resting potential* is reached. There is a certain *hyperpolarization overshoot* at which the *inner leaflet* is more negative than at rest but the *resting potential* will be re-established by *leaking currents*. Only when the *resting potential* is reached, the cell can be excited again.

When an *action potential* is initiated, it travels along the *axon* until it reaches the *axon terminals* (see figure 1.2). At the *synapse*, connecting the *axon terminal* of the *presynaptic cell* with the *dendrites* of the *postsynaptic cell*, the incoming *action potential* is converted into a chemical signal. *Voltage-gated calcium channels* in the *axon terminals* enable influx of calcium ions. This leads to vesicle fusion with the *presynaptic membrane* and to *neurotransmitter* release into the *synaptic cleft*. The membrane of the *pre-* and *postsynaptic cell* carries receptor proteins, which can be *ligand-gated ion channels*, or *G-protein coupled receptors*. Activation of *ligand-gated ion channels* can lead to influx of cations (*depolarization*) or anions (*hyperpolar-*

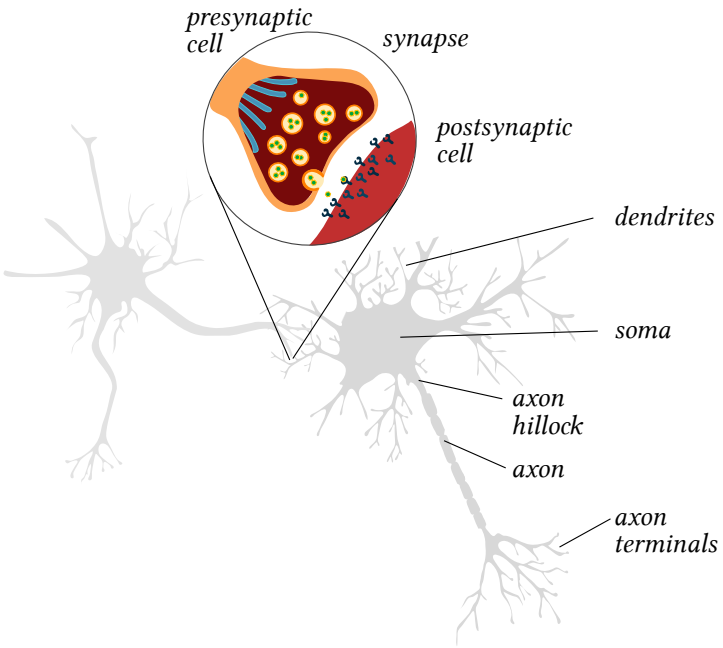

Figure 1.2: Neuronal cells with *soma*, *axon*, *dendrites*, and interconnections between different neuronal cells. Figure uses parts from `sv.wikipedia.org/wiki/Fil:Complete_neuron_cell_diagram_numbered.svg`

ization) into the *postsynaptic cell*. The probability to excite the *postsynaptic cell* is increased by *depolarization* and lowered by *hyperpolarization*. Therefore, cation influx into the *postsynaptic cell* is called *excitatory postsynaptic potential* and anion influx into the *postsynaptic cell* is called *inhibitory postsynaptic potential*. The *postsynaptic potentials* of all *dendrites* are considered to be integrated in the *soma* and when the *threshold potential* is reached a new *action potential* is generated.

1.1.1.1 *The Shape of the Action Potential*

The inherent shape of an *action potential* depends on the *time constants* of the *ionic currents* flowing across the membrane. They are related to the opening- and closing times of the *voltage-gated ion channels*. Many different *voltage-gated ion channel* with different *time constants* have been described. Their distribution differs among various types of neurons in the mammalian brain and so does the shape of the *action potential* (Baranauskas 2007).

The duration of an *action potential* differs between purkinje, pyramidal and dopamine containing neurons (Bean 2007). The *action potentials* of fast-spiking *purkinje neurons* with durations of 180 µs can be differentiated from the *action potentials* of regular and slow-spiking pyramidal and dopamine containing neurons with durations of 810 µs and 4 ms (Bean 2007).

The physiological relevance of the *action potential* shape is not well understood. Yet, it seems that the shape of a neuron's *action potential* and its firing pattern can not be clearly separated. Short duration *action potentials*

are observed in cells, firing at higher frequencies (Nowak et al. 2003). Also, long duration *action potentials* have been shown that lead to increased calcium influx into the *presynaptic cell* and thereby and influence the generated *postsynaptic potential* (Geiger & Jonas 2000).

The duration of *action potentials* in different cells can range from 0.25 to 5 ms. Usually, an *action potential* lasts about 1 ms.

1.1.2 *Synaptic & Dendritic Integration*

The all-or-nothing characteristic of *action potential* initiation is the reason that neuronal information is thought to be encoded by frequency and pattern of a sequence of *action potentials*. A sequence of *action potentials* contains a *rate code* and a *temporal code*. The *rate code* is based on the *mean firing rate* of a neuron. The exact information about the timing of neuronal discharge events is the basis for the *temporal code* (Gerstner et al. 1997, Brown 2007).

In the majority of neurons, a single synaptic response provides insufficient depolarization to trigger an *action potential*. Instead, in order to elicit an *action potential*, multiple potentials are summed up in the *postsynaptic cell*. The time scale of synaptic integration is dependent on the *time constants* of *postsynaptic receptors*. These *time constants* are widely distributed and range between 1-2 ms for *AMPA-type glutamate receptors*, and up to 0.8-10 s for *metabotropic glutamate receptors* (Bengtson et al. 2004, Smith et al. 2000). The average *time constant* for *postsynaptic integration* is about 20 ms giving an estimate about the timing of synaptic integration in the brain (Attwell & Gibb 2005, Attwell & Iadecola 2002).

The integration of *postsynaptic potentials* by propagation through the *dendritic tree* results in specialized spiking patterns, and is largely dependent on the computational abilities of the neuron (Silver 2010). While *postsynaptic potentials* propagate in the neuronal cell, they are integrated due to the active and passive properties of the *dendritic tree*.

Passive integration follows from the morphology of the *dendritic tree*. Since *distal dendrites* have a smaller diameter, lower local *membrane capacitance* and larger *input impedance*, *distal postsynaptic potentials* show larger amplitudes and faster response than *proximal synaptic potentials*. Although *proximal postsynaptic potentials* have a lower amplitude than fast, *distal postsynaptic potentials* they possess longer integration times. Non-linear summation of *postsynaptic potentials* occurs when the respective *synapses* are in close proximity because the driving force is reduced. Linear summation of *synaptic inputs* occurs when the *synapses* are spatially isolated and the *synaptic events* are temporally distributed. The *membrane resistance* is generally low. Thus, the amplitude of the propagating potentials declines with the distance. Fast *synaptic responses* become elongated and attenuated since the serial *membrane capacitance* is acting as a *low-pass filter*. Since *dendrites* become narrower with the distance from the *soma*, passive dendritic integration favours potential propagation directed away from the *soma*.

Beyond the passive properties of the *dendritic tree* morphology, integration of *postsynaptic potentials* is dependent on active conductances in *dendrites*. Depending on their gating characteristics, ion specificity and kinetics, dendritically expressed *voltage-gated channels* have the potential to amplify, dampen and shape the synaptic responses as they propagate through the *dendritic tree*.

Probably, there is no unique site for initiation of *action potentials* (Ibarz et al. 2003). Generation of *dendritic potentials* has been shown for different types of neurons. Also, backpropagation of *action potentials* into the *dendritic tree* has been observed, influencing synaptic plasticity, synaptic integration and neurotransmitter release from the *dendrites* (Magee 2000, Sidiropoulou et al. 2006). The ability of *dendrites* to actively support propagation, depends on their electrical history. Cumulative *sodium channel* inactivation is thought to increase attenuation of potentials that occur later in a sequence of *action potentials*. *Action potential* activation at a critical frequency around 100 Hz leads to potential summation and generation of local *calcium currents* even in *distal apikal dendrites* (Gulledge et al. 2005, Segev & Rall 1998).

1.2 *Interfacing the Brain*

Current and emerging neural prostheses and therapies are based on central nervous stimulation and recording (Ryu & Shenoy 2009). Electrodes are chronically implanted, and used as an interface to the electrically active neuronal tissue. There is a wide range of applications for neuroprosthetic devices facilitating electrophysiological recording and stimulation. Electrodes, used as neuronal interfaces must fulfil certain requirements with respect to electrochemical properties and biocompatibility.

Commonly, electrodes for neuronal interfacing are metallic conductors, located in the extracellular fluid. When two electrodes are placed into an electrolyte, electrode polarization occurs due to differences in the *equilibrium potential* of the electrode material (see figure 1.3a). Dependent on the polarity of the electrode, capacitive layers of hydrated ions form on the exposed surface of a polarized electrode (see figure 1.3c). The potential on the polarized electrode surface decreases exponentially with the distance from the electrode. Thus, a *compact double-layer* of hydrated ions forms directly on the surface, and *diffuse layers* establish in greater distance from the electrode. The *compact double-layer* of hydrated ions on the electrode surface can store charge and act like an electrical capacitance. When a signal is measured by the electrode, or transmitted from the electrode, *charge transfer* occurs across the *electrode-electrolyte interface*. The *resistance* of this *charge transfer* is dependent on the frequency of the measured or transmitted signal, and is therefore called *impedance*. The *impedance* of the *electrode-electrolyte interface* can be described by the *Randles cell* equivalent circuit (Geddes 1997). In the classical *Randles cell*, a *spreading resistance* R_s, representing the *ohmic resistance* of the electrolyte and electrode, and a *charge transfer resistance*

R_{ct} in parallel with a *double layer capacitance* C_{dl} is used to describe the *impedance* characteristics of a *first order systems* with a single *time constant* (see section 1.3.1).

This approximation seems sufficient to describe the frequency dependent resistance, and the *high-pass filter* properties of the *electrode-electrolyte interface* in ionic solution. Yet, description of the *tissue-electrode interface* is more complex, since *charge transfer* to the tissue faces the *capacitance* of the cell membrane, often approximated as *tissue capacitance*. Many different equivalent circuit models have been used to describe the *electrode-tissue interface*, and mostly an additional *serial RC circuit* is added to the *parallel RC circuit* of the *Randles Cell* to describe the *electrode-tissue interface* (Cantrell et al. 2008, Troy et al. 2006, Geddes 1997).

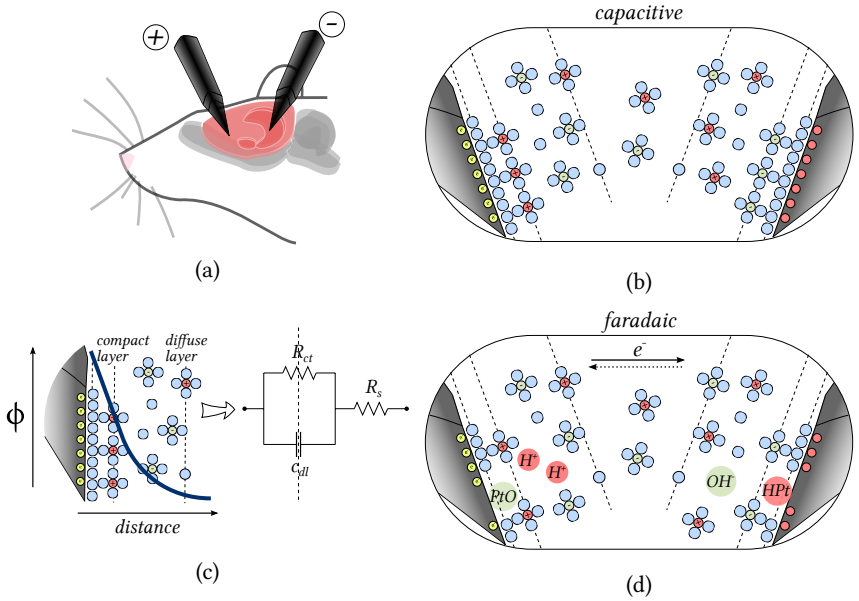

Figure 1.3: The *electrode-electrolyte interface* forms on the surface of polarized electrodes. Capacitive layers of hydrated ions mediate charge transfer between electrode and electrolyte.

1.2.1 *Recording of Neuronal Activity*

Action potential propagation along the neuronal membrane produces *current sinks* and *sources*, generating local dipoles, which add up throughout the anisotropic volume conductor of the *extracellular space*, whereby potentials of opposing polarity are cancelled out, and potentials of the same polarity are summed up.

Extracellular electrodes for neuronal recording are located at some distance to a particular cell membrane. Therefore, the potential which is measured at the electrode is always the integration of local dipoles generated by currents sinks and sources at the neuronal membrane and does not necessarily resemble the actual *action potential*. Depending on the distance between the

recording electrode and the neural membrane, integration occurs over a certain spatial range, resulting in *extracellular potentials* referring to single- or multiple events of neural discharge.

Fluctuations in the *extracellular electric field* result in reorganizations in the ordered layers of hydrated ions at the *electrode-electrolyte interface*. Thus, *ionic fluctuations* in the *extracellular electrolyte* are translated into electron flow in the electrode via *charge transfer* at the *electrode-electrolyte interface*. Yet, due to the *impedance* characterisitcs of the interface, the measured signal has a lower amplitude and is distorted by a certain *phase angle* (Logothetis 2003).

Since the processes at the *electrode-electrolyte interface* during recording are assumed to be capacitive (Moffitt & Mcintyre 2005, Butson & McIntyre 2005), the electrochemical challenges to the recording electrode are considerably low (see figure 1.3b). For high-quality signals, the distance between a neuron and electrode, as well as the respective size of each plays a major role. Thus, the spatial arrangement of multiple recording sites and ways to prevent glial sheathing, foreign-body response and electrode movement have to be considered for *recording electrode* design (Cogan 2008).

1.2.1.1 *Single Unit Recordings*

When an *extracellular recording electrode* with a *geometric surface area* approximately the size of the target structure is located near the *soma* or *axon*, the area of spatial summation is very small. Thus, small extracellular electrodes in close proximity to a cell compartment, can reflect *single unit spike activity*, and will reveal *firing rate* and *firing pattern* on the *single cell level*.

To record *single unit activity* close to different neuronal compartments, electrodes with a very small *geometric surface area* are desirable. Yet, the smaller the exposed surface of the electrode, the higher is the *electrode resistance* and the lower is the *double layer capacitance*. That results in a better *high-frequency response*, but also in larger noise levels, and low *signal-to-noise* ratios. The dominant noise source for *high impedance recordings* is thought to be *thermal noise* which originates from the thermal electron agitation in a conductor (*Johnson & Nyquist*) (Johnson 1928, Nyquist 1928). Since *thermal noise* is directly related to the *electrode impedance*, it is also related to the surface area of the electrode contact site. Thus, the surface area of the contact influences the signal amplitude recorded from the neuron (Lempka et al. 2006). To measure a sufficiently large signal, the electrode needs to be located even closer to the cell, which increases the risk to damage the cell. Therefore, the size of recording electrode contacts have to be well balanced in order to measure the desired activity. Electrodes for *single unit recordings* usually expose a *geometric surface area* smaller than $4x10^{-5}$ cm^2. Depending on the electrode material, *electrode impedances* range between 0.05 - 1 MΩ at 1 kHz (Cogan 2008).

Recordings of *single unit activity* are biased towards larger cells, since these produce considerably larger *extracellular field potentials* than smaller cells (Sakai et al. 1978, Menendez de la Prida et al. 2002). Larger neurons

with 20-30 µm diameter are estimated to generate a potential of more than 100 µV amplitude within a 100 µm radius. The measured amplitude decreases rapidly with the distance. For distances larger than 140 µm, *spikes* become indistinguishable from the background noise. Measurement of smaller, inhibitory neurons can therefore be difficult (Logothetis 2003).

Extracellular electric field potentials do not directly relate to *action potentials*. Yet, signals, resembling the actual *action potentials* can be measured with intracellular *glass capillary microelectrodes*. Simultaneous *intra-* and *extracellular recordings* along with mathematical simulations revealed information about the correlation of membrane currents and the *extracellular potential waveform*. Although the size of *soma* and *proximal dendrites* determine the amplitude of the *extracellular potential waveform*, the details of cell morphology have relatively little impact. Simulations of *W-shaped extracellular potential waveforms* suggest that the pattern of *action potential* initiation can be reflected in the *extracellular potential waveform* under the condition of uniform dendritic stimulation. Consequently, monitoring *extracellular potential waveforms* may provide insights into the pattern of *action potential initiation* (Gold et al. 2006).

1.2.1.2 *Multi Unit Recordings*

If a *recording electrode* is sufficiently far away from a *spiking neuron*, the single cell activity does not predominate the measured signal and the sum of potentials from a large area is recorded. Thus, the measured signal will be a mixture of fast *spike activity* from multiple cells and slow, *integrative activity* in the *dendritic tree*. The two components of *multi-unit activity* can be distinguished by frequency. A *high-pass cut-off* at 300 Hz can be applied to filter *multi-unit spike activity*, and a *low-pass cut-off* at 300 Hz is used to obtain *local field potentials*, which account for integrative events at the *synapse* and *dendritic tree* (Belitski et al. 2008, Kelly et al. 2010). The choice of *electrode impedance* can influence the weight of the signal contributions. An electrode with low *impedance* and large *geometric surface area* will facilitate recordings with good *signal-to-noise-ratio* from a large volume.

The amplitude of high-frequency *multi-unit spike activity* seems to be a function of the average cell size in the measured cell population. Large amplitudes are correlated with large cell size populations, and fast, *low-amplitude activity* is recorded from populations of small cells.

The summation range for fast *multi-unit spike activity* was estimated with a radius of 50-350 µm for electrodes with a recording site diameter of 100 µm and 40-120 kΩ *impedance* (Grover & Buchwald 1970, Legatt et al. 1980, Gray et al. 1995). The activity from each point within the sphere is weighted by a factor depending on the distance of the point from the tip of the electrode (Llinas & Nicholson 1971). When *multi-unit spike activity* is sampled from a radius of about 140 µm from the electrode tip, hippocampal cell density estimations suggest, that *multi-unit spike activity* can contain information from up to 1000 neurons (Boss et al. 1985, Aika et al. 1994, Henze et al. 2000). The activity of synchronous firing cells can be enhanced by summation and

thus detected over a larger distance (Huang & Buchwald 1977, Arezzo et al. 1979)

Local field potentials represent the *low-frequency* component of *multi-unit activity* (Mitzdorf 1985). The *local field potential* amplitude is correlated with the extent and geometry of *dendrites*. Synchronous activation of structures with longitudinal *dentrite-to-soma* arrangement produces strong dendrite-to-soma dipoles, visible in the recorded *local field potential*. Horizontal dendrite-to-soma arrangements, do not effectively contribute to the summation of *low-frequency multi-cell activity*. *Local field potentials* were reported to reflect a weighted average of synchronized dendrosynaptic components from neural populations within 0.5-3 mm from the electrode tip (Mitzdorf 1987, Juergens et al. 1999).

Similar to the frequency band classification of *electroencephalogram* recordings, *local field potential* activity is divided into δ (0-4 Hz), θ (4-8 Hz), α (8-12 Hz), β (12-24 Hz) and γ (24-40/80 Hz) band activity. The classification is based on the strong correlation of the activity in each band with a specific behavioural state. Rhythmic spiking with *β-band frequencies* around 5-12 Hz has been reported for principal neurons in the neocortex. In special cases like that, *spike activity* seems to be tightly correlated with the *local field potential* amplitude (Silva et al. 1991, Logothetis 2003).

1.2.2 *Intracerebral Electrical Stimulation*

To perform electrical stimulation of neuronal tissue, electrode polarization exceeding the electrode's equilibrium potential is achieved by an external bias potential. *Capacitive charge transfer* is possible by charging and discharging the *electrode-tissue interface*, which leads to *ionic rearrangements* in the proximity of the electrode (see figure 1.3b). This influences the *electric field* surrounding the cell membrane, and can drive the cell towards *depolarization* or *hyperpolarization*.

Although *capacitive charge transfer* is desirable for *electrical stimulation* since no chemical species are created or consumed (see figure 1.3b) reaching high *charge injection capacities* needed for electrical stimulation is almost impossible with standard electrode materials and purely *capacitive ionic charge separation*. Porous capacitor electrodes or highly dielectric coatings can increase the *charge injection capacity* but, in order to reach high levels of *charge injection*, *faradaic charge transfer* (see figure 1.3d) occurs on uncoated noble metal electrodes (Cogan 2008, Cogan et al. 2005).

For *faradaic charge transfer*, the electrode surface is *oxdized* or *reduced* in a reversible electrochemical reaction. Althought *electron transfer* occurs, chemical species are confined to the electrode surface and the noble metals or noble metal alloys are not consumed by the *faradaic reaction*. *Faradaic processes* at the surface of noble metal electrodes are therefore sometimes called *pseudocapacitive*. Still, all *faradic reactions* lead to changes in the electrolyte composition adjacent to the electrode. Thus, *faradic reactions* can result in

material	charge injection capacity	reference
gold	1-8 $\mu C/cm^2$	Niina et al. 2011
platinum	50-150 $\mu C/cm^2$	Rose & Robblee 1990
platinum iridium	90-300 $\mu C/cm^2$	Cogan et al. 2005

Table 1.1: Save *charge injection capacities* for different noble metal electrode materials measured *in vitro* by avoiding electrolysis of water.

irreversible tissue damage. Therefore, the safety of *charge injection* has to be considered at all times (Cogan 2008).

If the electrode is polarized more than the *charge injection capacity* allows, irreversible electrochemical reactions occur. Among them, electrolysis of water is the most common. For platinum electrodes, electrode dissolution due to formation of soluble metal complexes is common (Merrill et al. 2005).

Save *charge injection* values for different noble metal electrodes were measured *in vitro* by avoiding electrolysis of water (see table 1.1). They have to be carefully reconsidered for *in vivo* use, since the equilibrium potential *in vivo* is more positive than *in vitro* and less total charge for cathodal stimulation is available.

Beyond consideration of safe *charge injection* thresholds, delivery of biphasic, *charge balanced waveforms* is considered as measure to avoid irreversible reactions at the electrode surface. Ideally, *charge balanced waveforms* have cathodal and anodal phases with current amplitudes and durations that result in an overall zero net charge for the pulse. The overall delivered charge is the integral of the pulse. Current pulses are defined in terms of the charge delivered in the leading phase, the charge density in the leading phase, the current density, the pulse width in each phase, and the pulse frequency (Cogan 2008). Although the use of *charge balanced waveforms* is well established, the long term stability of most noble metals or noble metal alloys is unknown at positive bias. Generally, limitation of the *electrode potential* to within safe limits seems to be more important for safe stimulation than a perfectly *balanced waveform* (Donaldson & Donaldson 1986).

A neuronal prosthesis is supposed to deliver functional electrical stimulation within the limits of safe *charge injection thresholds* over a long period of time. Electrode material, surface area, stimulation amplitude, pulse widths, and frequency have to be chosen in order to exceed the *charge per phase threshold* for functional stimulation, without reaching the *charge density threshold* for safe stimulation. For functional *deep brain stimulation* in the *subthalamic nucleus*, *charge per phase thresholds* of 135-400 $nC/phase$ have been reported. Considering stimulation pulse widths of 60-200 µs and a large electrode surface area of 0.06 cm^2 *charge density thresholds* for *deep brain stimulation* electrodes can be as low as 2.6-6.7 $\mu C/cm^2$ (Kuncel & Grill 2004).

In practice, most electrodes used for nerve stimulation or surface electrodes for cortical stimulation are *macroelectrodes* with surface areas larger

than 0.001 cm^2. They can safely reach high functional *charge per phase thresholds* and still allow the use of materials with low *charge density thresholds*. With exception of the intracerebral electrodes used for *deep brain stimulation*, most penetration electrodes are microelectrodes with surface areas smaller than $2x10^{-5}$ cm^2. Since *charge per phase thresholds* of 0.4-4.6 $^{nC}/_{phase}$ for neuronal excitation of cerebral grey matter need to be reached, the allowed *charge density* on the electrode surface has to be less than 80 $^{\mu C}/_{cm^2}$ to achieve safe chronic stimulation (Geddes & Roeder 2003, Kuncel & Grill 2004, Merrill et al. 2005).

1.3 *Electrode Characterization*

1.3.1 *Impedance Spectroscopy*

Impedance spectroscopy is used to describe the *charge transfer* properties at the *electrode-electrolyte interface*. To determine the *frequency response* of the *elecrode-electrolyte interface* the *impedance* is measured over a broad frequency range. While applying a *low-amplitude* sinusoidal voltage or current excitation to the *device under test* the amplitude attenuation of the test signal is measured as *impedance* and the *phase shift* of the signal is measured as *phase angle*. Using *impedance spectroscopy*, electrode properties as well as properties of the surrounding medium are investigated. The resistive contribution of the electrolyte and electrode is measured at high frequencies, when the contribution of the *impedance* due to *charge transfer* at the *electrode-electrolyte interface* is low (Cogan 2008).

1.3.1.1 *Randles Cell Impedance*

A simple representation of the *impedance* of the *electrode-electrolyte interface* is the *Randles cell* (see figure 1.3c). A *spreading resistance* R_s in series with a *parallel RC* component with *double layer capacitance* C_{dl} and *charge transfer resistance* R_{ct} describes the electrolyte resistance in series with the frequency dependent resistance on the *electrode-electrolyte interface*. Due to the *frequency response* of the capacitance, the *impedance* of the *Randles cell* is a complex quantity. It can be displayed in *cartesian coordinates* with a *real part* (RE) and an *imaginary part* (IM) (see equation 1.1). The *Randles cell* incorporates only one *parallel RC circuit* and thus represents a *first-order system* with a single *time constant* $\tau = R_{ct}\ C_{dl}$. The *complex impedance* $Z(\omega)$ equals $Z(2\pi f)$, since $f = {\omega}/{2\pi}$ (Yuan et al. 2010).

$$
\begin{aligned}
Z(\omega) &= \underbrace{R_s + \frac{R_{ct}}{1+\omega^2\ {R_{ct}}^2\ {c_{dl}}^2}}_{Z_{RE}} \underbrace{- i\ \frac{\omega^2\ {R_{ct}}^2\ c_{dl}}{1+\omega^2\ {R_{ct}}^2\ {c_{dl}}^2}}_{Z_{IM}} \\
Z(\omega) &= \frac{Z_{IM}}{\sin\Phi} = \frac{Z_{RE}}{\cos\Phi} \\
\tan\Phi &= \frac{Z_{IM}}{Z_{RE}}
\end{aligned}
\tag{1.1}
$$

When the *imaginary part* Z_{IM} of the *complex impedance* $Z(\omega)$ is plotted versus the *real part* Z_{RE} for all different frequencies, the *spreading resistance* R_s and the *charge transfer resistance* R_{ct} can be determined as the intersections of a semicircle with the *real axis*. The representation of Z_{IM} and Z_{RE} in a *Nyquist plot* reflects the complex character of $Z(\omega)$ when displayed in *cartesian coordinates* (see figure 1.4).

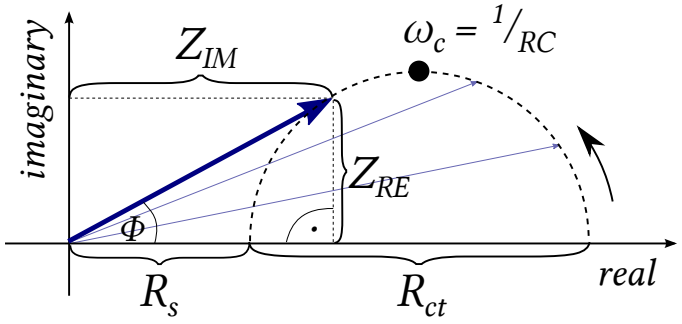

Figure 1.4: Representation of the *complex impedance* $Z(\omega)$ in cartesian coordinates. Plotting of Z_{IM} versus Z_{RE} on a *real-* and *imaginary axis*, results in a semicircle, representing a *first order system* with a single *time constant*. R_s and R_{ct} can be determinedfrom the intersections of the semi-circle with the real axis. C_{dl} can be calculated from the frequency and Z_{RE} at the apex of the semi-circle. The arrow indicates increasing frequencies.

By presenting the *complex impedance* in a *Nyquist plot*, the frequency information is lost in the graph. The frequency dependency of the magnitude of the *complex impedance* and the *phase angle* is commonly represented in a *Bode plot*. Here, the magnitude of the *complex impedance* is plotted against the frequency on a *log-log scale*, and the *phase shift* is plotted against the frequency on a *lin-log scale* (see figure 1.5). The *magnitude* representation of the *Bode plot* visualizes the properties of a *Randles cell* by means of amplitude attenuation. *Low-* and *high-frequency asymptotes* can be estimated. The *high-frequency asymptote* resembles purely ohmic amplitude attenuation of the signal (see figure 1.5a).

The phase representation of the *Bode plot* visualizes the *phase shift* of the signal. When a *phase shift* is applied to a realistic signal with a certain bandwidth the signal is distorted if the *phase delay* t_Φ varies between the different frequencies. The different frequency components of the signal are shifted by a different phase when the *phase delay* is not constant in the signal bandwidth. The *phase delay* t_Φ in the time-domain is proportional to the *phase shift* in the frequency domain with $t_\Phi(\omega) = {}^{\Phi(\omega)}/_{\omega}$. Thus, a constant *phase shift* over a certain bandwidth leads to signal distortion, whereas the signal is conserved when the *phase shift* is linear in the respective frequency band (see figure 1.5b).

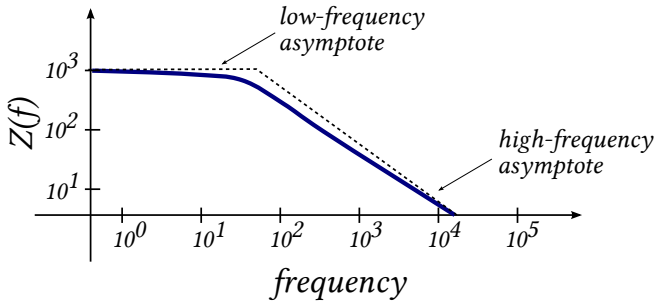

(a)

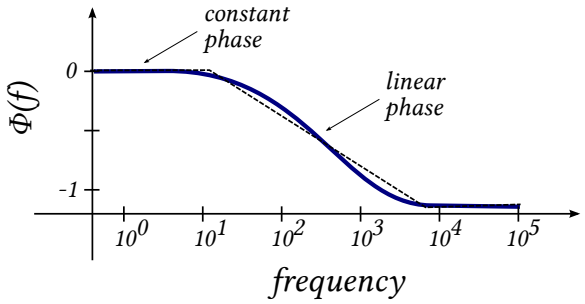

(b)

Figure 1.5: *Bode plot representation* of the magnitude and phase characteristics of the complex *impedance* $Z(\omega)$.

1.3.2 *Voltage Response*

To determine the polarization of an electrode during a current pulse, the *voltage response* is measured. The maximum polarization across the *electrode-electrolyte interface* is usually determined using a *three-electrode setup*.

1.4 *Neuronavigation*

Neuronavigation is a technique which is commonly used in neurosurgery. Generally, the term refers to *image-guided surgery*. The source of the image used as the basis for navigation differs between applications. Common intraoperative imaging methods are *computer tomography* and *magnetic resonance imaging*. Also, intraoperative *ultrasonography* and *fluoroscopy* can provide imaging in real time and thereby eliminate surgical inaccuracies (Stone & Rutka 2008). A promising new method for intraoperative imaging is *optical coherence tomography* (Xie et al. 2010).

Imaging of very small structures, however, is still difficult and inaccurate. Hence, the method of choice for neuronavigation in *deep brain stimulation* surgery is *intraoperative microelectrode recording*. To characterize the activity patterns of the target nucleus precisely, microelectrodes are inserted on the target trajectory and sequential measurements are performed, whereby neural firing rate and firing patterns are monitored in different depths (Gross et al. 2006).

1.4.1 *Targeting the Subthalamic Nucleus*

The trajectory to the *subthalamic nucleus* lies on a posterior coronal section of the rat brain. In order to reach the *subthalamic nucleus*, the *parietal association cortex*, *hippocampus*, *thalamus* and *zona incerta* have to be passed (see figure 1.6).

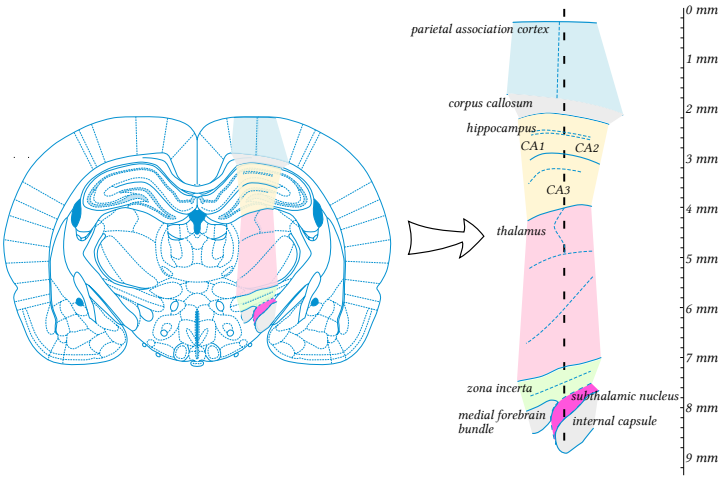

Figure 1.6: Neuronavigation on the trajectory to the *subthalamic nucleus* via the *parietal association cortex*, *hippocampus*, *thalamus*, *zona incerta* and *subthalamic nucleus*.

The cytoarchitectural organization of the *parietal association cortex* is similar to the *motor cortex*. The layered structure contains pyramidal cells in different shapes as the major cell population (Donoghue & Wise 1982). Three main classes of pyramidal cell were identified in the rat cortex according

syndrome	target	frequency	pulse width	amplitude
Parkinson's disease	*subthalamic nucleus*	145 Hz	60 µs	3.3 V
obsessive compulsive disorder	*anterior internal capsule*	100 Hz	210 µs	5.5 V
depression	*subgenual cingulate cortex*	130 Hz	90 µs	4 V
Tourette's syndrome	thalamic *CM/Pf*	130 Hz	60 µs	3.6 V

Table 1.2: Stimulation parameter for Obsessive compulsive disorder, Parkinson's disease, Depression and Tourette's syndrome in the respective target nuclei.

to morphological features. Spontaneous firing is either absent, or occurs in spontaneous bursts (Dégenètais et al. 2002).

The *hippocampus* is a layered structure, too. It is subdivided in CA1, CA2 and CA3 fields. Again, the principal cell type of the *hippocampus* is the pyramidal cell and spontaneous bursting was observed (Mazzoni et al. 2007).

In the *thalamus*, tonic firing neurons and thalamic bursters were reported to be active at the same time (Llinás & Steriade 2006). Dorsal to the highly active *thalamus* follows the *zona incerta*. In the *zona incerta*, low background activity has ben reportet (Merello et al. 2006). In the *subthalamic nucleus*, neurons are observed, which switch between single-spike activity and burst-firing mode (Beurrier et al. 1999).

1.5 *Deep Brain Stimulation*

Deep brain stimulation is a technique for neurostimulation. Electrodes are directly implanted into the region of the brain which is functionally related to the symptomatic pattern of the disease (DeLong & Wichmann 2007). The beneficial effects of *deep brain stimulation* in the *subthalamic nucleus* have been shown to be remarkable for the parkinsonian motor symptoms *rigor*, *tremor* and *akinesia* (Weaver et al. 2009). Along with the beneficial effects on the motor system, adverse effects of *deep brain stimulation* in the *subthalamic nucleus* have been reported. Short term problems occur due to intracerebral bleeding during surgery, lead misplacement and hardware issues. When the electrode implantation was unproblematic, tissue gliosis and reduced word fluency are the most abundant adverse side effects. Also, behavioural changes such as cognitive dysfunctions, depression and mania were reported (Temel et al. 2006, Saint-Cyr et al. 2000, Pillon et al. 2000).

Recently, *deep brain stimulation* is being explored for the treatment of other psychomotoric disorders, originating from structures outside the *basal ganglia*. Clinical studies examine *deep brain stimulation* in the *subgenual cingulate cortex* for *depression*, the *anterior internal capsule* for *obsessive-compulsive disorder* and the thalamic *centre median/parafascicular* nucleus

for *Tourette's syndrome* (Nuttin et al. 2003, Mayberg et al. 2005, Maciunas et al. 2007).

For all these applications, rectangular pulses with a frequency of 100-150 Hz and 60-90 µs pulse duration are delivered with stimulation amplitudes of 3-5 V (see table 1.2). The similarity of the stimulation parameter for all these applications is not based on a rational working hypothesis of electrical stimulation in the brain, but is more related to the fact that they are all based on the parameters for *deep brain stimulation* in the *subthalamic nucleus*, which were empirically determined over the last 15 years (Kuncel & Grill 2004).

1.5.1 *Mechanism of Action*

According to current understanding, the positive effect of *deep brain stimulation* on parkinsonian motor symptoms is paradox. Understanding the mechanism of *deep brain stimulation* means to solve the question how electrical stimulation, traditionally thought to activate neurons, results in the same effect as ablation of the target structure. It is debated, wether the functional ablation of the target nucleus is achieved by direct inhibition due to electrical stimulation (see section 1.5.1.1), or if electrical stimulation acts by local excitation (see section 1.5.1.2), which is translated to functional inhibition of the target by transmission through the neuronal network. There are different models to explain the one or the other hypothesis (Vitek 2002, McIntyre et al. 2004). Recent work even brought the role of astrocytes into focus (Vedam-Mai et al. 2011).

When referring to *deep brain stimulation* in a research context, the term *electrical high-frequency stimulation* is often used. This notation clearly determines that frequencies above 100 Hz must be used for effective electrical stimulation (Lozano et al. 2002). Also, *electrical high-frequency stimulation* does not imply the local confinement to *thalamic-* and *subthalamic areas* as it has been originally the case for the clinical term *deep brain stimulation*.

1.5.1.1 *Direct Inhibition*

Two models emphasize direct inhibition of the stimulated neurons. One of them, often referred to as *depolarization blockade* explains the effect of *electrical high-frequency stimulation* as a transient blockade of *voltage-gated currents* in subthalamic neurons. The model is based on the observation that a period of several minutes of neuronal silence follows *electrical high-frequency stimulation* in the *subthalamic nucleus* (Beurrier et al. 2001). Since indications of transmitter depletion were reported from imaging studies with *voltage-sensitive dyes*, *synaptic depression* was hypothesized as another reason for direct inhibition of the stimulated nucleus (Urbano et al. 2002).

1.5.1.2 *Local Excitation*

Although there are indications for direct inhibition of neurons due to electrical stimulation, increased transmitter release and firing activity have been found in efferent nuclei after *electrical high-frequency stimulation* (Windels et al. 2003, Anderson et al. 2003). Therefore, the models for local excitation seem to be more likely.

A model which is consistent with these data is the *disruption of pathological network activity*. This model proposes orthodromic activation of target neurons replacing the pathological network activity by a stimulus driven firing pattern (Hammond et al. 2008). It complies well with the observation that increased power in the β-band of *local field potentials* correlates with the severity of parkinsonian motor symptoms (Gatev et al. 2006, Hammond et al. 2007, Brown 2007). Also, pathological *low-frequency* rhythmic bursting near the tremor frequency at 7-10 Hz has been observed in animal models of the disease (Bergman et al. 1994, Raz et al. 2000). Normally uncorrelated firing across cells becomes synchronized at about twice that frequency (Nini et al. 1995). Recent electrophysiological studies and modelling approaches substantiate these findings (Dorval et al. 2010, Schiff 2010). The main message from this model is that the beneficial effects of *deep brain stimulation* might not be related to the firing rate of neurons but rather to the disruption of *low-frequency bursting*, disruption of synchrony in the beta band, or both (Hashimoto et al. 2003, Wilson et al. 2011).

Although these findings are consistent, they are lacking an explanation of the described effects on the molecular level. The model of *synaptic inhibition* might provide just that (Feuerstein et al. 2011). Here, the effect of *deep brain stimulation* is explained by activation of axon terminals that make synaptic connections with neurons near the stimulation electrode. Electrophysiological recordings of neuronal activity near the stimulation site revealed that synaptic events such as the release of an inhibitory neurotransmitter might lead to effective inhibition of the stimulated nucleus (Dostrovsky et al. 2000, Benazzouz et al. 1995). The inhibitory neurotransmitter *γ-aminobutyric acid* (GABA) was identified to be a key player to convey synaptic inhibition and its role was further elucidated (Benabid et al. 2002). Neurochemical studies in the *caudate putamen* of the rat showed that GABAergic interneurons with functional $GABA_A$ receptors are necessary to evoke a neurochemical effect of *electrical high-frequency stimulation* (Moser et al. 2003b). Also, increased GABA release from GABAergic interneurons was characterized as an immediate effect of *electrical high-frequency stimulation* (Li et al. 2004). Beyond that, a certain form of neuronal pre-activation was identified as a prerequisite for successful *electrical high-frequency stimulation* applied *in vitro* and *in vivo* (Li et al. 2006, Mantovani et al. 2006, Hiller et al. 2007).

1.5.2 *Approved Equipment for Deep Brain Stimulation*

Only in 1987, *deep brain stimulation* was first introduced as a definitive long term alternative to destructive thalamic surgery for patients with *Parkin-*

Parameter	Value
Voltage amplitude	0-10.5 V in steps of 0.1 V
Frequency	3-250 Hz
Pulse	60-450 µs in 30 µs increments
Cycling	1 s to 24 h *on/off*

Table 1.3: Medtronic© neurostimulator output capability. Data from (Coffey 2009).

son's disease (Benabid et al. 1987). From then, use of the technique advanced rapidly with more than 75 000 implanted *deep brain stimulation* devices today (Shah et al. 2010).

The most commonly used devices are the Medtronic© systems. They consist of concentric, polyurethane insulated leads with four electrode contact sites for brain implantation, burr hole caps to anchor the lead and seal the cranial opening and a battery powered neurostimulator unit for *subcutaneous* implantation into the *infraclavicular* pocket with *subcutaneous* extension cables to connect to the cranial leads.

The neurostimulator device can be fully programmed after implantation. Lead contacts can be selected to be positive, negative, on or off in any combination, the stimulation mode can be bipolar or monopolar with the neurostimulator case set to positive. The neurostimulator device delivers constant voltage, biphasic and charge-balanced pulse trains (Lilly 1961). Stimulation parameters can be adjusted according to table 1.3 and are independently programmable for each lead in dual channel applications.

Fully programmable physician- and patient controllers with more limited functions use skin contact radio frequency telemetry to program the neurostimulator. The neurostimulator batteries are not rechargeable, and typical stimulation paradigma for bilateral implants for *Parkinson's disease* yield a battery life of approximately 3.5 years (Coffey 2009).

The *food and drug association* approved leads for *deep brain stimulation* have an outer diameter of 1.27 mm and are 28 or 40 mm long with a polyurethane jacket which is exposed to the brain tissue. The leads are inserted through a stainless steel cannula which is withdrawn after insertion into the brain leaving the lead in place. Four annular *platinum/iridium* electrode contacts are exposed near the lead tip. The resistance of each conductor to contact pathway is lower than 100 Ω. At present, three models of *deep brain simulation* leads are available with different contact lengths and spacing dimensions regarding their intracerebral target site (see table 1.4).

The *geometric surface area* of all lead contact sites is 0.06 cm^2. The impedance of the implanted leads is approximately 1.2 kΩ at 1 kHz (Butson et al. 2006). Although the device is capable to deliver charge densities larger than 30 $\mu C/cm^2$, the value is considered as the threshold for safe stimulation (Lilly 1961).

Model number	Contact length	Contact spacing	Targets	Applications
3387	1.5 mm	1.5 mm	*thalamus*, *globus pallidus*, *subthalamic nucleus*	tremor, dystonia, epilepsy, Parkinson's disease
3389	1.5 mm	0.5 mm	*subthalamic nucleus*	Parkinson's disease
3391	3.0 mm	4.0 mm	*ventral striatum*, *internal capsule*	depression, obsessive compulsive disorder

Table 1.4: Leads for *deep brain stimulation* applications. Data from (Coffey 2009).

As it is today, implantation of *deep brain stimulation* systems is a multi-step procedure. The patient's head is mounted into a stereotaxic frame, and *magnetic resonance imaging* is used to determine the anatomical reference marks for neuronavigation. Under local anaesthesia, the skull is trepanated and four or five individual microelectrodes are inserted. Neuronavigation (see section 1.4) is performed, and the trajectory giving the most characteristic signal for the target region is chosen for lead implantation. In case of bilateral applications, this process is repeated for the other hemisphere. Then, under full anaesthesia, the neurostimulator device is implanted into the *infraclavicular* pocket, and the *subcutaneous* connections to the *deep brain stimulation* leads are placed.

1.5.3 *New Approaches to Deep Brain Stimulation*

Deep brain stimulation has become a tool to manage a range of neurological and psychiatric disorders. There is no fully acknowledged theory on the mechanism of action. Yet, there seems to be a relative specific mechanism on cellular level. Therefore, it seems wrong to adopt stimulation parameters empirically established to treat motor symptoms of *Parkinson's disease*, and use them in completely different neuronal circuits to treat *depression* and *Tourette's syndrome* (Shah et al. 2010). Current advances lead the way to *closed-loop systems* that could provide tailored stimulation to target the specific conditions (Osorio et al. 2001). Ultra-high resolution 7.5 T *magnetic resonance tomography* supports target identification and placement of *closed-loop systems*. The ability to built miniaturized, low-power *brain computer interface* microsystems that enable high-performance on-line signal processing facilitate computation for *closed-loop systems*. And, production of chronically implantable, biocompatible and stable probes, usable for stimulation and recording provide interfaces for *closed-loop systems* (Johnson et al. 2008).

Contemporary *brain computer interfaces* have been used very successfully. The *cochlear implant* and the *retinal stimulator* are the most widely used neural prostheses interfacing the nervous system (Cosetti & Waltzman 2011, Krisch & Hosticka 2007). Cortical *brain computer interfaces* use microelectrode arrays with low penetration depth to record activity from hundreds

of neurons to convey precise direction of hand movement (Georgopolous et al. 1986, Hochberg et al. 2006). Simultaneous firing patterns in the cortex were associated with limb movement in a three dimensional space and used to move a cursor on a computer screen or control a robotic arm (Schwartz et al. 1988, Taylor et al. 2002).

Brain computer interfaces for applications which are relevant for the target regions of *deep brain stimulation* are not common for several reasons. The encoding strategies in the *basal ganglia* are currently unknown (Parush et al. 2008). Electrode layouts for deeply penetrating microelectrodes exist, but typically have a small number of recording sites. Most commonly used microelectrodes do not support combined recording and stimulation. Yet, recent microelectrode layouts allow multi-channel recording and reflect the trend of probe development (Rousche et al. 2001, Stieglitz 2002)

Metal wire microelectrodes are the most widely used neural probes so far. Typically, electrolytically sharpened wires are used which are completely insulated except for an exposed area on the tip. Contact materials are *platinum*, *iridium*, *platinum-iridium*, *gold*, *stainless steel* or *tungsten*. Highly dielectric insulation materials such as *teflon*, *polyimide*, and *parylene* are used. Multi electrode arrays can be made by glueing individual metal wire electrodes together or by using wire bundles (Hammad et al. 2010, Tsytsarev et al. 2006). *Metal wire microelectrodes* are cheap and easy to produce but they can record activity only at their tip and increasing the number of recording sites implies increasing probe diameter. Due to the lack of automation, the probes differ between manufacturers and batches.

Silicon based neural probes are produced with high precision and accuracy using micromachining techniques. Using batch processes, the probes can be produced at low cost. Also, the use of silicon micromachining facilitates production of active probes with integrated signal processing circuitry. Photolithography enables placement of differently sized recording sites along the shaft of the electrode in well defined distances. Thus, a large number of recording sites can be located in a small volume. Examples of *silicon based probes* are the well known *Michigan probes* and the *Utah array* (HajjHassan et al. 2008), and the *ACREO* probes for deep tissue insertion (Hofmann et al. 2006, Jensen et al. 2006)

Many different layouts of single-shaft, multi-shaft, and three-dimensionally stacked *Michigan probes* are used. *Gold*, *platinum*, or *iridium* is used for recording sites. The insulation on top of *silicon substrate* is made from triple layers of *silicon dioxide*, *silicon nitride*, and *silicon dioxide*. Yet, due to the relatively large diameter, guide tools are needed for insertion into the brain. Mechanical instability and breaking of the probe during insertion is a huge problem (Kipke et al. 2003, Wise et al. 2004).

The *Utah arrays* are made from boron doped silicon substrates. The electrochemically sharpened probe tips are coated with *gold*, *platinum*, or *iridium* for recording and stimulation. *Polyimide* is used to coat the probes as the insulation layer with only the recording sites exposed. The probe length of the *Utah array* structures is limited to about 1.5 mm, and only one record-

ing site is located on the probe shaft, since the probe is produced vertically. Due to their stiffness, they are not suited for long term chronic implantation in humans (Normann et al. 1999, Suner et al. 2005).

For production of *polymer microelectrodes*, biocompatible polymers such as *polyimide* and *parylene* are used to support the conducting regions of the probes to form a biocompatible interface between the probe and the brain tissue. Flexible neural probes were produced with a gold metal layer for recording sites sandwiched between two *polyimide* layers. The use of flexible probes reduces tissue irritation, since the electrode can move with the brain. A large problem is electrode insertion, since they are not stiff enough. Also, moisture absorption by the polymer can lead to probe failure (Rousche et al. 2001, Takeuchi et al. 2004).

1.5.4 *Animal Models of Parkinson's Disease*

Parkinson's disease is a progressive neurodegenerative disorder. The severity and type of symptoms depends on the time since onset, the rapidity of functional decline and the treatment. Positive motor symptoms are tremor at rest, muscular rigidity and involuntary movements as side effect of *dopamine* substitution therapy. Also, negative motor symptoms such as poverty or slowing of movement and postural disturbances occur. Apart from the motor deficits, psychomotor signs are cognitive dysfunction, dementia and depression.

Idiopathic *Parkinson's disease* is characterized by degeneration of dopaminergic neurons. The axons of dopaminergic neurons, located in the *substantia nigra pars compacta* run along the *medial forebrain bundle* and terminate in the *dorsal striatum*. Dopaminergic neurons in the *retrorubral area in the midbrain* project to the *ventrocaudal putamen*, and dopaminergic neurons in the *ventral tegmental area* project to the *nucleus accumbens*. From these three pathways, the nigrostriatal pathway seems to be most heavily damaged by the loss of dopaminergic neurons in *Parkinson's disease*.

Beyond the loss of *dopamine*, damage has been found in noradrenergic, cholinergic and serotonergic cell populations, which may play an important role in the psychomotor aspects of *Parkinson's disease* (Jellinger 1990).

A neurotoxin that leads to degeneration of mainly dopaminergic neurons is *6-hydroxydopamine*. It is taken up into dopaminergic and noradrenergic neurons and causes degeneration of nerve terminals by oxidative stress while mitochondrial respiratory enzymes are blocked (Glinka et al. 1997).

To test therapeutic strategies, experimental models of *Parkinson's disease* are used. In preclinical research, the catecholamine neurotoxin *6-hydroxydopamine* is mostly injected into the *substantia nigra pars compacta*, *medial forebrain bundle* or the *caudate putamen* (Deumens et al. 2002).

Following neurotoxin injection, compensatory responses to loss of dopamine are observed including increased metabolic turnover and heightened activity in the remaining dopaminergic cells as well as increased postsynaptic *dopamine* receptor density and sensitivity. Compensatory responses to

dopamine depletion are the reason for rotational behaviour after unilateral lesions of the dopaminergic system. They cause an asymmetry in striatal activity compared between the lesioned and unlesioned side making the animal to rotate away from the side of greater activity (Ungerstedt 1971).

Subcutaneous administration of the *dopamine* releasing agent amphetamine creates a *dopamine* imbalance favouring the nonlesioned side and leads to ipsilateral turning behaviour. This imbalance can even be detected with 50 % loss of dopaminergic neurons. The *dopamine* receptor agonist *apomorphine* induces contralateral rotation due to denervation supersensitivity (Ungerstedt 1971). Postsynaptic supersensitivity occurs only when most of the dopaminergic neurons are lost. Thus, rats with light lesions show no rotational asymmetry in response to *apomorphine* . Therefore, *apomorphine* was reported to be a better predictor of extensive *6-hydroxydopamine* lesions (Hudson et al. 1993).

1.5.4.1 *Medial Forebrain Bundle Lesions*

6-hydroxydopamine injection into the *medial forebrain bundle* leads to a near total destruction of dopaminergic terminals arising from the *substantia nigra pars compacta* and the *ventral tegmental area*. The loss of *dopamine* usually occurs rapidly and complete and the expected rotational behaviour is observed with unilateral lesions. Yet, more specific degeneration of dopaminergic neurons in the *nigrostriatal pathway* resembles the pattern of neurodegeneration observed in human idiopathic *Parkinson's disease* more closely. Further, bilateral *medial forebrain bundle lesions* lead to adipsia and aphagia in the lesioned animal (Ungerstedt 1971).

1.5.4.2 *Substantia Nigra Lesions*

Lesions of the *substantia nigra pars compacta* are used to produce a more selective model with moderate *dopamine* depletion in which the number of lesioned dopaminergic neurons correlates with *apomorphine* induced turning behaviour (Carman et al. 1991). Bilateral models of *Parkinson's disease* by injection of *6-hydroxydopamine* into the *substantia nigra* on both sides have been achieved (Deumens et al. 2002).

1.5.4.3 *Striatal Lesions*

Highest selectivity can be reached by lesions in different parts of the *caudate putamen*. The ventrolateral sector receives input from motor and sensimotor areas of the neocortex, and *dopamine* innervation originate mainly from the *substantia nigra pars compacta*. The dorsomedial sector receives a mixed innervation from *substantia nigra pars compacta* and *ventral tegmental area*. Different behavioural responses can be induced choosing one or more lesion sites in the *caudate putamen*. Neurotoxin injections into the ventrolateral *caudate putamen* lead to *apomorphine* induced rotations when *dopamine* depletion of more than 90 % is achieved (Kirik et al. 1998).

Lesions in the *ventrolateral caudate putamen* have been reported to be most suitable for modelling Parkinson's disease (Deumens et al. 2002). Injection of *6-hydroxydopamine* into the *ventrolateral caudate putamen* leads to decreased dopaminergic input. This results in diminished activation of D_1 and D_2 receptors, leading to less inhibition of the *subthalamic nucleus* via the direct and indirect way (DeLong & Wichmann 2007). This causes the overactivity of the *subthalamic nucleus*, which is reported to be the reason for generation of motor symptoms in *Parkinson's disease* (Kreitzer & Malenka 2008). Concurrent implantation of a stimulation electrode into the *subthalamic nucleus* makes the striatal model for *Parkinson's disease* a tool to study the effects of *subthalamic deep brain stimulation* in the animal model of *Parkinson's disease* (see figure 1.7).

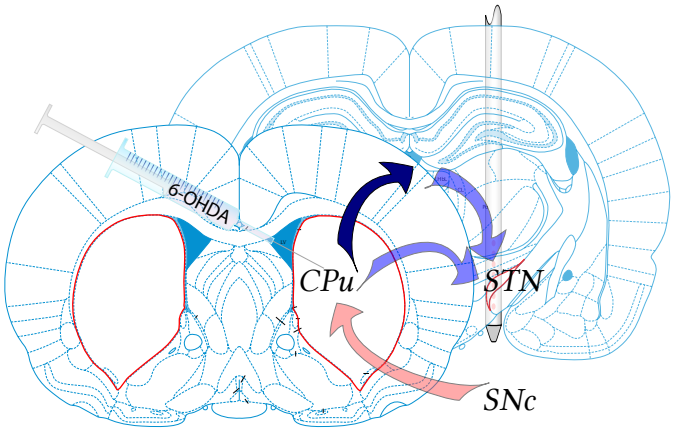

Figure 1.7: The *nigrostriatal pathway* in the rat brain with dopaminergic projections (red) from the *substantia nigra pars compacta* (SNc) to the *caudate putamen*, and GABAergic neurons (blue) with direct or indirect connection to the *subthalamic nucleus* (DeLong & Wichmann 2007)

1.6 *Aim of the Current Work*

It is the design of the electrode that determines which type of neuronal activity is recorded or which neuronal elements are subjected to electrical stimulation. Since the mechanism of electrical stimulation in the brain is not fully understood and many variables of the neural tissue and implications of probe design are still unknown it is advisable to test the development states of new types of neural probes under realistic conditions.

Two types of neural probes are presented in this work. Both probe types are bimodal probes for recording and electrical stimulation. The presented *Linear Array Probe* design is a more conventional lateral array of recording sites arranged along a thin steel shaft with a stimulation site on the tip of the shaft. The presented *Flexible Array Probe* design features a lateral array of mixed recording and stimulation sites arranged on *polyimide* film as carrier. The use of flexible probes for intracerebral applications is a very new

approach and has been rarely used before. To allow a certain measure of comparability between the probe layouts only the deepest stimulation site on the tip of the *Flexible Array Probe* design was used.

The presented probes were designed for feedback controlled electrical stimulation in the *subthalamic nucleus* of the rat brain, and the probes' development is directed towards *closed-loop systems* for *deep brain stimulation* in patients suffering from *Parkinson's disease*.

The probes' lateral array design with recording sites evenly spaced over a depth of 1 mm at the end of the shaft and a stimulation site at the tip assumes that the appropriate feedback signal is to be found in the parallel circuits of the *subthalamic nucleus* or its direct neighbours. The size of the stimulation sites was chosen to record high-frequency neuronal activity related to neuronal discharges in the close vicinity of the recording site. That is in agreement with the assumption that the feedback signal is to be found in the closer vicinity of the stimulation site. Yet, the size of the recording sites was chosen to be large enough to record activity from more than a single neuron with low thermal noise levels. That implies, that activity can be recorded even when neuronal elements are farther away from the recording site but also that the activity recorded from the electrode is not necessarily originating from a single neuronal element.

The neuronal probes used in the work at hand were tested under real conditions. The testing procedure was focused towards finding probable candidates for a feedback signal for feedback controlled subthalamic *deep brain stimulation* with regards to the assumptions that were made by probe design.

The whole purpose of feedback controlled *deep brain stimulation* in patients suffering from *Parkinson's disease* is to reduce the amount of current injected into the tissue even when its not immediately necessary to diminish stimulation induced side effects and increase battery life of the stimulation devices. Therefore, the search for feedback parameters was confined towards the long term neuronal response to electrical stimulation in a time range of one minute.

Previous work that focused on the effect of neuronal stimulation and used electropysiological recordings to analyse this effect was concerned with the immediate short term response of neural activity to electrical stimulation. Especially studies concerned with high-frequency neuronal response are mostly limited to a time range of a few seconds.

Yet, evidence exist that there is a long term effect of *high-frequency electrical microstimulation* on neuronal discharge activity. The studies which lead to such conclusions are mostly performed on the level of *neurochemistry*. It has been shown that the inhibitory neurotransmitter *γ-aminobutyric acid* increased after *high-frequency microstimulation* in the awake and freely moving animal over a time range of minutes (Hiller et al. 2007). Related studies give rise to the assumption that GABAergic interneurons with functional $GABA_A$ receptors are specific targets for *high-frequency microstimulation* (Moser et al. 2003b, Li et al. 2004, 2006, Mantovani et al. 2006, Hiller et al. 2007).

The aim of this thesis is to find candidate parameters that provide information about high-frequency neural discharge after *high-frequency microstimulation* in a long time range and could be used as feedback parameters for *closed-loop systems* for *deep brain stimulation* developed with the new type of bimodal probes which were used in the project. Along with that, the possibility of an effect of *high-frequency microstimulation* that leads to a specific increase or decrease in spike activity of certain neural elements should be investigated.

2

MATERIALS AND METHODS

2.1 *Probes for Neural Recording and Stimulation*

In the presented work, we used stiff type *Linear Array Probes* as well as *Flexible Array Probes* for neural single unit recording and microstimulation. The probes were provided by the *"Institut für Mikrotechnik Mainz GmbH"* as part of the research project BiCIRTS, which was funded by the *German Minitry of Research* (BMBF).

2.1.1 *Linear Array Probes*

The *Linear Array Probes* (see figure 2.1) provide seven recording sites and one stimulation site. The array of recording sites is arranged along the probe shaft over a distance of 750 µm with a centre-to-centre distance of 125 µm starting 400 µm from the tip. A single recording site has a surface area of 3.85×10^{-5} cm^2. The stimulation site is located at the tip of the electrode and has a surface area of 1.13×10^{-4} cm^2. All electrode contact sites are made from gold. The contacts are embedded in a stainless steel shaft with 300 µm diameter and a total length of 10 mm. The stainless steel shaft is used as ground for recording and current sink for stimulation. It is connected to the plug housing. A housed mini-PCB with female jack (*HRS, ST60-10P*) provides the connection interface.

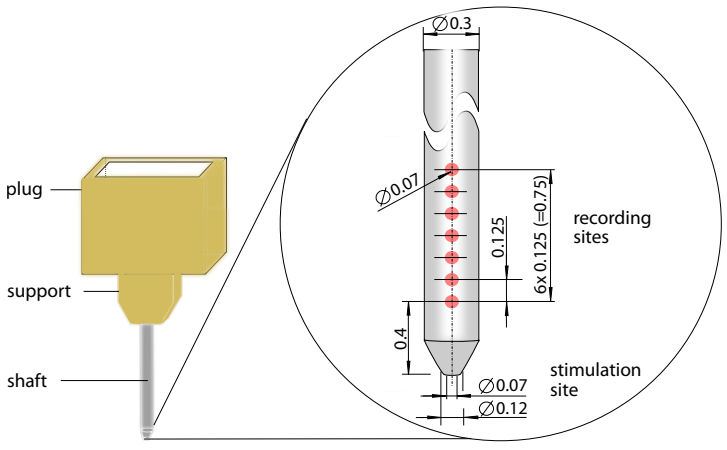

Figure 2.1: *Linear Array Probe* with seven recording sites and one stimulation site on the tip of the electrode.

2.1.2 *Flexible Array Probes*

The *Flexible Array Probe* (see figure 2.2) was microfabricated from electrospun *polyimide*. *Gold* contact sites were vapour deposited and galvanically reinforced. The probe was manufactured on 8 inch silicone wafers. Many different layouts were produced. Designs, accomodating up to 22 recording sites with an area of $4x10^{-6}$ cm^2 to $1.6x10^{-5}$ cm^2 and ten additional stimulation sites with an area of $3.6x10^{-5}$ cm^2 were feasible with conductor path width and distance of 10 µm on a 750 µm wide shaft. All probe layouts feature alternating recording and stimulation sites as well as large surface ground contacts and a reinforced punch hole at the tip to facilitate tissue insertion (see section 2.4.3.2).

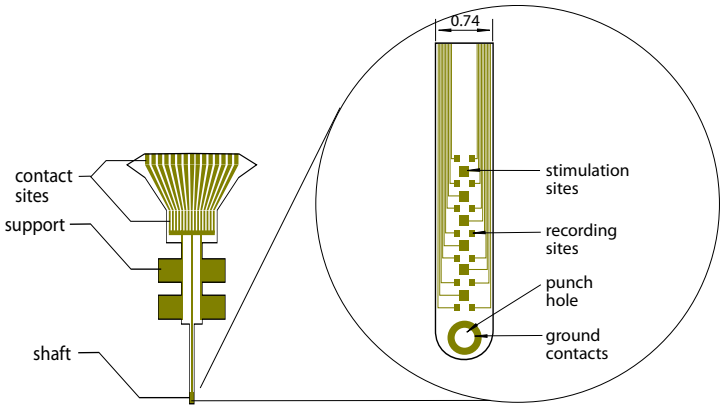

Figure 2.2: *Flexible Array Probe* schematic with alternating recording and stimulation sites.

For the neural recording and microstimulation experiments, two different probe layouts were used (see figure 2.3 and section 2.4). Both layouts feature large area ground contacts which are distributed between the recording and stimulation sites and a punching hole at the probe tip.

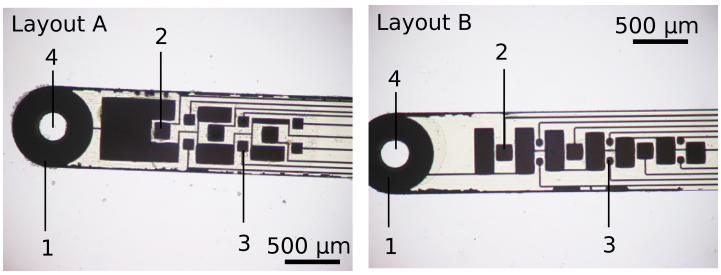

Figure 2.3: *Flexible Array Probe* layouts used for neural recording and microstimulation. Large area ground contacts (1) are distributed between stimulation (2) and recording sites (3). A punching hole on the tip facilitates tissue insertion.

Layout A provides three $3.6x10^{-5}$ cm^2 stimulation contacts, arranged linearly in the middle of the probe shaft and six $1.6x10^{-5}$ cm^2, off-centred record-

ing sites, placed between the stimulation contacts. Layout B is equipped with the same number of contacts. The recording sites are $4x10^{-6}$ cm^2 in size and the large area ground contacts are placed between the recording and stimulation sites.

Both layouts provide ten enforced *gold* contacts with 0.5 mm pitch for connection. To equip the connections interface with the same connector as used for the *Linear Array Probes*, a small PCB was designed using a *Graphical Layout Editor* (*EAGLE v5.11.0, CadSoft*). The PCB accommodated solder patches for a rotary lock FFC connector (*Omron, XF2M-1015-1*) on the front and for the female jack (see section 2.1.1) on the back. Both connectors were soldered to the PCB. The connection interface on the *Flexible Array Probe* was stabilized and adjusted to 0.3 mm thickness using several layers of sticky tape and was then inserted into the FFC connector (see figure 2.4).

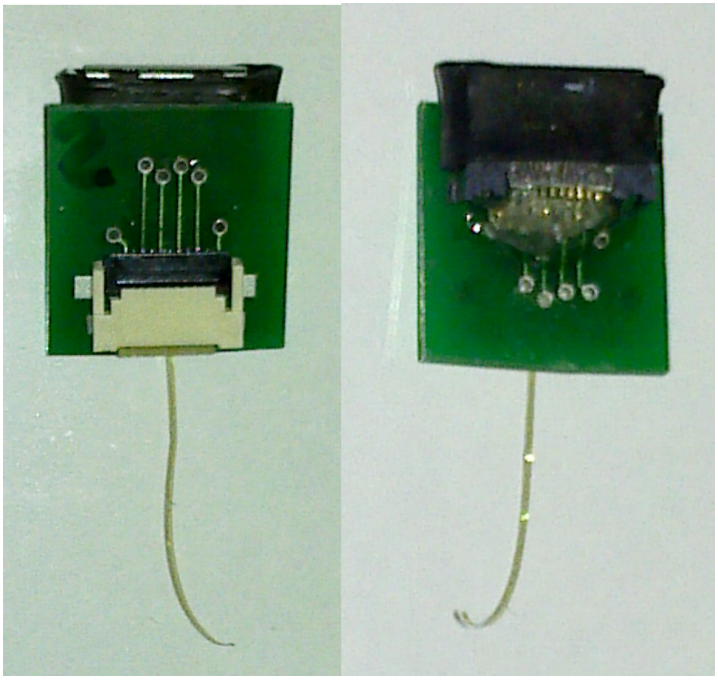

Figure 2.4: *Flexible Array Probe* assembled with connection interface.

2.1.3 *Connection to Commercial Hardware*

All probes were connected to the commercial hardware for neural recording and stimulation (see section 2.2.1 and section 2.2.2) using the same female jack (*HRS, ST60-10P*) connection interface.

For each probe, a self-made adapter to the 32 channel ZIF-Clip® headstage Adapter (*ZCA-NN32, Tucker Davis Technologies*) was manufactured from a male mobile connector (*HRS, ST40-10P*) which was connected to a male pin connector (*Samtec, MOLC-140-01*) compatible to the ZCA-NN32 headstage adapter. The channel configuration of each probe was matched to the channel configuration of the commercial hardware (see section 2.2). The probes'

Table 2.1: Charge densities at the stimulation sites of *Linear-* and *Flexible Array Probes*during stimulation with rectangular pulses with 60 µs duration and 0.1-0.4 mA current amplitude.

current [mA]	0.1 mA	0.2 mA	0.3 mA	0.4 mA
charge per phase (60 µs)	6 nC	12 nC	18 nC	24 nC
Linear Array Probes				
charge density ($1.13x10^{-4}$ cm^2)	0.053 mC/cm^2	0.106 mC/cm^2	0.159 mC/cm^2	0.212 mC/cm^2
Flexible Array Probes				
charge density ($3.6x10^{-5}$ cm^2)	0.167 mC/cm^2	0.333 mC/cm^2	0.500 mC/cm^2	0.667 mC/cm^2

ground contact was connected to reference and ground of the headstage adapter, which were shortcut together. An external two pin socket for the stimulation site and ground was provided on the outer side of the MOLC and later connected to the current controlled stimulator.

2.2 *Hardware*

2.2.1 *Stimulation Hardware*

For electrical stimulation a single-channel current controlled stimulus isolator (*Isostim A320, WPI Inc.*) was used. The rechargeable stimulator is powered by sixteen 9 V alkaline batteries and has a compliance voltage of 100 V. The device was run in continuous mode, pulse interval and pulse width were set to 8 ms and 60 μs. Stimulus currents of 0.0-0.4 mA were applied. A continuous waveform DC pulse with 8 µs current rise time and 10 µs current fall time was generated by internal timing. The stimulus isolator was connected to the electrode so that the current was flowing from the stimulation contact site to the electrode ground. An oscilloscope (*TDS2004B, Tektronix, Inc.*) was used to monitor the *voltage response* of the electrode. The stimulation pulse waveform was recorded using NI LabVIEW SignalExpress (*v2004, National Instruments*).

Calculated charge densities per phase during current controlled stimulation with 0.1-0.4 mA current amplitude and 60 µs pulse width at the *Linear-* and *Flexible Array Probe* stimulation sites are shown in table 2.1

2.2.2 *Recording Hardware*

For multi-channel neural recordings an RZ5 BioAmp Processor (*Tucker Davis Technologies*) was used. Two battery powered 16-channel Medusa pream-

plifiers (*RA16PA, Tucker Davis Technologies*) were used. The preamplifiers provide 24.414 kHz maximum sampling rate, 100 kΩ input *impedance* and 3 dB *frequency response* between 2 Hz and 7.5 kHz. The 32-channel ZIF-Clip® digital headstage and the ZCA-NN32 headstage adapter were used to connect the bimodal probes via the self-made adapter (see section 2.1). For the chronic experiments with freely behaving animals, the AC32 motorized commutator was used.

2.3 *Impedance Spectroscopy*

Impedance and *phase angle* of all electrode sites were measured using a LCR-800 *impedance* spectrometer (*Good Will Instruments Co., Ltd*).

Using the standard *three electrode setup*, a sinusoidal waveform with frequencies between 0.1 and 100 kHz and 10 mV amplitude was applied between a large area *platinum counter electrode* and a non-polarizable *Ag/AgCl reference electrode*. The signal was measured using the electrode contact site as *working electrode*. All measurements were performed in 0.9 % *saline* solution which was constantly agitated using a magnetic stirrer.

The LCR-800 *impedance* spectrometer was controlled via a MATLAB® interface (*MATLAB 2008a, The MathWorks*) (see Appendix B). A *frequency sweep experiment* was performed (see Appendix B) and a frequency spectrum was recorded for the *impedance* and *phase angle* with n = 8. Each experiment was carried out three times. Mean values and standard deviations were calculated. The data were fitted using the *leastsq* method from the *Scipy optimize* module (Jones et al. 2001). The fit function Z_{fit} for the *complex impedance* $Z(\omega)$ described by the *Randles cell* equivalent circuit was used to estimate the parameter R_s, R_{ct} and C_{dl} (see equation 2.1 and section 1.3.1). Variances were determined from the diagonal of the covariance matrix.

$$
\begin{aligned}
Z_{RE} &= R_s \; + \; \frac{R_{ct}}{1 + \omega^2 \; {R_{ct}}^2 \; {C_{dl}}^2} \\
Z_{IM} &= - \; i \; \frac{\omega^2 \; {R_{ct}}^2 \; c_{dl}}{1 + \omega^2 \; {R_{ct}}^2 \; {C_{dl}}^2} \\
Z_{fit} &= \frac{Z_{IM}}{-1 \; \sin\left(\arctan\left(\frac{Z_{IM}}{Z_{RE}}\right)\right)}
\end{aligned}
\tag{2.1}
$$

The χ^2 error of the fit was calculated using equation 2.2 by taking the sum of the squared difference between the measure *impedance* Z_{exp} and the fitted *impedance* Z_{fit}, weighted by Z_{exp}.

$$
\chi^2 = \sum \left(Z_{exp} - Z_{fit}\right)^2 / Z_{fit} \tag{2.2}
$$

The fitted *impedance* Z_{fit} and *phase angle* Φ are presented in a *Bode plot* with the absolute values plotted against the frequency on a semilogarithmic scale. For the *Nyquist plot*, the real and imaginary parts Z_{RE} and Z_{IM} of

the measured *impedance* were calculated and plotted against each other (see equation 2.3).

$$\begin{aligned} Z_{RE} &= Z_{exp}\left(\cos\left(rad\left(\Phi_{exp}\right)\right)\right) \\ Z_{IM} &= \left|Z_{exp}\left(\sin\left(rad\left(\Phi_{exp}\right)\right)\right)\right| \end{aligned} \tag{2.3}$$

The *impedance* values of recording and stimulation sites were analysed at 1 kHz. Mean values and standard deviations of the 1 kHz *impedances* for all recording and stimulation sites were calculated and compared to each other.

2.4 *Chronic Experiments*

Neuronal recording and *high frequency microstimulation* experiments with bimodal *Linear-* and *Flexible Array Probes* were conducted in awake and freely moving rats with chronically implanted probes. A stereotaxic surgery was carried out to ensure precise probe insertion into the *subthalamic nucleus*. Animals received a lesion of striatonigral *dopamine* by injection of neurotoxin solution into the *ventrolateral caudate putamen* or sham treatment by injection of 0.9 % *saline* into the same area. While the probe was lowered into the brain tissue in steps of 200 µm, the neuronal activity was measured at each depth and *neuronavigation* was performed. For the measurements, a ground screw was placed into the skull and electrical connections were made as described in section 2.2.2. The target area for electrophysiological recording and *high frequency microstimulation* was the *subthalamic nucleus*. After insertion, the probe was fixed to the skull by using dental cement and skull screws for fixation as anchors. After the surgery, the animals were allowed to recover, and experiments were performed to establish the effect of electrical and chemical stimulation on the neuronal activity in the target structure.

2.4.1 *Animals*

All procedures with animals were reviewed and approved by the University of Lübeck and the Ministry for Agriculture, the Environment and Rural Areas, Schleswig-Holstein, Germany, and were conducted in accordance with the NIH guide for the Care and Use of laboratory animals. Male Wistar rats were used and housed separately under standard lightning conditions (12 h light-dark cycle, lights on at 06:00 am), 22 ℃ and 40 % humidity with free access to food and water.

2.4.2 *Surgical Procedure*

The stereotaxic surgery for precise probe insertion was carried out after a standard protocol (see Appendix E). Prior to the surgery, animals received initial inhalation anaesthesia with *isoflurane* (*HDG9623, Baxter*). Deep anaesthesia and analgesia was induced by *intraperitoneal* injection of 80 $^{mg}/_{kg}$ *ke-*

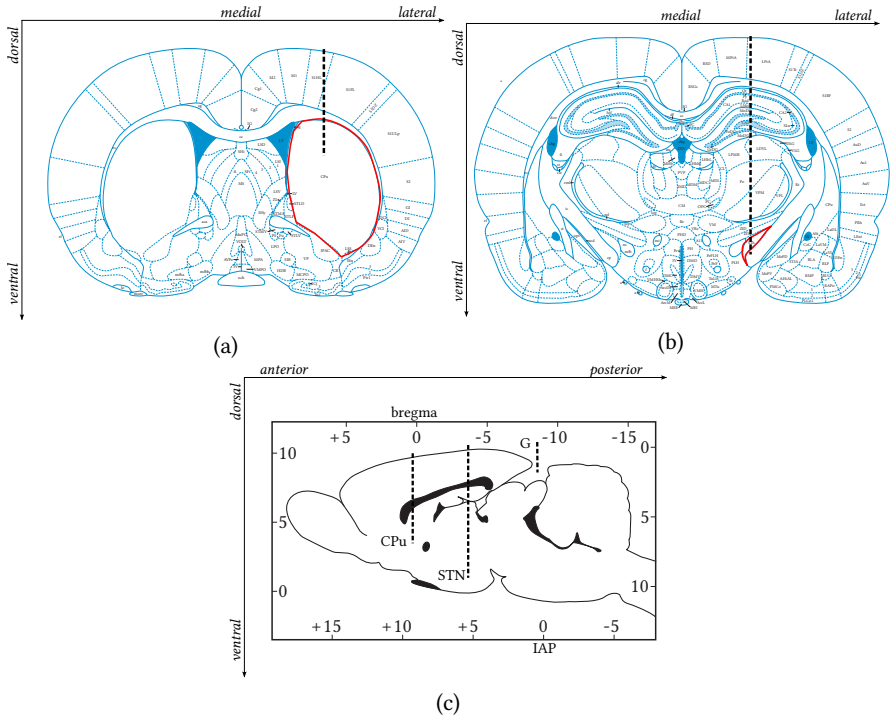

Figure 2.5: The *ventrolateral caudate putamen* (CPu) in 2.5a was targeted for injection of *neurotoxin* or *saline* in the chronic experiment. The *subthalamic nucleus* (STN) in 2.5b was targeted in chronic and acute experiments for neural recordings and electrical microstimulation. The longitudinal section through the rat brain in 2.5c shows all trajectories for the targeted areas, as well as the ground screw position. Figures from (Paxinos & Watson 2007), modified.

tamine (*Ketavet®, Pfizer*) and 1 $^{mg}/_{kg}$ *xylazine* (*Rompune®, Bayer*). To refresh anaesthesia, if necessary, one third of the initial dose was injected. Additionally, animals received injection of 1 ml 0.9 % *saline* and 5 % *glucose*. While under anaesthesia, the animal was placed on a 35 °C heating pad, driven by a circulation pump thermostat (*VWR International*).

A stereotaxic frame for small animals (*Stoelting Co.*) was used for accurate mounting of the animal and fixation via ear-bars in the auditory canals and an incisor bar for upper jaw fixation.

The carefully shaved scalp was opened by a 2-3 cm long sagittal cut along the middle line. Suture material was used to stretch the skin and create a wide operation area. The *periosteum* was removed, and the *cranium* was prepared by rigorous rubbing with cotton Q-tips until the *frontal, longitudinal* and *inter-aural fissures* were clearly visible.

A navigation rod with a hypodermic needle tip was mounted to the *stereotaxic frame*. Stereotaxic navigation was carried out under microscopic control (see figure 2.7) with the help of an imaging zoom lens mounted to a CCD camera on a stand, which was independent from the stereotaxic frame (*Imaging Zoom Lens, 0.7X-4.5X, NT53-347, Steel post components NT03-609, NT58-994, NT58-955, NT58-974, NT54-976, Edmund Optics, FireWire CCD Color Cam-*

era DFK 41BF02.H, The Imaging Source). The live image was displayed on the computer screen (*AVT Smart View v1.13.1, Allied Vision Technologies GmbH*).

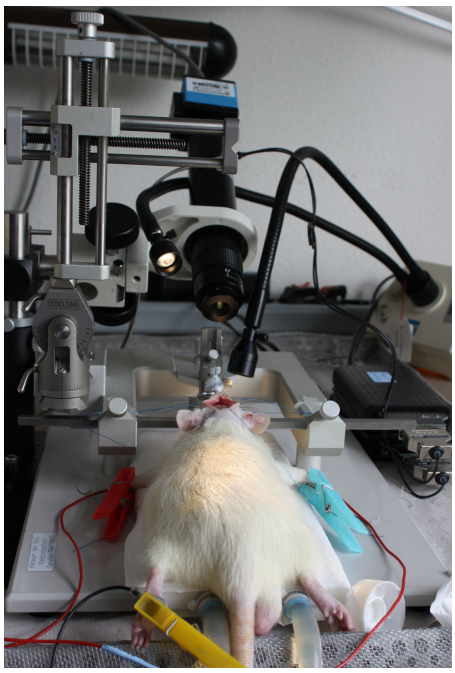

Figure 2.6: Setup for stereotaxic surgery. Anaesthetized animal mounted in stereotaxic frame. Microscopic cameras are placed on an additional stand.

The *anterior-posterior* (AP) *medial-lateral* (ML) and *dorsal-ventral* (DV) coordinates of the skull reference marks, *bregma* (B) and *inter-aural point* (IAP), were determined. Also, the DV coordinates of the left- and rightmost points of the inter-aural fissure (IAL and IAR) were gauged.

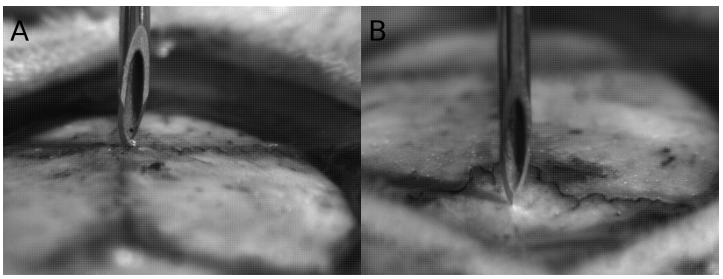

Figure 2.7: Reference *bregma* (A) and interaural point (B).

The AP tilt Δ_{AP} and ML tilt Δ_{ML} were calculated (see equation 2.4). When Δ_{ML} or Δ_{AP} exeeded a tolerance value of 0.02 cm, the skull position in the stereotaxic frame was readjusted, and measurements were repeated.

$$\begin{aligned} \Delta_{AP} &= DV_B - DV_{IAP} \\ \Delta_{ML} &= ML_{IAL} - ML_{IAR} \end{aligned} \tag{2.4}$$

target	AP [cm]	ML [cm]	trepanation [mm]
CPu, right	$AP_{CPu} = AP_B + 0.02$	$ML_{CPu} = ML_B - 0.3$	1.4
STN, right	$AP_{STN} = AP_{IAP} + 0.02$	$ML_{IAP} = ML_B - 0.3$	2.1
Ground screw	$AP_G = AP_{IAP} + 0.25$	$ML_G = ML_{IAP} + 0.25$	0.9
Fixation screw 1	$AP_{F1} = AP_{STN} + 0.3$	$ML_{F1} = ML_{STN} + 0.2$	0.9
Fixation screw 2	$AP_{F2} = AP_{STN} + 0.3$	$ML_{F2} = ML_{STN} - 0.2$	0.9
Fixation screw 3	$AP_{F3} = AP_{STN} - 0.3$	$ML_{F3} = ML_{STN} - 0.2$	0.9
Fixation screw 4	$AP_{F4} = AP_{STN} - 0.2$	$ML_{F4} = ML_{STN} + 0.2$	0.9

Table 2.2: ML and AP coordinates for stareotaxic targets according to (Paxinos & Watson 2007).

Starting from the skull reference marks, the coordinates of the target area according to the *Rat Brain Atlas* (Paxinos & Watson 2007) were calculated as shown in table 2.2. The resulting AP and ML trepanation points were marked on the skull surface.

After labeling the trepanation points, the skull bone was carefully perforated using a high speed micro drill (*Fine Science Tools, Inc.*) and the respective drill-head according to table 2.2 (*Micro Drill Steel Burrs, 0.9, 1.4, 2.1 mm, Fine Science Tools, Inc.*). A piece of silicone rubber tube was put around the drill head to avoid irritation of the *dura mater* and *cortex* tissue.

The trepanation was carefully cleaned from bone fragments and blood. The *dura mater* above the probe insertion points was carefully removed using sharp, delicate forceps (*Fine Science Tools, Inc.*). To prevent tissue desiccation, a drop of high viscosity silicone oil (*Mw 10000, Sigma-Aldrich*) was applied.

Skull screws (*1.17 x 4.0 mm Bone Screws, Fine Science Tools, Inc.*) were placed to the respective trepanation and were fastened with approximately three revolutions. The ground screw (G) was soldered to a short silver wire and a pin connector and connected to the ground and reference of the biosignal amplifier (see section 2.2.2).

2.4.3 *Probe Insertion & Neuronavigation*

For step-by-step probe insertion, a PILine® micropositioning stage with integrated linear encoder and controller (*M-663 Linear Motor Stage and C-867 Controller, Physik Instrumente (PI) GmbH & Co. KG*) was used. The stage was mounted to the navigation rod on the stereotaxic frame by a custom-made aluminium clamp as shown in figure 2.8 (*Workshop, University of Lübeck*). The *Linear Array Probe* housing or the support for the *Flexible Array Probes* (see section 2.4.3.2) were fixed to the holder on the opposite site of the clamp. The piezo drive of the micropositioning stage locks the position when no

power is supplied. That way, no AC noise was introduced into the neural recordings when the drive was on hold.

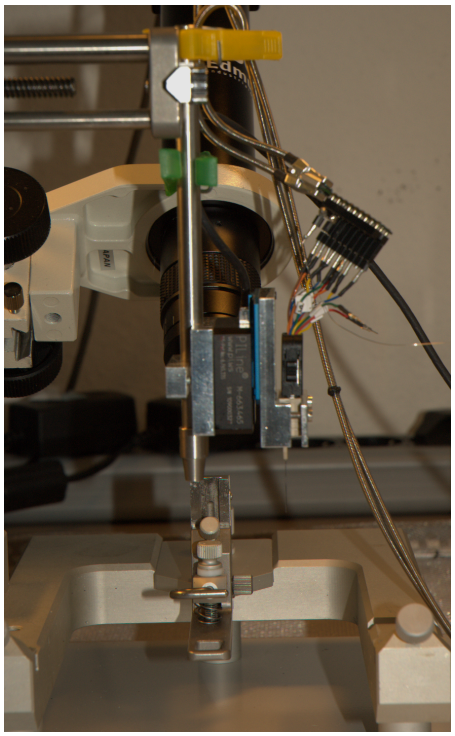

Figure 2.8: Micropositioning stage, mounted to the stereotaxic frame via the navigation rod with a custom made clamp. A holder for probe insertion is present on the clamp.

2.4.3.1 *Insertion of Linear Array Probes*

For insertion, the *Linear Array probe* was mounted to the micropositioning stage via the holder on the custom made clamp (see figure 2.8). Using the stereotaxic frame the probe tip was referenced to *bregma* and the *inter-aural point* under microscopic control. The AP and ML target coordinates for the probes were calculated according to table 2.2, and adjusted via the stereotaxic frame. The micropositioning stage displacement was set to zero and the probe tip was adjusted to the height of the skull surface above the target point (DV_S), using the stereotaxic frame. From here, the DV displacement of the probe was adjusted, using the software controlled micromanipulation stage, only. Target depths for the respective targets are summarized in table 2.3.

The *Linear Array Probe* was lowered into the cerebral tissue in steps of 200 µm with a speed of 0.4 $^{mm}/_{s}$ by linear displacement of the micropositioning stage. Between each step, the neural activity pattern was recorded. The target depths in table 2.3 were used as guideline values. The final target depth was determined based on the patterns of neural activity which were recorded for each step (see section 1.4).

target	DV
CPu, right	DV_{CPu} = 0.45 cm
STN, right	DV_{STN} = 0.74 cm

Table 2.3: Target depths for target areas in the brain according to (Paxinos & Watson 2007).

2.4.3.2 *Insertion of Flexible Array Probes*

Insertion of *Flexible Array Probes* was achieved differently (see figure 2.9). Instead of mounting the *Flexible Array Probe* itself a support needle (*DN 2730K, Dental Needle, Terumo®*) was inserted into the probe holder on the micropositioning stage. The support needle was referenced to *bregma* and the *inter-aural point* and the *subthalamic nucleus* target coordinate was calculated as described for the *Linear Array Probe*.

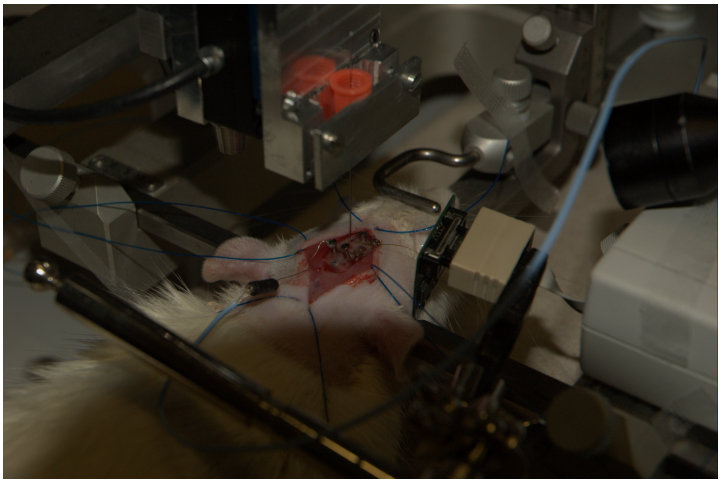

Figure 2.9: Insertion of Flexible Array Probes.

To place the Flexible Array probe on the skull, a 0.75 % *agarose* gel was prepared with 0.9 % *saline*. A little cube was cut and placed between the four fixation screws around the trepanation hole (see figure 2.10a and figure 2.10b). The *Flexible Array Probe* was placed onto the *agarose* gel and adhered to the wet surface (see figure 2.10c). The punching hole on the tip of the *Flexible Array Probe* was picked up with the sharp tip of the support needle (see figure 2.10d), and the target coordinates were adjusted by slowly dragging the *Flexible Array Probe* along. When the AP and ML target coordinates were reached, the stereotaxic frame was adjusted to the DV_S value for the support needle (see figure 2.10e). Then, the *Flexible Array Probe* was inserted into the brain by linear displacement of the micromanipulation stage in steps of 200 µm with 0.4 $^{mm}/_{s}$ (see figure 2.10f). At each step neural activity was recorded and the target depth was determined. When the target area was reached, the support needle was twisted slightly and slowly retracted.

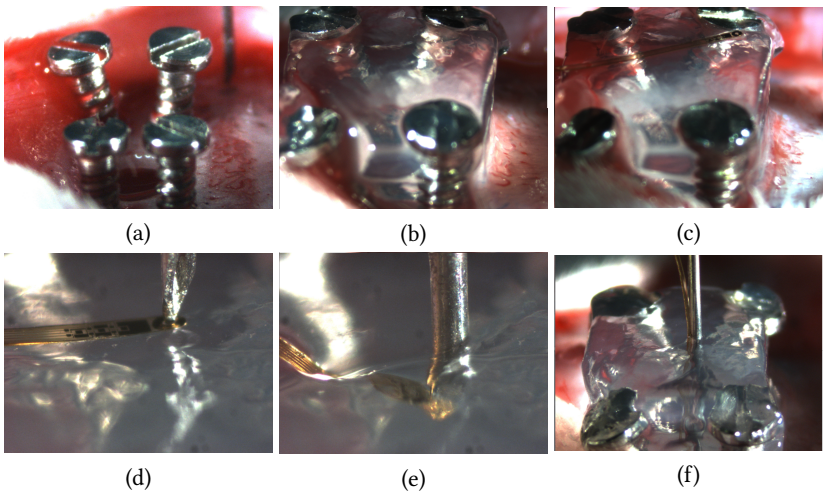

Figure 2.10: Insertion of *Flexible Array Probes* using a support needle.

2.4.4 *Probe Implantation*

When the electrode target area was verified by *neuronavigation*, the probes were implanted to facilitate chronic *high frequency microstimulation* and multi-channel neuronal recording in the awake and freely moving animal (see figure 2.11).

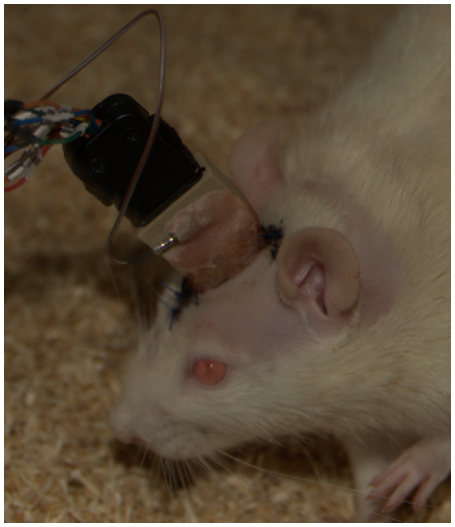

Figure 2.11: Probe implant with connected plug for chronic experiments in the freely behaving animal.

The probes were fixed onto the skull using the fixation screws as anchors. The implantation technique was different for *Linear-* and *Flexible Array Probes*, since the *Linear Array Probes* were reusable and explantation without causing damage to the electrode had to be ensured.

2.4.4.1 *Implantation of Linear Array Probes*

To fix the *Linear Array Probes* tightly to the skull and yet allow for easy explantation, probe fixation occured only via the probe housing. A little plug for the probes' support adapter (see figure 2.1) was built around the fixation screws (see figure 2.12a) using cold-curing, two-component, dental resin (*Ref 64707794, Heraeus Kulzer*). For that, a silicone spacer was placed between the skull screws so that the trepanation was covered. The outer surface of the silicone spacer was treated with high viscosity silicone oil and then wrapped with dental cement (see figure 2.12b). The silver wire, contacting the ground screw was integrated into the dental resin plug. When the dental cement cured, the silicone spacer was removed (see 2.12c) and the electrode was lowered into the brain (see 2.12c). When the target depth was reached, the space between the dental resin plug and the probe's support adapter was filled with silicone oil and the probe housing was fixed to the dental resin plug using thick layers of dental cement. The pin plug connection to the ground screw was integrated on the outer side of the dental resin implant. The surface of the implant was smoothed by washing with 0.9 % *saline* and shaping with wet Q-tips. Sharp edges were removed using a scalpel or bone cutter tool. The scalp was stretched around the implant and the wound was closed with surgical suture. The wound was purged with sterile *saline* solution and *betaisadonna* (*povidone-iod, Mundipharma GmbH*) was applied generously as antiseptic. When the *Linear Array Probe* needed to be recovered from the implant, the animal was decapitated under deep anaethesia with *isoflurane*. The whole implant was removed from the skull. A sharp scalpel blade was used to lever the probe housing from the dental resin implant.

2.4.4.2 *Implantation of Flexible Array Probes*

The *Flexible Array probes* were not recovered from the implant. After probe insertion, the support needle was removed and the whole *agarose* block, still supporting the probe, was covered with dental resin. When the first layer of dental resin was cured, the *Flexible Array Probe* plug housing was set upright and generously wrapped with dental resin. As for the *Linear Array Probe* implantation, the pin connector to the ground screw was integrated on the outer side of the dental resin implant. The implant was smoothed and the wound was closed and disinfected.

2.4.5 *Lesioning Procedure & Sham Treatment*

The *high frequency microstimulation* and *multi-channel neuronal recording* experiments were carried out in the awake and freely moving animal. Rats received lesion or sham treatment. In lesioned animals, neurotoxin solution was injected into the *ventrolateral caudate putamen*. Thereby, denervation of *dopaminergic, nigrostriatal afferents* was reached. Sham-treated animals received injection of 0.9 % *sodium chloride* into the same target area.

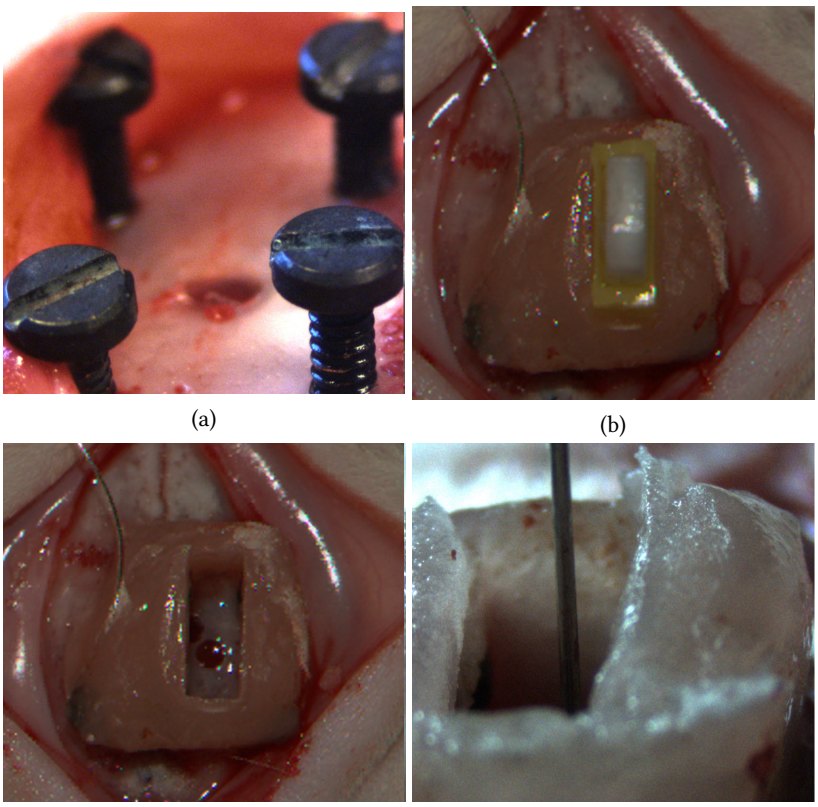

Figure 2.12: Implantation method for the *Linear Array Probe* allowing explantation of the probe when the experiment was complete.

The neurotoxin solution was prepared according to section 2.4.5.1. Saline solution (*sterile, pyrogen-free, Berlin Chemie*) was degassed by sonication (see below) and used as purchased. Injection into the *ventrolateral caudate putamen* was performed using the microinjection system described in section 2.4.5.2. Before injection, the tip of the injection needle was referenced to *bregma*, and the needle tip target coordinates were calculated according to table 2.2. After moving the needle tip to the AP and ML target coordinates, the syringe was loaded with neurotoxin or *saline* solution, and the tubing system was purged with 50 µl of the solution which was loaded earlier. Then, the needle tip was slowly lowered to the desired depth in the *ventrolateral caudate putamen* (see table 2.3) using the DV drive of the stereotaxic frame. With the help of a microperfusion pump, 0.5 $\mu l/min$ were injected for 10 min. The needle was left *in situ* for five minutes and then slowly retracted.

2.4.5.1 *Neurotoxin Preparation*

The neurotoxin solution was freshly prepared just before injection and was handled in the dark and on ice. Sterile, pyrogen-free 0.9 % *saline* (*Berlin Chemie*) was sonicated (*Bandelin Sonorex TK52H, Schalltec GmbH*) for 10 min to remove oxygen from the liquid. 50 mM *ascorbic acid* (*Ref A7506, Sigma-*

Aldrich) and *6-hydroxydopamine* (*Ref 2547, Tocris*) stock solutions were prepared in sonicated *saline*. Then, 254 µl *6-hydroxydopamine* (50 mM), 76 µl *ascorbic acid* (50 mM) and 670 µl 0.9 % *saline* were mixed and final concentrations of 12.7 mM *6-hydroxydopamine* and 3.8 mM *ascorbic acid* were established.

2.4.5.2 *Microinjection System*

A 100 µl GasTight® syringe (*1710, Hamilton Bonaduz AG*) was connected to 20 cm low diameter polyethylene tubing (*ID 0.4 mm, OD 0.8 mm, Portex, Smiths Medical*) and an injection needle (*Hypodermic Needle, 27G, Braun Melsungen AG*) by low-volume tubing adaptors (*Ref 340 9500, CMA Microdialysis AB*). A microdialysis probe adaptor was glued to the injection needle with epoxy resin, and the needle was mounted to the stereotaxic frame via a microdialysis probe clip (*Ref 8309013, CMA Microdialysis AB*) and navigation rod (see figure 2.13). The syringe was filled with the solution and placed into a microperfusion pump (*Typ540101, TSE Systems Internationl Group*).

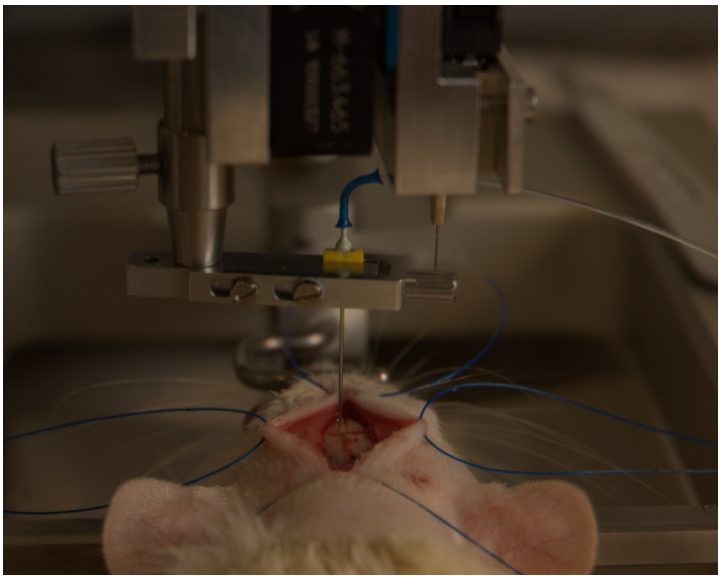

Figure 2.13: Microinjection into the ventrolateral Caudate Putamen.

2.4.6 *Microstimulation and Recording Freely Behaving Animals*

Three days after probe insertion, *high frequency microstimulation* and *multi site neuronal recordings* were performed in the awake and freely moving animal (see figure 2.14). The animal was placed into a 60 cm diameter bowl test cage (*Rotameter System for Small Animals, TSE Systems*) and the implanted probes were connected to the commercial hardware for stimulation and recording as described in section 2.2. The pin connector for the skull screw ground was connected to the amplifier's ground and reference (see figure 2.11), as was the ground contact of the implanted probe and the an-

ode (positive terminal) of the *WPI Isostim A320 Isostim* stimulus isolator. The stimulation site at the tip of the implanted probe was connected to the cathode (negative terminal) of the stimulator. The seven recording sites of the implanted probe were connected to the *ZIF Clip headstage* as described in section 2.2.

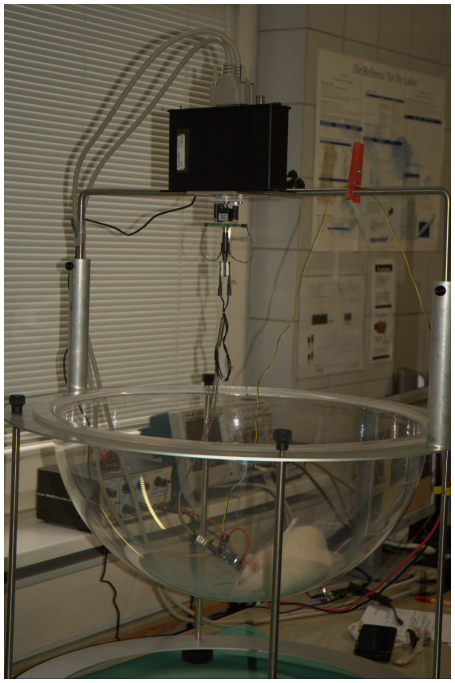

Figure 2.14: Setup for the Chronic Experiment.

A passive voltage probe (10x) was connected to stimulation ground and source to measure the *voltage response* to current controlled stimulation on the implanted electrode using a digital oscilloscope *TDS2004B, Tektronix*. Data were recorded using *LabView Signal Express Data Aquisition Software*.

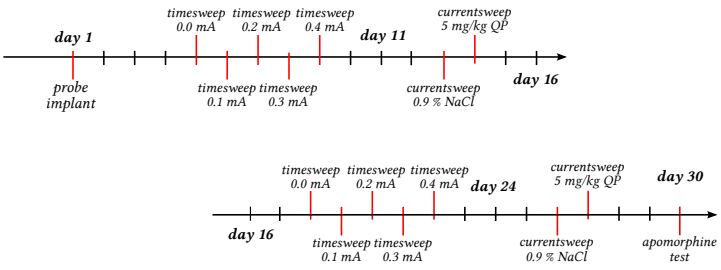

Figure 2.15: Animals with implanted probes were investigated for a period of up to 30 days. During this time *timesweep* experiments were performed with different stimulation current amplitudes, and *currentsweep* experiments were performed with subcutaneous injection of 5 $^{mg}/_{kg}$ *quinpirole* (QP) or 0.9 % sodium chloride, 30 minutes before the experiment. At the end of the procedure, an *apomorphine test* was performed.

Wavetrain data were recorded with 24.414 kHz on seven channels via the recording sites of the implanted probe. For instant visualization, the recorded *wavetrain*data were bandpass filtered between 300 - 3000 Hz. Filtered and unfiltered raw data were stored in *TDT data tanks* in blocks of 60 s duration. The recording site, closest to the stimulation contact was recorded as channel 7.

When indicated, electrical *high frequency microstimulation* was applied between the *stimulation site* and *ground* of the implanted probe by monophasic, cathodal, constant current pulses with 60 µs duration and 8 ms interval. The pulse width and duty cycle of the rectangular pulses was constant for all experiments. As indicated, the current amplitude varied between 0.0, 0.1, 0.2, 0.3 and 0.4 mA.

Electrical *high frequency microstimulation* and neuronal *multi- channel recording* was performed in different experiments (see figure 2.15). Two sets of *timesweep* and *currentsweep* experiments, and an *apomorphine test* were performed in each animal with chronically implanted probes.

2.4.6.1 *Timesweep Experiments*

Timesweep experiments (see figure figure 2.16) were carried out in week one and three. The *wavetrain signal* was continuously recorded for 30 min in blocks of 60 s. Single trains of 60 s electrical *high frequency stimulation* were applied with different duration between the trains. The current amplitude was constant for all trains of stimulation. While *high frequency microstimulation* was applied, *rotational behaviour* was observed and video footage was recorded. Also, the *voltage response* to current stimulation was recorded using an oscilloscope and *LabView Signal Express Data Aquisition Software.*

Five *timesweep* experiments were carried out on consecutive days with increasing current amplitude in week one and three. The protocol for the *timesweep* experiment is listed in Appendix E.

2.4.6.2 *Currentsweep Experiments*

Currentsweep experiments (see figure figure 2.17) were performed in week two and four according to the time schedule in figure 2.15. The *wavetrain* signal was continuously recorded for 35 min in blocks of 60 s. Single trains of 60 s *high frequency stimulation* were applied with 5 min duration between the trains. Eventually, the recording blocks were extended before and after stimulation so that the stimulation artefact could be detected later. With each train of stimulation, the current amplitude was increased by 0.1 mA. While *high frequency microstimulation* was applied, *rotational behaviour* was observed and video footage was recorded. The *voltage response* to current stimulation was recorded using an oscilloscope, and *LabView Signal Express Data Aquisition Software.*

Two consecutive *currentsweep* experiments were carried out in week two and four. The first *currentsweep* experiment was performed 30 min after subcutaneous injection of 0.9 % *sodium chloride* and the second *currentsweep* ex-

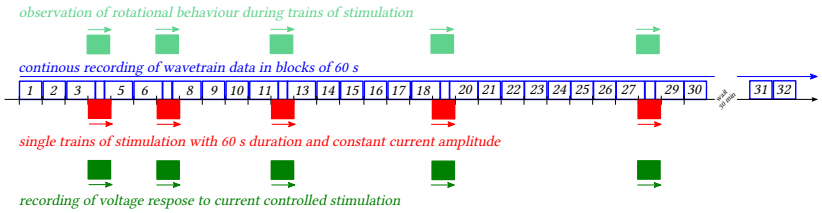

Figure 2.16: In the *timesweep* experiment, the *wavetrain* signal was recorded continuously in blocks of 60 s duration (blue squares). Single trains of *high frequency microstimulation* of 60 s duration were applied after 3, 6, 11, 18 and 27 min with increasing time interval between stimulation (red boxes). Eventually, the recording blocks were extended before and after stimulation so that the stimulation artefact could be detected later. The current amplitude was kept constant in the *timesweep* experiment. While *high frequency microstimulation* was applied, video footage was recorded to analyse *rotational behaviour* (light green boxes) and *voltage response* to current controlled stimulation was recorded using an oscilloscope (dark green boxes).

periment was performed 30 min after subcutaneous injection of 5 mg/kg *quinpirole*. The protocol for the *currentsweep* experiment is listed in Appendix E.

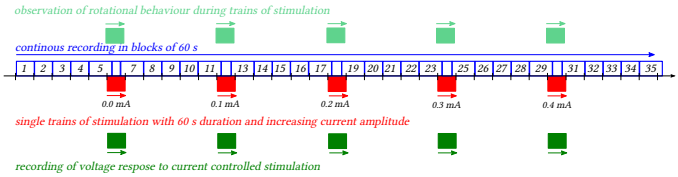

Figure 2.17: In the *currentsweep* experiment, the *wavetrain* signal was recorded continuously in blocks of 60 s duration (blue squares). Single trains of *high frequency microstimulation* of 60 s duration were applied after 5, 11, 17, 23 and 29 min with constant time interval between stimulation (red boxes). For each stimulation sequence, the current amplitude was increased by 0.1 mA. While *high frequency microstimulation* was applied, video footage was recorded to analyse *rotational behaviour* (light green boxes), and *voltage response* to current stimulation was recorded using an oscilloscope (dark green boxes).

2.4.6.3 *Apomorphine Test*

The *apomorphine test* was carried out at the end of the procedure, before animals were sacrificed and brains removed. For the *apomorphine test*, animals were placed into the bowl test cage, and *rotational behaviour* was observed continously. The *wavetrain* signal was recorded in blocks of 60 s at certain timepoints during the experiment (see figure figure 2.18). After 10 min, the animal received subcutaneous injection of 5 mg/kg *apomorphine*. After that, rotations were continously observed and blocks of *wavetrain* data

were recorded for 35 min. The protocol for the *apomorphine test* is listed in Appendix E. After the *apomorphine test*, animals were decapitated under deep *isoflurane* anaesthesia, and brains were removed.

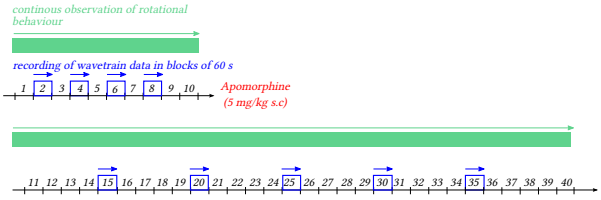

Figure 2.18: In the *apomorphine test*, the *wavetrain* signal was recorded blocks of 60 s duration after 1, 3, 5, 7, 14, 20, 25, 30 and 35 min (blue squares). Subcutaneous injection of 5 mg/kg *apomorphine* was applied after 10 min. Video footage was recorded during the whole experiment to analyse *rotational behaviour* before and after *apomorphine* injection (light green boxes).

2.5 *Data Analysis*

2.5.1 *Groups & Parameters*

2.5.1.1 *Neuronavigation*

Two treatment groups were derived for the *neuronavigation* experiments (see section 2.4.3, and figure 2.19, light blue area). Each block of recorded data was exported as described in Appendix C. The parameters used to quantify neuronal activity, were calculated for the whole data block as described in section 2.5.4 and *spike detection* was performed according to section 2.5.5.

2.5.1.2 *Apomorphine Response*

Four treatment groups were derived for the *apomorphine test* experiments (see section 2.4.6.3 and figure 2.19. light green area). Each block of recorded data was exported as described in Appendix C. The parameters used to quantify neuronal activity were calculated for the whole data block as described in section 2.5.4 and *rotational behaviour* was analyzed according to section 2.5.1.6.

2.5.1.3 *Multi-site Recording and Microstimulation Experiments*

Eight treatment groups were derived for *time-* and *currentsweep* experiments (see sections 2.4.6.1 2.4.6.2, and figure 2.19, light red area). In each group, *high frequency microstimulation* was applied with 0.0, 0.1, 0.2, 0.3 and 0.4 mA. Each block of recorded data was exported as described in Appendix C. The exported data were sorted into the respective groups as listed in Listing D.1

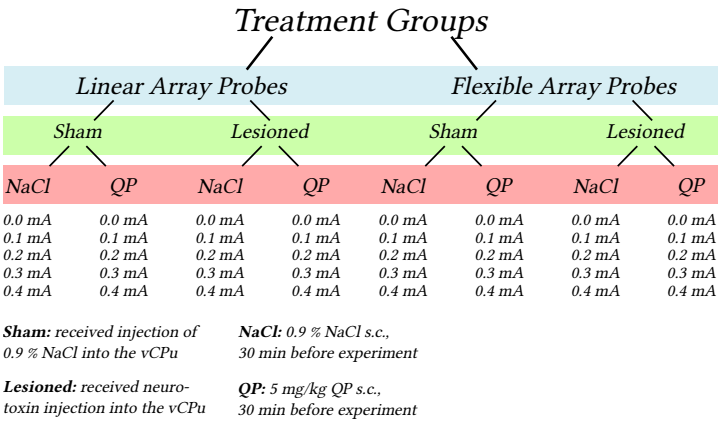

Figure 2.19: Treatment groups for *neuronavigation* (light blue), *apomorphine test* (light green), as well as *time-* and *currentsweep* experiments (light red).

2.5.1.4 *Basal Neuronal Activity*

Basal neuronal activity (see section 3.4) was determined from the blocks of data that were recorded before any electrical stimulation was applied. Parameters used to quantify basal neuronal activity were calculated from the whole data block as described in section 2.5.4.

2.5.1.5 *Voltage Response*

The *voltage respose* to current stimulation on the electrode's stimulation sites was recorded with 1 MHz using a digital oscilloscope connected parallel to *ground* and *source* of the stimulus isolator. The *voltage response* between *Linear-* and *Flexible Array Probes* was compared and the long term performance of the implanted probes was established by comparing the *voltage response* in the early set of experiments in week one with the late set of experiments in week four (see section 3.3).

2.5.1.6 *Rotational Behaviour*

Rotational behaviour in each group was analysed from the videos taken while *high frequency microstimulation* was applied, or before and after *apomorphine* injection. Full rotations were counted in the video footage, and rotations per minute were calculated.

2.5.1.7 *Neuronal Response to High Frequency Microstimulation*

To determine the neuronal response to *high frequency microstimulation* (see section 3.6) the exported and sorted data were merged to obtain *wavetrain data blocks* containing *wavetrain* data before, during and after *high frequency microstimulation* (see section 2.5.2.2). Then, the *stimulation artefact* was removed using gradient based edge detection (see section 2.5.3). Parameters that were used to quantify the response of the neuronal network to *high frequency microstimulation* were calculated as described in section 2.5.4 for

each second. Single-unit spike events were extracted from the *wavetrain* data as described in section 2.5.5 and the response of single-unit spike activity to *high frequency microstimulation* was analysed as described in section 2.5.6.

2.5.2 *Signal Processing*

2.5.2.1 *Wavetrain Data*

Wavetrain data blocks of 60 s duration recorded before, during and after *high frequency microstimulation* were merged together for each group and each channel to obtain a continuous *wavetrain* (see figure 2.20).

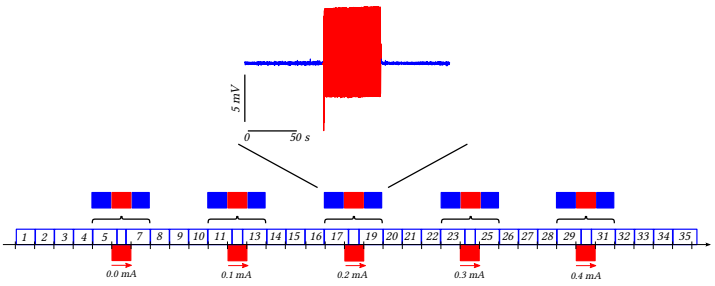

Figure 2.20: *Wavetrain* data were merged from three blocks of recorded data. The *wavetrain* represents the recorded signal before, during and after *high frequency microstimulation*. The stimulation artefact is marked in red. Unfiltered data are shown.

2.5.2.2 *Stimulation Artefact*

The *stimulation artefact* (see figure 2.21) is shown for *Linear-* (blue) and *Flexible Array Probes* (green). When *high frequency stimulation* was turned on manually by a turning switch on the stimulus isolator, the amplifier goes into saturation immediately. A sharp edge is visible in the *wavetrain* data (see figure 2.21a).

The close-up view of the *stimulation artefact* in figure 2.21b shows that, with our setup, it is impossible to record neuronal activity between the stimulation pulses since the system stays in saturation in the 8 ms time period between the pulses. As the stimulus isolator is turned off a sharp edge is visible as soon as the system desaturates (see figure 2.21c). It takes up to 400 ms until the 50 Hz noise becomes visible again in the unfiltered *wavetrain* data. The system goes back to initial conditions only about 900 ms after saturation. This behaviour is similar for *Linear-* and *Flexible Array Probes*.

2.5.3 *Edge Detection*

The *stimulation artefact* was removed from the *wavetrain* using gradient based edge detection (see Listing D.3). The gradient of the one dimensional data $\nabla data(t)$ was calculated and a threshold filter was applied with $thr =$

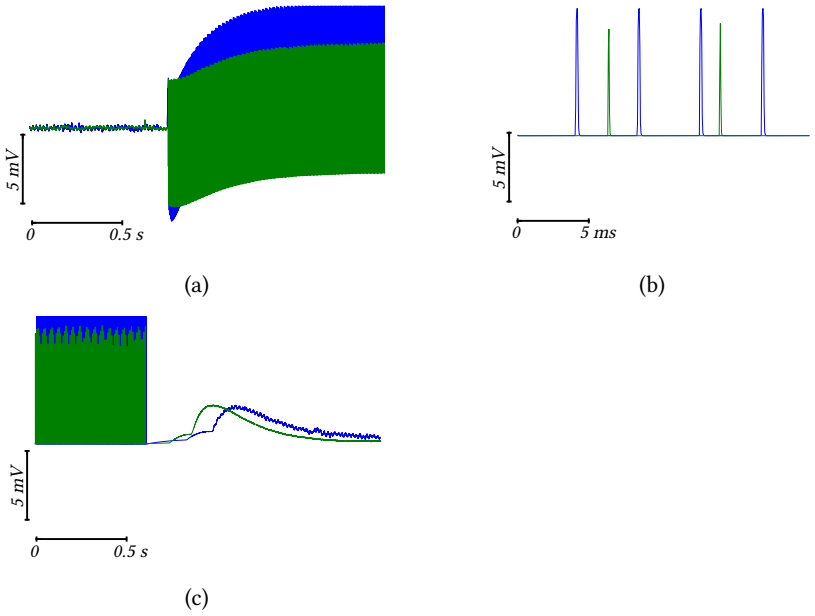

Figure 2.21: The *stimulation artefact* as recorded with *Linear-* (blue) and *Flexible Array Probes* (green).

$10 * mean(data)$ ($data_{thr}(t) = |\nabla data(t)| > thr$). The first timepoint t_{min} of $data_{thr}(t)$ was used as the left edge of the stimulation artefact and the last timepoint t_{max} of $data_{thr}(t)$ was used as the right edge of the stimulation artefact. The result of the edge detection is shown in figure 2.22.

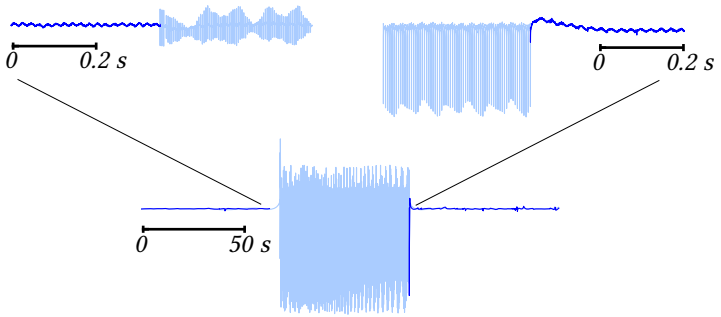

Figure 2.22: Edge detection from merged *wavetrain* data. The unfiltered *wavetrain* signal with the *stimulation artefact* is shown in light blue. The data after edge detection is shown in dark blue.

2.5.4 *Wavetrain Derived Parameters*

Statistical parameters derived from *wavetrain* data were determined from the merged *wavetrain* signal after removal of the *stimulation artefact* (see Listing D.3). Data were filtered at 400-4000 kHz using a standard 4th order *Butterworth* digital filter.

The *root mean sqare* is the mean value of the squared data, and was calculated as shown in equation 2.5

$$d_{rms} = \sqrt{\frac{1}{n}\sum_{i=1}^{n} d_i^2} \tag{2.5}$$

The *spectral density* was calculated to characterize the frequency content of the signal. The *mean spectral density* was used to determine the magnitude of the signal over all frequencies between 400-4000 Hz. For the *spectral density* calculation, the *matplotlib.pyplot.psd* function was used with $n = 256$, and $F_s = 24414$ Hz. The one dimensional vector of *wavetrain data* was divided into i segments with length n, and $|fft(i)|^2$ of each segment was calculated.

2.5.5 *Spike Detection & Clustering*

Spike detection was performed from the merged *wavetrain* signal after removal of the *stimulation artefact* (see Listing D.3). Data were bandpass filtered at 400-4000 kHz using a standard 4th order *Butterworth* digital filter.

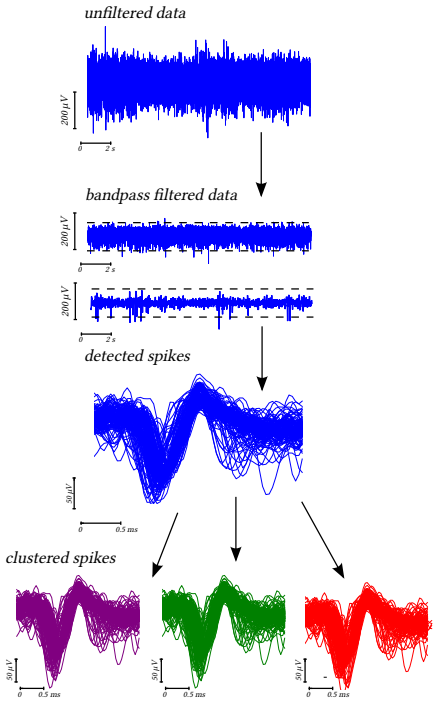

Figure 2.23: Spike detection from merged *wavetrain* data.

Spikes were detected using a median based threshold filter (see equation 2.6) as proposed by Quiroga et al. (Quiroga 2004). Detected spikes were stored in 64 dp vectors and aligned at the maximum.

$$thr = 5x\frac{median(|data|)}{0.6745} \tag{2.6}$$

The detected *spike shapes* were grouped using *kmeans clustering* after feature extraction by *principal component analysis*. For that the *C Clustering Library* was used together with the package *Pycluster* (de Hoon et al. 2004). *Principal component analysis* was used to extract spike shape features from all spike shapes. Feature vectors were determined from the eigenvalues of the covariance matrix and were clustered using *kmeans* clustering with $k = 10$ as number of clusters. The stepwise procedure from unfiltered *wavetrain* data to the clustered spike shapes is shown in figure 2.23

2.5.6 *Spike Event Analysis*

Spike detection and clustering was performed for each block of merged and filtered *wavetrain* data on each channel (see figure 2.24). The times of the spike events in each cluster were plotted as *rasterplot* before and after *high frequency microstimulation*. From the spike event times, inter-spike intervals were calculated. A normed histogram of the inter-spike intervals (isi) was created using 100 bins. Parameters, describing the distribution of inter-spike intervals for each cluster were calculated to line out changes in the spiking activity before and after *high frequency microstimulation* (see Listing D.3).

2.5.6.1 *Median Inter Spike Interval*

The median of the inter-spike intervals $\widetilde{isi}_{-HFS}$ and $\widetilde{isi}_{+HFS}$ were determined in each cluster, representing the centre of gravity of the inter-spike interval distribution. To obtain a normalized measure $\widetilde{isi}_{-HFS}/(\widetilde{isi}_{-HFS}+\widetilde{isi}_{+HFS})$ and $\widetilde{isi}_{+HFS}/(\widetilde{isi}_{-HFS}+\widetilde{isi}_{+HFS})$ were calculated.

2.5.6.2 *Number of Spike Events*

The normalized number of spike events represents the *mean firing rate per minute* $n_{-HFS}/(n_{-HFS}+n_{+HFS})$ and $n_{+HFS}/(n_{-HFS}+n_{+HFS})$ was calculated for each cluster.

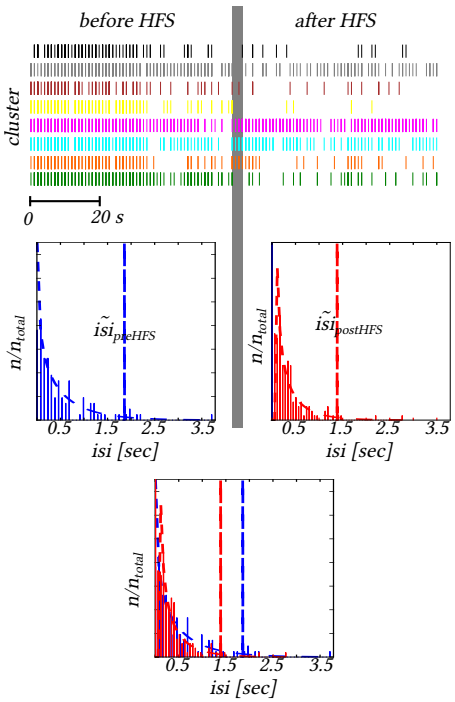

Figure 2.24: Spikes were detected and spike shapes were clustered in each channel. The times of the spike events in each cluster were plotted as *rasterplots* before and after *high frequency microstimulation* (HFS). From the spike event times, inter-spike intervals were calculated and the distribution of the inter-spike intervals was plotted as a *histogram plot* before and after HFS. The resulting probability density function was fitted using a gamma distribution. The median of the inter-spike intervals was calculated and compared.

2.5.6.3 *Spike Entropy*

The spike entropy was calculated from the inter-spike interval histogram as a measure of regularity of spike events. h_{-HFS} and h_{+HFS} were calculated from equation 2.7.

$$\begin{aligned} p(s_i) &= \frac{1}{\sum_{i=1}^{n} s_i} \\ h(s) &= \sum_{i=1}^{n} p(s_i) * log_2(p(s_i)) \end{aligned} \tag{2.7}$$

3

RESULTS

3.1 *Probe Characterization*

The *frequency response* of the *Linear-* and *Flexible Array Probes* was characterized by *impedance spectroscopy* in the 0.1-100 kHz frequency range. The mean values and standard errors of the *impedance* Z and *phase angle* ϕ were calculated for the recording and stimulation sites of all electrodes and displayed in *Bode- and Nyquist representation*. The approximate *Randles cell* parameters were determined from the *impedance spectra*. Also, the graphs were fitted with the *Randles cell* equivalent circuit representation and the fit parameter R_s, R_{ct} and C_{dl} were calculated (see table 3.2).

3.1.1 *Linear Array Probe Impedance Spectra*

Figure 3.1 shows the *frequency response* of the *Linear Array Probe* recording- and stimulation sites in *Bode- and Nyquist representation*. The *impedance* Z is plotted against the frequency on a double-logarithmic scale (see figure 3.1a). The curves for the best fit are included for recording- and stimulation sites. At low frequencies, high *impedance* values are observed striving towards R_{ct}. For high frequencies, low *impedances* are observed striving towards the value for R_s. For frequencies lower than 10 kHz, recording and stimulation sites can be clearly distinguished from each other by means of *impedance*.

Figure 3.1b provides a close-up view on the characteristic areas in the *Bode representation* of the *impedance spectrum*. The linear region of the curve at 7-10 kHz was fitted using nonlinear regression resulting in a line in the double-logarithmic coordinate system and is displayed together with the *low-frequency asymptote* at R_{ct} and the *high-frequency asymptote* at R_s. From that, the *cut-off frequency* ω_c was determined. It lies beyond the physiological frequency range for recording- and stimulation sites (see table 3.2). At 1 kHz, the *impedance* of the recording sites is 63.04 % higher than the *impedance* at the stimulation sites.

The *phase angle* Φ is plotted against the frequency on a semi-logarithmic scale and the curves for the best fit are included for recording- and stimulation sites (see figure 3.1c). The phase shift at recording- and stimulation sites is similar over the whole frequency range. At 0.2-2 kHz and at frequencies higher than 10 kHz, the curve is linear. At 2-5 kHz, phase angles are constant. The close-up view at 1 kHz emphasizes the similarity between phase shifts at recording and stimulations sites and the transition from the linear to the constant phase occurring at 2 kHz (see figure 3.1d).

The *Nyquist plot* in figure 3.1e represents the complex nature of the measured impedance. The real- and imaginary parts were calculated from the *im-*

pedance Z and *phase angle* Φ and displayed in a cartesian coordinate system. The curves of the best fit are included for recording- and stimulation sites. The lower intersection with the *real-axis* is similar to the fitted R_s value. The diameter of the semicircle is similar to the fitted R_{ct} value at the recording- and stimulation sites. The *solution resistance* R_s at the origin of the semi-circle does not differ much between recording- and stimulation sites whereas the diameter of the semi-circle differs considerably and seems to be dependent on the size of the contact area. The curve shape of the *Nyquist plot* describes a single semi-circle. In general, the *Randles cell* fit represents the measured *impedance* values for frequencies lower than 10 kHz. For higher frequencies, the fit seems to be inappropriate to describe the data.

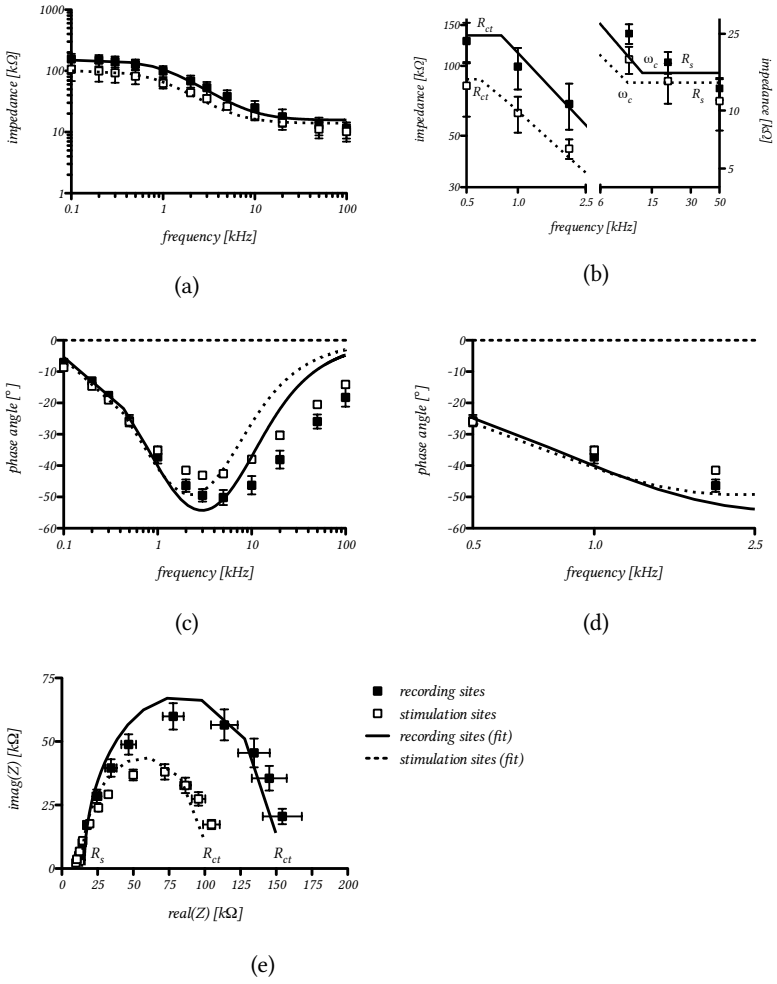

Figure 3.1: *Frequency response* of *Linear Array Probes. Bode-* and *Nyquist representations* of *impedance* and *phase angle* measurements are fitted using the *Randles cell* equivalent circuit.

3.1.2 *Flexible Array Probe Impedance Spectra*

Figure 3.2 shows the *frequency response* of the *Flexible Array Probe* recording- and stimulation sites in *Bode- and Nyquist representation.*

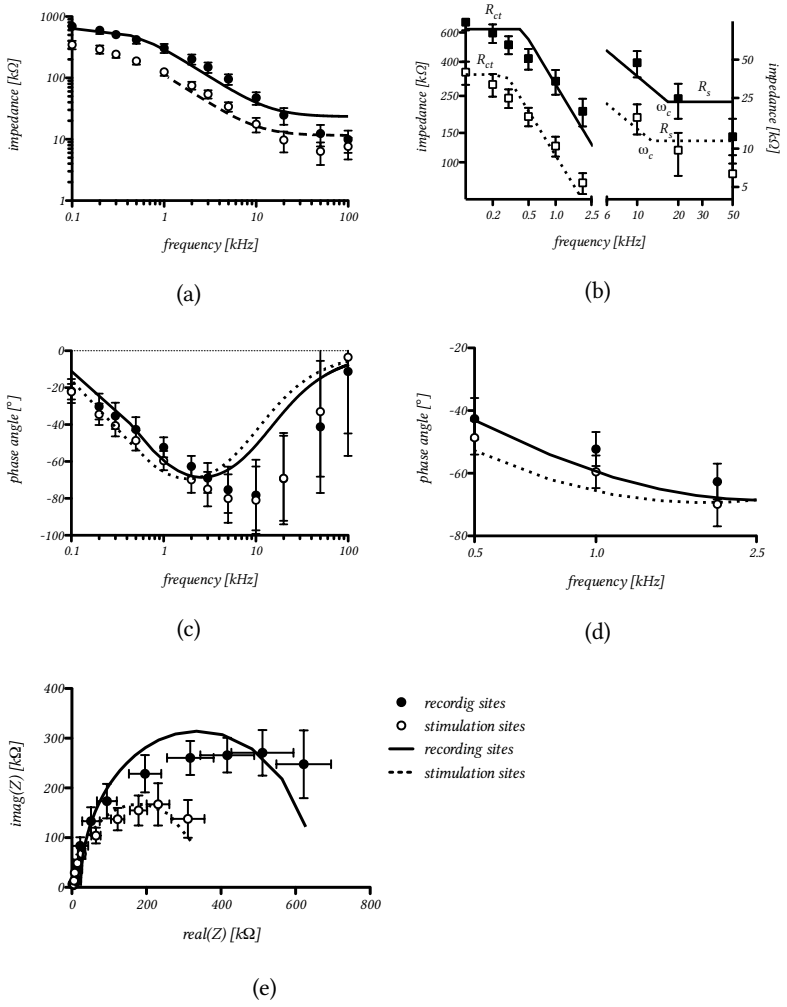

Figure 3.2: *Frequency response* of *Flexible Array Probes. Bode-* and *Nyquist representations* of *impedance* and *phase angle* measurements fitted using the *Randles cell* equivalent circuit.

The *impedance* Z is plotted against the frequency on a double-logarithmic scale (see figure 3.2a) and the curves for the best fit are included for recording- and stimulation sites. At low frequencies, high *impedance* values are observed striving towards R_{ct}. For high frequencies, low impedances are observed, striving towards the value for R_s. Recording and stimulation sites can be clearly distinguished from each other over the whole frequency range by means of *impedance.*

Figure 3.1b provides a close-up view on the characteristic areas in the *Bode representation* of the *impedance* Z. The linear region of the curve at 1-9 kHz was fitted using nonlinear regression resulting in a line in the double-

Table 3.1: Paramters of the *Randles cell* equivalent circuit determined from the *impedance spectra* in *Bode-* and *Nyquist representation.*

	Linear Array Probes		Flexible Array Probes	
	recording sites	stimulation sites	recording sites	stimulation sites
R_s	11.11±3.29 kΩ	10.18±3.20 kΩ	24.76±7.58 kΩ	7.67±2.99 kΩ
R_{ct}	155.81±34.09 kΩ	106.25±38.13 kΩ	692.26±73.18 kΩ	346.86±55.03 kΩ
C_{dl}	2.06±0.19 nF	2.21±0.07 nF	3.03±0.05 nF	5.09±1.29 nF

logarithmic coordinate system and is displayed together with the *low-frequency asymptote* at R_{ct} and the *high-frequency asymptote* at R_s. From that, the *cut-off frequency* of the *high-pass filter* ω_c was determined for recording- and stimulation sites (see table 3.2). The *cut-off frequencies*, however, lie beyond the physiological range at frequencies > 13 kHz. At 1 kHz, the *impedance* of the recording sites is 40.94 % higher than the *impedance* of the stimulation sites.

The *phase angle* Φ is plotted against the frequency on a semi-logarithmic scale (see figure 3.2c) and the curves for the best fit are included for recording- and stimulation sites. the phase shift at recording- and stimulation sites is similar over the whole frequency range. The close-up view at 1 kHz shows that the transition from the linear into the constant phase occurs at 1 kHz and therefore earlier than with the *Linear Array Probes*.

The *Nyquist plot* for the complex *impedance* of the *Flexible Array Probes* is shown in figure 3.2e. The real- and imaginary parts were calculated from the *impedance* Z and *phase angle* Φ, and displayed in a cartesian coordinate system. The curves for the best fit are included for recording- and stimulation sites. The curve shape of the *Nyquist plot* does not describe a full semi-circle. The intersection with the real axis occurs close to the fitted value for R_s and is similar for recording- and stimulation sites. Yet, there is no indication of a second semi-circle. Therefore, a first order system with a single *time constant* seems suitable to describe the *frequency response* of the *Flexible Array Probes* but the *Randles cell* might be too limited since it fails to describe the data at frequencies higher than 2 kHz.

3.1.2.1 *Randles Cell Parameters*

The parameter of the *Randles cell* equivalent circuit R_s, R_{ct} and C_{dl} were determined from *Bode-* and *Nyquist plot*. R_s was determined from the *impedance* at the high-frequency asymptote of the *Bode plot* and R_{ct} was determined from the *impedance* at the low frequency asymptote of the *Bode plot*. The *double layer capactitance* C_{dl} was calculated from the *Nyquist plot* with $C_{dl} = 1/2\pi f R$ whereas the real part of the *impedance* Z and the frequency at the apex were used (see table 3.1).

The parameters of the *Randles cell* equivalent circuit were also calculated from the least squares fit of the *impedance spectra*. The variance for the fitted

Table 3.2: Paramters of the *Randles cell* equivalent circuit determined by fitting the *impedance spectra* using a least squares fitting method.

	Linear Array Probes		Flexible Array Probes	
	recording sites	stimulation sites	recording sites	stimulation sites
R_s	15.68 kΩ	13.96 kΩ	23.26 kΩ	11.54 kΩ
R_{ct}	135.51 kΩ	87.58 kΩ	628.64 kΩ	336.29 kΩ
χ^2	5.16 kΩ	4.47 kΩ	67.65 kΩ	20.30 kΩ
C_{dl}	1.23 nF	2.17 nF	0.51 nF	1.40 nF

parameters was taken from the diagonal of the covariance matrix. Variances were always smaller than 1 % of the value of the fitted parameter. The χ^2 error of the fit was calculated by taking the sum of the squared difference between the measured and the fitted *impedance* weighted by the measured *impedance* (see table 3.2).

3.1.2.2 *Impedance - Area Relationship*

The measured *impedance* at 1 kHz for the different geometric surface areas of the electrode contact sites are compared in figure 3.3a. The 1 kHz *impedance* is plotted against the geometric surface area of the electrode contact site. The data points were fitted by a log-log fit and a logarithmic relation between contact site surface area an *impedance* at 1 kHz was determined.

Phase angle values at 1 kHz do not seem to be related to the surface area. The values for the geometric surface area of the electrode contact sites as well as values for *impedance* and *phase angle* are summarized in table 3.3.

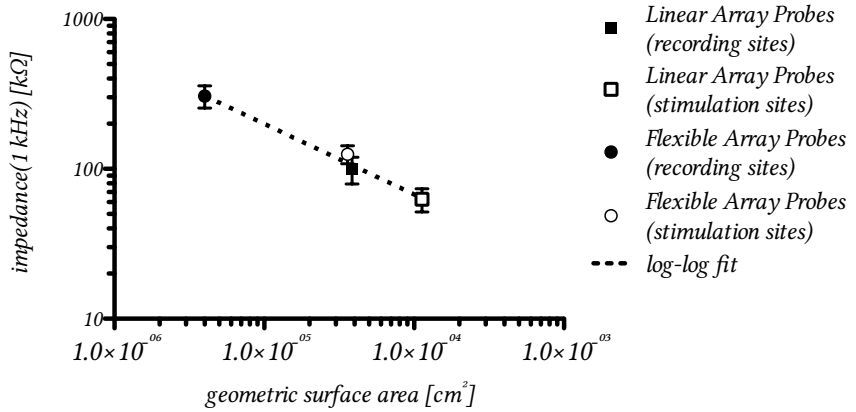

(a)

Figure 3.3: Relationship between the geometric surface area of the electrode contact sites and the measured *impedance* at 1 kHz.

Table 3.3: Geometric surface areas of the electrode contact sites as well as 1 kHz *impedances* and *phase angles*.

	Linear Array Probes		Flexible Array Probes	
	recording sites	stimulation sites	recording sites	stimulation sites
area [cm^2]	$3.85x10^{-5}$	$1.13x10^{-4}$	$4.00x10^{-6}$	$3.60x10^{-5}$
Z [kΩ]	99.40 ± 20.27	62.66 ± 11.08	306.19 ± 51.72	125.38 ± 17.07
Φ[°]	-52.27 ± 5.43	-59.51 ± 5.20	-52.27 ± 5.43	-35.13 ± 1.24

3.2 *Neuronavigation*

The *in vivo* performance of *Flexible-* and *Linear Array Probes* was determined by *neuronavigation*. Regular measurements were performed while driving the probes deeper into the cerebral tissue on a determined trajectory. Based on anatomical and functional data (Paxinos & Watson 2007), the depth on the trajectory to the target structure was assigned to four different brain regions which were marked in the figures with alternating grey and white bars. Roughly, these four regions correspond to *cortex*, *hippocampus*, *thalamus* and *zona incerta/subthalamic nucleus* in the rat brain.

3.2.1 *Wavetrain Appearance*

Wavetrains were recorded and classified according to their region of origin (see figure 3.4). In general, both probe types show a good performance measuring *wavetrain* patterns from selected channels. The *wavetrain* signal for *Linear Array Probes* looks smooth at 0-2 mm and 2-4 mm. Despite low noise levels, little spike activity was observed in these regions. A larger amount of spike activity was measured with *Flexible Array Probes* at 2-5 mm. At 4-7 mm, distinct regular spiking and bursting activity was measured with both probe types. Generally, large single spikes were preferentially found in the *wavetrains* recorded with *Linear Array Probes* whereas lower amplitude bursts were often found in *Flexible Array Probe* recordings. Recordings in the *subthalamic nucleus* were very similar between *Linear-* and *Flexible Array Probes*. Large single spikes were observed together with bursts in the same recording.

3.2.2 *Mean Spike Shapes*

From the *wavetrain* data, measured in the respective depth area, spikes were extracted. Random spikes, extracted from *wavetrains* measured in the respective region were plotted in figure 3.5. In general, spike shapes measured in different depths do not differ much. Spikes were found in almost every re-

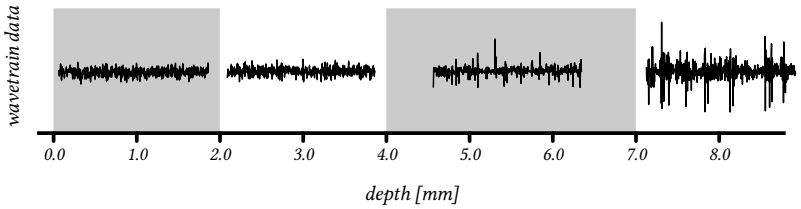

(a) Linear Array Probes

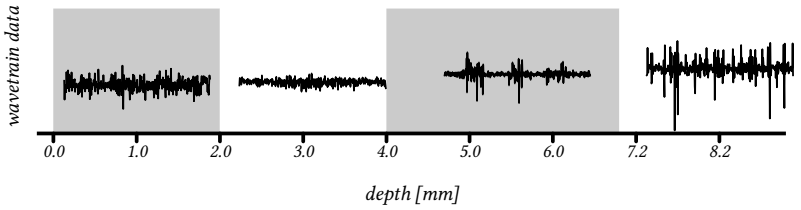

(b) Flexible Array Probes

Figure 3.4: *Wavetrains*, recorded during *neuronavigation* along the trajectory to the *subthalamic nucleus* using *Linear-* and *Flexible Array Probes*.

gion with both probe types. Using *Linear Array Probes*, the spikes are much clearer in deeper regions (see figure 3.5a).

To see if different spike shapes can be measured from different regions and to determine features in which the spike shapes generally differ, the mean value of all spike shapes measured in the respective region was calculated and plotted in figure 3.6. Spike shapes, measured with *Linear Array Probes* generally belong to two types. Spikes, measured at 4-7 mm, seem to have a more pronounced hyperpolarized region before the positive peak and are slightly less hyperpolarized after the positive peak. Spike shapes from other regions cannot be distinguished by any feature when measured with the *Linear Array Probes*. Thus, there seems to be no correlation between the mean spike shape of all spikes measured in an area and the predominant type of neurons in that area.

Spike Measurements with the *Linear Array Probes* can be distinguished by three different features. The hyperpolarized region preceding the peak, the peak amplitude and the hyperpolarized region following the peak. Showing different combinations of these three features spike shapes from three regions can be distinguished from each other when measured with *Flexible Array Probe* (see figure 3.6b). Spikes, measured at 0-2 mm and 4-7 mm have a larger amplitude than spikes from the other areas but cannot be distinguished from each other. Spikes, measured at 2-4 mm, show a less pronounced hyperpolarized region following the peak whereas spikes, measured at 7-8.4 mm, show a less pronounced hyperpolarized region preceding the peak than spikes from all the other areas. Still, the mean spike shape of

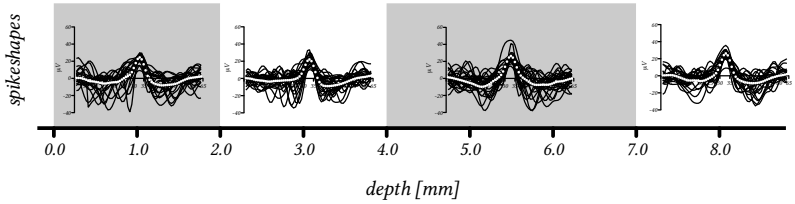

(a) Linear Array Probes

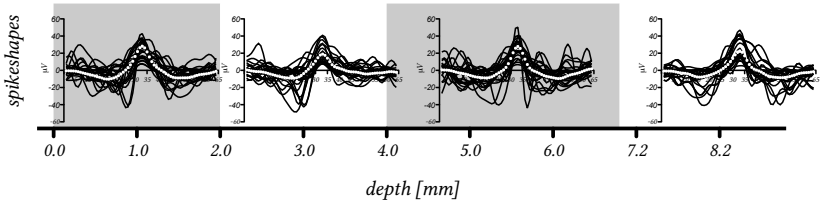

(b) Flexible Array Probes

Figure 3.5: Spike shapes, observed during *neuronavigation* along the trajectory to the *subthalamic nucleus* using *Linear-* and *Flexible Array Probes*.

an area seems not to be useful for *neuronavigation*, since many spike have to be measured in order to find reliable differences.

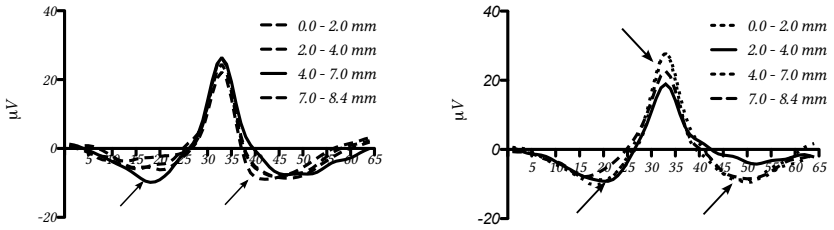

(a) Linear Array Probes

(b) Flexible Array Probes

Figure 3.6: Spike shapes observed in certain cerebral areas along the trajectory to the *subthalamic nucleus* measured with *Linear-* and *Flexible Array Probes*.

3.2.3 *Wavetrain Based Parameters*

Although the occurence of certain *wavetrain* patterns can be linked to depth of recording and therefore to a respective brain region, the prediction of a brain area by *wavetrain* pattern is not very accurate since no sharp distinction can be made between two subsequent *wavetrains*. *Neuronavigation* by means of spike shape analysis seems inadvisable. Instead of using *wavetrain* patterns or spike shapes for *neuronavigation*, *wavetrain based param-*

Table 3.4: Turning points calculated from the 10th order polynomial fit of the *root mean square activity profile* of *Linear-* and *Flexible Array Probes*.

	Turning point depth [mm]				
Linear Array Probes	0.9	2.4	4.0	6.0	7.3
Flexible Array Probes	1.2	2.5	3.9	6.1	7.6

eters were calculated for each depth step as proposed by Menne et al. and Ramrath et al. (Menne 2005, Ramrath et al. 2009) and plotted against the depth of the electrode tip in the brain. Mean values and standard errors of *root mean square amplitude*, *mean firing rate*, *mean spectral density* and *spike entropy* were calculated for all probe types. Using these values, *activity profiles* were generated for the target trajectory by plotting the data against the depth of the electrode tip. All *activity profiles* were fitted with a 10th order polynomial which, by visual impression, described the data best. The turning points of the fitted functions were determined using the second and third derivatives and marked in the graphs (see figures 3.7-3.10).

3.2.3.1 *Root Mean Square*

The *root mean square activity profile* for *Linear-* and *Flexible Array Probes* is shown in figure 3.7. The *root mean square activity profile* measured with *Linear Array Probes* shows a clear biphasic increase along the trajectory to the *subthalamic nucleus*. Two stationary phases are separated by phases of roughly linear increase. The values range from about 3 µV at low depths to around 5 µV at the target.

The *root mean square activity profile* measured with *Flexible Array Probes* shows the same range of amplitude, but larger error bars than observed with *Linear Array Probes*. Although no clear biphasic shape can be delineated from the graph, an increase of the *root mean square* is observed along the target trajectory.

The turning points, calculated from the *root mean square activity profile* measured with *Linear Array Probes* align well with the end of the marked *cortical region* at 2.0 mm and with the beginning and end of the marked *thalamic region* at 4.0 mm and 7.0 mm. Another turning point is found at 6.1 mm and aligns with the depth of the border to the *ventral posteromedial thalamic nucleus* according to (Paxinos & Watson 2007). Even if the *root mean square activity profile* measured with the *Flexible Array Probes* shows no clear structure, the location of the turning points align with the turning points found in the *root mean square activity profile* measured with *Linear Array Probes* (see table 3.4).

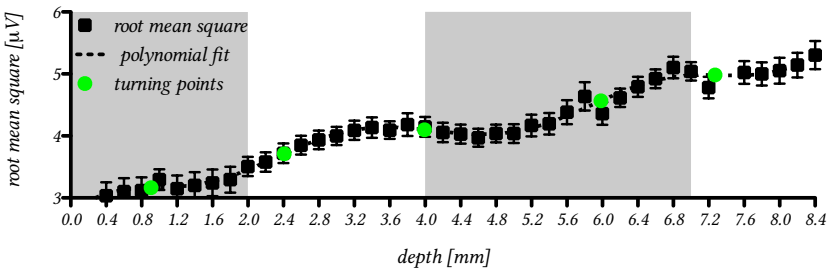

(a) Linear Array Probes

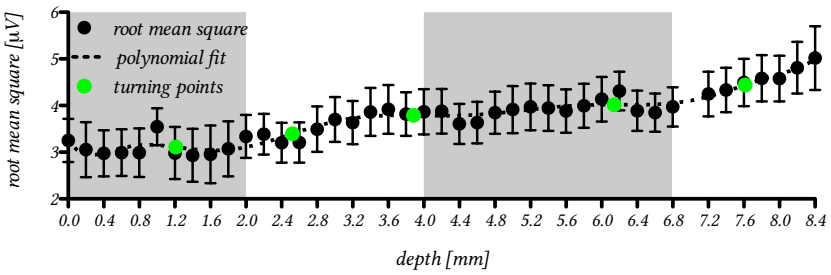

(b) Flexible Array Probes

Figure 3.7: *Root mean square activity profiles* calculated from the *wavetrain* signal while *neuronavigation* along the trajectory to the *subthalamic nucleus* was performed using *Linear-* and *Flexible Array probes*. The turning points of the polynomial fit align with the transitions between cerebral structures.

3.2.3.2 *Mean Spectral Density*

The *mean spectral density profile* shows the negative decadic logarithm of the *mean spectral density* at 300-3000 Hz plotted against depth. Being the negative value, a negative slope reflects an increase in *spectral activity*. The *spectral density profile* measured with *Linear Array Probes* shows a biphasic shape similar to the *root mean square activity profile*. Here, three constant phases at 0-2 mm, 3-4 mm, and 7-8 mm alternate with two linear phases at 2-3 mm and 5-7 mm. The *spectral density profile* measured with *Flexible Array Probes* has no characteristic structure and large error bars.

The turning points, calculated from the *mean spectral density profile* measured with *Linear Array Probes* align well with the end of the marked *cortical region* at 2.0 mm as well as with the beginning marked *thalamic region* at 4.0 mm. A turning point, marking the end of the *thalamic region*, is missing. Instead, the possible marker for the transition to the *ventral thalamus* is present at 5.7 mm. The *mean spectral density profile* shows an additional turning point at 7.8 mm, which marks the depth of the *subthalamic nucleus* at the electrode tip according to (Paxinos & Watson 2007). The turning points of the *mean spectral density profile* measured with *Linear Array Probes* appear as well in the *mean spectral density profile* measured with *Flexible Array Probes* (see table 3.5).

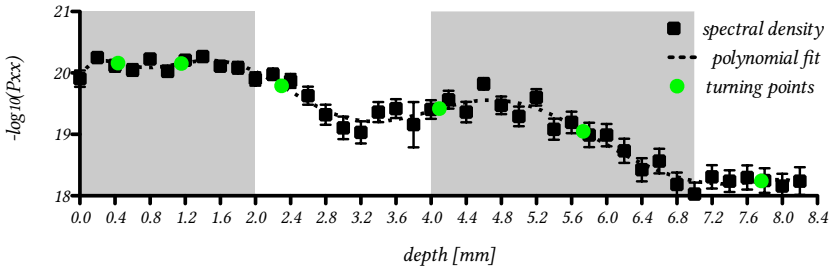

(a) Linear Array Probes

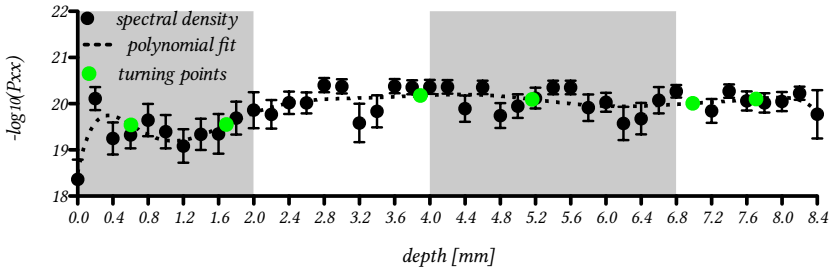

(b) Flexible Array Probes

Figure 3.8: The *mean spectral density* represented by the negative decadic logarithm of the *mean spectral density* at 300-3000 Hz while *neuronavigation* was performed along the trajectory to the *subthalamic nucleus* using *Linear-* and *Flexible Array Probes*.

3.2.4 *Spike Based Parameters*

From the *wavetrain* data, measured in the respective depth area, spike signals were extracted. Spike based parameters were calculated from the timing of the spike events occurring in the respective region.

3.2.4.1 *Mean Firing Rate & Entropy*

From the timing of the detected spikes, *mean firing rate* and *entropy* were calculated. *Spike activity profiles* (see figure 3.9) and *entropy profiles* (see figure 3.10) were plotted. The curve shape for both differs from the curve shape of the *activity profiles* derived from *wavetrain* data. Few spikes were detected

Table 3.5: Turning points calculated from the 10th order polynomial fit of the spectral activity profile of Linear- and Flexible Array Probes.

	Turning point depth [mm]				
Linear Array Probes	0.4	2.3	4.1	5.7	7.8
Flexible Array Probes	0.6	1.7	3.9	7.0	7.7

in the *cortical region* with *Linear Array Probes*. The *spike activity*- and *entropy profiles* are flat in this region. In *hippocampus*, at 2-4 mm, *spike activity* is rising and then falling again. Linearly rising *spike activity* is observed at 4.8-6.8 mm, which is the depth of *thalamus* in the rat brain. After 7.0 mm, the *spike activity* is constant.

More *spike acitvity* in the *cortex* was measured with *Flexible Array Probes* whereas little was observed in *hippocampus*. The *spike activity* was rising in alignment with the marked area for the *thalamus* at 4 mm but large error bars make it difficult to delineate a clear curve shape.

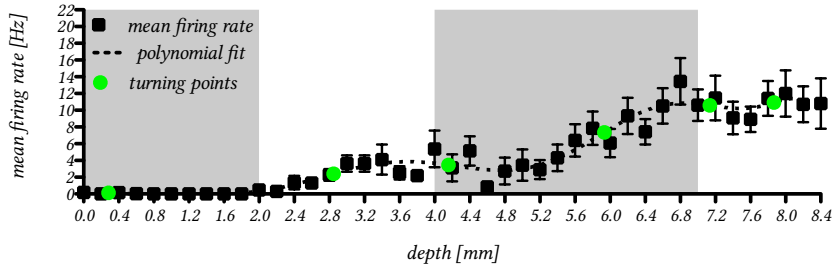

(a) Linear Array Probes

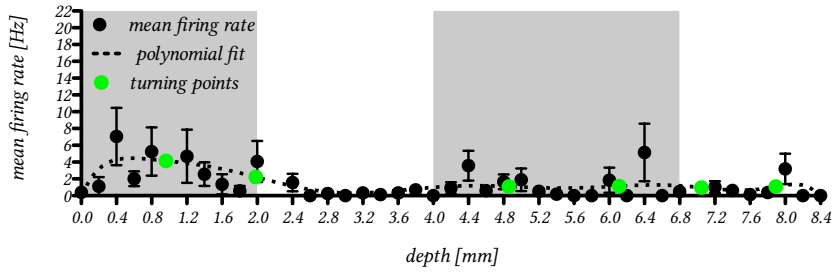

(b) Flexible Array Probes

Figure 3.9: Spike activity represented as *mean firing rate*, calculated from the number of spikes while *neuronavigation* along the trajectory to the *subthalamic nucleus* was performed using *Linear*- and *Flexible Array Probes*.

The turning points, calculated from the polynomial fit of the *spike activity profiles* and measured with *Linear Array Probes*, do not align with the beginning but with the end of the marked *cortical region* at 4.0 mm. Also, the turning points at the possible transition to *ventral thalamic* region at 6.0 mm and to the *subthalamic nucleus* can be found in the *spike activity profiles*. Again, most turning points reappear in the *spike activity profiles* measured with *Flexible Array Probes* (see table 3.6).

The *entropy profile* measured with *Linear*- and *Flexible Array Probes* has much the same shape as the *spike activity profile* with smaller error bars in the profile measured with *Linear Array Probes* and larger error bars in the profile measured with *Flexible Array Probes* (see figure 3.10). The *entropy* is related to the firing rate. The more spikes were detected, the more regular the timing of the spike events.

Table 3.6: Turning points calculated from the 10th order polynomial fit of the *spike activity profile* of *Linear-* and *Flexible Array Probes*.

	Turning point depth [mm]					
Linear Array Probes	1.0	2.8	4.2	6.0	7.1	7.9
Flexible Array Probes	1.0	2.0	4.9	6.1	7.0	7.9

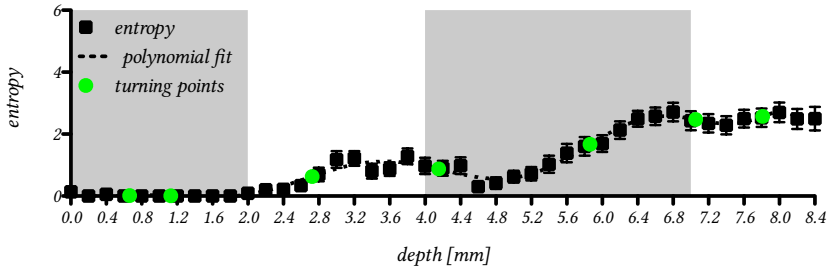

(a) Linear Array Probes

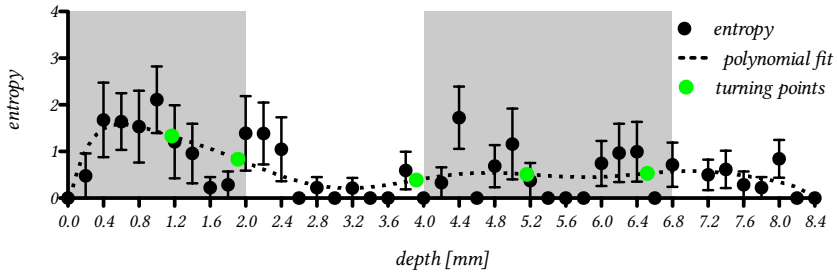

(b) Flexible Array Probes

Figure 3.10: *Entropy profile* with the *entropy* being calculated from spike times at each step while *neuronavigation* along the trajectory to the *subthalamic nucleus* was performed using *Linear-* and *Flexible Array Probes*

.

The turning points, calculated from the polynomial fit of the *entropy profile* measured with *Linear Array Probes* do not differ much from the turning points determined from the *mean firing rate*. When the *entropy profile* was measured with *Flexible Array Probes*, only four turning points were observed missing the markers at 7.0 mm and 7.8 mm (see table 3.7).

3.2.4.2 *Turning Points of the Activity Profile*

Turning points for all *activity profiles* measured with *Linear-* and *Flexible Array Probes* disregarding the respective amplitude are summarized in figure 3.11. Brain regions and borders for *cortex*, *hippocampus*, *thalamus* and

Table 3.7: Turning points calculated from the 10th order polynomial fit of the *entropy profile* of *Linear-* and *Flexible Array Probes*.

	Turning point depth [mm]					
Linear Array Probes	0.7	2.7	4.2	6.0	7.1	7.8
Flexible Array Probes	1.2	2.0	4.0	6.5	7.0	7.7

zona incerta/subthalamic nucleus with values taken from Paxinos et al. (Paxinos & Watson 2007) are marked by alternating grey and white areas.

Additionally, dotted lines mark the first turning point observed in a group. Clearly, the dotted lines align with the grey and white marked areas. The dotted lines in the *cortical region* are shifted by 0.2 mm but align for the deeper regions. Two additional dotted lines at 5.6 mm and 7.8 mm align with the determined values for the dorsal border of the *ventral posteromedial thalamic nucleus* and the *subthalamic nucleus*.

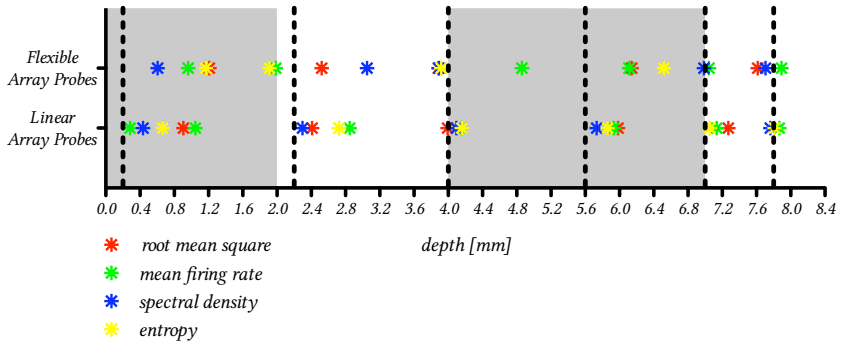

Figure 3.11: Turning points calculated from *root mean square activity-*, *spectral density-*, *spike activity-*, and *entropy profiles* with their amplitude set to y=1. Dotted lines mark the fist turning point in a group, determined from the profiles measured with *Linear Array Probes*.

3.3 *Voltage Response*

Current controlled electrical stimulation with 0.0-0.4 mA was applied via the stimulation sites of *Linear-* and *Flexible Array Probes* at different time points after implantation. Figure 3.12 shows the average voltage response to a 60 µs current pulse with 0.0-0.4 mA via the *Linear-* and *Flexible Array Probe* stimulation sites after one- and four weeks of implantation. The *voltage response curves* display charge- and discharge phases with exponential rise and decay which are typical for *RC circuits*. After charging, a maximal potential, depending on the current amplitude, is reached. After one week of implantation (see figures 3.12a and 3.12c), higher maximum electrode poten-

tials are reached than after for weeks of implantation. This effect is especially prominent at current amplitudes higher than 0.2 mA (see figures 3.12b and 3.12d). The average maximum electrode potential at 0.4 mA drops by 62 % between week one and four of implantation with both probe types.

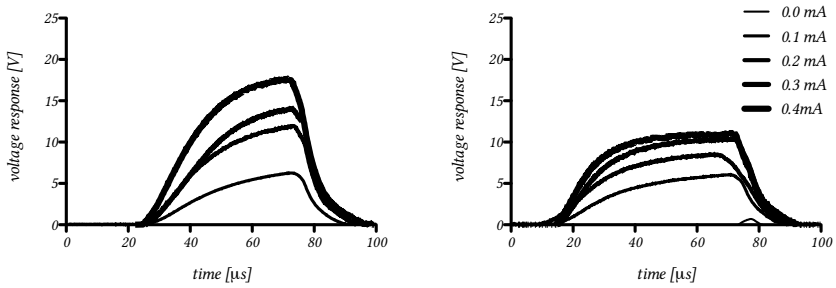

(a) Linear Area Probes (1 week)

(b) Linear Area Probes (4 weeks)

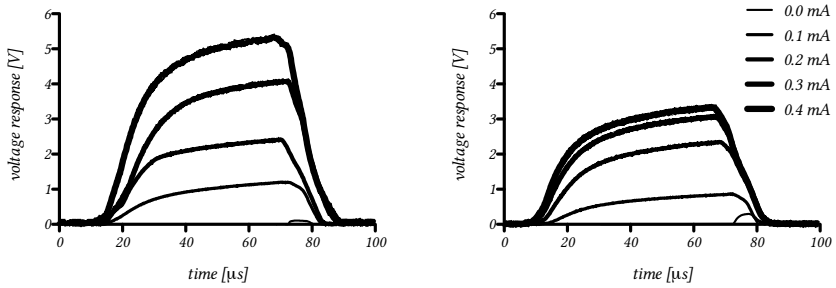

(c) Flexible Area Probes (1 week)

(d) Flexible Area Probes (4 weeks)

Figure 3.12: *Voltage response* to current stimulation on the stimulation site of chronically implanted *Linear-* and *Flexible Array Probes*. Measurements were taken after one and four weeks of implantation.

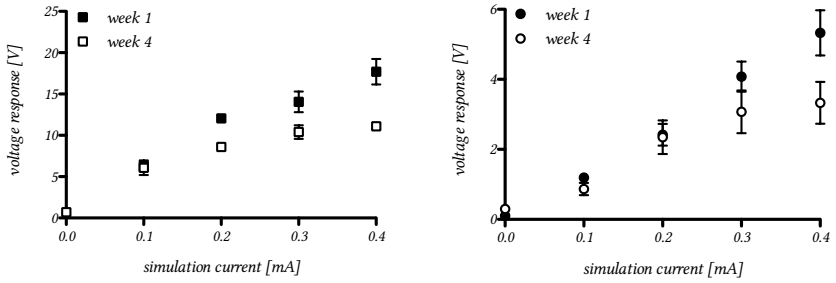

(a) Linear Area Probes

(b) Flexible Area Probes

Figure 3.13: Maximum electrode potentials determined from the *voltage response* to current controlled stimulation with 0.0-0.4 mA at the *Linear-* and *Flexible Array Probe* stimulation sites.

The maximum electrode potential was determined from the *voltage response* of the different probe types after one and four weeks of implanta-

Table 3.8: Maximum electrode potential during 0.1 and 0.4 mA current controlled stimulation at *Linear-* and *Flexible Array Probe* stimulation sites.

current	Linear Array Probes		Flexible Array Probes	
	week 1	week 4	week 1	week 4
0.1 mA	6.3±0.57 V	6.1±0.88 V	1.2±0.09 V	0.9±0.17 V
0.4 mA	17.7±1.54 V	11.1±0.3 V	5.33±0.64 V	3.3±0.6 V

tion. Maximum electrode potentials are shown in figure 3.13. The *voltage response* at *Linear Array Probe* stimulation sites after one and four weeks of implantation diverges from 0.2 mA stimulation amplitude upwards. The *voltage response* at *Flexible Array Probe* stimulation sites after one and four weeks implantation diverges from 0.3 mA upwards.

This effect was further investigated, and the *time constant* τ was determined for the average *voltage response* at *Linear-* and *Flexible Array Probe* stimulation sites during stimulation with 0.1-0.4 mA current amplitude. Exponential increase of potential was assumed, so that $V(t) = V(1 - e^{-t/\tau})$, and $V(t) = 1 - e^{-1} = 0.63$ when $t = \tau$. Therefore, τ values for *Linear-* and *Flexible Array Probes* at week one and four, were taken from the curves displayed in figure 3.12 as the time points where the potential reached 63.2 % of its maximum value, and displayed in figures 3.14a and 3.14b. The τ values seem to be scattered randomly for the different time points with *Linear-* and *Flexible Array probes*. Therefore a single *time constant* τ was calculated from the mean value and standard error of the extracted τ values at 0.1-0.4 mA and the one- and four week time points for each of the two probe types (see table 3.9).

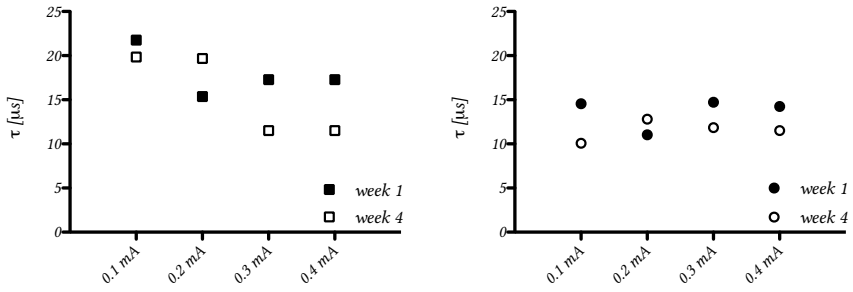

(a) Linear Area Probes (b) Flexible Area Probes

Figure 3.14: Time constants of the exponential capacitive increase in potential after current stimulation at *Linear-* and *Flexible Array Probe* stimulation sites, after one and four weeks of implantation

Table 3.9: Time constants for the voltage response of *Linear-* and *Flexible Array Probes*, calculated from the voltage response curves at 0.1-0.4 mA after one and four weeks of implantation.

	τ [µs]
Linear Array Probes	16.78 ± 1.34
Flexible Array Probes	12.60 ± 0.62

3.4 *Basal Neuronal Activity*

The neuronal activity in lesioned and sham-treated animals was determined using the root mean square value as parameter of the *wavetrain* signal, and the mean firing rate as parameter calculated from detected spike events. The basal neuronal activity was measured in lesioned as well as sham-treated animals after subcutaneous injection of 0.9 % *sodium chloride*, 5 mg/kg, *apomorphine* and 5 mg/kg *quinpirole* (see figure 3.15).

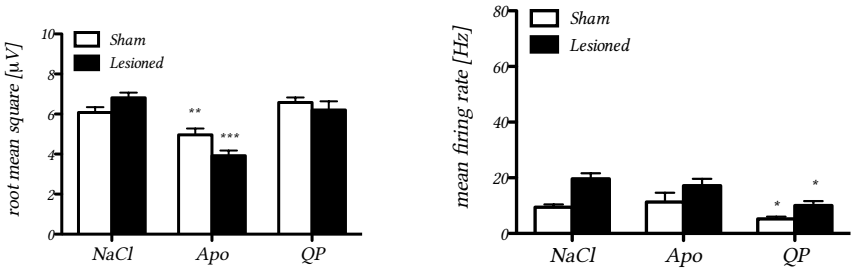

(a) (b)

Figure 3.15: Neuronal activity in lesioned and sham-treated animals after injection with 0.9 % *sodium chloride* (NaCl), 5 mg/kg *quinpirol* (QP) and 5 mg/kg *apomorphine* (Apo), administered by subcutaneous injection prior to the measurement. The neuronal activity is represented by the root mean square value of the measured *wavetrain* signal and mean firing rate of detected spike events measured with *Linear Array Probes* in the awake and unrestrained animal.

The dopamine depletion in the *caudate nucleus* in lesioned animals does not seem to affect the basal neuronal activity as measured by the root mean square value (see figure 3.15a). A two-way ANOVA test confirms that the lesion has the same effect on the above described treatments (F = 2.16, DFn = 1, DFd = 341, p = 0.1164) and that the basal neuronal activity of lesioned and sham-treated animals is not significantly different (F=0.42, DFn=1, DFd=341, p = 0.5179).

The selective $D_{2,3}$ dopamine receptor agonist *quinpirole* does not influence the basal neuronal activity compared to *sodium chloride*. The non-selective dopamine receptor agonist *apomorphine*, however, leads to a decrease in

overall subthalamic activity. This decrease is observed in both, lesioned and sham-treated animals. The effect is significant with $p = 0.0017$ for sham-treated and $p < 0.001$ for lesioned animals (unpaired t-test, two-tailed). Along with that, the two-way ANOVA reveals a highly significant effect of the treatment on the neuronal activity as measured using the root mean square value of the *wavetrain* signal ($F = 14.04$, $DFn = 2$, $DFd = 341$).

Whereas no difference between lesioned and sham-treated animals can be observed from the root mean square value of the *wavetrain* signal, the lesion does lead to an increase in the mean firing rate of detected spike events for the above described treatments. A two-way ANOVA confirms that the lesion has a significant effect on the above described treatments ($F = 7.28$, $DFn = 1$, $DFd = 272$, $p = 0.0074$). This effect is the same for all treatments ($F = 0.41$, $DFn = 2$, $DFd = 272$, $p = 0.6625$). A post-hoc t-test revealed a significantly decreased mean firing rate under *quinpirole* treatment as compared to *sodium chloride*, with $p = 0.033$ for lesioned and $p = 0.017$ for sham-treated animals.

3.5 *Rotational Behaviour*

3.5.1 *Apomorphine Induced Rotational Behaviour*

Rotational behaviour was studied to determine the extent of the nigrostriatal denervation in lesioned and sham-treated animals using subcutaneous injection of the non-selective dopamine agonist *apomorphine* (Da Cunha et al. 2008) (see figure 3.16). *Apomorphine* treatment leads to a significant increase in the number of full rotations per minute in lesioned animals with $p < 0.001$ (unpaired t-test, two-tailed). Yet, although not significant with $p = 0.4950$, an increased number of rotations was also observed in a few sham-treated animals. The preferred direction of *apomorphine* induced rotational behaviour was clockwise, ipsilateral to the side of probe implantation (see figure 3.17).

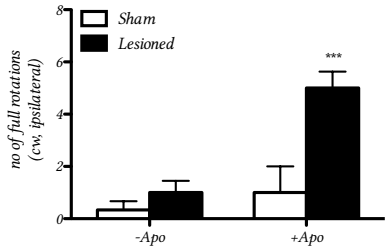

Figure 3.16: *Rotational response* to treatment with 5 mg/kg *apomorphine* in lesioned and sham-treated animals. The number of full rotations per minute is displayed for each group.

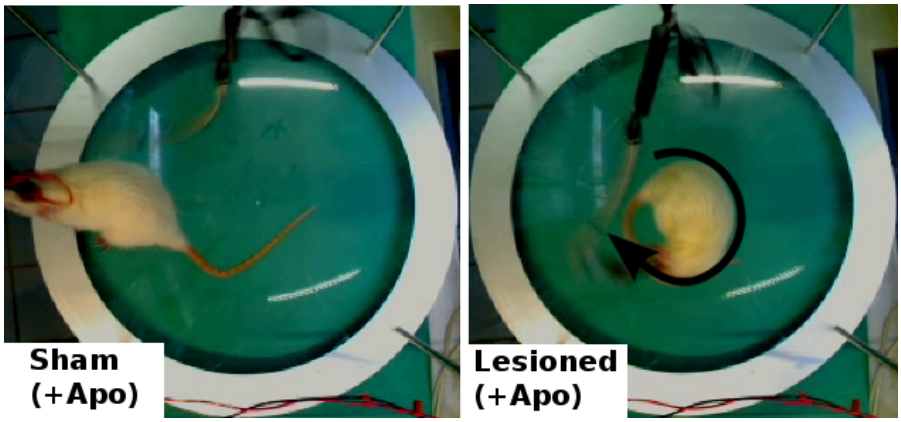

Figure 3.17: *Apomorphine* induced ipsilateral rotational behaviour in lesioned animals. Sham-treated animals showed very little or no directed rotational behaviour.

3.5.2 *Rotational Behaviour Induced by Subthalamic High-frequency Microstimulation*

Rotational behaviour is not only induced by pharmacological stimulation of the dopaminergic activity but also by *subthalamic high-frequency microstimulation*. Constant current pulses with 0.0, 0.2 and 0.3 mA amplitude at the stimulation site of the implanted probe were used to determine the efficacy of the applied electrical stimulation on a behavioural level (see figure 3.18). Thirty minutes after subcutaneous injection of 0.9 % *sodium chloride* (+NaCl) or 5 $^{mg}/_{kg}$ *quinpirole* (+QP), lesioned and sham-treated animals were subjected to *high-frequency microstimulation* (HFS) with currents of 0.0, 0.2 and 0.3 mA.

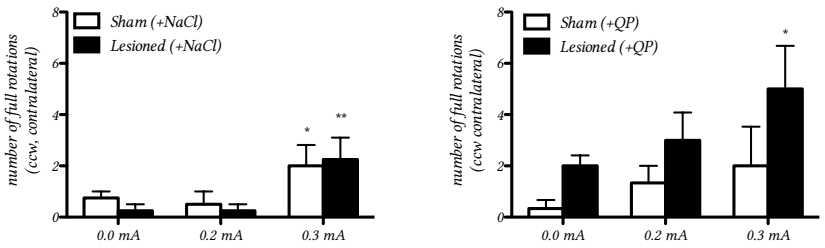

(a) (b)

Figure 3.18: *Rotational response* induced by *subthalamic high-frequency microstimulation* at the stimulation site of implanted *Linear Array Probes*. Stimulation was applied in lesioned and sham-treated animals after subcutaneous injections of 0.9 % *sodium chloride* (+NaCl) and 5 $^{mg}/_{ml}$ *quinpirole*.

When lesioned and sham-treated animals were treated with 0.9 % *sodium chloride*, increased *rotational response* was observed at 0.3 mA (see figure 3.18a) with p = 0.0264 and p = 0.0041 (unpaired t-test, two-tailed).

When animals received *quinpirole* injection, increased *rotational response* is observed in lesioned animals compared to sham-treated animals for all current amplitudes (two-way ANOVA, p = 0.0392). Increased *rotational response* compared to 0.0 mA stimulation is observed at 0.2 mA. The effect is increasing at 0.3 mA (see figure 3.18b). Due to large error bars, significance with p = 0.0134 can only be established for 0.3 mA constant current stimulation in lesioned animals pre-treated with subcutaneous injection of 5 $^{mg}/_{kg}$ *quinpirole* (unpaired t-test, two-tailed).

When *high-frequency microstimulation* was applied in the *subthalamic nucleus*, the preferred direction of the *rotational response* was counterclockwise, contralateral to the side of probe implantation (see figure 3.17).

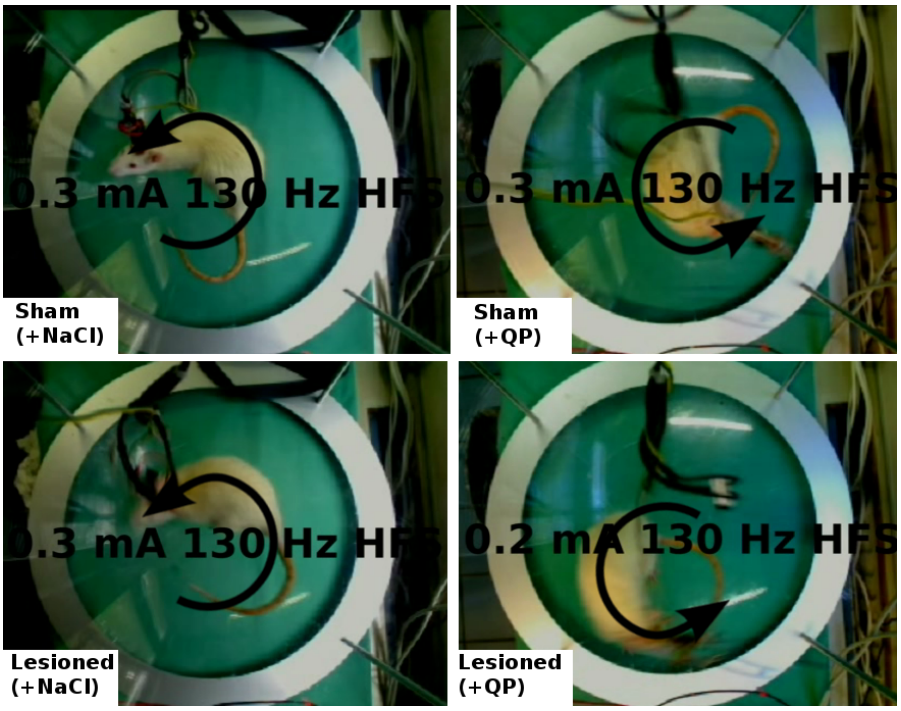

Figure 3.19: *Subthalamic high-frequency microstimulation* induced counterclockwise rotational behaviour, directed contralateral to the side of the stimulation, in lesioned and sham-treated animals.

3.6 *Network Response to High-frequency Microstimulation*

The electrophysiological response to *subthalamic high-frequency microstimulation* with 0.0, 0.1, 0.2, 0.3 and 0.4 mA was measured in lesioned and sham-treated animals after injection of 0.9 % *sodium chloride* and in sham-treated animals after injection of 5 $^{mg}/_{ml}$ *quinpirole*. Constant current stimulation was applied via the stimulation site at the tip of the *Linear Array Probes* and via the deepest stimulation site at the *Flexible Array Probes*. The *wavetrain* signal was recorded for 60 s before *high-frequency microstimula-*

tion (HFS) was applied for 60 s and for 60 s after *high-frequency microstimulation* was applied.

3.6.1 *Signature Curves of Neuronal Activity*

From the *wavetrain* signal, recorded with 24.414 kHz, the *root mean square per second* and the *mean spectral density per second* were calculated and normalized to the median of the baseline before HFS (-60, -2). *Signature curves*, representing the mean value of all experiments (n > 3), are displayed for all channels. Since the experiment was carried out to characterize the non immediate effect of *subthalamic high-frequency stimulation* events occurring from -2 to 2 s are greyed out and not included in the analysis.

When *Linear Array Probes* were used for *high-frequency microstimulation* and electrophysiological recordings, clean signature curves were recorded for channels 1 to 7 (see figure 3.20).

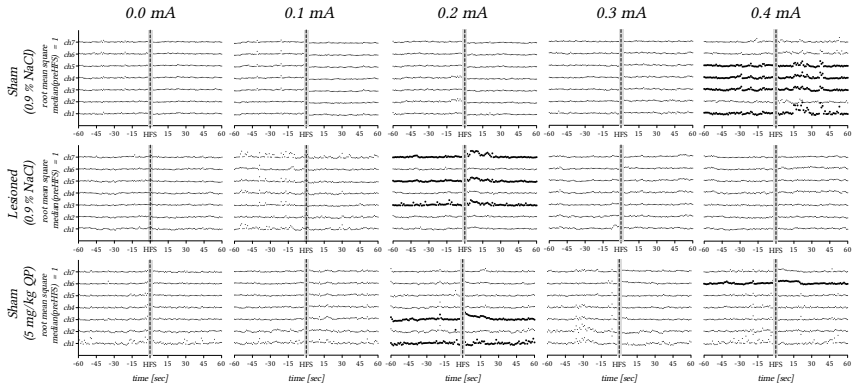

Figure 3.20: *High-frequency microstimulation* and *multi-site recording* was carried out with implanted *Linear Array Probes*. The normalized *root mean square per second* was calculated from the *wavetrain* signal and is displayed for a period of 60 s before *high-frequency microstimulation* was applied (before HFS, -60 to -2 s) and for a period of 60 s after *high-frequency microstimulation* was applied (after HFS, 2 to 60 s). *High frequency microstimulation* was applied for 60 s and is indicated by a dotted line in each graph. The delayed network response at > 2 s after *high-frequency microstimulation* is evaluated. Events, occurring between -2 and 2 s, are greyed out and are not included in the analysis.

In sham-treated animals which received injection of 0.9 % *sodium chloride* 30 min before the measurement, a delayed electrophysiological response to *high-frequency microstimulation* is observed at 0.4 mA on channels 1,3 and 5 about 15 s after *high-frequency microstimulation* ceases. The *root mean square per second* increases for a period of about 15 s until it returns to baseline level.

In sham-treated animals which received subcutaneous injection of 5 $^{mg}/_{ml}$ *quinpirole*, the *root mean square per second* increases on channels 3, 5 and 7 about 3 s after *high-frequency microstimulation* ceases. The increase lasts

about 15 s. Similar results are observed in lesioned animals which receive injection of *sodium chloride*. Although the peak amplitude is considerably lower, increased *root mean square per second* is observed directly after stimulation with 0.2 mA and after 0.4 mA stimulation with about 15 s delay.

Although recording with *Flexible Array Probes* results in noisier data and less clear *signature curves* in figure 3.21, the *root mean square per second* increases after 0.2 mA *high-frequency microstimulation* via the deepest stimulation site in all groups.

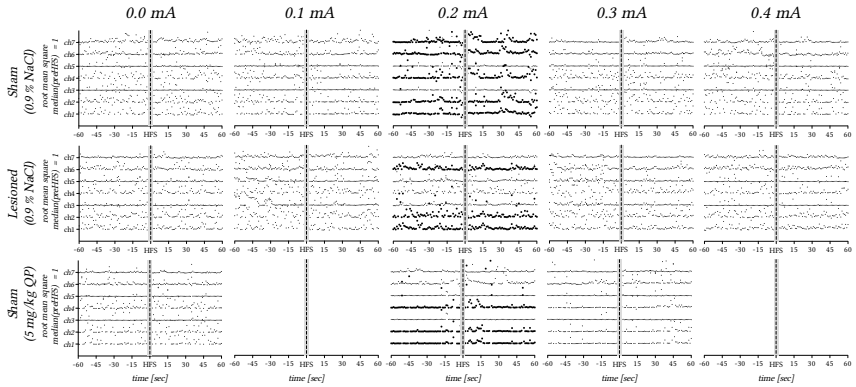

Figure 3.21: *High-frequency microstimulation* and *multi-site recording* was carried out with implanted *Flexible Array Probes*. The normalized *root mean square per second* was calculated from the *wavetrain* signal and is displayed for a period of 60 s before *high-frequency microstimulation* was applied (before HFS, -60 to -2 s) and for a period of 60 s after *high-frequency microstimulation* was applied (after HFS, 2 to 60 s). *High-frequency microstimulation* was applied for 60 s and is indicated by a dotted line in each graph. The delayed network response at > 2 s after *high-frequency microstimulation* is evaluated. Events, occurring between -2 and 2 s are greyed out and are not included in the analysis. Little data were available for 0.1 and 0.4 mA in sham-treated animals which received injection of *quinpirole*.

In sham-treated animals, receiving *sodium chloride* injection, a biphasic increase in *root mean square per second* occurs after 0.2 mA *high-frequency microstimulation* with the first peak at about 2 - 15 s and the second peak at about 30 - 40 s.

Low amplitude *root mean square per second* increase occurs about 4 s after 0.2 mA *high-frequency microstimulation* in lesioned animals which, before the measurement, received *sodium chloride* injection . A similar response is observed in sham-treated animals which received injection of 5 $^{mg}/_{ml}$ *quinpirole* prior to the experiment. Little data were obtained for 0.1 and 0.4 mA *high-frequency microstimulation* in sham-treated animals which received injection of *quinpirole*.

To verify the results obtained from the *root mean square per second*, the *mean spectral density per second* was calculated to obtain a second parameter based on the *wavetrain* signal data. The normalized *mean spectral density per second*, allows to make the same statements for implanted *Linear Array Probes* and *Flexible Array Probes* as the *root mean square per second*.

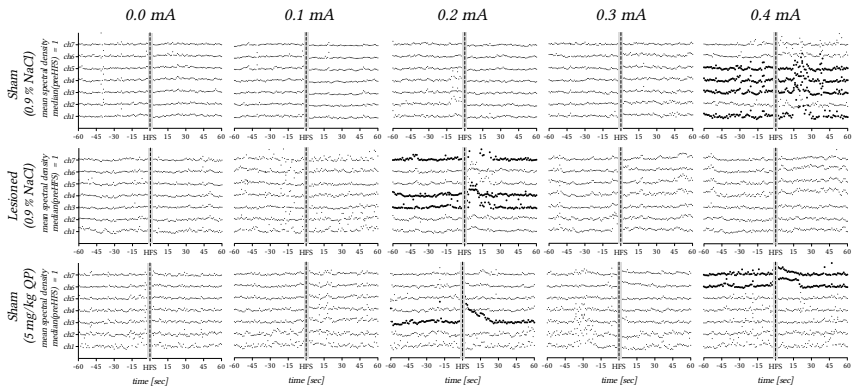

Figure 3.22: *High frequency microstimulation* and *multi-site recording* was carried out with implanted *Linear Array Probes*. The normalized *mean spectral density per second* was calculated from the *wavetrain* signal and is displayed for a period of 60 s before *high-frequency microstimulation* was applied (before HFS, -60 to -2 s) and for a period of 60 s after *high-frequency microstimulation* was applied (after HFS, 2 to 60 s). *High frequency microstimulation* was applied for 60 s and is indicated by a dotted line in each graph. The delayed network response at > 2 s after *high-frequency microstimulation* is evaluated. Events, occurring between -2 and 2 s, are greyed out and are not included in the analysis.

Figures 3.22 and 3.23 show the *signature curves* for the *mean spectral density per second*, before and after *high-frequency microstimulation* was applied in animals with implanted *Linear-* and *Flexible Array Probes*. For both electrode types, the *mean spectral density per second* peaks occur largely simultaneous with the *root mean square per second* peaks described above. The *mean spectral density per second* peak amplitude is more pronounced compared to the *root mean square per second* peak amplitude. Accordingly, the *mean spectral density per second* seems to be more sensitive to artefacts and noise since the signature curves are not as clean as for the *root mean square per second.*

3.6.2 *Averaged Network Response*

Statistically relevant data about the effect of *high-frequency microstimulation* on the *root mean square per second* and the *mean spectral density per second* were obtained from all channels that show a response to *high-frequency microstimulation* at the respective current amplitude (see figures 3.20 to 3.23.

The effect of *high-frequency microstimulation* on the *root mean square per second* and the *mean spectral density per second* with implanted *Linear Array Probes* is summarized in figure 3.24.

Mean value and standard error of the normalized *root mean square per second* and *mean spectral density per second* are plotted against time in seconds for sham-treated animals which received injection of 0.9 % *sodium chloride* before and after 0.4 mA *high-frequency microstimulation*, for lesioned

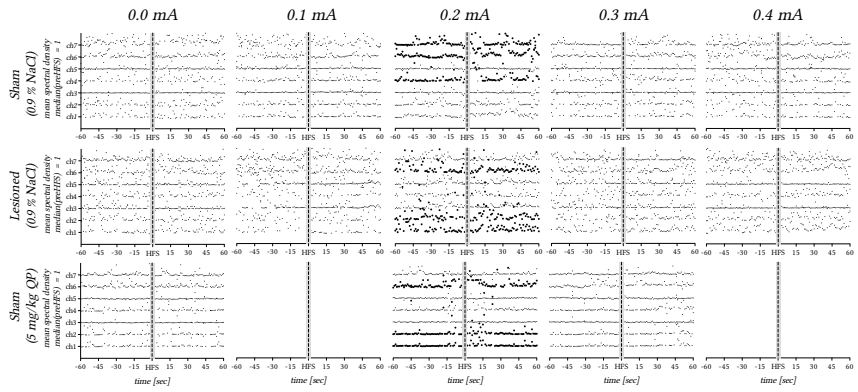

Figure 3.23: *High frequency microstimulation* and *multi- site recording* was carried out with implanted *Flexible Array Probes*. The normalized *mean spectral density per second* was calculated from the *wavetrain* signal and is displayed for a period of 60 s before *high-frequency microstimulation* was applied (before HFS, -60 to -2 s) and for a period of 60 s after *high-frequency microstimulation* was applied (after HFS, 2 to 60 s). *High frequency microstimulation* was applied for 60 s and is indicated by a dotted line in each graph. The delayed network response at > 2 s after *high-frequency microstimulation* is evaluated. Events, occurring between -2 and 2 s, are greyed out and are not included in the analysis. Little data were available for 0.1 and 0.4 mA in sham-treated animals which received *quinpirole injection*.

animals which received injection of 0.9 % *sodium chloride* before and after 0.2 mA *high-frequency microstimulation* and for sham-treated animals which received *quinpirole* injection before and after 0.2 mA *high-frequency microstimulation*.

The *area under the curve* (AUC) for both *wavetrain* data based parameters (see figures 3.24c and 3.24d) was calculated from the sum of the respective *wavetrain* based parameter per second from 15 to 30 s for sham-treated animals which received injection of *sodium chloride* injection, and from 4 to 19 s for lesioned animals which received *sodium chloride* injection and sham-treated animals receiving injection of *quinpirole*. The *area under the curve* after *high-frequency microstimulation* in each group is compared to the respective *area under the curve* from -17 to -2 s before *high-frequency microstimulation* was applied.

In sham-treated animals which received injection of *sodium chloride*, *wavetrain* based parameter clearly increase 15 s for about 15 s after 0.4 mA stimulation. A second and third peak with shorter duration and smaller amplitude occur about 35 s and 55 s after *high-frequency microstimulation* ceased. The maxima of this oscillatory response lie at 22, 37 and 53 s resulting in a mean interval of 15.5 s between peaks. Thus, an oscillatory frequency of 0.065 Hz is calculated. The *area under the curve* of the first peak after *high-frequency microstimulation* is significantly larger compared to the *area under the curve* before *high-frequency microstimulation* with $p < 0.0001$ for the *root mean square per second* and $p = 0.007$ for the *mean spectral density* (unpaired t-test, two-tailed).

In lesioned animals, pretreated with *sodium chloride*, the response to stimulation with 0.2 mA occurs faster, already after about 4 s after *high-frequency microstimulation* ceased. Two overlapping peaks are visible. The first peak occurs from 4 to 15 s and the second from 15 to 20 s with smaller amplitude. The peak maxima lie at 6 s and 19 s with a 15 s interval between peaks. The increase in the *area under the curve* of the *root mean square per second* after *high-frequency microstimulation* is significant compared to the *area unter the curve* before *high-frequency microstimulation* with p = 0.0174 (unpaired t-test, two-tailed).

In sham-treated animals receiving *quinpirole* injection, the response to 0.2 mA stimulation occurs, similar to lesioned animals, directly after *high-frequency microstimulation* from 3 to 20 s. The response amplitude is smaller compared to the lesioned group. Although multiple peaks cannot be distinguished, the relatively long duration of the response indicates that the response to *high-frequency microstimulation* might, too, originate from oscillatory activity as it is observed in animals that do not receive *quinpirole* treatment. Despite the small response amplitude, the area under the curve increases significantly after 0.2 mA *high-frequency microstimulation* compared to the *area unter the curve* before *high-frequency microstimulation* with p = 0.0079 for the *root mean square per second* and p = 0.0056 for the *mean spectral density per second* (unpaired t-test, two-tailed).

The effect of *high-frequency microstimulation* on the *root mean square per second* and the *mean spectral density per second* with implanted *Linear Array Probes* is summarized in figure 3.25. Data are presented as explained for figure 3.24.

Mean value and standard error of the normalized *root mean square per second* and *mean spectral density per second* are plotted against time in seconds for sham-treated animals which received *sodium chloride* injection before and after 0.2 mA *high-frequency microstimulation*, for lesioned animals which received *sodium chloride* injection before and after 0.2 mA *high-frequency microstimulation* and for sham-treated animals which received *quinpirole* injection before and after 0.2 mA *high-frequency microstimulation.*

The *area under the curve* (AUC) for both *wavetrain* data based parameters (see figures 3.24c and 3.24d) was calculated from the sum of the respective *wavetrain* based parameter per second from 4 to 19 s in all groups and compared to the *area under the curve* from -17 to -2 s before *high-frequency microstimulation* was applied.

In sham-treated animals which received *sodium chloride* injection, *wavetrain* based parameter show a triphasic increase as seen with implanted *Linear Array Probes* after 0.2 mA stimulation occurring not delayed but directly after *high-frequency microstimulation* ceased. The maxima of this oscillatory response lie at 9, 34 and 53 s resulting in a mean interval of 22.0 s between peaks with an oscillatory frequency of 0.045 Hz. The *area unter the curve* of the first peak after *high-frequency microstimulation* is significantly larger compared to the *area under the curve* before *high-frequency microstimulation* with p = 0.0047 (unpaired t-test, two-tailed).

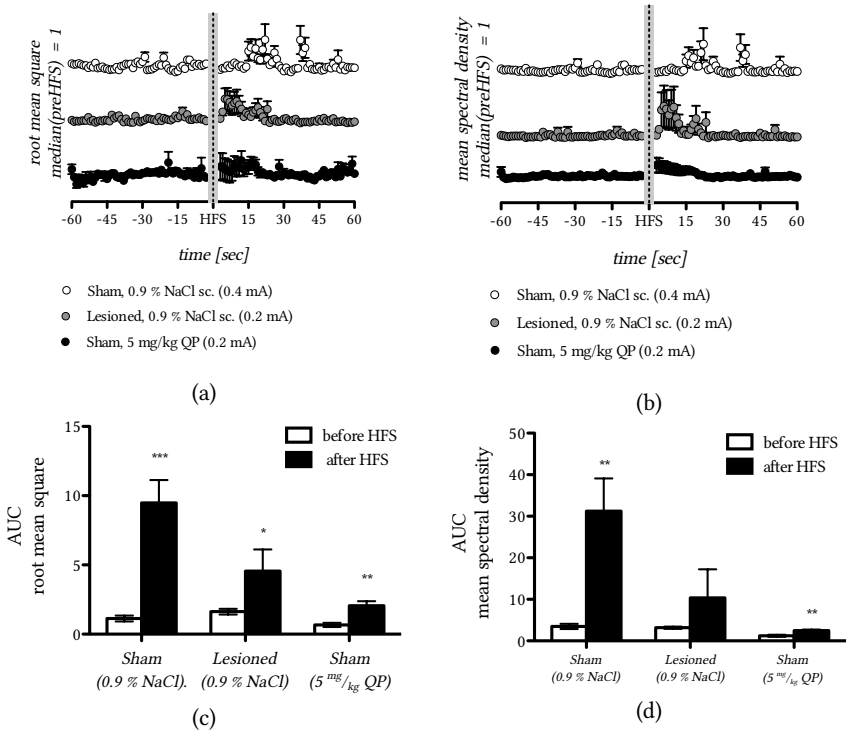

Figure 3.24: Neuronal response to *high-frequency microstimulation* quantified by means of *wavetrain* based parameters, in animals with implanted *Linear Array Probes*. Mean values and standard error of the relevant signature curves are shown. The *area under the curve* of the largest peak after *high-frequency microstimulation* (after HFS) is compared to the *area under the curve* before *high-frequency microstimluation* (before HFS) of the respective group.

In lesioned animals, pretreated with *sodium chloride*, the response occurs, as well, directly after *high-frequency microstimulation* with 0.2 mA. The biphasic increase is visible in the *mean spectral density per second*. The peak maxima lie at 6 s and 16 s with 10 s interval between peaks. The increase in the *area under the curve* of the *root mean square per second* and *mean spectral density* after *high-frequency microstimulation* is significant compared to the *area under the curve* before *high-frequency microstimulation* with $p < 0.0001$ (unpaired t-test, two-tailed).

In sham-treated animals, which received *quinpirole* injection the response to 0.2 mA stimulation is similar to the response described for implanted *Linear Array Probes*. Despite lower amplitudes, the *area under the curve* for the *root mean square per second* and the *mean spectral density per second* are significantly different with $p = 0.0002$ and $p = 0.0103$ since the standard deviation is considerably smaller for animals receiving *quinpirole* injection (unpaired t-test, two-tailed).

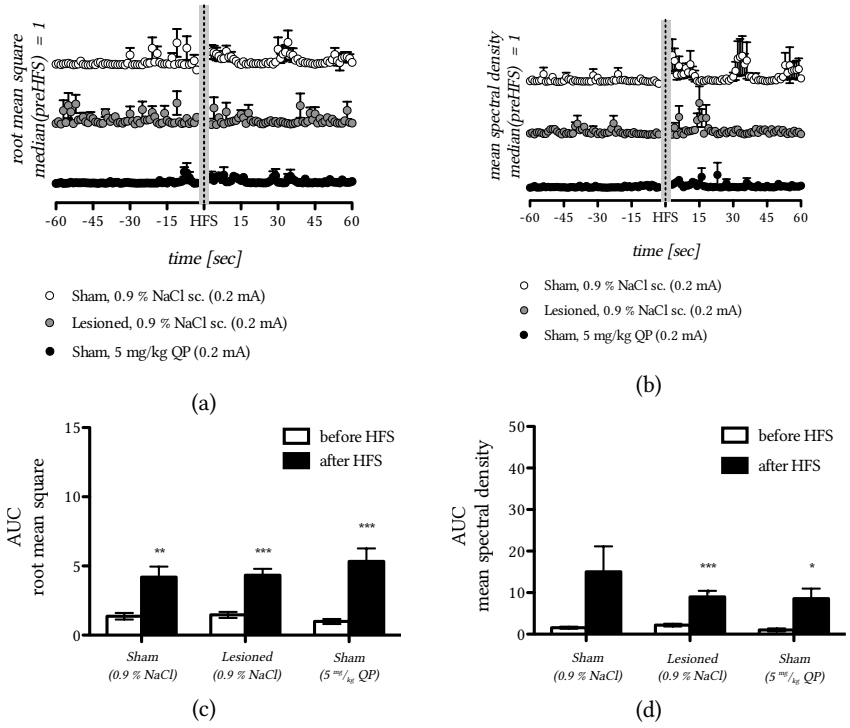

Figure 3.25: Neuronal response to *high-frequency microstimulation* quantified by means of *wavetrain* based parameters, in animals with implanted *Flexible Array Probes*. Mean values and standard error of the relevant signature curves are shown. The *area under the curve* of the largest peak after *high-frequency microstimulation* (after HFS) is compared to the *area under the curve* before *high-frequency microstimluation* (before HFS) of the respective group.

3.7 *Single Unit Response to High-frequency Microstimulation*

The effect of *high-frequency microstimulation* on single unit spike activity in the vicinity of the stimulation site was investigated. Spike events were detected from the recorded *wavetrain* signal for a period of 60 s before and 60 s after *high-frequency microstimulation*. Similar spike shapes, occurring in the *wavetrain* signal of each channel were grouped into clusters. The parameters Δn, Δisi, and $\Delta entropy$ were calculated from the difference in number and frequency of spike events before and after *high-frequency microstimluation*. To group spike shapes occurring in a set of experiments, the mean spike shape of the individual spikes in each group was clustered again. Groups of spike shapes with individual parameters Δn, Δisi, and $\Delta entropy$ were obtained, and, in each group of spike shapes (clusters), the relative sum of the parameters $\sum(\Delta n)$, $\sum(\Delta isi)$, $\sum(\Delta entropy)$ was calculated.

If $\sum(\Delta n)$, $\sum(\Delta isi)$ or $\sum(\Delta entropy)$ in a certain cluster was greater than zero, the individual values Δn, Δisi, and $\Delta entropy$ of spikes in this cluster were, in tendency, larger after *high-frequency microstimulation*.

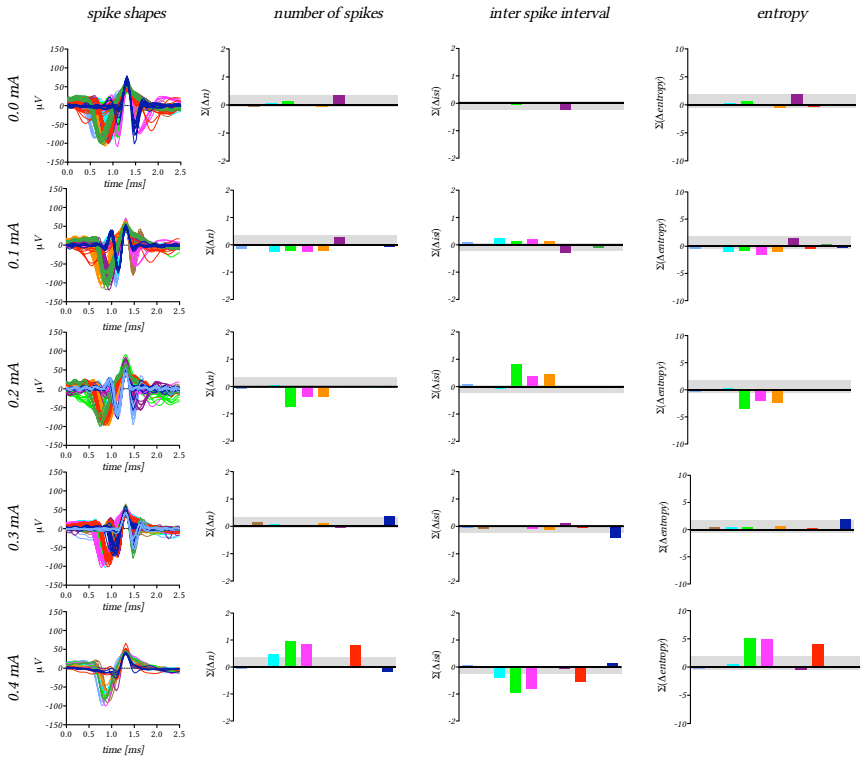

Figure 3.26: Spike activity in sham-treated animals with implanted *Linear Array Probes* was analysed after 0.0, 0.1, 0.2, 0.3 and 0.4 mA *high-frequency microstimulation* (rows 1 - 5). For each stimulation current, spike shapes were grouped. Each colour represents a group of spike shapes. The parameters $\sum(\Delta n)$, $\sum(\Delta isi)$ and $\sum(\Delta entropy)$ were calculated from the spike activity in each group before and after *high-frequency microstimulation* was applied (column 2 - 4). The threshold for random events is derived from the range of parameter values at 0.0 mA stimulation and is marked as a grey area in all subfigures. Increased spike activity is likely when parameters exceed the threshold in positive direction and decreased spike activity ins likely when parameters exceed the threshold in negative direction.

If $\sum(\Delta n)$, $\sum(\Delta isi)$ or $\sum(\Delta entropy)$ in a certain cluster was less than zero, the individual values Δn, Δisi, and $\Delta entropy$ of spikes in this cluster were, in tendency, smaller after *high-frequency microstimulation*. For $\sum(\Delta n)$ that means that, if $\sum(\Delta n) > 0$, the overall number of spike events was larger, and spike activity increased after *high-frequency microstimulation*. For $\sum(\Delta isi)$ that means that, if $\sum(\Delta isi) > 0$, the intervals between spike events were larger and spike activity decreased after *high-frequency microstimulation*. For $\sum(\Delta entropy)$ that means that, if $\sum(\Delta entropy) > 0$, the entropy of the spike events was larger after *high-frequency microstimulation* and spikes occurred more regular with predetermined timing.

Random increase and decrease, however, occurs for all parameters. Therefore, the threshold for random events was determined from the range (min to max) of $\sum(\Delta n)$, $\sum(\Delta isi)$ and $\sum(\Delta entropy)$ values when 0.0 mA current stimulation was applied.

When the values of all three parameters describing a certain cluster of spikes exceed the threshold of random events, it is likely that *high-frequency microstimulation* with the respective current induced altered spike activity in this distinct cluster. If $\sum(\Delta n)$ and $\sum(\Delta entropy)$ exceed the threshold of random events for a certain cluster in positive direction, and $\sum(\Delta isi)$ exceeds the threshold of random events for the same cluster in negative direction, increased spike activity due to *high-frequency microstimulation* is reported for this cluster. Decreased spike activity due to *high-frequency microstimulation* is reported for this cluster, when $\sum(\Delta n)$ and $\sum(\Delta entropy)$ and $\sum(\Delta isi)$ behave the opposite way.

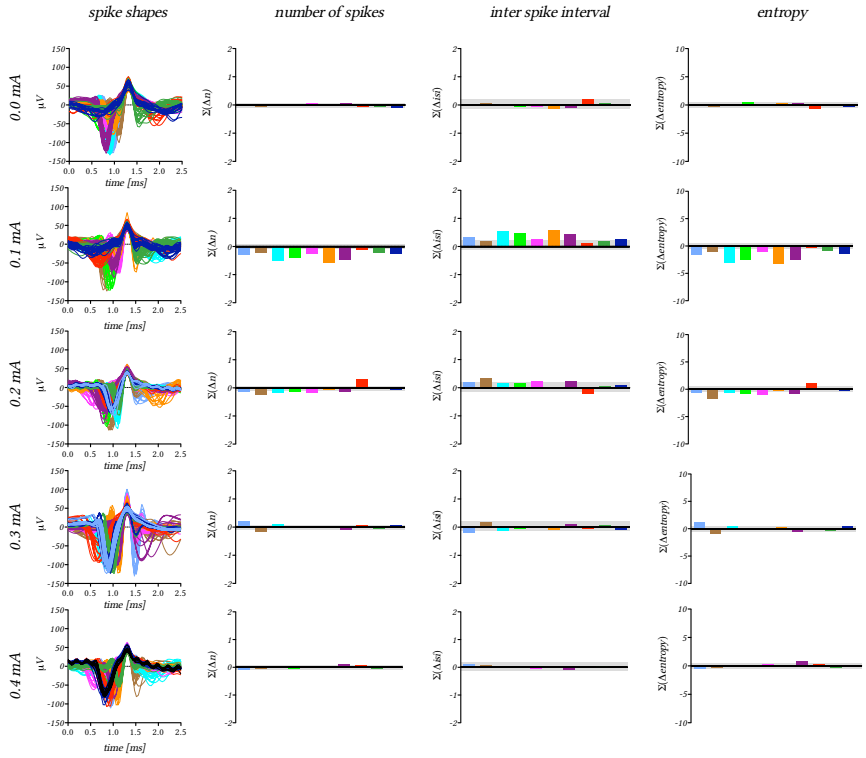

Figure 3.27: Spike activity in lesioned animals with implanted *Linear Array Probes* was analysed after 0.0, 0.1, 0.2, 0.3 and 0.4 mA *high-frequency microstimulation* (rows 1-5). For each stimulation current spike shapes were grouped and each colour represents a certain group of spike shapes. The parameters $\sum(\Delta n)$, $\sum(\Delta isi)$ and $\sum(\Delta entropy)$ were calculated from the spike activity in each group before and after *high-frequency microstimulation* was applied (column 2-4). The threshold for random events is derived from the range of parameter values at 0.0 mA stimulation and is marked as a grey area in all subfigures. Increased spike activity is likely when parameters exceed the threshold in positive direction and decreased spike activity ins likely when parameters exceed the threshold in negative direction.

3.7.1 *Single Unit Activity at Implanted Linear Array Probes*

The spike shapes and the parameters $\sum(\Delta n)$, $\sum(\Delta isi)$ and $\sum(\Delta entropy)$, derived from the spike activity before and after *high-frequency microstimulation* with 0.0, 0.1, 0.2, 0.3 and 0.4 mA measured with implanted *Linear Array Probes* are shown in figure 3.26 for sham-treated animals and in figure 3.27 for lesioned animals.

The detected spike events for all current amplitudes recorded with *Linear Array Probes* show the shape of clear *extracellular single unit activity* with 1-2 ms duration (see figure 3.26 and figure 3.27, column 1). Spike shapes differ by the width and amplitude of the initial hyperpolarisation peak, in the range of 0.25-1 ms and -100 to - 20 µV. Initial hyperpolarisation, however, seems to be no obligatory feature. The positive peak ranges between 50 and 100 µV in amplitude and is usually wider than the initial hyperpolarisation peak. In some cases, hyperpolarisation occurs after the positive peak. Hyperpolarisation peaks that follow after the positive peak are with durations up to 0.5 ms narrower than initial hyperpolarization peaks and usually also smaller in amplitude.

The shape of the detected spike event is not influenced by *high-frequency microstimulation*. The described general features of spike shapes, recorded with Linear Array Probes, do not differ in lesioned and sham-treated animals.

The parameters $\sum(\Delta n)$, $\sum(\Delta isi)$ and $\sum(\Delta entropy)$ derived from spike event number and timing, are shown in figure 3.26 and figure 3.27 in columns 1 to 3. The threshold of random events, determined from the range of all parameter values at 0.0 mA (row 1), is marked as a grey area in all subfigures.

In figures 3.26 and figure 3.27 it is visible, that, in certain clusters, the value of $\sum(\Delta n)$, $\sum(\Delta isi)$ and $\sum(\Delta entropy)$ exceeds the threshold of random events in positive or negative direction when *high-frequency microstimulation* is applied.

When all three parameters, describing a certain cluster exceed the threshold and behave in the above described way the cluster is marked with a large dot in the respective scatter plot in figures 3.28 and 3.29. If increased spike activity due to *high-frequency microstimulation* is detected for a certain cluster, the respective dot appears in the right column of the scatter plot. If decreased spike activity due to *high-frequency microstimulation* is recorded for a certain cluster, the respective dot appears in the left column of the scatter plot. When altered spike activity is detected for a certain cluster, the mean value of all individual spike shapes in this cluster is shown in row 4.

Altered spike activity in sham-treated animals with implanted *Linear Array Probes* occurs after 0.1 mA current stimulation (see figure 3.26 row 1) in cluster 2, 4 and 5, after 0.2 mA current stimulation (see figure 3.26 row 2) in cluster 3, 4 and 5, after 0.3 mA current stimulation (see figure 3.26 row 3) in cluster 9 and after 0.4 mA current stimulation (see figure 3.26 row 4) in cluster 2, 4, 5 and 7.

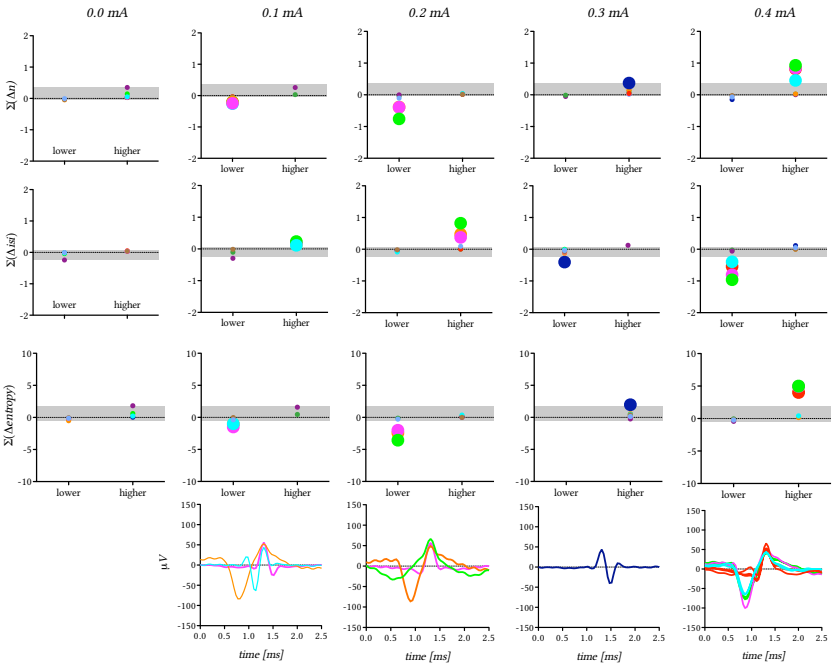

Figure 3.28: Increased and decreased spike activity in sham-treated animals with implanted *Linear Array Probes*. Stimulation currents of 0.0, 0.1, 0.2, 0.3 and 0.4 mA *high-frequency microstimulation* are directly compared with each other in columns 1 to 5. The right column in each scatter plot shows clusters in which parameter values are higher, after *high-frequency microstimulation*, indication increased spike activity. The left column in each scatter plot shows clusters in which parameter values are lower after *high-frequency microstimulation*. The scatter plots for the $\sum(\Delta n)$, $\sum(\Delta isi)$ and $\sum(\Delta entropy)$ are aranged in rows 1 to 3. The mean spike shapes for the clusters in which decreased or increased spike activity was detected are shown in row 4.

Altered spike activity in lesioned animals with implanted *Linear Array Probes* occurs after 0.1 mA current stimulation (see figure 3.27 row 1) in many clusters (0, 2, 3, 5, 6). After 0.2 mA current stimulation, imbalances, exceeding the random level only slightly, occur in cluster 1 and 7 (see figure 3.27 row 2). After 0.3 mA current stimulation (see figure 3.27 row 3) only cluster 0 shows an above threshold increase, and after 0.4 mA current stimulation (see figure 3.26 row 4) no effect is observed.

Spike activity increase and decrease in sham-treated and lesioned animals with implanted *Linear Array Probes* in response to *high-frequency microstimulation* with increasing amplitude is directly compared in figure 3.30.

In sham-treated animals, 0.2 mA stimulation seems to be most effective to suppress spiking in certain clusters. In lesioned animals, the most effective suppression is observed already at 0.1 mA. Increasing spike activity in certain clusters is observed at 0.3 and 0.4 mA stimulation, whereas 0.4 mA stimulation seems to be most effective in sham-treated animals. In lesioned animals, only a few clusters respond with increased spiking activity after 0.2

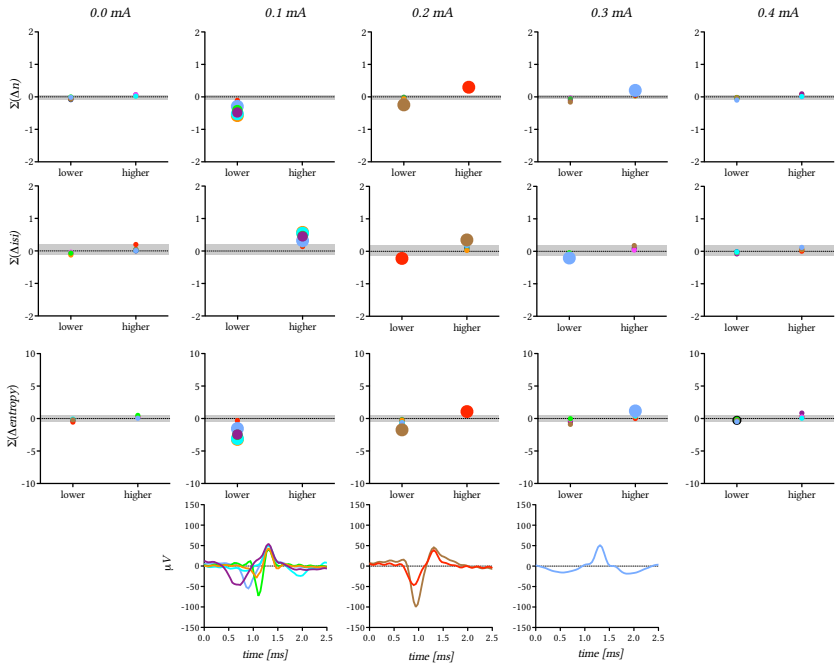

Figure 3.29: Increased and decreased spike activity in lesioned animals with implanted *Linear Array Probes*. Stimulation currents of 0.0, 0.1, 0.2, 0.3 and 0.4 mA *high-frequency microstimulation* are directly compared with each other in columns 1 to 5. The right column in each scatter plot shows clusters in which parameter values are higher, after *high-frequency microstimulation*, indication increased spike activity. The left column in each scatter plot shows clusters in which parameter values are lower after *high-frequency microstimulation*. The scatter plots for the $\sum(\Delta n)$, $\sum(\Delta isi)$ and $\sum(\Delta entropy)$ are aranged in rows 1 to 3. The mean spike shapes for the clusters in which decreased or increased spike activity was detected are shown in row 4.

and 0.3 mA. Suppression of spiking activity in lesioned animals is observed at lower currents. Only a few clusters show increased spiking activity after high current, *high-frequency microstimulation* in lesioned animals. High current, *high-frequency microstimulation* in sham-treated animals leads to a clear increase of spiking activity in certain clusters.

3.7.2 *Single Unit Activity at Implanted Flexible Array Probes*

The spike shapes and the parameters $\sum(\Delta n)$, $\sum(\Delta isi)$ and $\sum(\Delta entropy)$, derived from the spike activity before and after *high-frequency microstimulation* with 0.0, 0.1 and 0.2 mA, measured with implanted *Flexible Array Probes* are shown in figure 3.31 for sham-treated animals and in figure 3.32 for lesioned animals.

The detected spike events for all current amplitudes recorded with Flexible Array Probes show the shape of *extracellular single unit activity*. The duration of events measured is 0.5-2.5 ms (see figure 3.26 and figure 3.27,

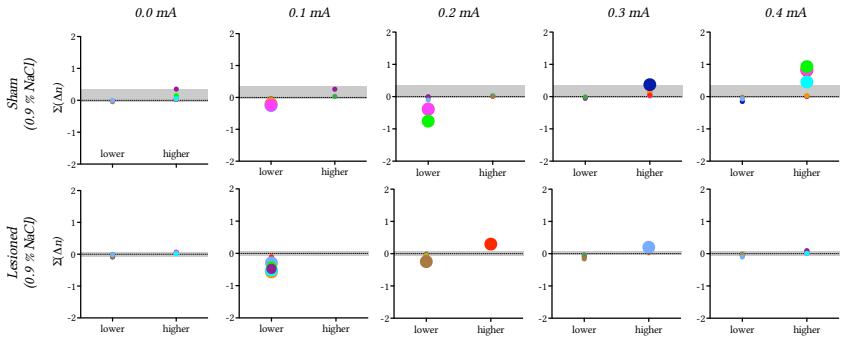

Figure 3.30: Comparinson between the stimulation current dependency of spike activity increase and decrease in sham-treated and lesioned animals with implanted *Linear Array Probes*. The $\sum(\Delta n)$ parameter is shown for sham-treated animals (row 1) and lesioned animals (row 2) at 0.1 - 0.4 mA *high-frequency microstimulation* (columns 1 - 4).

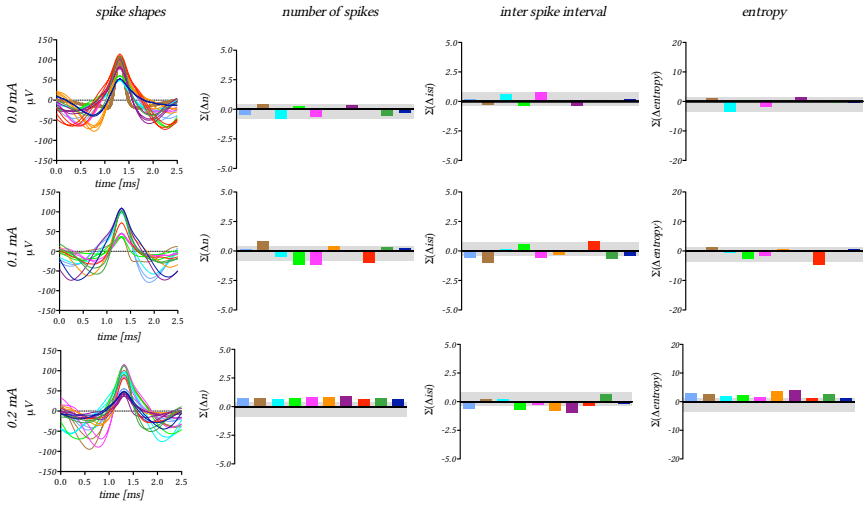

Figure 3.31: Spiking behaviour in sham-treated animals with implanted *Flexible Array Probes* was analysed after 0.0, 0.1, 0.2 mA *high-frequency microstimulation*. The spike shapes of the individual spike events in each group are shown in the first coloumn. The $\sum(\Delta n)$, $\sum(\Delta isi)$ and $\sum(\Delta entropy)$ parameters, derived from the number of spikes, the interval between spikes and the spike entropy, are shown in column 2, 3, 4. The range of random imbalances occurring at 0.0 mA (row 1) is used as a threshold to detect imbalances in spiking behaviour occurring due to *high-frequency microstimulation* with 0.1 and 0.2 mA (rows 2, 3).

column 1). Spike shapes are mostly distinguished by the amplitude of the positive peak, which is in the range of 50-100 µV. A long initial hyperpolarization peak with up to 1 ms duration and -70 µV amplitude. Spike events, missing initial hyperpolarization are also recorded. The overall duration of these events is usually shorter. A second hyperpolarisation peak occurs after the positive peak in most cases. The amplitude and duration of the sec-

ond hyperpolarization is in the same range of the initial hyperpolarization period. Spike events recorded with *Flexible Array Probes* seem to be more symmetric, than spike events, recorded with *Linear Array Probes*.

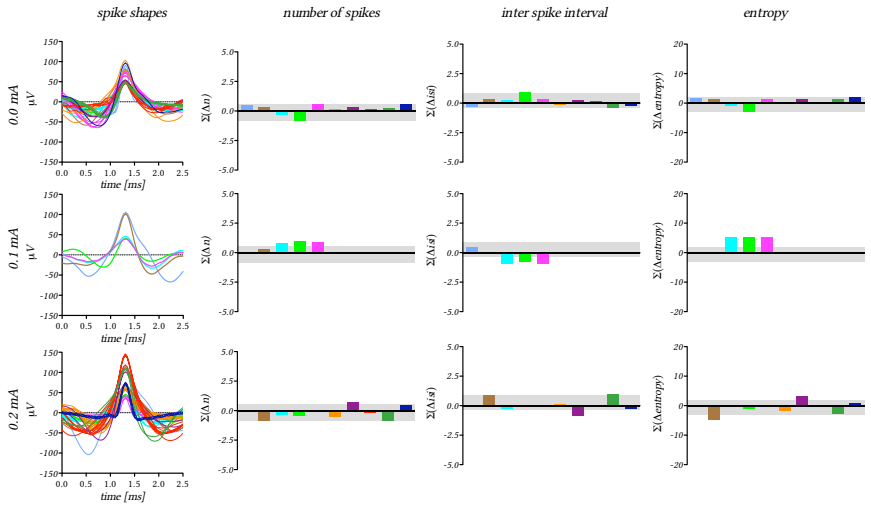

Figure 3.32: Spiking behaviour in lesioned animals with implanted *Flexible Array Probes* was analysed after 0.0, 0.1, 0.2 mA *high-frequency microstimulation*. The spike shapes of the individual spike events in each group are shown in the first coloumn. The $\sum(\Delta n)$, $\sum(\Delta isi)$ and $\sum(\Delta entropy)$ parameters, derived from the number of spikes, the interval between spikes and the spike entropy, are shown in column 2, 3, 4. The range of random imbalances occurring at 0.0 mA (row 1) is used as a threshold to detect imbalances in spiking behaviour occurring due to *high-frequency microstimulation* with 0.1 and 0.2 mA (rows 2, 3).

The shape of the detected spike event is not influenced by *high-frequency microstimulation*. The described general features of spike shapes, recorded with Linear Array Probes do not differ in lesioned and sham-treated animals.

When all three parameters, describing a certain cluster, exceed the threshold and behave in the above described way, the cluster is marked with a large dot in the respective scatter plot in figures 3.33a and 3.33b.

If increased spike activity due to *high-frequency microstimulation* is detected for a certain cluster, the respective dot appears in the right column of the scatter plot. If decreased spike activity due to *high-frequency microstimulation* is recorded for a certain cluster, the respective dot appears in the left column of the scatter plot. When altered spike activity is detected for a certain cluster, the mean value of all individual spike shapes in this cluster is shown in row 4.

In sham-treated animals with implanted *Flexible Array Probes*, decreased spike activity occurs after 0.1 mA only in cluster 7. Increased spike activity in cluster 0, 3, 5 and 6 is observed after 0.2 mA *high-frequency microstimulation* in sham-treated animals with implanted *Flexible Array Probes*.

In lesioned animals with implanted *Flexible Array Probes* spike acticity increases stimulation in cluster 3 and 4 after 0.1 mA. After 0.2 mA, min-

imal increased spike activity occurs in cluster 6 in lesioned animals with implanted *Flexible Array Probes*.

Spike activity is most effectively induced with 0.1 mA current stimulation in lesioned animals, and with 0.2 mA current stimulation in sham-treated animals. Also, it seems more likely to see increased spiking activity in certain clusters after *high-frequency microstimulation*.

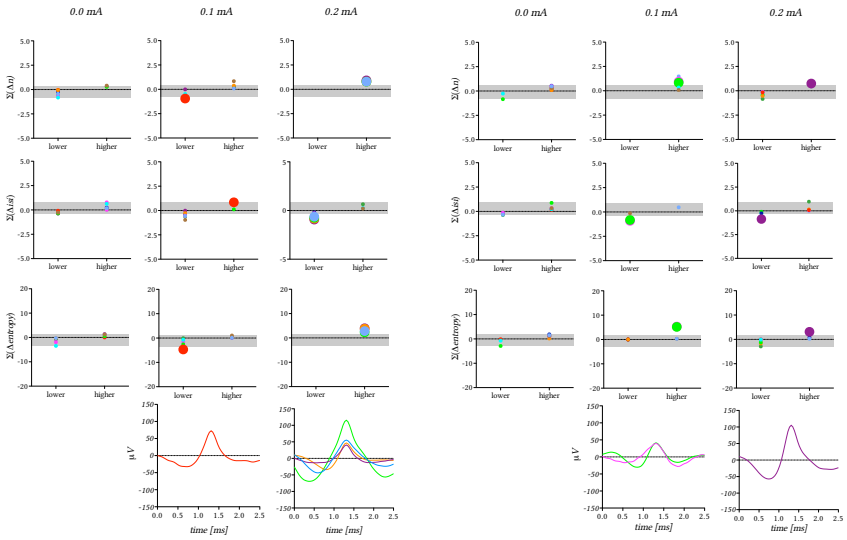

(a) Sham (b) Lesioned

Figure 3.33: Increased and decreased spike activity in sham-treated ans lesioned animals with implanted *Flexible Array Probes*. Stimulation currents of 0.0, 0.1 and 0.2 mA *high-frequency microstimulation* are directly compared with each other in columns 1 to 3. The right column in each scatter plot shows clusters in which parameter values are higher, after *high-frequency microstimulation*, indication increased spike activity. The left column in each scatter plot shows clusters in which parameter values are lower after *high-frequency microstimulation*. The scatter plots for the $\sum(\Delta n)$, $\sum(\Delta isi)$ and $\sum(\Delta entropy)$ are aranged in rows 1 to 3. The mean spike shapes for the clusters in which decreased or increased spike activity was detected are shown in row 4.

4

DISCUSSION

Deep brain stimulation in the subthalamic nucleus is a well established clinical treatment. Yet, in the last 15 years, the technique did not advance considerably. Today, more and more *deep brain stimulation* implants are given to younger patients and treatment of parkinsonian motor symptoms by subthalamic *deep bain stimulation* remains but one of a widespread range of applications in various cerebral target regions. The dramatic increase in number of implanted *deep brain stimulation* devices and the increased demand in long-term stability which comes with longer total implantation times, creates the need for improved techniques and devices (Coffey 2009).

Currently, device development is directed towards closed-loop systems enabling feedback-controlled *deep brain stimulation* in a clinically relevant setting. The battle for improved *deep brain stimulation* devices is fought on different levels. Miniaturized multi-channel bioamplifiers with signal processing modalities and low-power consumption are developed together with high-efficiency stimulation devices and high-capacity batteries for power supply. Major research efforts are focused towards the development of new neuronal probes as cerebral interfaces for neuronal recording and stimulation (Stieglitz 2002, HajjHassan et al. 2008).

Modern neuronal probes provide multiple channels for high-resolution neuronal recordings and are required to integrate modalities for electrical stimulation to facilitate feedback-controlled *deep brain stimulation*. Ideally, recording and stimulation sites are distributed over a wide area. This allows to acquire neuronal feedback from many different neuronal elements. Further, presence of multiple recording and stimulation sites allows to compensate implantation inaccuracies facilitating single-step probe implantation followed by neuronavigation. Ideally, probes would support automated *neuronavigation* procedures to allow quick and precise probe insertion, keeping surgery times at a minimum. Yet, to avoid cerebral bleeding and tissue damage by insertion, lead sizes must be kept as small as possible (Coffey 2009, Menne 2005).

The need for small lead sizes, and a multitude of recording and stimulation sites poses a problem which requires to rethink the current mode how electrical stimulation is applied to the tissue. Currently, large size macroelectrodes are used. Yet, it is shown, that the effect of the electrical stimulation in the tissue mainly depends on the charge which is injected per pulse. If high charge densities in small electrodes can be reached without causing electrolytic damage and material deposition in the tissue, electrical stimulation via small sized microelectrodes would be as effective (HajjHassan et al. 2008).

To allow for feedback controlled high-frequency microstimulation, probe performance of chronically implanted probes needs to be ensured over a

long time range. Foreign body response leads to exclusion of the probe from the neuronal tissue. The use of flexible probes produced from biocompatible materials leads to minimized tethering forces. Thereby, micromovements of the probe are avoided (Biran et al. 2005).

Research on the device perspective goes along with research about the performance of the newly developed devices in the tissue. New studies indicate that the effect of electrical stimulation in the tissue might be a specific effect on GABAergic neurons, but there is still no widely accepted molecular mechanism that explains the actions of *deep brain stimulation* (Feuerstein et al. 2011). Thus, finding parameters for feedback controlled stimulation is difficult and requires empirical observation for the respective probe type and target area.

In the current work, we used a new type of a *metal microelectrode* with metal microwires inserted into a metal tube cannula and microwire contact sites arranged as a lateral array along the probe shaft. A stimulation modality is provided by a larger microwire contact site at the tip of the electrode.

Metal microelectrodes represent the most widely used neural probes. They are easy to produce and reliable for long term chronic implantations. Yet, they come with the problem that increasing the number of recording sites requires increasing the number of wires which results in a linear increase in overall probe size and causes undesirable neural tissue damage. The *Linear Array Probes* that were used in the current work take advantage of the *metal wire microelectrodes* used earlier (Hammad et al. 2010, Porada et al. 2000, Tsai & Yen 2003) and overcome the limitations of standard *metal wire microelectrodes* by borrowing from the linear array design of neural probes developed using MEMS processing (Wise et al. 2004). The layout of the *silicon on insulator* based ACREO probes produced using a MEMS based process are the design model for the probes used in the current study (Hofmann et al. 2006, Kindlundh et al. 2004, Norlin et al. 2002). By combination of the two leading techniques for production of neural probes, bimodal neural interfaces for high-resolution neuronal recording with stable and ultra-thin shaft design were produced.

The design of the *Flexible Array Probe* takes the advantages of the *Linear Array Pobes* even one step further. The polymer *polyimide* is used as a carrier for metal contact sites to form a biocompatible interface between the probe and the brain tissue (Richardson et al. 1993). Due to the flexible design, tethering forces to the probe are reduced by 65–94 % (Subbaroyan et al. 2005). Thus, the probe is floating in the brain tissue and micromovements of the electrode are reduced drastically. Although flexible probes have been used as surface electrodes on the cortex, intracerebral implantation of these probes has been an issue (Kisban et al. 2007). Here, we report long term chronic recordings and stimulation with *Flexible Array Probes* intracerebrally implanted into the *subthalamic nucleus* using a precise stereotaxic technique. Since this has, to our knowledge, never been done before, we use *Linear Array Probes* to provide a standard for comparison of *Flexible Array*

Probe performance to the best known technique for two-directional neuronal interfacing.

To demonstrate clinical relevance of the new designs of neuronal interfaces, we propose an automizeable technique for *neuronavigation* along the full depth of a stereotaxic trajectory. Thereby, we show that implantation of the new probes could be achieved in a one step process which, together with fast precise and objective information about the current location in the brain, would save valuable time in a stereotaxic surgery (Moll et al. 2005).

By performing acute recording in all regions along the trajectory to the *subthalamic nucleus* we show that both probe types are capable of recording high quality *single-* and *multi-unit potentials*, especially in the *basal ganglia* and the *thalamus*. At the same time, the *impedance* of *Linear-* and *Flexible Array Probes* is tailored to support recording of neuronal background activity. This makes them an ideal tool for *neuronavigation* relying on the various levels of neuronal activity (Johansson et al. 2009, Starr et al. 2006).

Beyond recording of neuronal activity, we used the stimulation modality on both probe types to exert functional *high-frequency microstimulation* in the *subthalamic nucleus* in the rat. By repeating sequences of *high-frequency microstimulation* with different current amplitudes over a time period of four weeks, we established the suitability of *Linear-* and *Flexible Array Probes* for long term usage. For stimulation, we used *charge per phase* values which were reported as functionally effective. But since the *geometric surface area* of *Linear-* and *Flexibe Array Probes* is so small, keeping threshold values for functional stimulation was at the cost of high *current densities*. Thus, we drove the electrodes towards the limits of their *current delivery capacity* and risk occurence of *faradic reactions* on the electrode surface (Kuncel & Grill 2004). Yet, recording and stimulation performance of *Linear-* or *Flexible Array Probes* was not notably impaired after repeated *high-frequency microstimulation*.

In addition to acute recordings of neuronal activity and concurrent *high-frequency microstimulation* in the *subthalamic nucleus*, we provide data about the long term performance of chronically implanted *Linear-* and *Flexible Array Probes*. Even after four weeks of implantation it was still possible to record neuronal activity in the freely behaving animal, to detect the neuronal response to *high-frequency microstimulation* and to induce *rotational behaviour* in response to *high-frequency microstimulation*. By monitoring the voltage response to current stimulation on *Linear-* and *Flexible Array Probes*, we determined how the *foreign-body response* of the tissue influences the effect of stimulation. We provide neurophysiological evidence that, even when *Flexible Array Probes* are implanted deep into the brain tissue, *biocompatibility* is improved compared to the rigid *Linear Array Probes* tethered to the skull as it has been shown using post-mortem histology (Biran et al. 2007, Richter et al. 2012).

On top of the device perspective, we analysed the effect of *subthalamic high-frequency microstimulation* on the behavioural level by observing *rotational response* to *high-frequency microstimulation* (Bergmann et al. 2004).

Additionally, we provide possible feedback parameters for the closed-loop approach of feedback-controlled *deep brain stimulation* which are derived from neuronal response to *high-frequency microstimulation* on a semi-transient time scale.

Also, our results indicate a specific effect of *high-frequency electrical stimulation* on spike activity since certain neuronal elements seem to be activated or inhibited as a result of electrical stimulation with different current amplitudes. These results corroborate findings from current neurochemical research (Feuerstein et al. 2011).

Taking together the results presented in the current work, we present bimodal neural interfaces for chronic implantation into neuronal tissue allowing high resolution neuronal recording and functional electrical stimulation over a long time range. Further, we present candidate parameters for feedback controlled *deep brain stimulation* and evidence supporting modern theories on the fundamental mechanism of action of electrical stimulation in neuronal tissue.

Linear- and Flexible Array Probe recording sites are tailored to record high-quality neuronal discharge activity with low thermal noise content

Before the above described probes were implanted, the *frequency response* was determined on all stimulation- and recording sites. Thereby, quality control of the recording- and stimulation sites was performed and information about the frequency range of the recorded signals was gathered. *Impedance spectroscopy* measures the phase shift of a signal and its attenuation over a certain frequency range. The *frequency response* of an electrode depends on the *electrode-electrolyte interface* on its polarized surface in ionic solution. According to the surrogate equivalent circuit, the signal is attenuated and shifted in phase. Yet, how much attenuation occurs is dependent on the frequency of the signal.

Neuronal activity produces different kinds of electrical signals referring to different neuronal processes and containing different kinds of information. The different types of neuronal activity can be distinguished by their frequency content, as for example, low frequency *local field potentials* and high-frequency *neuronal discharge activity* which can be detected close to neuronal elements. High frequency *neuronal discharge activity*, measured by extracellular electrodes, originates from the summation of ionic currents across the neuronal membrane (Logothetis 2003). The volume, over which the summation occurs, determines if *single-* or *multi-unit potentials* are measured. Thus, the quality of the measurement of neuronal activity directly depends on the design of the electrode and its interface with the surrounding electrolyte.

By choosing the electrode design, it is possible to tune the electrode towards the neuronal activity with the most information content for the respective application. For the current study, electrodes were desirable that provide high-quality *multi-* and *single-unit potentials* and low noise levels to

facilitate long term *in vivo* measurement. In the current study, we focused on high-frequency neuronal activity as represented by *single-* and *multi-unit spike activity*. Yet, we expect that it is possible to extract *local field potentials* from the low-frequency range of the measured signal.

The biggest energy content in the frequency spectrum of *single-unit potentials* has been shown to reside in the frequency range between 300 Hz and 6 kHz with the maximum at approximately 1 kHz (Grünes & Roubik 2008). Electrodes, which are supposed to measure *single-unit potentials*, must be provided with small diameter recording sites which show a good *frequency response* in this frequency range. Electrodes with small dimensions, ideal for *single-unit recordings* display high *impedances* and increased *thermal noise* content in the recorded signal. Therefore, high *impedance* electrodes mostly are exclusive to large amplitude *single-unit potentials* in close vicinity to the recording site. To record neuronal spiking patterns from more than a single neuronal element, electrodes with low noise levels are required. Thus, size requirements can not be as strict as for *single-unit recordings*. When *multi-unit potentials* are recorded, larger diameters of recording sites are used.

To measure the full range of patterns resulting from high-frequency *neuronal discharge activity*, it is essential that electrodes possess well balanced *impedance* characteristics which allow them to record *neuronal discharge activity* over a wide area. This is of importance to characterize the response to *subthalamic high-frequency microstimulation* on the single cell level, since *high-frequency microstimulation* affects many cells in an area wider than the area from which signals can be recorded. According to the results in the current work, the effect of *high-frequency stimulation* can be inhibitory or excitatory towards different neuronal elements.

The *Linear-* and *Flexible Array Probes* were designed to measure extracellular *single-* and *multi-unit potentials*, resulting from the described high-frequency discharge processes at the neuronal membrane. The *impedance spectra* of *Linear-* and *Flexible Array Probes* show the *frequency response* of a *high-pass filter*, leading to stronger attenuation of low-frequency neuronal activity. By the linear slope of the phase shift in the frequency range between 0.3-6 kHz a constant phase delay between frequencies can be assumed so that signal distortion is supposedly minimal. Thus, *Linear-* as well as *Flexible Array Probes* are tailored to measure high-frequency neuronal discharge activity with low levels of *thermal noise*. *Linear Array Probe* recording sites have a characteristic 1 kHz *impedance* of 99.40$\pm$20.27 kΩ whereas *Flexible Array Probe* recording sites have a 1 kHz *impedance* of 306.19$\pm$51.72 kHz.

The 1 kHz *impedance* at the *Flexible Array Probe* recoding sites is, with 300 kΩ, about three times larger, than the 1 kHz *impedance* on the *Linear Array Probes*. Thus, *Flexible Array Probe* recordings might be prone to contain higher ratios of *thermal noise*. Still, the *impedance* of the *Flexible Array Probe* recording sites is well below 1 MΩ which is reported as criterion to measure *single-unit activity* exclusively. Thus, larger noise levels and clearer single spike events at the recording sites of the *Flexible Array Probes* explain the differences between *Linerar-* and *Flexible Array Probes* with respect to

neuronavigation. Here, *Flexible Array Probes* performed better in areas with high density of neurons and high spike activity, whereas the performance of *Linear Array Probes* was stable in all regions, since *Linear Array Probes* are capable of detecting neuronal background activtity in a relatively large volume.

Around 1 kHz, the *phase angle* is linear, implying a constant phase delay for that frequency range. This safely allows to assume little distortion for signals originating from *high-frequency neural discharge*. Yet, signal distortion was not investigated in the work at hand, and detailed descriptions cannot be made.

The 1 kHz *impedance* values, measured for *Linear-* and *Flexible Array Probes*, comply with impedances of equally sized pobes, found in the literature. At 1 kHz, a *impedance* of 355.75 kΩ was measured at $9x10^{-6}$ cm^2 *gold/chromium* recording sites of flexible, *polyimide* based microelectrodes (Rousche et al. 2001). Silicon based microelectrodes with exposed tips of $1.6x10^{-5}$ cm^2 were reported having 1 kHz impedances of 250±91 kΩ and were used to record neuronal spike activity in the motor cortex with post-hoc clustering of *single-unit activity* (Suner et al. 2005). Electrodes with a 1 kHz *impedance* of 1 MΩ are reported to record clean *single-unit activity* (Seifried et al. 2011, Miocinovic et al. 2007). Following from their *frequency response*, *Linear-* and *Flexible Array Probes* are tailored to provide high quality recordings of mixed *single-* and *multi-unit neuronal discharge activity*. From the recordings, *single-unit potentials* might be extracted by post-hoc *spike detection and clustering*

A surrogate equivalent circuit can be used to deduct the building blocks of the electrode-electrolyte interface

Beyond measuring the impedance spectra, we attempted to use the data to model and describe the surrogate equivalent circuit which characterizes the *electrode-electrolyte* interface in ionic solution.

Impedance models describe the *electrode-electrolyte interface*. Thus, they allow to deduct the components that lead to an electrode's specific *frequency response*. Mostly, equivalent circuits are used to model the *impedance* characteristics of an electrode (Geddes 1997, Franks et al. 2005, McAdams et al. 1995). The variety of existing *impedance* models is overwhelming. Due to absence of a generalized approach, models are adjusted and optimized depending on the application. The simplest approach and building block in many *impedance* models is the *Randles cell*. The *Randles cell* does not account for diffusion processes, different ionic species and, most importantly, for the capacitance of the tissue surrounding the electrode (Onaral & Schwan 1982, Butson & McIntyre 2005). Therefore, the *impedance* model described in this work, characterizes the electrode in an ionic electrolyte and needs to be extended for implanted electrodes by follow-up work.

Still, the *Randles cell* is a good starting point to develop an *impedance* model for *Linear-* and *Flexible Array Probes*. At low signal amplitudes of 10 mV, which were used for *impedance* measurements, the *Randles cell* mo-

del fits the measured *impedance* data well. Thus, the model allows some assumptions about the *electrode-electrolyte interface* on *Linear-* and *Flexible Array Probes* at low current amplitudes.

From fitting the *impedance spectra* measured at *Linear-* and *Flexible Aray Probe* recording- and stimulation sites with the *Randles cell* equivalent circuit, we learn about the properties of the *electrode-electrolyte interface* and the characteristics of the *charge transfer* between electrode and electrolyte. For frequencies larger than the determined *cut-off frequency*, which is > 9 kΩ for the different types of contact sites, *charge transfer* becomes ohmic whereby the *impedance* turns closer towards the *spreading resistance* which represents the serial resistance R_s of electrode and electrolyte. Therefore, the *spreading resistance* is similar for the different types of contact sites and independent from the *geometric surface area*. Since the determined *cut-off frequencies* are far beyond the physiological range, charge transfer processes at the *electrode-electrolyte interface* are, by the definition of the surrogate circuit model, opposed by a *capacitive resistance* which depends on the frequency of the transferred signal.

The frequency dependent resistance increases towards lower frequencies. At the *low-frequency asymptote* of the *high-pass filter*, the *charge transfer resistance* R_{ct} is reached which, in the surrogate equivalent circuit, is the resistance in the *parallel RC* component. Since the *parallel RC* component of the *Randles cell* describes the *ordered double layer* of ions at the polarized electrode surface, the *charge transfer resistance* varies between the different contact sites which were investigated. The *charge transfer resistance* depends on the geometric surface area of the contact site. It is larger at smaller contact sites. As show in the current work, a logarithmic relationship exists between the *geometric surface area* of the *Linear-* and *Flexible Array Probe* recording- and stimulation sites and their *impedance* at 1 kHz, which is close to the *low-frequency asymptote*.

Since the *charge transfer resistance* is relevant for low frequencies in the physiological range and, most importantly, for frequencies around 100 Hz with which *high-frequency microstimulation* in neuronal tissue is usually applied, it plays a major role in equivalent circuit models including the tissue capacitance as a *serial RC* element in addititon to the *Randles cell*. Using such models, the characteristics of the *voltage response* at the *electrode-tissue interface* during electrical stimulation can be explored (Wei & Grill 2009).

Using the *Nyquist plot* to represent the characteristics of the complex impedance of the *electrode-electrolyte interface*, the *charge transfer resistance* and the *spreading resistance* can be determined from the intersection with the real axis, since both are ohmic resistances. The *double layer capacitance* C_{dl} is responsible for the phase shift of the signal and can be determined from the apex of the *Nyquist plot*. As it can be seen from the values of the *double layer capacitance* for the different types of electrodes measured in the current work, the values for C_{dl} are smaller for recording sites and larger for stimulation sites. This is expected, since *capacitance* and *geometric surface area* are directly proportional with $C = \epsilon_r \epsilon_0 A/d$. But also, the *capacitance*

differs between *Linear-* and *Flexible Array Probes*. This is probably due to the material properties of the capacitance with ϵ_r being the *relative static permittivity*, defining material properties. Since the dielectric of the *double layer capacitance* is represented by ordered water dipoles at the interface between electrode and electrolyte, the properties of the dielectic of the capacitance are mainly determined by diffusion kinetics resulting in the relaxation of the ordered *double layer*. These diffusion kinetics might be influenced by the properties of the electrode surface. Surface roughness of the electrode may play a major role in the properties of the dielectric of the *double layer capacitance* (McAdams et al. 1995). Thus, we can conclude that, due to the different manufacturing processes, the surface roughness of the gold contact sites at *Linear-* and *Flexible Array Probes* is different, leading to different values for the *double layer capacitance* at the *electrode-electrolyte interface*. Yet, the effects of the *double layer capacitance* are not strong enough to be visible in the logarithmic relationship between geometric surface area and impedance, since both probe types can be fitted into the same line in the double logarithmic coordinate system.

Since only one apex can be determined from the *Nyquist plot*, which is the shape of a single semi-circle, one can conclude that the *electrode-electrolyte interface* is determined by a single capacitance. Thus, the processes at the *electrode-electrolyte interface* can be described by a first-order electrochemical reaction with a single *time constant*.

The electrode's voltage response depends on the current density at the stimulation site

The voltage response to current controlled stimulation at the stimulation sites of *Linear-* and *Flexible Array Probes* describes a waveform which is typical for *RC circuits*. This indicates that the *charge transfer* during *high-frequency microstimulation* might be based on the same principles as described above for the *electrode-electrolyte interface*. *Parallel RC circuits* have been used in many studies to model the *charge transfer* at a stimulation electrode in the complex electrolyte of the brain (Gileadi et al. 1976, Robinson 1968, Wei & Grill 2009). Yet, a series combination of resistance and capacitance seems to be necessary to include the properties of the tissue (Onaral & Schwan 1982, Ragheb & Geddes 1990, Ragheb et al. 1992, Schwan 1968). With a combination of *serial RC* and *parallel RC*, the complex *impedance* of the *electrode-tissue interface* would be dependent on *frequency*, as well as *current density*. The study of Onaral & Schwan showed, that the *series resistance* decreased and the *series capacitance* increased with increasing *current density* at a frequency of 100 Hz (Onaral & Schwan 1982). Wei et al. reported that high *current densities* at the stimulation site lead to lower *impedance* magnitudes at the *electrode-tissue interface* (Wei & Grill 2009).

The findings, that the *impedance* is dependent on the *current density*, and that the *impedance* at a certain frequency decreases, when the *charge density* increases are directly applicable to the results found for the *voltage response* on the stimulation sites of *Linear-* and *Flexible Array Probes*. The maximum

electrode potentials for the larger surface stimulation sites of *Linear Array Probes* are larger than the maximum electrode potentials for the stimulation sites of *Flexible Array Probes* with smaller *geometric surface area*. Intuitively, that seems to be paradox, since electrodes with higher *impedance* are expected to have larger resistivity than electrodes with low *impedance*. When the properties of the *serial RC circuit*, representing the tissue *resistance* and *capacitance*, are taken into account, the results become explicable by increased *current density* at small sized electrode surfaces.

When it is assumed that the stimulation electrode is surrounded by a layer of electrolyte with high conductivity, the *voltage response* at the stimulation site is dependent on the *charge transfer resistance*, which becomes the *faradic resistance* in the *electrode-tissue interface* model of Wei et al, and the current density at the electrode surface. Wei et al. reason that the monotonic decrease of *faradaic resistance* with increasing frequency may reflect that, at high frequencies, the voltage polarity across the electrode changes so rapidly that the electrochemical reactants for the reactions to be reversed are more readily available adjacent to the electrode surface. The frequency dependence of the *double layer capacitance* at the *electrode-electrolyte interface* was suggested to be a result of the rearrangement of ordered dipoles, which act as a dielectric in the *double layer capacitance* (Bockris & Conway 1958, Geddes 1997, McAdams et al. 1995). Further, the authors explain that the decrease of *faradic resistance* with increasing *current density*, seen when electrode entered the nonlinear region, is due to the initiation of new reaction mechanisms at the electrode surface, capable of accommodating the increased current beyond the limits of the available reacting species. The increase of *double layer capacitance* with increasing *current density*, seen when electrode entered the nonlinear region, is possibly due to the increased fraction of the electrode surface covered by adsorbed chemical species with a preferential orientation at the interface acting to separate charge (Ragheb & Geddes 1990, Geddes 1997). Reversible *faradic reactions* on *thin-film gold* were investigated by et al. (Pettit et al. 2006). Formation of adsorbed hydroxide species on the *gold* surface as shown in equation 4.1 was reported. The adsorbed hydroxide species (OH_{ads}) may retain a partial negative charge depending on the electrolyte. The reversible *faradic reaction* in equation 4.1 occurred in 0.1 M NaF + 1 mM NaF solution at a *cathodic charge density* of 0.40 $^{mC}/_{cm^2}$ and an *anodic charge density* of 0.35 $^{mC}/_{cm^2}$. Accordingly, *faradic reactions* may also occur on the *stainless steel* shaft of the *Linear Array Probes*. The *faradic resistance* on *stainless steel* is lower compared to noble metals and electrochemistry might occur at even lower charge densities (Mayer et al. 1992).

$$Au + H_2O \longleftrightarrow Au{-}OH_{ads} + H^+ + e^- \tag{4.1}$$

The results of Wei et al. demonstrate that the *faradic resistance* decreased and the *double layer capacity* increased which results in a decrease of the magnitude of the *impedance* at the *electrode-tissue interface* when the *current density* at the electrode increases.

Since the stimulation sites of the *Linear-* and *Flexible Array Probe* are made of *gold*, *faradic reactions* are expected to occur at *charge densities* of about 0.4 $^{mC}/_{cm^2}$ (Pettit et al. 2006). For *high-frequency microstimulation* current amplitudes of 0.1-0.4 mA were used and pulse duration was 60 µs. Thus, at stimulation sites of *Flexible Array Probes*, *current densities* of 0.33 $^{mC}/_{cm^2}$ are reached at 0.2 mA current amplitude and *current densities* are >0.4 $^{mC}/_{cm^2}$ at larger current steps. Since the geometric surface area of *Linear Array Probes* was larger, *current densities* do not exceed the 0.4 $^{mC}/_{cm^2}$ threshold and are 0.21 $^{mC}/_{cm^2}$ at the maximal stimulation current of 0.4 mA.

Still, as it is indicated by the observed values for the *double layer capacitance* at *Linear-* and *Flexible Array Probes*, the ratio between *electrochemical surface area* and *geometric surface area* might be larger at *Flexible Array Probes*, leading to increased *charge delivery capacity*. Yet, a value for the *charge delivery capacity* cannot be derived from the results in the current work. To characterize the ratio of *faradic reactions* at the stimulation site of *Flexible Array Probe* this value needs to be established in terms of follow-up work.

In conclusion, higher ratios of *faradic reactions* are likely to occur at the stimulation sites of *Linear Array Probes* as, in the current work, lower *impedances* for the *voltage response* at *Flexible Array Probes* are observed.

In current research, *impedance models* which integrate processes occurring at high potentials, are used to characterise the *voltage response* of the electrode. Mostly, models are based on the *Randles Cell*, but incorporate *faradic charge transfer* processes. Stimulation resistances of < 5 kΩ during *high-frequency microstimulation* with 5.98×10^{-2} cm^2 *Medtronic* macroelectrodes were measured by Wei et al. (Wei & Grill 2009). Using a 8×10^{-6} cm^2 *iridium oxide* microelectrode, a *charge transfer* resistance of 73 kΩ was established after stimulation (Weiland & Anderson 2000). The *impedance* during stimulation was estimated to be 88.89 kΩ at a 3.6×10^{-6} cm^2 *Michigan* probe contact sites (Field & Ghovanloo 2006). The data are difficult to compare to the measurements which were made in the work at hand, but resistances < 10 kΩ during stimulation at small sized *Michigan probe* contact sites corroborate the conclusion that high *current densities* lead to a lower *charge transfer resistance* and thus lower *impedances* for the *voltage response* to current controlled *high-frequency microstimulation* in the brain.

At this point, it becomes very clear that the *impedance* model of the *Randles cell* must be expanded and optimized to understand the *charge transfer* processes which occur at the stimulation sites of the bimodal *Linear-* and *Flexible Array Probes* during *high-frequency microstimulation*. Although, the *Randles cell* model worked well for low signal amplitudes in ionic electrolyte, adaptations have to be made to account for *tissue capacitance* and *resistance* as well as for *non-capacitive charge transfer* during neuronal stimulation exceeding reported *charge per phase* values necessary to achieve an effect on neuronal activity.

Beyond the modelling perspective, increased *charge densities* and higher probability of *faradic reactions* at the stimulation sites of *Flexible Array Pro-*

bes explain the lower *impedances* we observed for the *voltage response* at *Flexible Array Probes* compared to *Linear Array Probes* with larger *geometric surface areas*.

The voltage response at Flexible Array Probe stimulation sites is less affected by long term implantation

When current controlled *high-frequency microstimulation* is applied at the stimulation sites of *Linear-* and *Flexible Array Probes*, curve shapes of the *voltage response* look like the *RC waveforms* which were described above. The *Linear-* and *Flexible Array Probes* were implanted for four weeks and changes in the *voltage response* can be determined between the acute stage in the first week after implantation and the chronic stage after four weeks of implantation. Although the *time contants*, determined from the exponential increase in potential remained stable over time, the maximum electrode potential determined from the peak maxima of the *voltage response* to current controlled *high frequency microstimulation* at *Linear-* and *Flexible Array Probes* was different between the first week and the last week of implantation. The effect was dependent on the current amplitude of *high-frequency microstimulation*.

At *Linear Array Probe* stimulation sites, the maximum electrode potential was lower after four weeks of implantation as compared to the maximum electrode potential after one week of implantation for stimulation amplitudes with >0.1 mA constant current. The effect was stronger with higher currents. At *Flexible Array Probe* stimulation sites, the effect was visible at higher stimulation amplitudes with currents >0.2 mA. The effect was stronger with higher currents, but still less pronounced than the effect observed at *Linear Array Probe* stimulation sites. This means, that the *resistances* for *high-frequency microstimulation* with higher currents were lower in the *chronic stage* than in the *acute stage*. Further, the observed effect was more pronounced and visible at lower currents at *Linear Array Probes*. Thus, allowing the conclusion that the long term performance of *polyimide* based *Flexible Array Probes* with respect to *high-frequency microstimulation* outruns the performance of rigid, metal based neural probes.

The effect, that the characteristics of the *charge transfer* are altered depending on the duration of the implantation has been reported in many studies (Hemm et al. 2004). It can, again, be described by the *serial RC* properties of the *electrode-tissue interface* at low frequencies and high *charge densities* (Yousif et al. 2007, 2008). Using such *impedance models*, it has been shown that the *electrode-tissue interface* at the neural implant influences the induced electric field by shunting the current in the *acute stage*, and shielding the tissue from the stimulus at the *chronic stage* so that there is a need to top up the stimulating amplitude (Yousif et al. 2007, 2008).

Commonly, when material is implanted into the cerebral tissue, a so-called *foreign body response* is observed. In many studies, it is reported that the electrode is isolated from neuronal tissue by *encapsulation tissue*, which contains reactive astrocytes, meningeal fibroblasts and macrophages. The *for-*

eign body response result in so-called *glial sheathing* excluding the electrode from neuonal cells. *Glial sheathing* supposedly acts as an electrical insulator towards recording and stimulation electrodes. It hinders diffusion and, by the encapsulation, the distance between the electrode and adjacent neurons increases (Schultz & Willey 1976, Turner et al. 1999, Roitbak & Syková 1999, Biran et al. 2005). In a simplified approach which helps to explain the occurring changes at the *electrode-tissue interface*, two stages are defined. The so-called *acute stage* after probe insertion is characterized by cerebrospinal fluid filling a *peri-electrode space* between the electrode surface and the tissue. In the *acute stage*, the comlex electrolyte of the cerebrospinal fluid is surrounding the newly implanted electrode. At the so-called *chronic stage*, encapsulation tissue forms at the electrode surface and excludes the electrode from the tissue (Yousif et al. 2007).

Investigation of the stimulation waveforms in the *acute* and *chronic stage* was performed by Yousif & Liu. The authors found different shapes of *RC waveforms* in the *acute* and *chronic stage*. Smaller maximum electrode potentials in the *chronic stage* as compared to the *acute stage* were reported, too (Yousif & Liu 2009). It was proposed that, to explain these results, it is crucial to consider the *electrode-brain interface* situated in a *peri-electrode space* filled with highly conductive electrolyte in addition to a layer of homogeneous neural tissue (Yousif et al. 2007, Xie et al. 2006, Butson & McIntyre 2005). It was shown that the composition of the *peri-electrode space* changes after electrode implantation from *extracellular fluid* of high conductivity and low permittivity to *reactive giant cells* of high *impedance* and permittivity. Thus, at acute stages after implantation, the *tissue capacitance* dominates with the *low-pass filter* behaviour of the serial *RC circuit* and, at chronic stages after implantation, the *capacitance* of the encapsulation itself takes over leading to waveform attenuation of the *voltage response* to current coltrolled *high-frequency microstimulation*.

Assuming a peri-electrode space which is, as proposed by Yousif et al., filled with electrolyte in the *acute stage*, the *charge density* dependency of the *electrode-tissue impedance* at *Linear-* and *Flexible Array Probes* explained above is valid for the first week after implantation.

Later, in the *chronic stage* after four weeks of implantation, Yousif et al. proposed the formation of a *capacitive layer* wrapped tightly around the electrode in form of a layer of encapsulation tissue which the authors called *giant reactive cells*. Yousif et al. proposed that, as the *impedance* of the *electrode-tissue interface* is governed by the described *RC circuit* in the *acute stage*, the *impedance* of the *electrode-tissue interface* at the *chronic stage* is governed by the *capacitance* of the *encapsulation layer* which attenuates the waveform of the *voltage response* to current controlled *high-frequency microstimulation*.

Taken together, the implications of *encapsulation capacitance* and *current density* effects might lead to the properties which are observed at the stimulation sites of *Linear-* and *Flexible Array Probes* when current controlled *high-frequency microstimulation* was repeatedly performed over a time period of four weeks.

The observed attenuation of the *voltage response* was smaller when *Flexible Array Probes* were used. That implies, that the proposed high capacitive layer in the *chronic stage* (Yousif et al. 2007) was less developed when *Flexible Array Probes* were used. In a comparative study with rigid electrodes tethered to the skull and untethered rigid electrodes with a flexible link were floating in the brain tissue, it was observed that initial inflammation and glial sheathing around the electrode implantation site was diminished in untethered electrodes (Biran et al. 2007). Also, it was shown that the *glial sheath* was almost fully developed already after two weeks (Biran et al. 2005). These data suggest that histological evaluation of the implanted *Flexible Array Probes* might lead to the finding of a thinner capacitive layer around *Flexible Array Probes* which is probably not only due to the *biocompatibility* of the *polyimide* carrier material, but also due to the lack of *tethering forces* at the *Flexible Array Probe* which is floating int the brain tissue (Biran et al. 2005, 2007, Lago et al. 2007).

Microstructured probes foster precise neuronavigation in areas with high neuronal activity

The performance of each implanted probe was tested by *neuronavigation* which was performed during probe insertion prior to implantation. With *impedances* in the 100 kΩ range, using bipolar configuration and recording, contact sizes of 20 µm should be capable of isolating *single-* and *multi-unit potentials* reflecting neural group activity on the level of *high-frequency neuronal discharge* (Gross et al. 2006). Phasically, as well as tonically active neurons were observed, as well as burst-firing neurons, in the respective region (Sterio et al. 2002). Recorded *wavetrains*, however, rarely showed *single-unit activity* exclusively. *Multi-unit activity*, such as the simultaneous activity of bursting and tonically active cells was often observed on the *wavetrain* signal of a single channel. Yet, using post-hoc *spike detection* and *spike shape clustering*, *single-unit spike activity* could be isolated.

Originally, the clinical approach to *neuronavigation* includes mapping of the *subthalamic nucleus* to find the best target area for *deep brain stimulation* (Machado et al. 2006, Coenen et al. 2008). To delineate the target structure, the characteristics and patterns of *neuronal discharges* on the *wavetrain* signal were used. Additionally, using microstimulation, the nature of the evoked responses of the neurons in the target nucleus allowed further characterization (Gross et al. 2006, Starr et al. 2006).

Today, automated, parameter based methods gain importance due to development of computer aided *neuronavigation* systems. Impedance aided *neuronavigation* was among the first parameter based methods used. It allows delineation of grey- and white matter (Johansson et al. 2009, Laitinen et al. 1966). Further, the change in mean signal amplitudes was shown to indicate passage from structure of grey matter to another (Yokoyama et al. 1998). Novak et al. used the spectral density of the neural background activity as parameter for *neuronavigation* (Novak et al. 2007). It was shown,

that parameter based *neuronavigation* is accurate as well as objective (Novak et al. 2011).

Following the work of Menne & Ramrath (Menne 2005, Ramrath et al. 2009), four different parameters for *neuronavigation* were calculated in the work at hand. The *root mean square* of the *wavetrain data* is a measure of signal amplitude, which is not biased by negative values, as is the mean value of the signal, which was used in (Yokoyama et al. 1998). The *mean spectral density* was used according to (Novak et al. 2011). Both, the *root mean square* and the *mean spectral density* represent measures of neuronal background activity, based on recorded *wavetrain data* (Novak et al. 2007, Logothetis 2003, Shin et al. 2007). Beyond neuronal background activity, statistical parameters of spike activity were used in order to reflect the observer based method of *neuronavigation*, which is directed towards the frequency and pattern of spike events in the observed area (Gross et al. 2006, Kipke et al. 2008). To extract *spike events* from the *wavetrain data*, *spike detection* and *clustering* was performed for each channel as to obtain events resulting from *single-unit neuronal discharge activity* (Logothetis 2003, Quiroga 2004, Seifried et al. 2011). Then, the *mean firing rate* was calculated to indicate the relative abundance of *spike events* in the respective region. The *spike entropy* was determined as a measure of regularity of occurring *spike events* (Molina-Picó et al. 2011).

Activity profiles, created from the *wavetrain* parameters, showed reproducible patterns. Although different in amplitude, the trend of the *root mean square* and *mean spectral density* was comparable for all probes of one type. The *activity patterns*, recorded for *Linear-* and *Flexible Array Probes* were different since the higher *impedance* of *Flexible Array Probes* leads to reduction of the *neural background* component of the recorded signal, but to increased ratios of *thermal noise* in the recorded signal (Abidian & Martin 2008).

The *activity profiles*, created from *neuronal discharge activity* were more variable from measurement to measurement. Since the radius in which spikes were detected in the vicinity of the probe is probably lower than 100 µm (Logothetis 2003), the detection of high-quality *spike activity* is always also a matter of luck. Yet, the *mean firing rate* is related to the *spike entropy*, since both *activity profiles* show the same trend.

Observing the curve trends of the *activity patterns*, it becomes obvious that activity is increasing or decreasing when the border between brain structures is crossed. This effect was obvious in the studies of Yokoyama et al. and Novak et al. as well. Therefore, *turning points* were determined from the polynomial fit of the activity pattern. Surprisingly, although the curve trends seemed different between *Linear-* and *Flexible Array Probes* and the different parameters which were determined, the estimated *turning points* fit well with the borders between brain structures as compared to the histological atlas of the rat brain (Paxinos & Watson 2007).

Generally, the *turning points* fit better with the borders of areas when *activity profiles* were created from *Linear Array Probe* measurements. In the *thalamus* and *subthalamic nucleus*, theoretical borders fit well with the *activ-*

ity profiles generated from *Flexible Array Probe* measurements. High spiking activity is a reported feature of these regions (Hutchison et al. 1998, Novak et al. 2011, Gross et al. 2006).

Since *Linear Array Probes* allow to measure neuronal background activity in a larger volume, their performance at *neuronavigation* might be more stable compared to the performance of *Flexible Array Probes* even when little high amplitude spike activity is present close to the electrode. In regions with high spike activity, *Linear Array Probes* allow high quality recordings of *multi-unit activity*. Although noise levels in *Flexible Array Probe* recordings are larger and less background neuronal activity is recorded, *Flexible Array Probes* perform well in the deep brain regions of the *thalamus* and *subthalamic nucleus* and qualify to map out borders between *deep brain structures* with high spike activity.

Thus, *Flexible Array Probes* support mapping procedures focused on the *basal ganglia*. This fits to the strategy which is currently applied in clinics (Moll et al. 2005). Using *Linear Array Probes* with lower impedances, whole depth *neronavigation* becomes possible, which is an interesting feature as more and more target regions for *deep brain stimulation* lie outside of the *basal ganglia* and in regions with less spontaneous firing activity (Nuttin et al. 2003, Mayberg et al. 2005, Maciunas et al. 2007).

Injections of 6-hydroxydopamine lead to a partial loss of nigrostriatal dopamine without producing striatal dopamine supersensitivity

Unilateral injections of the neurotoxin *6-hydroxydopamine* into the *ventrolateral caudate putamen* were performed to model the loss of dopaminergic neurons in the *substantia nicra pars compacta*, which is observed in patients with *Parkinson's disease* (Schapira 1999, DeLong & Wichmann 2007).

The neurotoxin *6-hydroxydopamine*, which is taken up via the catecholamine transporter system, specifically destroys catecholamine containing cells (Ungerstedt 1968, Hökfelt & Ungerstedt 1973). Striatal injections of the neurotoxin lead to degeneration of nigrostriatal dopaminergic neurons and terminals. The dopaminergic denervation becomes evident within three days (Neve et al. 1982). Despite the acute onset, the disappearance of nigrostriatal dopaminergic neurons is reported to be a progressive process. The main decrease in dopaminergic activity seems to happen within two weeks after injection but is not complete until after eight weeks (Neve et al. 1982, Sauer & Oertel 1994). The progressive characteristics of this process are probably caused by rapid destruction of dopaminergic terminals and subsequent retrograde degeneration of nigral dopaminergic cell bodies due to a lack of target derived trophic support (Cadet et al. 1991, Carman et al. 1991, Sauer & Oertel 1994).

Therefore, the dopaminergic lesion in animals which received *6-hydroxydopamine* injection is most probably not a complete lesion and residual dopaminergic activity in the striatum must be taken into account. Even if interpretation of the results might be more difficult, it has been argued that partial lesions of nigrostriatal *dopamine* have greater relevance for models

of *Parkinson's disease*, since loss of dopaminergic cells is not complete in diseased patients either (Kirik et al. 1998).

When the lesioned animals in the work at hand are challenged with low doses of the non-selective *dopamine* agonist *apomorphine*, they express *rotational behaviour*, which is directed towards the side of the lesion. The direction of the induced turning behaviour can be explained as a function of the loss of dopaminergic neurons and striatal *dopamine* depletion. Animals with loss of dopaminergic neurons below a certain level do not present turning behaviour, whereas those with increased, but partial loss of dopaminergic neurons present *ipsilateral* turning behaviour. Those animals, that lost almost all dopaminergic neurons present *contralateral* turning behaviour (Da Cunha et al. 2008). These findings are compatible with the results of a recent study in which post-synaptic *dopamine* receptor supersensitivity was reported, only when more than 60 % of *dopamine* activity was lost (Francardo et al. 2011). In that case, compensatory *dopamine* receptor upregulation on the side of the lesion would lead to *dopamine* receptor supersensitivity and administration of *apomorphine* would lead to increased dopaminergic activation on the lesioned side compared to the unlesioned side. Thus, *contralateral rotational behaviour* would be induced. This effect is reported for many studies involving *6-hydroxydopamine* injections into the *substantia nigra* or *medial forebrain bundle* (Hudson et al. 1993, Moser et al. 2003a, Canales & Graybiel 2000). The occurrence of *ipsilateral* lesions is an indication, that the loss of dopaminergic activity is less than 60 %, but is still large enough that the imbalance in dopaminergic activity becomes evident, favouring the unlesioned side, when the dopaminergic agent *apomorphine* is administered systemically.

Taking into account, that the loss of dopamine activity is not complete in patients suffering from *Parkinson's disease*, incomplete lesions of the nigrostriatal dopaminergic pathway might represent a better animal model for *Parkinson's disease*. The incomplete lesion following injection of *6-hydroxydopamine* into the *ventrolateral caudate nucleus* of the rat, even shows a pattern of progression which is an important factor for the typical phenotype of neurodegenerative disorders. Although for these reasons, incomplete striatal lesions should be preferred over complete lesions of the nigrostriatal pathway induced by injection of *6-hydroxydopamine* into the *medial forebrain bundle* or the *substantia nigra*, hemiparkinsonian models investigating *rotational response* often resort to the classical complete lesions since reliable unidirectional *rotational behaviour* is observed with these models (Deumens et al. 2002).

In the current work, a model is presented in which partial lesions of the nigrostriatal system are induced reliably by injection of *6-hydroxydopamine* into the *ventrolateral caudate nucleus*. The described method does not cause *dopamine receptor supersensitivity* on the side of the lesion. Thus, global dopamine activation will lead to ipsiversive *rotational behaviour* whereas the number of rotations is similar to the numbers of rotations observed in models with complete lesions of the nigrostriatal pathway (Moser et al. 2003a).

Therefore, the described model might present an option to model *Parkinson's disease* in the rat more realistically whereby *rotational behaviour* is preserved as a parameter from which the effect of experimental interventions can be quantified conveniently.

Subthalamic microstimulation compensates striatal dopamine loss

Opposed to *ipsilateral rotations* caused by apomorphine, *contralateral rotations* could be induced by *subthalamic high-frequency microstimulation* in lesioned, as well as sham-treated rats.

These results corroborate the successful stereotaxic implantation of *Linear Array Probes* into the *subthalamic nucleus*. Comparable studies have shown that induction of *contralateral rotations* only occurs when *high-frequency microstimulation* is applied in the *subthalamic nucleus* or the region of the *zona incerta* dorsal to the *subthalamic nucleus* (Chang et al. 2003, Bergmann et al. 2004). Administration of *high-frequency microstimulation* using the implanted *Flexible Array Probes* eventually leads to rotations in some cases but results were unreproducible and not conclusive. Therefore, it seems likely that implantation with a guiding rod could not ensure the required precision to target the *subthalamic nucleus* precisely (see section 2.4.3.2). Consequently, the following discussion is limited on the implications of the *rotational behaviour* induced by *subthalamic high-frequency microstimulation* at *Linear Array Probe* stimulation sites.

Balanced neuronal activity in the *basal ganglia motor circuit* and its *subcircuits* is supposed to be a pre-requisite for movement and movement control. The *striatum* and the *subthalamic nucleus* receive input from the *cerebral cortex* whereas the internal segment of the *globus pallidus* and the *substantia nigra pars reticulata* provide output to the *thalamus* and *brainstem*.

Whereas activation of excitatory D_1 *dopamine* receptors on striatal GABAergic neurons leads to inhibition of the *basal ganglia output nuclei* via a monosynaptic *direct pathway*, the activation of inhibitory $D_{2/3}$ *dopamine* receptors on striatal GABAergic neurons leads to disinhibition of the *basal ganglia output nuclei* via a polysynaptic *indirect pathway* which includes the external *globus pallidus* and the *subthalamic nucleus* .

When *striatal dopamine* is released, the balanced action of the direct and indirect pathways results in a net reduced output activity of the *basal ganglia* which eventually translates into increased movement through inhibition of *thalamocortical projection neurons* (Wichmann & DeLong 1996, DeLong & Wichmann 2007).

Thus, the *apomorphine* induced *ipsilateral rotations* directly follow from DeLong's explanation of the *basal ganglia motor circuit* (DeLong & Wichmann 2007). Compared to the lesioned side, the unlesioned side receives increased dopaminergic activation, by additive effect of physiological *dopamine* and *apomorphine*. This leads to increased movement on the unlesioned side, resulting in *ipsilateral rotations*. According to this model, the *contralateral rotations*, that are induced by *subthalamic high-frequency stimulation*, result from decreased *basal ganglia output activity* on the stimu-

lated side. This decrease in activity seems to be largely independent from the striatal *dopamine* content, since the effect is the same in lesioned and sham-treated animals. A net decrease in *subthalamic output activity* might result from *direct inhibition* of *subthalamic projection neurons* or from retrograde activation of *inhibitory GABA medium spiny neurons* as frequently discussed (Vitek 2002, Feuerstein et al. 2011). These results show that *subthalamic high-frequency microstimulation* with 0.3 mA current amplitudes delivered via *Linear Array Probe* stimulation sites is sufficient to overcompensate the loss of *dopamine* in the striatum. Since overcompensation is a method to quantify the efficacy of *high-frequency microstimulation*, but not a desired therapeutic effect, current amplitudes for therapeutic *high-frequency microstimulation* are probably much smaller than 0.3 mA.

The clinical usefulness of neural probes providing *high-frequency microstimulation* depends on the ability to provide safe levels of therapeutic stimulation over a long time range of chronic implantation (Cogan 2008). The ideal electrode for neuronal stimulating satisfies the following requirements which were defined by Merrill et al.: *Material tissue compatibility*, *mechanical stability*, *efficacy of stimulation*, *safety of stimulation* and *stability of performance* (Merrill et al. 2005).

To be compatible with the neuronal tissue, the electrode material should not induce neuronal damage or excessive foreign body response. The materials used in *Linear-* and *Flexible Array Probes* are *stainless steel*, *gold* and *polyimide*. According to the classification by Stensaas, *gold* is a *non-reactive* electrode material where little or no gliosis occurred, and normal brain tissue with synapses was observed within 5 µm distance to the *electrode-tissue interface* (Stensaas & Stensaas 1978, Merrill et al. 2005). The shaft of the *Linear Array Probe* is made from *stainless steel*. The material was determined to be *non-toxic* as a piece of *stainless steel* which was implanted for two month into the cerebral cortex of the cat did not lead to significantly greater tissue damage than a puncture made from the same material which was immediately withdrawn (Dymond et al. 1970). The support material of the *Flexibe Array Probes* is *polyimide*. This material was reported to be *biocompatible* and thus, should be perfectly suited for long-term implantation (Stieglitz & Meyer 1999). Although, swelling and unstable performance in the first week has been an issue in some studies, stable long-term performance of *polyimide based probes* has been established (Rousche et al. 2001, Lago et al. 2007, Kisban et al. 2007, Richardson et al. 1993). In the current work, we did not recognize any indications of initial unstable performance, but after implantation, animals were allowed to recover for three days at least and swelling as well as initial tissue reactions might have been subsided by this time.

Although *mechanical stability* can be an issue with glass pipette microelectrodes or silicon based electrodes since breaking of the implanted electrodes was reported, the materials used in the current work are not prone to break or shatter. The probes were most sensitive during implantation. If ever, probes tended to break during mounting. Intracerebral implantation of *polyimide* based microelectrodes presents a methodical challenge. Ongoing

research focusses towards development of biodegradable coatings to provide transient stability facilitating insertion of flexible probes (Lind et al. 2010, Kozai & Kipke 2009, Hassler et al. 2011). In the current work, a *stainless steel* support cannula was used, mounted onto a punch hole at the tip of the *Flexible Array Probe* to drag the probe into the tissue. Although this technique might be prone to inaccuracies, it allows to perform *neuronavigation* during insertion and would facilitate functional testing at the target. Advancing the *support-cannula based method*, used in the current work, could yield precise implantation together with on-line use of recording and stimulation modalities at the *Flexible Array Probe*. After implantation, micromovements of probes which were tethered to the skull have shown to increase *tissue gliosis* (Biran et al. 2007). Due to reduction of tethering forces, micromovements of flexible probes are supposed to be minimal (Subbaroyan et al. 2005).

Stimulation efficacy of *Linear Array Probes* has been demonstrated in the current work by eliciting *rotational behaviour* in *hemiparkinsonian rats* with incomplete lesions of the nigrostriatal pathway. Although *rotational response* was not reproducible in animals with implanted *Flexible Array Probes*, that does not mean that *high-frequency microstimulation* via *Flexible Array Probes* in ineffective. Functional electrical stimulation is supposed to trigger above threshold depolarization of some portion of the neuronal membrane and to elicit action potentials (Merrill et al. 2005). Excitability of neuronal tissue varies depending on the density of neurons around the stimulation electrode and the passive and active properties of the neuronal membrane close to the stimulation electrode. Since there is no precise algorithm which predicts neuronal excitability, stimulation parameters for functional neuronal stimulation have always been determined empirically (Kuncel & Grill 2004, Volkmann et al. 2002). Although thresholds for functional electrical stimulation in the tissue can be as low as 0.001 $\mu C/phase$ in the cortex or nervous tissue, clinically effective *deep brain stimulation* is usually performed at charge per phase values of 0.1-0.4 $\mu C/phase$ (Cogan 2008, Kuncel & Grill 2004, Merrill et al. 2005). Thus, during one cathodic *deep brain stimulation* pulse, a charge of *0.1-0.4* µC is injected into the tissue. Transferring this amount of charge via a macorelectrode with a *geometric surface area* of 0.06 cm^2 results in moderate charge densities of 2.3-6.7 $\mu C/cm^2$. Safety limits for *deep brain stimulation* via macroelectrodes are established at charge densities around 30 $\mu C/cm^2$ (Merrill et al. 2005, Kuncel & Grill 2004).

Transferring the charge needed for functional *deep brain stimulation* via small sized microelectrodes results in *charge densities* which lie far beyond the clinically established limits for safe stimulation. Yet, functional subthalamic *deep brain stimulation* in the rat has been observed after charge injection of 10 nC per phase (Bergmann et al. 2004). Neurochemical response to *high-frequency microstimulation* was observed in the *nucleus caudatus* of the rat at 18 nC per phase (Hiller et al. 2007). Although *charge densities* of 4.8 $\mu C/cm^2$ exceeded the safety threshold reported by McCreery et al., Hiller et al. did not observe any tissue damage due to the stimulation (McCreery et al. 1990, Hiller et al. 2007).

Harnack et al. investigated noble metal microelectrodes and did not find any tissue damage with current densities of 26 $\mu C/cm^2$ (Harnack et al. 2004). In the current study, injected charge per phase values of 6-24 nC for functional *high-frequency microstimulation* were comparable to those reported by earlier studies (Hiller et al. 2007, Harnack et al. 2004). Yet, due to the small geometric surface area, *charge densities* of 53-212 $\mu C/cm^2$ at *Linear Array Probe* stimulation sites and 167-667 $\mu C/cm^2$ at *Flexible Array Probe* stimulation sites were way beyond any reported value for safe stimulation. Still, successful *high-frequency microstimulation* was carried out repeatedly over a time period of one month. During that time period, *voltage response* at the electrode did not change much at *Flexibe Array Probes* where *charge densities* were highest. The *voltage response* at *Linear Array Probes* changed slowly over a time period of weeks, but not after each individual stimulation cycle. Further, using *cyclic voltammetry* at *thin-film gold* electrodes in electrolyte, Petitt et al. determined the threshold for electrolysis to occur at a *cathodic charge density* of 400 $\mu C/cm^2$ (Pettit et al. 2006). Although histological evaluation of the tissue damage, inflicted by *high-frequency microstimulation* with the parameters used in the current work, has to be performed by follow-up work to make a clear statement, some results indicate that the high *charge densities* observed at *Linear-* and *Flexible Array Probe* stimulation sites might still be acceptable.

Taken together, the results of the current work show that bimodal *Linear Array Probes* with a microelectrode sized stimulation modality can be used to exert effective stimulation of neuronal tissue which is sufficient to induce behavioural effects. Thus, the use of bimodal microelectrodes might proof to be the right choice as neuronal interfaces for future feedback controlled *deep brain stimulation* devices, even so more distinguished stimulation sequences and possible tissue damage need to be investigated.

Quinpirol results in the same net effect as subthalamic high-frequency microstimulation

When challenged with the selective *dopamine* $D_{2/3}$ receptor agonist *quinpirole*, *contralateral rotations* were observed in lesioned, but not in sham-treated animals.

Following DeLong's model of the *basal ganglia motor circuit*, systemic administration of *quinpirole* activates the *indirect pathway* and leads to increased disinhibition of the external *globus pallidus*. GABAergic inhibition of the *subthalamic nucleus* follows, resulting in enhanced motor activity on the stimulated site. Thus, *contralateral rotational behaviour* is induced.

When *high-frequency microstimulation* was applied in *quinpirole* treated animals, *contralateral rotations* increased with current amplitude in lesioned and sham-treated animals. A larger number of rotations was observed in lesioned animals, compared to sham-treated animals.

Already in 1987, *quinpirole* was proposed as an antiparkinsonian drug, reversing the effects of known monoamine antagonists and not prone to induce behavioral supersensitivity. Yet, the substance, and D_2 *dopamine* re-

ceptors agonists in general were rarely used in animal models of *parkinson's disease* since it was shown that, for D_2 receptor activation, 50–60 % *dopamine* activity needs to be preserved (Dziewczapolski et al. 1996, Hu et al. 1990, Kreiss et al. 1997). When *quinpirole* was administered after pretreatment with a *dopamine* agonist, it was shown to inhibit pathological subthalamic firing behaviour, which it also the net effect reported for *deep brain stimulation* (Park et al. 2007, Shen & Johnson 2012, Benabid et al. 2005).

From the basal neuronal activity in sham-treated and lesioned animals, pre treated with *sodium chloride*, *apomorphine* or *quinpirole*, it becomes obvious, that the lesion does not influence the *background neuronal activity*, but leads to an increase in *spike activity* as reflected by the *mean firing rate*, wich increases from 9.41±1.01 Hz in sham-treated animals to 19.64±2.01 Hz in lesioned animals, when not additionally challenged. In a primate model of *parkinson's disease*, the spontaneous firing rate of *subthalamic neurons* was significantly increased from 19±10 Hz before, to 26±15 Hz after treatment with MPTP (Bergman et al. 1994). Similar results were observed in the *6-hydroxydopamine* rat model (Strauss et al. 2008, Benazzouz et al. 1993, Chang et al. 2003), and are evident in *clinical studies* in patients with *parkinsons's disease* (Lozano et al. 2002, Vitek 2002).

When sham-treated and lesioned animals were additionally challenged with *apomorphine*, the *mean firing rate* is not affected, but the *neuronal background activity* decreases. This is in agreement with the findings for the rotational activity. Beneficial activity of *apomorphine* has been reported for the management of sudden, unexpected and refractory levodopa-induced 'off' states in fluctuating *parkinson's disease* (Deleu et al. 2004, Di Rosa et al. 2003).

Challenged with the selective *dopamine* $D_{2/3}$ agonist *quinpirole*, the firing rate in subthalamic neuons is decreased in sham-treated and lesioned animals compared to treatment with *sodium chloride*. In lesioned animals, the *mean firing rate* under *quinpirole* treatment is reduced to normal levels of 10.03± 1.61 Hz. In patch-clamp studies, it has been shown that *quinpirole* mimicked the *dopamine* action in the *subthalamic nucleus* more effectively than a *dopamine* D_1 receptor agonist (Zhu et al. 2002). Also, it was reported that, D_2 like *dopamine* receptors and muscarinic M_3 receptors may regulate the excitability of *subthalamic neurons* by acting presynaptically to alter GABA release (Shen & Johnson 2000). Selective GABA release as a mechanistic basis of *high-frequency stimulation* used for the treatment of neuropsychiatric diseases was discussed by Feuerstein et. al (Feuerstein et al. 2011).

Subthalamic high-frequency stimulation leads to very low frequency oscillatory activity

The response to *subthalamic high-frequency microstimulation* was observed over a time range of 1 min after stimulation. In sham-treated animals, three peaks of *neuronal background activity* were observed, occurring at < 0.1 Hz with decreasing amplitude. The first peak occured about 15 s after *high-*

frequency microstimulation ceased. In lesioned animals, the first peak occurred directly after the stimulation. The frequency seemed to increase so that the peaks overlapped. The same effect was observed in sham-treated animals, which received systemic injection of *quinpirole* before the experiment.

Very slow or *infra-slow oscillations* occurring at < 0.1 Hz are known for over 50 years (Aladjalova 1957). Recent fMRI studies provide consistent evidence that, during the resting state, the brain exhibits prominent fluctuations at <0.1 Hz in the BOLD signal, that identify functional anatomical networks, termed resting state networks (Damoiseaux et al. 2006, De Luca et al. 2006, Fox et al. 2007, Mantini et al. 2007). The relationship between these fluctuations and neuronal activity are under debate (Hughes et al. 2011, Logothetis 2010). Although the origins of *infra slow oscillations* are not well understood, a key involvement of the thalamus is proposed (Zhang et al. 2008). There, *infra slow oscillations* have been observed in anaesthetized and freely moving animals, and are evident in *local field potential-*, *single-unit-* and *intracellular recordings* (Lorincz et al. 2009). Since strong *apomorphine* induced periodicities in firing rate are observed in the output nuclei of the basal ganglia, is has been proposed, that *infra slow oscillations* are modulated by *dopamine* receptor activation (Ruskin et al. 1999, 2003). Our results show, that decreased *dopamine* activity induced by a *nigrostriatal* lesion, or by administration of the *dopamine* $D_{2/3}$ receptor agonist *quinpirole*, leads to decreased amplitude and increased frequency of recorded *infra slow oscillations* in response to *subthalamic high-frequency microstimulation*. In compliance with that, Ruskin et al reported, a shift of *infra slow oscillation frequency* toward shorter periods, after treatment with *apomorphine* as well as simultaneous D_1 and D_2 receptor activation.

From the results of the current study, and available data in the literature, we conclude, that *infra slow oscillations* in connection with *deep brain stimulation* might provide a further aspect of *subthalamic high-frequency microstimulation*. By their long time range, *infra slow frequency oscillations* could provide a parameter for *feedback controlled deep brain stimulation* in the future.

Subthalamic High frequency stimulation leads to specific excitation and inhibition of neural elements

Recent neurochemical studies suggest that a selective release of the neurotransmitter GABA might be the unique mechanism of *high-frequency stimulation* in the brain (Feuerstein et al. 2011). In 2011, Feuerstein et al. summarized the work that has been done on finding a unique mechanism of action of *high-frequency stimulation* in the *central nervous system*. The authors traced various observations made in connection with *high-frequency stimulation* back to a common denominator, which they defined as the specific release of GABA from axon terminals of GABAergic cells. A wide spectrum of *in vitro* and *in vivo* studies was shown to support the formulated hypothesis (Mantovani et al. 2006, 2009, Li et al. 2004, 2006, Hiller et al. 2007, Löffler

et al. 2008). Yet, most of these studies were providing neurochemical evidence for the GABA hypothesis.

A highly specific mechanism of action like this is still controversially discussed since the possibility of bulk excitation or inhibition of neuronal tissue by *high-frequency microstimulation* is preferred by many researchers.

In the current work, *single-unit activity* was isolated from recordings of *multi-unit neuronal discharge activity* before and after *high-frequency stimulation* was applied in the *subthalamic nucleus*. The frequency and pattern of *single-unit spike activity* was analyzed in response to *high-frequency microstimulation*. By comparison of the frequency and pattern of specific *single-unit spike activity* before and after stimulation, we found that *single-unit spike activity* in certain groups decreased, increased or remained constant. Thus, we conclude, that *high-frequency stimulation* does not lead to bulk excitation or inhibition of neuronal elements, but rather exerts a specific effect on certain neuronal elements. Therefore, our data corroborate a specific effect of *high-frequency microstimulation* on neuronal elements in the *subthalamic nucleus*.

Using *Linear-* and *Flexible Array Probes*, *multi-unit spike activity* was recorded in response to *high-frequency microstimulation* via recording and stimulation modalities. Using *spike detection* and *kmeans clustering* of the detected *spikes' principal components*, *spike shapes* were grouped into different clusters. With durations of up to 2.5 ms and amplitudes in the range of 30-150 mV, the clustered *spike shapes* showed characteristic features of *single-unit extracellular potentials* (Lewicki 1999, Quiroga 2004, Pavlov et al. 2007).

Although clear *spike shapes* were detected, this does not allow to draw conclusions about the type of neuronal element from which the activity is recorded. Gold et al. analyzed *spike shapes* of extracellularly recorded potentials and concluded that, although sizes of the *soma* and *proximal dendrites* constitute an important factor determining the amplitude of the detected *spike shape*, the details of cell morphology have relatively little impact (Gold et al. 2006). Therefore, the detected *spike shape* might mainly relate to the orientation of the electrode to the source of *neuronal discharge activity*.

Comparing the frequencies and patterns of *single-unit potentials* before and after *high-frequency microstimulation*, we detected increasing as well as decreasing activity in some clusters. In other clusters, activity remained the same before and after stimulation. Interestingly, decreased activity seems to be induced at lower current amplitudes than increased activity. To draw conclusions about the origin of the observed inhibition and excitation, further experiments need to be conducted blocking specific transmembrane currents.

Yet, performing extracellular recordings of *neuronal discharge activity* and *subthalamic high-frequency microstimulation* with bimodal *Linear-* and *Flexible Array Probes* we succeeded to detect a specific effect of electrical stimulation on neuronal *spike activity* in the awake and freely moving animal.

Thus, our study can corroborate the previous findings of a specific effect of *high-frequency stimulation* of neurochemistry.

M. R. Abidian & D. C. Martin. Experimental and theoretical characterization of implantable neural microelectrodes modified with conducting polymer nanotubes. *Biomaterials*, 29(9):1273--1283, 2008. doi: 10.1016/j.biomaterials.2007.11.022.Experimental.

Y. Aika, J. Q. Ren, K. Kosaka, & T. Kosaka. Quantitative analysis of GABA-like-immunoreactive and parvalbumin-containing neurons in the CA1 region of the rat hippocampus using a stereological method, the disector. *Experimental brain research. Experimentelle Hirnforschung. Expérimentation cérébrale*, 99(2):267--76, Jan. 1994. ISSN 0014-4819. URL `http://www.ncbi.nlm.nih.gov/pubmed/7925807`.

N. A. Aladjalova. Infra-slow rhythmic oscillations of the steady potential of the cerebral cortex. *Nature*, 179(4567):957--9, May 1957. ISSN 0028-0836. URL `http://www.ncbi.nlm.nih.gov/pubmed/13430746`.

M. Anderson, N. Postupna, & M. Ruffo. Effects of High-Frequency Stimulation in the Internal Globus Pallidus on the Activity of Thalamic Neurons in the Awake Monkey. *Journal of Neurophysiology*, 89: 1150--1160, 2003.

J. Arezzo, A. D. Legatt, & H. G. Vaughan. Topography and intracranial sources of somatosensory evoked potentials in the monkey. I. Early components. *Electroencephalography and clinical neurophysiology*, 46(2): 155--72, Feb. 1979. ISSN 0013-4694. URL `http://www.ncbi.nlm.nih.gov/pubmed/86423`.

D. Attwell & A. Gibb. Neuroenergetics and the kinetic design of excitatory synapses. *Nature reviews. Neuroscience*, 6(11):841--9, Nov. 2005. ISSN 1471-003X. doi: 10.1038/nrn1784. URL `http://www.ncbi.nlm.nih.gov/pubmed/16261178`.

D. Attwell & C. Iadecola. The neural basis of functional brain imaging signals. *Trends in neurosciences*, 25(12):621--5, Dec. 2002. ISSN 0166-2236. URL `http://www.ncbi.nlm.nih.gov/pubmed/12446129`.

G. Baranauskas. Ionic Channel Function in Action Potential Generation: Current Perspective. *Molecular Neurobiology*, 35(2):129--150, July 2007. ISSN 0893-7648. doi: 10.1007/s12035-007-8001-0. URL `http://www.springerlink.com/index/10.1007/s12035-007-8001-0`.

B. P. Bean. The action potential in mammalian central neurons. *Nature Reviews Neuroscience*, 8(6):451--465, June 2007. ISSN 1471-003X. doi: 10.1038/nrn2148. URL `http://www.ncbi.nlm.nih.gov/pubmed/17514198`.

A. Belitski, A. Gretton, C. Magri, Y. Murayama, M. A. Montemurro, N. K. Logothetis, & S. Panzeri. Low-frequency local field potentials and spikes in primary visual cortex convey independent visual information. *The Journal of neuroscience : the official journal of the Society for Neuroscience*, 28(22):5696--709, May 2008. ISSN 1529-2401. doi: 10.1523/JNEUROSCI.0009-08.2008. URL `http://www.ncbi.nlm.nih.gov/pubmed/18509031`.

A. L. Benabid, P. Pollak, A. Louveau, S. Henry, & J. de Rougemont. Combined (Thalamotomy and Stimulation) Stereotactic Surgery of the VIM Thalamic Nucleus for Bilateral Parkinson Disease. *Proceedings of the Meeting of the American Society for Stereotactic and Functional Neurosurgery*, 50:344--346, 1987.

A. L. Benabid, A. Benazzous, & P. Pollak. Mechanisms of Deep Brain Stimulation. *Movement Disorders*, 17(Suppl. 3):S73--S74, 2002. doi: 10.1002/mds.10145.

A.-L. Benabid, B. Wallace, J. Mitrofanis, R. Xia, B. Piallat, S. Chabardes, & F. Berger. A putative generalized model of the effects and mechanism of action of high frequency electrical stimulation of the central nervous system. *Acta Neurologica Belgica*, 105:149--157, Oct. 2005. ISSN 0300-9009. URL `http://www.ncbi.nlm.nih.gov/pubmed/16255153`.

A. Benazzouz, C. Gross, J. Féger, T. Boraud, & B. Bioulac. Reversal of rigidity and improvement in motor performance by subthalamic high-frequency stimulation in MPTP-treated monkeys. *The European journal of neuroscience*, 5(4):382--9, Apr. 1993. ISSN 0953-816X. URL `http://www.ncbi.nlm.nih.gov/pubmed/8261116`.

A. Benazzouz, B. Piallat, P. Pollak, & A.-L. Benabid. Responses of substantia nigra pars reticulata and globus pallidus complex to high frequency stimulation of the subthalamic nucleus in rats: electrophysiological data. *Neuroscience Letters*, 189:77--80, 1995.

C. P. Bengtson, A. Tozzi, G. Bernardi, & N. B. Mercuri. Transient receptor potential-like channels mediate metabotropic glutamate receptor EPSCs in rat dopamine neurones. *The Journal of physiology*, 555(Pt 2):323--30, Mar. 2004. ISSN 0022-3751. doi: 10.1113/jphysiol.2003.060061. URL `http://www.pubmedcentral.nih.gov/articlerender.fcgi?artid=1664846&tool=pmcentrez&rendertype=abstract`.

H. Bergman, T. Wichmann, B. Karmon, & M. R. DeLong. The primate subthalamic nucleus. II. Neuronal activity in the MPTP model of parkinsonism. *Journal of neurophysiology*, 72(2):507--20, Aug. 1994. ISSN 0022-3077. URL `http://www.ncbi.nlm.nih.gov/pubmed/7983515`.

O. Bergmann, C. Winter, W. Meissner, D. Harnack, A. Kupsch, R. Morgenstern, & T. Reum. Subthalamic high frequency stimulation induced rotations are differentially mediated by D1 and D2 receptors.

Neuropharmacology, 46(7):974--83, June 2004. ISSN 0028-3908. doi: 10.1016/j.neuropharm.2004.01.007. URL http://www.ncbi.nlm.nih.gov/pubmed/15081794.

C. Beurrier, P. Congar, B. Bioulac, & C. Hammond. Subthalamic nucleus neurons switch from single-spike activity to burst-firing mode. *Journal of Neuroscience*, 19(2):599--609, Jan. 1999. ISSN 0270-6474. URL http://www.ncbi.nlm.nih.gov/pubmed/9880580.

C. Beurrier, B. Bioulac, J. Audin, & C. Hammond. High-frequency stimulation produces a transient blockade of voltage-gated currents in subthalamic neurons. *Journal of Neurophysiology*, 85(4):1351--1356, Apr. 2001. ISSN 0022-3077. URL http://www.ncbi.nlm.nih.gov/pubmed/11287459.

R. Biran, D. C. Martin, & P. a. Tresco. Neuronal cell loss accompanies the brain tissue response to chronically implanted silicon microelectrode arrays. *Experimental neurology*, 195(1):115--26, Sept. 2005. ISSN 0014-4886. doi: 10.1016/j.expneurol.2005.04.020. URL http://www.ncbi.nlm.nih.gov/pubmed/16045910.

R. Biran, D. C. Martin, & P. A. Tresco. The brain tissue response to implanted silicon microelectrode arrays is increased when the device is tethered to the skull. *Journal of Biomedical Materials Research*, 82(1): 169--178, 2007. doi: 10.1002/jbm.a.

J. O. Bockris & B. E. Conway. Determination of the Faradaic Impedance at Solid Electrodes and the Electrodeposition of Copper. *The Journal of Chemical Physics*, 28(4):707, Apr. 1958. ISSN 00219606. doi: 10.1063/1.1744219. URL http://link.aip.org/link/?JCPSA6/28/707/1.

B. D. Boss, G. M. Peterson, & W. M. Cowan. On the number of neurons in the dentate gyrus of the rat. *Brain research*, 338(1):144--50, July 1985. ISSN 0006-8993. URL http://www.ncbi.nlm.nih.gov/pubmed/3896391.

P. Brown. Abnormal oscillatory synchronisation in the motor system leads to impaired movement. *Current opinion in neurobiology*, 17(6):656--64, Dec. 2007. ISSN 0959-4388. doi: 10.1016/j.conb.2007.12.001. URL http://www.ncbi.nlm.nih.gov/pubmed/18221864.

C. R. Butson & C. C. McIntyre. Tissue and electrode capacitance reduce neural activation volumes during deep brain stimulation. *Clinical Neurophysiology*, 116:2490--2500, Oct. 2005. ISSN 1388-2457. doi: 10.1016/j.clinph.2005.06.023. URL http://www.ncbi.nlm.nih.gov/pubmed/16125463.

C. R. Butson, C. B. Maks, & C. C. McIntyre. Sources and effects of electrode impedance during deep brain stimulation. *Clinical Neurophysiology*, 117:

447--454, Feb. 2006. ISSN 1388-2457. doi: 10.1016/j.clinph.2005.10.007. URL http://www.ncbi.nlm.nih.gov/pubmed/16376143.

J. L. Cadet, R. Last, V. Kostic, S. Przedborski, & V. Jackson-Lewis. Long-term behavioral and biochemical effects of 6-hydroxydopamine injections in rat caudate-putamen. *Brain research bulletin*, 26(5):707--13, May 1991. ISSN 0361-9230. URL http://www.ncbi.nlm.nih.gov/pubmed/1933391.

J. J. Canales & A. M. Graybiel. A measure of striatal function predicts motor stereotypy. *Nature neuroscience*, 3(4):377--83, Apr. 2000. ISSN 1097-6256. doi: 10.1038/73949. URL http://www.ncbi.nlm.nih.gov/pubmed/10725928.

D. R. Cantrell, S. Inayat, A. Taflove, R. S. Ruoff, & J. B. Troy. Incorporation of the electrode-electrolyte interface into finite-element models of metal microelectrodes. *Journal of neural engineering*, 5(1):54--67, Mar. 2008. ISSN 1741-2560. doi: 10.1088/1741-2560/5/1/006. URL http://www.ncbi.nlm.nih.gov/pubmed/18310811.

L. S. Carman, F. H. Gage, & C. W. Shults. Partial lesion of the substantia nigra: relation between extent of lesion and rotational behavior. *Brain research*, 553(2):275--83, July 1991. ISSN 0006-8993. URL http://www.ncbi.nlm.nih.gov/pubmed/1681983.

J.-Y. Chang, L.-H. Shi, F. Luo, & D. J. Woodward. High frequency stimulation of the subthalamic nucleus improves treadmill locomotion in unilateral 6-hydroxydopamine lesioned rats. *Brain research*, 983(1-2): 174--84, Sept. 2003. ISSN 0006-8993. URL http://www.ncbi.nlm.nih.gov/pubmed/12914978.

V. Coenen, A. Prescher, T. Schmidt, P. Picozzi, & F. L. H. Gielen. What is dorso-lateral in the subthalamic Nucleus (STN)?--a topographic and anatomical consideration on the ambiguous description of today's primary target for deep brain stimulation (DBS) surgery. *Acta neurochirurgica*, 150(11):1163--5; discussion 1165, Nov. 2008. ISSN 0942-0940. doi: 10.1007/s00701-008-0136-x. URL http://www.ncbi.nlm.nih.gov/pubmed/18958389.

R. J. Coffey. Deep brain stimulation devices: a brief technical history and review. *Artificial Organs*, 115:208--220, Mar. 2009. ISSN 1525-1594. doi: 10.1111/j.1525-1594.2008.00620.x. URL http://www.ncbi.nlm.nih.gov/pubmed/18684199.

S. F. Cogan. Neural stimulation and recording electrodes. *Annual review of biomedical engineering*, 10(275):275--309, Jan. 2008. ISSN 1523-9829. doi: 10.1146/annurev.bioeng.10.061807.160518. URL http://www.ncbi.nlm.nih.gov/pubmed/18429704.

S. F. Cogan, P. R. Troyk, J. Ehrlich, & T. D. Plante. In vitro comparison of the charge-injection limits of activated iridium oxide (AIROF) and platinum-iridium microelectrodes. *IEEE transactions on bio-medical engineering*, 52(9):1612--4, Sept. 2005. ISSN 0018-9294. doi: 10.1109/TBME.2005.851503. URL http://www.ncbi.nlm.nih.gov/pubmed/16189975.

M. K. Cosetti & S. B. Waltzman. Cochlear implants: current status and future potential. *Expert review of medical devices*, 8(3):389--401, May 2011. ISSN 1745-2422. doi: 10.1586/erd.11.12. URL http://www.ncbi.nlm.nih.gov/pubmed/21542710.

C. Da Cunha, E. C. Wietzikoski, M. M. Ferro, G. R. Martinez, M. A. B. F. a. Vital, D. Hipólide, S. Tufik, & N. S. Canteras. Hemiparkinsonian rats rotate toward the side with the weaker dopaminergic neurotransmission. *Behavioural brain research*, 189(2):364--72, June 2008. ISSN 0166-4328. doi: 10.1016/j.bbr.2008.01.012. URL http://www.ncbi.nlm.nih.gov/pubmed/18328580.

J. S. Damoiseaux, S. A. R. B. Rombouts, F. Barkhof, P. Scheltens, C. J. Stam, S. M. Smith, & C. F. Beckmann. Consistent resting-state networks across healthy subjects. *Proceedings of the National Academy of Sciences of the United States of America*, 103(37):13848--53, Sept. 2006. ISSN 0027-8424. doi: 10.1073/pnas.0601417103. URL http://www.pubmedcentral.nih.gov/articlerender.fcgi?artid=1564249&tool=pmcentrez&rendertype=abstract.

G. D. Dawson. Investigations on a patient subject to myoclonic seizures after sensory stimulation. *Journal of Neurology, Neurosurgery, and Psychiatry*, 10(4):141--62, Nov. 1947. ISSN 0022-3050. URL http://www.pubmedcentral.nih.gov/articlerender.fcgi?artid=498225&tool=pmcentrez&rendertype=abstract.

M. J. L. de Hoon, S. Imoto, J. Nolan, & S. Miyano. Open source clustering software. *Bioinformatics (Oxford, England)*, 20(9):1453--4, June 2004. ISSN 1367-4803. doi: 10.1093/bioinformatics/bth078. URL http://dl.acm.org/citation.cfm?id=1092875.1092876.

M. De Luca, C. F. Beckmann, N. De Stefano, P. M. Matthews, & S. M. Smith. fMRI resting state networks define distinct modes of long-distance interactions in the human brain. *NeuroImage*, 29(4):1359--67, Feb. 2006. ISSN 1053-8119. doi: 10.1016/j.neuroimage.2005.08.035. URL http://www.ncbi.nlm.nih.gov/pubmed/16260155.

E. Dégenètais, A.-M. Thierry, J. Glowinski, & Y. Gioanni. Electrophysiological properties of pyramidal neurons in the rat prefrontal cortex: an in vivo intracellular recording study. *Cerebral cortex*, 12:1--16, Jan. 2002. ISSN 1047-3211. URL http://www.ncbi.nlm.nih.gov/pubmed/11734528.

D. Deleu, Y. Hanssens, & M. G. Northway. Subcutaneous apomorphine : an evidence-based review of its use in Parkinson's disease. *Drugs & aging*, 21(11):687--709, Jan. 2004. ISSN 1170-229X. URL http://www.ncbi.nlm.nih.gov/pubmed/15323576.

M. DeLong & T. Wichmann. Circuits and Circuit Disorders of the Basal Ganglia. *Arch Neurol*, 64:20--24, 2007.

R. Deumens, A. Blokland, & J. Prickaerts. Modeling Parkinson's disease in rats: an evaluation of 6-OHDA lesions of the nigrostriatal pathway. *Experimental Neurology*, 175:303--137, June 2002. ISSN 0014-4886. doi: 10.1006/exnr.2002.7891. URL http://www.ncbi.nlm.nih.gov/pubmed/12061862.

A. E. Di Rosa, A. Epifanio, A. Antonini, F. Stocchi, G. Martino, L. Di Blasi, A. Tetto, G. Basile, D. Imbesi, P. La Spina, G. Di Raimondo, & L. Morgante. Continuous apomorphine infusion and neuropsychiatric disorders: a controlled study in patients with advanced Parkinson's disease. *Neurological sciences : official journal of the Italian Neurological Society and of the Italian Society of Clinical Neurophysiology*, 24(3):174--5, Oct. 2003. ISSN 1590-1874. doi: 10.1007/s10072-003-0116-0. URL http://www.ncbi.nlm.nih.gov/pubmed/14598073.

N. D. Donaldson & P. E. Donaldson. When are actively balanced biphasic ('Lilly') stimulating pulses necessary in a neurological prosthesis? I. Historical background; Pt resting potential; Q studies. *Medical & biological engineering & computing*, 24(1):41--9, Jan. 1986. ISSN 0140-0118. URL http://www.ncbi.nlm.nih.gov/pubmed/3959609.

J. P. Donoghue & S. P. Wise. The motor cortex of the rat: cytoarchitecture and microstimulation mapping. *The Journal of comparative neurology*, 212(1):76--88, Nov. 1982. ISSN 0021-9967. doi: 10.1002/cne.902120106. URL http://www.ncbi.nlm.nih.gov/pubmed/6294151.

A. D. Dorval, A. M. Kuncel, M. J. Birdno, D. a. Turner, & W. M. Grill. Deep brain stimulation alleviates parkinsonian bradykinesia by regularizing pallidal activity. *Journal of neurophysiology*, 104(2):911--21, Aug. 2010. ISSN 1522-1598. doi: 10.1152/jn.00103.2010. URL http://www.pubmedcentral.nih.gov/articlerender.fcgi?artid=2934941&tool=pmcentrez&rendertype=abstract.

J. O. Dostrovsky, R. Levy, J. P. Wu, W. D. Hutchison, R. R. Tasker, & A. M. Lozano. Microstimulation-induced inhibition of neuronal firing in human globus pallidus. *Journal of Neurophysiology*, 84:570--574, July 2000. ISSN 0022-3077. URL http://www.ncbi.nlm.nih.gov/pubmed/10899228.

A. M. Dymond, L. E. Kaechele, J. M. Jurist, & P. H. Crandall. Brain tissue reaction to some chronically implanted metals. *Journal of neurosurgery*,

33(5):574--80, Nov. 1970. ISSN 0022-3085. doi: 10.3171/jns.1970.33.5.0574. URL http://www.ncbi.nlm.nih.gov/pubmed/5479495.

G. Dziewczapolski, M. A. Mora, L. B. Menalled, F. J. E. Stéfano, M. Rubinstein, & O. S. Gershanik. Threshold of dopamine content and D1 receptor stimulation necessary for the expression of rotational behavior induced by D2 receptor stimulation under normo and supersensitive conditions. *Naunyn-Schmiedeberg's Archives of Pharmacology*, 355(1): 30--35, Dec. 1996. ISSN 0028-1298. doi: 10.1007/PL00004914. URL http://www.springerlink.com/content/4272m9u16lklvw1a/.

T. J. Feuerstein, M. Kammerer, C. H. Luecking, A. Moser, & C. H. Lücking. Selective GABA release as a mechanistic basis of high frequency stimulation used for the treatment of neuropsychiatric diseases. *Naunyn Schmiedeberg's Archives of Pharmacology*, in press(1):1--20, July 2011. ISSN 1432-1912. doi: 10.1007/s00210-011-0644-8. URL http://www.ncbi.nlm.nih.gov/pubmed/21533988.

R. M. Field & M. Ghovanloo. Simulation of the Capacitive Double Layer at the Interface between Microelectrodes and Cortical Tissue Using Comsol Multiphysics and SPICE Modeling. *Proceedings of the COMSOL User Conference, Boston*, C:7, 2006.

M. D. Fox, A. Z. Snyder, J. L. Vincent, & M. E. Raichle. Intrinsic fluctuations within cortical systems account for intertrial variability in human behavior. *Neuron*, 56(1):171--84, Oct. 2007. ISSN 0896-6273. doi: 10.1016/j.neuron.2007.08.023. URL http://www.ncbi.nlm.nih.gov/pubmed/17920023.

V. Francardo, A. Recchia, N. Popovic, D. Andersson, H. Nissbrandt, & M. A. Cenci. Impact of the lesion procedure on the profiles of motor impairment and molecular responsiveness to L-DOPA in the 6-hydroxydopamine mouse model of Parkinson's disease. *Neurobiology of disease*, 42(3):327--40, June 2011. ISSN 1095-953X. doi: 10.1016/j.nbd.2011.01.024. URL http://www.ncbi.nlm.nih.gov/pubmed/21310234.

W. Franks, I. Schenker, P. Schmutz, & A. Hierlemann. Impedance characterization and modeling of electrodes for biomedical applications. *IEEE Transactions on Biomedical Engineering*, 52(7):1295--1302, July 2005. ISSN 0018-9294. doi: 10.1109/TBME.2005.847523. URL http://www.ncbi.nlm.nih.gov/pubmed/16041993.

G. Fritsch & E. Hitzig. Electric excitability of the cerebrum (Uber die elektrische Erregbarkeit des Grosshirns). *Epilepsy & Behavior*, 15(2): 123--130, June 2009. ISSN 1525-5069. doi: 10.1016/j.yebeh.2009.03.001. URL http://www.ncbi.nlm.nih.gov/pubmed/19457461.

P. Gatev, O. Darbin, & T. Wichmann. Oscillations in the basal ganglia under normal conditions and in movement disorders. *Movement*

disorders : official journal of the Movement Disorder Society, 21(10): 1566--77, Oct. 2006. ISSN 0885-3185. doi: 10.1002/mds.21033. URL http://www.ncbi.nlm.nih.gov/pubmed/16830313.

L. a. Geddes. Historical evolution of circuit models for the electrode-electrolyte interface. *Annals of biomedical engineering*, 25(1): 1--14, 1997. ISSN 0090-6964. URL http://www.ncbi.nlm.nih.gov/pubmed/9124725.

L. a. Geddes & R. Roeder. Criteria for the Selection of Materials for Implanted Electrodes. *Annals of Biomedical Engineering*, 31(7):879--890, July 2003. ISSN 0090-6964. doi: 10.1114/1.1581292. URL http://www.springerlink.com/openurl.asp?id=doi:10.1114/1.1581292.

J. R. Geiger & P. Jonas. Dynamic control of presynaptic Ca(2+) inflow by fast-inactivating K(+) channels in hippocampal mossy fiber boutons. *Neuron*, 28(3):927--39, Dec. 2000. ISSN 0896-6273. URL http://www.ncbi.nlm.nih.gov/pubmed/11163277.

A. P. Georgopolous, A. B. Schwartz, & R. E. Kettner. Neuronal Population Coding of Movement Direction. *Science*, 233:1416--1419, 1986.

W. Gerstner, a. K. Kreiter, H. Markram, & a. V. Herz. Neural codes: firing rates and beyond. *Proceedings of the National Academy of Sciences of the United States of America*, 94(24):12740--1, Nov. 1997. ISSN 0027-8424. URL http://www.pubmedcentral.nih.gov/articlerender.fcgi?artid=34168&tool=pmcentrez&rendertype=abstract.

E. Gileadi, E. Kirowa-Eisner, J. Penciner, & K. G. Weil. Interfacial Electrochemistry – An Experimental Approach, Addison-Wesley, Advanced Book Program, Reading, Massachusetts 1975, 525 Seiten, Preis: US $ 19.50. *Berichte der Bunsengesellschaft für physikalische Chemie*, 80 (8):826, Aug. 1976. ISSN 0005-9021. doi: 10.1002/bbpc.19760800841. URL http://onlinelibrary.wiley.com/doi/10.1002/bbpc.19760800841/abstract.

Y. Glinka, M. Gassen, & M. B. Youdim. Mechanism of 6-hydroxydopamine neurotoxicity. *Journal of neural transmission. Supplementum*, 50:55--66, Jan. 1997. ISSN 0303-6995. URL http://www.ncbi.nlm.nih.gov/pubmed/9120425.

C. Gold, D. a. Henze, C. Koch, & G. Buzsáki. On the origin of the extracellular action potential waveform: A modeling study. *Journal of Neurophysiology*, 95(5):3113--3128, May 2006. ISSN 0022-3077. doi: 10.1152/jn.00979.2005. URL http://www.ncbi.nlm.nih.gov/pubmed/16467426.

C. M. Gray, P. E. Maldonado, M. Wilson, & B. McNaughton. Tetrodes markedly improve the reliability and yield of multiple single-unit

isolation from multi-unit recordings in cat striate cortex. *Journal of neuroscience methods*, 63(1-2):43--54, Dec. 1995. ISSN 0165-0270. URL http://www.ncbi.nlm.nih.gov/pubmed/8788047.

R. E. Gross, P. Krack, M. C. Rodriguez-Oroz, A. R. Rezai, & A.-L. Benabid. Electrophysiological Mapping for the Implantation of Deep Brain Stimulators for Parkinson's Disease and Tremor. *Movement Disorders*, 21 (Suppl. 14):S259--S283, 2006.

F. S. Grover & J. S. Buchwald. Correlation of cell size with amplitude of background fast activity in specific brain nuclei. *Journal of neurophysiology*, 33(1):160--71, Jan. 1970. ISSN 0022-3077. URL http://www.ncbi.nlm.nih.gov/pubmed/5411511.

R. Grünes & K. Roubik. Technical Support of Intracranial Single Unit Activity Measurement. In *World Academy of Science, Engineering and Technology*, page 4, 2008. URL http://citeseerx.ist.psu.edu/viewdoc/summary?doi=10.1.1.193.5362.

A. T. Gulledge, B. M. Kampa, & G. J. Stuart. Synaptic integration in dendritic trees. *Journal of neurobiology*, 64(1):75--90, July 2005. ISSN 0022-3034. doi: 10.1002/neu.20144. URL http://www.ncbi.nlm.nih.gov/pubmed/15884003.

L. F. Haas. Hans Berger (1873–1941), Richard Caton (1842–1926), and electroencephalography. *Journal of Neurology, Neurosurgery, and Psychiatry*, 74(5):653, May 2003. ISSN 0022-3050. URL http://www.pubmedcentral.nih.gov/articlerender.fcgi?artid=1738411&tool=pmcentrez&rendertype=abstract.

M. HajjHassan, V. Chodavarapu, & S. Musallam. NeuroMEMS: Neural Probe Microtechnologies. *Sensors*, 8(10):6704--6726, Oct. 2008. ISSN 1424-8220. doi: 10.3390/s8106704. URL http://www.mdpi.com/1424-8220/8/10/6704/.

S. Hammad, S. Löffler, K. Mankodiya, D. Krapohl, M. Pohl, A. Moser, & V. Tronnier. Niotrode Array for Rodent Brain Recording Electrical testing. In *Proceedings of Biomedizinische Technik*, pages 3--6, 2010.

C. Hammond, H. Bergman, & P. Brown. Pathological synchronization in Parkinson's disease: networks, models and treatments. *Trends in neurosciences*, 30(7):357--64, July 2007. ISSN 0166-2236. doi: 10.1016/j.tins.2007.05.004. URL http://www.ncbi.nlm.nih.gov/pubmed/17532060.

C. Hammond, R. Ammari, B. Bioulac, & L. Garcia. Latest View on the Mechanism of Action of Deep Brain Stimulation. *Movement Disorders*, 23 (15):2111--2121, 2008.

D. Harnack, C. Winter, W. Meissner, T. Reum, A. Kupsch, & R. Morgenstern. The effects of electrode material, charge density and stimulation

duration on the safety of high-frequency stimulation of the subthalamic nucleus in rats. *Journal of Neuroscience Methods*, 138:207--126, Sept. 2004. ISSN 0165-0270. doi: 10.1016/j.jneumeth.2004.04.019. URL http://www.ncbi.nlm.nih.gov/pubmed/15325129.

T. Hashimoto, C. M. Elder, M. S. Okun, S. K. Patrick, & J. L. Vitek. Stimulation of the subthalamic nucleus changes the firing pattern of pallidal neurons. *The Journal of neuroscience : the official journal of the Society for Neuroscience*, 23(5):1916--23, Mar. 2003. ISSN 1529-2401. URL http://www.ncbi.nlm.nih.gov/pubmed/12629196.

C. Hassler, J. Guy, M. Nietzschmann, J. F. Staiger, & T. Stieglitz. Chronic intracortical implantation of saccharose-coated flexible shaft electrodes into the cortex of rats. *Conference proceedings : ... Annual International Conference of the IEEE Engineering in Medicine and Biology Society. IEEE Engineering in Medicine and Biology Society. Conference*, 2011:644--7, Jan. 2011. ISSN 1557-170X. doi: 10.1109/IEMBS.2011.6090143. URL http://www.ncbi.nlm.nih.gov/pubmed/22254391.

S. Hemm, N. Vayssiere, G. Mennessier, L. Cif, M. Zanca, P. Ravel, P. Frerebeau, & P. Coubes. Evolution of brain impedance in dystonic patients treated by GPI electrical stimulation. *Neuromodulation : journal of the International Neuromodulation Society*, 7(2):67--75, Apr. 2004. ISSN 1094-7159. doi: 10.1111/j.1094-7159.2004.04009.x. URL http://www.ncbi.nlm.nih.gov/pubmed/22151186.

D. A. Henze, Z. Borhegyi, J. Csicsvari, A. Mamiya, K. D. Harris, & G. Buzsáki. Intracellular features predicted by extracellular recordings in the hippocampus in vivo. *Journal of neurophysiology*, 84(1):390--400, July 2000. ISSN 0022-3077. URL http://www.ncbi.nlm.nih.gov/pubmed/10899213.

A. Hiller, S. Loeffler, C. Haupt, M. Litza, U. G. Hofmann, & A. Moser. Electrical High Frequency Stimulation Induces GABA Outflow in Freely Moving Rats. *J Neurosci Methods*, 159:286--290, 2007.

L. R. Hochberg, M. D. Serruya, G. M. Friehs, J. a. Mukand, M. Saleh, A. H. Caplan, A. Branner, D. Chen, R. D. Penn, & J. P. Donoghue. Neuronal ensemble control of prosthetic devices by a human with tetraplegia. *Nature*, 442(7099):164--71, July 2006. ISSN 1476-4687. doi: 10.1038/nature04970. URL http://www.ncbi.nlm.nih.gov/pubmed/16838014.

A. L. Hodgkin & A. F. Huxley. A Quantitative Description of Membrane Current and its Application to Conduction and Excitation in Nerve. *J Physiol.*, 117:500--544, 1952.

U. G. Hofmann, A. Folkers, F. Mösch, T. Malina, K. M. L. Menne, G. Biella, P. Fagerstedt, E. De Schutter, W. Jensen, K. Yoshida, D. Hoehl, U. Thomas, M. G. Kindlundh, P. Norlin, & M. de Curtis. A novel high channel-count

system for acute multisite neuronal recordings. *IEEE transactions on bio-medical engineering*, 53(8):1672--7, Aug. 2006. ISSN 0018-9294. doi: 10.1109/TBME.2006.877807. URL http://www.ncbi.nlm.nih.gov/pubmed/16916102.

T. Hökfelt & U. Ungerstedt. Specificity of 6-hydroxydopamine induced degeneration of central monoamine neurones: an electron and fluorescence microscopic study with special reference to intracerebral injection on the nigro-striatal dopamine system. *Brain research*, 60(2): 269--97, Oct. 1973. ISSN 0006-8993. URL http://www.ncbi.nlm.nih.gov/pubmed/4763613.

X. T. Hu, S. R. Wachtel, M. P. Galloway, & F. J. White. Lesions of the nigrostriatal dopamine projection increase the inhibitory effects of D1 and D2 dopamine agonists on caudate-putamen neurons and relieve D2 receptors from the necessity of D1 receptor stimulation. *The Journal of neuroscience : the official journal of the Society for Neuroscience*, 10(7): 2318--29, July 1990. ISSN 0270-6474. URL http://www.ncbi.nlm.nih.gov/pubmed/1973947.

C. M. Huang & J. S. Buchwald. Interpretation of the vertex short-latency acoustic response: a study of single neurons in the brain stem. *Brain research*, 137(2):291--303, Dec. 1977. ISSN 0006-8993. URL http://www.ncbi.nlm.nih.gov/pubmed/589456.

J. L. Hudson, C. G. van Horne, I. Strömberg, S. Brock, J. Clayton, J. Masserano, B. J. Hoffer, & G. a. Gerhardt. Correlation of apomorphine- and amphetamine-induced turning with nigrostriatal dopamine content in unilateral 6-hydroxydopamine lesioned rats. *Brain research*, 626(1-2): 167--74, Oct. 1993. ISSN 0006-8993. URL http://www.ncbi.nlm.nih.gov/pubmed/8281427.

S. W. Hughes, M. L. Lorincz, H. R. Parri, & V. Crunelli. Infra-slow (<0.1 Hz) oscillations in thalamic relay nuclei: basic mechanisms and significance to health and disease states. *Progress in brain research*, 193(C):145--62, Jan. 2011. ISSN 1875-7855. doi: 10.1016/B978-0-444-53839-0.00010-7. URL http://www.pubmedcentral.nih.gov/articlerender.fcgi?artid=3173874&tool=pmcentrez&rendertype=abstract.

W. D. Hutchison, R. J. Allan, H. Opitz, R. Levy, J. O. Dostrovsky, a. E. Lang, & a. M. Lozano. Neurophysiological identification of the subthalamic nucleus in surgery for Parkinson's disease. *Annals of neurology*, 44(4): 622--8, Oct. 1998. ISSN 0364-5134. doi: 10.1002/ana.410440407. URL http://www.ncbi.nlm.nih.gov/pubmed/9778260.

J. Ibarz, O. Herreras, J. Mira, & J. Álvarez. *Computational Methods in Neural Modeling*, volume 2686 of *Lecture Notes in Computer Science*. Springer Berlin Heidelberg, Berlin, Heidelberg, June 2003. ISBN 978-3-540-40210-7. doi: 10.1007/3-540-44868-3. URL http://www.springerlink.com/content/q042y126hawdy22h/.

K. Jellinger. New developments in the pathology of Parkinson's disease. *Advances in neurology*, 53:1--16, Jan. 1990. ISSN 0091-3952. URL http://www.ncbi.nlm.nih.gov/pubmed/1978509.

W. Jensen, K. Yoshida, & U. G. Hofmann. In-vivo implant mechanics of flexible, silicon-based ACREO microelectrode arrays in rat cerebral cortex. *IEEE transactions on bio-medical engineering*, 53(5):934--40, May 2006. ISSN 0018-9294. doi: 10.1109/TBME.2006.872824. URL http://www.ncbi.nlm.nih.gov/pubmed/16686416.

J. D. Johansson, P. Blomstedt, N. Haj-Hosseini, a. T. Bergenheim, O. Eriksson, & K. Wå rdell. Combined diffuse light reflectance and electrical impedance measurements as a navigation aid in deep brain surgery. *Stereotactic and functional neurosurgery*, 87(2):105--13, Jan. 2009. ISSN 1423-0372. doi: 10.1159/000202977. URL http://www.ncbi.nlm.nih.gov/pubmed/19223697.

J. Johnson. Thermal Agitation of Electricity in Conductors. *Physical Review*, 32(1):97--109, July 1928. ISSN 0031-899X. doi: 10.1103/PhysRev.32.97. URL http://prola.aps.org/abstract/PR/v32/i1/p97_1.

M. D. Johnson, S. Miocinovic, C. C. McIntyre, & J. L. Vitek. Mechanisms and Targets of Deep Brain Stimulation in Movement Disorders. *Neurotherapeutics*, 5(2):294--308, 2008.

E. Jones, T. Oliphant, & P. Peterson. SciPy: Open source scientific tools for Python, 2001. URL http://www.scipy.org/.

E. Juergens, A. Guettler, & R. Eckhorn. Visual stimulation elicits locked and induced gamma oscillations in monkey intracortical- and EEG-potentials, but not in human EEG. *Experimental brain research. Experimentelle Hirnforschung. Expérimentation cérébrale*, 129(2):247--59, Nov. 1999. ISSN 0014-4819. URL http://www.ncbi.nlm.nih.gov/pubmed/10591899.

R. C. Kelly, M. A. Smith, R. E. Kass, & T. S. Lee. Local field potentials indicate network state and account for neuronal response variability. *Journal of computational neuroscience*, 29(3):567--79, Dec. 2010. ISSN 1573-6873. doi: 10.1007/s10827-009-0208-9. URL http://www.ncbi.nlm.nih.gov/pubmed/20094906.

M. Kindlundh, P. Norlin, & U. G. Hofmann. A neural probe process enabling variable electrode configurations. *Sensors and Actuators B: Chemical*, 102(1):58--51, 2004. doi: 10.1016/j.snb.2003.10.009. URL http://dx.doi.org/10.1016/j.snb.2003.10.009.

D. R. Kipke, R. J. Vetter, J. C. Williams, & J. F. Hetke. Silicon-substrate intracortical microelectrode arrays for long-term recording of neuronal spike activity in cerebral cortex. *IEEE transactions on neural systems and rehabilitation engineering : a publication of the IEEE Engineering in*

Medicine and Biology Society, 11(2):151--5, June 2003. ISSN 1534-4320. doi: 10.1109/TNSRE.2003.814443. URL http://www.ncbi.nlm.nih.gov/pubmed/12899260.

D. R. Kipke, W. Shain, G. Buzsáki, E. Fetz, J. M. Henderson, J. F. Hetke, & G. Schalk. Advanced neurotechnologies for chronic neural interfaces: new horizons and clinical opportunities. *The Journal of neuroscience : the official journal of the Society for Neuroscience*, 28(46):11830--8, Nov. 2008. ISSN 1529-2401. doi: 10.1523/JNEUROSCI.3879-08.2008. URL http://www.ncbi.nlm.nih.gov/pubmed/19005048.

D. Kirik, C. Rosenblad, & A. Björklund. Characterization of behavioral and neurodegenerative changes following partial lesions of the nigrostriatal dopamine system induced by intrastriatal 6-hydroxydopamine in the rat. *Experimental neurology*, 152(2):259--77, Aug. 1998. ISSN 0014-4886. doi: 10.1006/exnr.1998.6848. URL http://www.ncbi.nlm.nih.gov/pubmed/9710526.

S. Kisban, S. Herwik, K. Seidl, B. Rubehn, A. Jezzini, M. A. Umiltà, L. Fogassi, T. Stieglitz, O. Paul, & P. Ruther. Microprobe array with low impedance electrodes and highly flexible polyimide cables for acute neural recording. *Conference proceedings : ... Annual International Conference of the IEEE Engineering in Medicine and Biology Society. IEEE Engineering in Medicine and Biology Society. Conference*, 2007:175--8, Jan. 2007. ISSN 1557-170X. doi: 10.1109/IEMBS.2007.4352251. URL http://www.ncbi.nlm.nih.gov/pubmed/18001917.

T. D. Y. Kozai & D. R. Kipke. Insertion shuttle with carboxyl terminated self-assembled monolayer coatings for implanting flexible polymer neural probes in the brain. *Journal of neuroscience methods*, 184(2): 199--205, Nov. 2009. ISSN 1872-678X. doi: 10.1016/j.jneumeth.2009.08.002. URL http://www.pubmedcentral.nih.gov/articlerender.fcgi?artid=3165009&tool=pmcentrez&rendertype=abstract.

D. S. Kreiss, C. W. Mastropietro, S. S. Rawji, & J. R. Walters. The Response of Subthalamic Nucleus Neurons to Dopamine Receptor Stimulation in a Rodent Model of Parkinson ' s Disease. *J Neurosci*, 17(17):6807--6819, 1997.

A. C. Kreitzer & R. C. Malenka. Review Striatal Plasticity and Basal Ganglia Circuit Function. *Neuron*, 60(4):543--554, 2008. ISSN 0896-6273. doi: 10.1016/j.neuron.2008.11.005. URL http://dx.doi.org/10.1016/j.neuron.2008.11.005.

I. Krisch & B. J. Hosticka. Restoring visual perception using microsystem technologies: engineering and manufacturing perspectives. *Acta neurochirurgica. Supplement*, 97(Pt 2):473--80, Jan. 2007. ISSN 0065-1419. URL http://www.ncbi.nlm.nih.gov/pubmed/17691337.

A. M. Kuncel & W. M. Grill. Selection of stimulus parameters for deep brain stimulation. *Clinical Neurophysiology*, 115:2431--2441, Nov. 2004. ISSN 1388-2457. doi: 10.1016/j.clinph.2004.05.031. URL http://www.ncbi.nlm.nih.gov/pubmed/15465430.

N. Lago, K. Yoshida, K. P. Koch, & X. Navarro. Assessment of biocompatibility of chronically implanted polyimide and platinum intrafascicular electrodes. *IEEE transactions on bio-medical engineering*, 54(2):281--90, Feb. 2007. ISSN 0018-9294. doi: 10.1109/TBME.2006.886617. URL http://ieeexplore.ieee.org/xpl/freeabs_all.jsp?arnumber=4067115.

L. Laitinen, G. G. Johansson, & P. Sipponen. Impedance and phase angle as a locating method in human stereotaxic surgery. *Journal of neurosurgery*, 25(6):628--33, Dec. 1966. ISSN 0022-3085. doi: 10.3171/jns.1966.25.6.0628. URL http://www.ncbi.nlm.nih.gov/pubmed/5332653.

A. D. Legatt, J. Arezzo, & H. G. Vaughan. Averaged multiple unit activity as an estimate of phasic changes in local neuronal activity: effects of volume-conducted potentials. *Journal of neuroscience methods*, 2(2): 203--17, Apr. 1980. ISSN 0165-0270. URL http://www.ncbi.nlm.nih.gov/pubmed/6771471.

S. F. Lempka, M. D. Johnson, D. W. Barnett, M. A. Moffitt, K. J. Otto, D. R. Kipke, & C. C. McIntyre. Optimization of microelectrode design for cortical recording based on thermal noise considerations. *Conference proceedings : ... Annual International Conference of the IEEE Engineering in Medicine and Biology Society. IEEE Engineering in Medicine and Biology Society. Conference*, 1:3361--4, Jan. 2006. ISSN 1557-170X. doi: 10.1109/IEMBS.2006.259432. URL http://www.ncbi.nlm.nih.gov/pubmed/17947023.

M. S. Lewicki. A review of methods for spike sorting : the detection and classification of neural action potentials. *Comput. Neural Systems*, 9: 53--78, 1999.

T. Li, F. Qadri, & A. Moser. Neuronal electrical high frequency stimulation modulates presynaptic GABAergic physiology. *Neuroscience letters*, 371 (2-3):117--21, Nov. 2004. ISSN 0304-3940. doi: 10.1016/j.neulet.2004.08.050. URL http://www.ncbi.nlm.nih.gov/pubmed/15519740.

T. Li, A. Thümen, & A. Moser. Modulation of a neuronal network by electrical high frequency stimulation in striatal slices of the rat in vitro. *Neurochemistry International*, 48:83--86, Jan. 2006. ISSN 0197-0186. doi: 10.1016/j.neuint.2005.09.004. URL http://www.ncbi.nlm.nih.gov/pubmed/16310287.

J. C. Lilly. Injury and Excitation by Electric Currents - The Balanced Pulse-Pair Waveform. In Daniel E. Sheer, editor, *Electrical Stimulation of*

the Brain., pages 60--64. Univ. of Texas Press for Hogg Foundation for Mental Health, 1961.

G. Lind, C. E. Linsmeier, J. Thelin, & J. Schouenborg. Gelatine-embedded electrodes-a novel biocompatible vehicle allowing implantation of highly flexible microelectrodes. *Journal of neural engineering*, 7(4): 046005, June 2010. ISSN 1741-2552. doi: 10.1088/1741-2560/7/4/046005. URL http://www.ncbi.nlm.nih.gov/pubmed/20551508.

R. Llinas & C. Nicholson. Electrophysiological properties of dendrites and somata in alligator Purkinje cells. *Journal of neurophysiology*, 34(4): 532--51, July 1971. ISSN 0022-3077. URL http://www.ncbi.nlm.nih.gov/pubmed/4329778.

R. R. Llinás & M. Steriade. Bursting of thalamic neurons and states of vigilance. *Journal of neurophysiology*, 95(6):3297--308, June 2006. ISSN 0022-3077. doi: 10.1152/jn.00166.2006. URL http://www.ncbi.nlm.nih.gov/pubmed/16554502.

S. Löffler, S. Vogt, U. G. Hofmann, & M. A. Striatal microstimulation in awake animals depends on NMDA receptor activity. *Biomed Eng*, 53: 126--128, 2008.

N. K. Logothetis. The underpinnings of the BOLD functional magnetic resonance imaging signal. *The Journal of Neuroscience*, 23(10):3963--71, May 2003. ISSN 1529-2401. URL http://www.ncbi.nlm.nih.gov/pubmed/12764080.

N. K. Logothetis. Bold claims for optogenetics. *Nature*, 468(7323):E3--4; discussion E4--5, Nov. 2010. ISSN 1476-4687. doi: 10.1038/nature09532. URL http://www.ncbi.nlm.nih.gov/pubmed/21107378.

F. López-Muñoz & C. Alamo. Historical evolution of the neurotransmission concept. *Journal of neural transmission (Vienna, Austria : 1996)*, 116(5): 515--33, May 2009. ISSN 1435-1463. doi: 10.1007/s00702-009-0213-1. URL http://www.ncbi.nlm.nih.gov/pubmed/19350218.

M. L. Lorincz, F. Geall, Y. Bao, V. Crunelli, & S. W. Hughes. ATP-dependent infra-slow (<0.1 Hz) oscillations in thalamic networks. *PloS one*, 4(2): e4447, Jan. 2009. ISSN 1932-6203. doi: 10.1371/journal.pone.0004447. URL http://dx.plos.org/10.1371/journal.pone.0004447.

A. M. Lozano, J. Dostrovsky, R. Chen, & P. Ashby. Deep brain stimulation for Parkinson's disease: disrupting the disruption. *The Lancet Neurology*, 1:225--231, Aug. 2002. ISSN 14744422. doi: 10.1016/S1474-4422(02)00101-1. URL http://linkinghub.elsevier.com/retrieve/pii/S1474442202001011.

A. Machado, A. R. Rezai, B. H. Kopell, R. E. Gross, A. D. Sharan, & A.-L. Benabid. Deep brain stimulation for Parkinson's disease: surgical

technique and perioperative management. *Movement disorders : official journal of the Movement Disorder Society*, 21 Suppl 1:S247--58, June 2006. ISSN 0885-3185. doi: 10.1002/mds.20959. URL http://www.ncbi.nlm.nih.gov/pubmed/16810722.

R. J. Maciunas, B. N. Maddux, D. E. Riley, C. M. Whitney, M. R. Schoenberg, P. J. Ogrocki, J. N. Albert, & D. J. Gould. Prospective randomized double-blind trial of bilateral thalamic deep brain stimulation in adults with Tourette syndrome. *Journal of Neurosurgery*, 107:1004--1014, 2007. doi: 10.3171/JNS-07/11/1004.

J. C. Magee. Dendritic integration of excitatory synaptic input. *Nature reviews. Neuroscience*, 1(3):181--90, Dec. 2000. ISSN 1471-003X. doi: 10.1038/35044552. URL http://www.ncbi.nlm.nih.gov/pubmed/11257906.

D. Mantini, M. G. Perrucci, C. Del Gratta, G. L. Romani, & M. Corbetta. Electrophysiological signatures of resting state networks in the human brain. *Proceedings of the National Academy of Sciences of the United States of America*, 104(32):13170--5, Aug. 2007. ISSN 0027-8424. doi: 10.1073/pnas.0700668104. URL http://www.pubmedcentral.nih.gov/articlerender.fcgi?artid=1941820&tool=pmcentrez&rendertype=abstract.

M. Mantovani, V. Van Velthoven, H. Fuellgraf, T. J. Feuerstein, & A. Moser. Neuronal electrical high frequency stimulation enhances GABA outflow from human neocortical slices. *Neurochemistry international*, 49: 347--350, Oct. 2006. ISSN 0197-0186. doi: 10.1016/j.neuint.2006.02.008. URL http://www.ncbi.nlm.nih.gov/pubmed/16600434.

M. Mantovani, A. Moser, C. A. Haas, J. Zentner, & T. J. Feuerstein. GABA(A) autoreceptors enhance GABA release from human neocortex: towards a mechanism for high-frequency stimulation (HFS) in brain? *Naunyn-Schmiedeberg's Archives of Pharmacology*, 380:45--58, July 2009. ISSN 1432-1912. doi: 10.1007/s00210-009-0410-3. URL http://www.ncbi.nlm.nih.gov/pubmed/19296090.

H. S. Mayberg, A. M. Lozano, V. Voon, H. E. McNeely, D. Seminowicz, C. Hamani, J. M. Schwalb, & S. H. Kennedy. Deep brain stimulation for treatment-resistant depression. *Neuron*, 45:651--660, Mar. 2005. ISSN 0896-6273. doi: 10.1016/j.neuron.2005.02.014. URL http://www.ncbi.nlm.nih.gov/pubmed/15748841.

S. Mayer, L. A. Geddes, J. D. Bourland, & L. Ogborn. Faradic resistance in the electrode/electrolyte interface. *Medical & Biological Engineering & Computing*, 30(5):538--542, 1992. doi: 10.1007/BF02457834.

A. Mazzoni, F. D. Broccard, E. Garcia-Perez, P. Bonifazi, M. E. Ruaro, & V. Torre. On the dynamics of the spontaneous activity in neuronal networks. *PloS one*, 2(5):e439, Jan. 2007. ISSN 1932-6203. doi:

10.1371/journal.pone.0000439. URL http://www.pubmedcentral.nih.gov/articlerender.fcgi?artid=1857824&tool=pmcentrez&rendertype=abstract.

E. McAdams, A. Lackermeier, J. McLaughlin, D. Macken, & J. Jossinet. The linear and non-linear electrical properties of the electrode-electrolyte interface. *Biosensors and Bioelectronics*, 10(1-2):67--74, Jan. 1995. ISSN 09565663. doi: 10.1016/0956-5663(95)96795-Z. URL http://dx.doi.org/10.1016/0956-5663(95)96795-Z.

D. B. McCreery, W. F. Agnew, T. G. Yuen, & L. Bullara. Charge density and charge per phase as cofactors in neural injury induced by electrical stimulation. *IEEE transactions on bio-medical engineering*, 37(10):996--1001, Oct. 1990. ISSN 0018-9294. URL http://www.ncbi.nlm.nih.gov/pubmed/2249872.

C. C. McIntyre, M. Savasta, L. Kerkerian-Le Goff, & J. L. Vitek. Uncovering the mechanism(s) of action of deep brain stimulation: activation, inhibition, or both. *Clinical Neurophysiology*, 115(6):1239--1248, June 2004. ISSN 1388-2457. doi: 10.1016/j.clinph.2003.12.024. URL http://www.ncbi.nlm.nih.gov/pubmed/15134690.

L. Menendez de la Prida, F. Suarez, & M. A. Pozo. The effect of different morphological sampling criteria on the fraction of bursting cells recorded in the rat subiculum in vitro. *Neuroscience letters*, 322(1):49--52, Mar. 2002. ISSN 0304-3940. URL http://www.ncbi.nlm.nih.gov/pubmed/11958841.

K. M. L. Menne. *Computerassistenz zur Implantation von Tiefenhirnstimulatoren - Von der Merkmalsbestimmung für Gehirnsignale zur Datenbank für Elektrophysiologie*. Dissertation, Universität zu Lübeck, 2005.

M. Merello, E. Tenca, & D. Cerquetti. Neuronal activity of the zona incerta in Parkinson's disease patients. *Movement disorders : official journal of the Movement Disorder Society*, 21(7):937--43, July 2006. ISSN 0885-3185. doi: 10.1002/mds.20834. URL http://www.ncbi.nlm.nih.gov/pubmed/16534763.

D. R. Merrill, M. Bikson, & J. G. R. Jefferys. Electrical stimulation of excitable tissue : design of efficacious and safe protocols. *Journal of Neuroscience Methods*, 141:171--198, 2005. doi: 10.1016/j.jneumeth.2004.10.020.

S. Miocinovic, A. M. Noecker, C. B. Maks, C. R. Butson, & C. C. McIntyre. Cicerone: stereotactic neurophysiological recording and deep brain stimulation electrode placement software system. *Acta neurochirurgica. Supplement*, 97(Pt 2):561--7, Jan. 2007. ISSN 0065-1419. URL http://www.ncbi.nlm.nih.gov/pubmed/17691348.

U. Mitzdorf. Current source-density method and application in cat cerebral cortex: investigation of evoked potentials and EEG phenomena. *Physiological reviews*, 65(1):37--100, Jan. 1985. ISSN 0031-9333. URL http://www.ncbi.nlm.nih.gov/pubmed/3880898.

U. Mitzdorf. Properties of the evoked potential generators: current source-density analysis of visually evoked potentials in the cat cortex. *The International journal of neuroscience*, 33(1-2):33--59, Mar. 1987. ISSN 0020-7454. URL http://www.ncbi.nlm.nih.gov/pubmed/3610492.

M. A. Moffitt & C. C. Mcintyre. Model-based analysis of cortical recording with silicon microelectrodes. *Clinical Neurophysiology*, 116(116): 2240--2250, 2005. doi: 10.1016/j.clinph.2005.05.018.

A. Molina-Picó, D. Cuesta-Frau, M. Aboy, C. Crespo, P. Miró-Martínez, & S. Oltra-Crespo. Comparative study of approximate entropy and sample entropy robustness to spikes. *Artificial intelligence in medicine*, 53(2): 97--106, Oct. 2011. ISSN 1873-2860. doi: 10.1016/j.artmed.2011.06.007. URL http://www.ncbi.nlm.nih.gov/pubmed/21835600.

C. K. E. Moll, A. Struppler, & A. K. Engel. Intraoperative Mikroelektrodenableitungen in den Basalganglien des Menschen. Neuroforum. *Neuroforum*, 1(05):11--20, 2005.

A. Moser, A. Gieselberg, B. Ro, C. Keller, & F. Quadri. Deep brain stimulation: response to neuronal high frequency stimulation is mediated through GABAA receptor activation in rats. *Neuroscience Letters*, 341:57--60, Apr. 2003a. ISSN 03043940. doi: 10.1016/S0304-3940(03)00133-2. URL http://linkinghub.elsevier.com/retrieve/pii/S0304394003001332.

A. Moser, A. Thuemen, & F. Quadri. Modulation of striatal serotonin and opioid receptor mRNA expression following systemic N-methyl-norsalsolinol administration. *Journal of the Neurological Sciences*, 216:109--112, Dec. 2003b. ISSN 0022510X. doi: 10.1016/S0022-510X(03)00226-0. URL http://linkinghub.elsevier.com/retrieve/pii/S0022510X03002260.

K. A. Neve, M. R. Kozlowski, & J. F. Marshall. Plasticity of neostriatal dopamine receptors after nigrostriatal injury: relationship to recovery of sensorimotor functions and behavioral supersensitivity. *Brain research*, 244(1):33--44, July 1982. ISSN 0006-8993. URL http://www.ncbi.nlm.nih.gov/pubmed/6288182.

O. Niina, T. Hirotaka, K. Yoshiuki, K. Toshiya, K. Risato, T. Tetsu, & H. Jari. Comparison of electrode materials for the use of retinal prosthesis. *Bio-medical materials and engineering*, 21(2):83--97, Jan. 2011. ISSN 1878-3619. doi: 10.3233/BME-2011-0658. URL http://www.ncbi.nlm.nih.gov/pubmed/21654065.

a. Nini, A. Feingold, H. Slovin, & H. Bergman. Neurons in the globus pallidus do not show correlated activity in the normal monkey, but phase-locked oscillations appear in the MPTP model of parkinsonism. *Journal of neurophysiology*, 74(4):1800--5, Oct. 1995. ISSN 0022-3077. URL http://www.ncbi.nlm.nih.gov/pubmed/8989416.

P. Norlin, M. Kindlundh, A. Mouroux, K. Yoshida, & U. G. Hofmann. A 32-site neural recording probe fabricated by DRIE of SOI substrates. *Journal of Micromechanics and Microengineering*, 12(4):414, 2002. ISSN 0960-1317. doi: http://dx.doi.org/10.1088/0960-1317/12/4/312. URL http://stacks.iop.org/0960-1317/12/i=4/a=312.

R. a. Normann, E. M. Maynard, P. J. Rousche, & D. J. Warren. A neural interface for a cortical vision prosthesis. *Vision research*, 39(15):2577--87, July 1999. ISSN 0042-6989. URL http://www.ncbi.nlm.nih.gov/pubmed/10396626.

P. Novak, S. Daniluk, S. a. Ellias, & J. M. Nazzaro. Detection of the subthalamic nucleus in microelectrographic recordings in Parkinson disease using the high-frequency (> 500 hz) neuronal background. Technical note. *Journal of neurosurgery*, 106(1):175--9, Jan. 2007. ISSN 0022-3085. doi: 10.3171/jns.2007.106.1.175. URL http://www.ncbi.nlm.nih.gov/pubmed/17236505.

P. Novak, A. W. Przybyszewski, A. Barborica, P. Ravin, L. Margolin, & J. G. Pilitsis. Localization of the subthalamic nucleus in Parkinson disease using multiunit activity. *Journal of the neurological sciences*, pages 6--11, Aug. 2011. ISSN 1878-5883. doi: 10.1016/j.jns.2011.07.027. URL http://www.ncbi.nlm.nih.gov/pubmed/21855895.

L. G. Nowak, R. Azouz, M. V. Sanchez-Vives, C. M. Gray, & D. a. McCormick. Electrophysiological classes of cat primary visual cortical neurons in vivo as revealed by quantitative analyses. *Journal of neurophysiology*, 89(3):1541--66, Mar. 2003. ISSN 0022-3077. doi: 10.1152/jn.00580.2002. URL http://www.ncbi.nlm.nih.gov/pubmed/12626627.

B. J. Nuttin, L. A. Gabriels, P. R. Cosyns, B. A. Meyerson, S. Andreewitch, S. G. Sunaert, A. F. Maes, P. J. Dupont, J. M. Gybels, F. Gielen, & H. G. Demeulemeester. Long-term electrical capsular stimulation in patients with obsessive-compulsive disorder. *Neurosurgery*, 52(6):1263--1274, 2003. doi: 10.1227/01.NEU.0000064565.49299.9A.

H. Nyquist. Thermal Agitation of Electric Charge in Conductors. *Physical Review*, 32(1):110--113, July 1928. ISSN 0031-899X. doi: 10.1103/PhysRev.32.110. URL http://prola.aps.org/abstract/PR/v32/i1/p110_1.

B. Onaral & H. P. Schwan. Linear and nonlinear properties of platinum electrode polarisation. Part 1: frequency dependence at very low

frequencies. *Medical & Biological Engineering & Computing*, 20(3): 299--306, May 1982. ISSN 0140-0118. doi: 10.1007/BF02442796. URL http://www.springerlink.com/content/u421764pl7738027/.

I. Osorio, M. G. Frei, B. F. Manly, S. Sunderam, N. C. Bhavaraju, & S. B. Wilkinson. An introduction to contingent (closed-loop) brain electrical stimulation for seizure blockage, to ultra-short-term clinical trials, and to multidimensional statistical analysis of therapeutic efficacy. *Journal of clinical neurophysiology : official publication of the American Electroencephalographic Society*, 18(6):533--44, Nov. 2001. ISSN 0736-0258. URL http://www.ncbi.nlm.nih.gov/pubmed/11779966.

Y. S. Park, M. F. Jeon, B. H. Lee, & J. W. Chang. Lesion of subthalamic nucleus in parkinsonian rats : effects of dopamine d(1) and d(2) receptor agonists on the neuronal activities of the substantia nigra pars reticulata. *Journal of Korean Neurosurgical Society*, 42(6):455--61, Dec. 2007. ISSN 2005-3711. doi: 10.3340/jkns.2007.42.6.455. URL http://www.pubmedcentral.nih.gov/articlerender.fcgi?artid=2588170&tool=pmcentrez&rendertype=abstract.

N. Parush, D. Arkadir, A. Nevet, G. Morris, N. Tishby, I. Nelken, & H. Bergman. Encoding by response duration in the basal ganglia. *Journal of neurophysiology*, 100(6):3244--52, Dec. 2008. ISSN 0022-3077. doi: 10.1152/jn.90400.2008. URL http://www.ncbi.nlm.nih.gov/pubmed/18842956.

A. Pavlov, V. A. Makarov, I. Makarova, & F. Panetsos. Sorting of neural spikes : When wavelet based methods outperform principal component analysis. *Natural Computing*, 6:269--281, 2007. doi: 10.1007/s11047-006-9014-8.

G. Paxinos & C. Watson. *The rat brain in stereotaxic coordinates*. Academic Press, 2007. ISBN 0125476124. URL http://books.google.com/books?id=0prYfdDbh58C&pgis=1.

J. M. S. Pearce. Emil Heinrich Du Bois-Reymond (1818–96). *Journal of Neurology, Neurosurgery and Psychiatry*, 71(5), 2001. doi: 10.1136/jnnp.71.5.620.

W. Penfield & E. Boldrey. Somatic Motor and Sensory Representation in the Cerebral Cortex of Man As Studied By Electrical Stimulation. *Brain*, 60(4):389--443, 1937. ISSN 0006-8950. doi: 10.1093/brain/60.4.389. URL http://brain.oxfordjournals.org/cgi/doi/10.1093/brain/60.4.389.

C. M. Pettit, P. C. Goonetilleke, C. M. Sulyma, & D. Roy. Combining impedance spectroscopy with cyclic voltammetry: measurement and analysis of kinetic parameters for faradaic and nonfaradaic reactions on thin-film gold. *Analytical chemistry*, 78(11):3723--9, June 2006. ISSN

0003-2700. doi: 10.1021/ac052157l. URL http://www.ncbi.nlm.nih.gov/pubmed/16737229.

B. Pillon, C. Ardouin, P. Damier, P. Krack, J. L. Houeto, H. Klinger, A. M. Bonnet, P. Pollak, A. L. Benabid, & Y. Agid. Neuropsychological changes between "off" and "on" STN or GPi stimulation in Parkinson ' s disease. *Neurology*, 55:411--418, 2000.

I. Porada, I. Bondar, W. B. Spatz, & J. Krüger. Rabbit and monkey visual cortex: more than a year of recording with up to 64 microelectrodes. *Journal of neuroscience methods*, 95(1):13--28, Jan. 2000. ISSN 0165-0270. URL http://www.ncbi.nlm.nih.gov/pubmed/10776811.

R. Q. Quiroga. Unsupervised Spike Detection and Sorting with Wavelets and Superparamagnetic Clustering. *Neural Computation*, 16:1661--1687, 2004.

T. Ragheb & L. A. Geddes. Electrical properties of metallic electrodes. *Medical & biological engineering & computing*, 28(2):182--6, Mar. 1990. ISSN 0140-0118. URL http://www.ncbi.nlm.nih.gov/pubmed/2376994.

T. Ragheb, S. Riegle, L. A. Geddes, & V. Amin. The impedance of a spherical monopolar electrode. *Annals of biomedical engineering*, 20(6):617--27, Jan. 1992. ISSN 0090-6964. URL http://www.ncbi.nlm.nih.gov/pubmed/1449230.

L. Ramrath, S. Vogt, W. Jensen, U. G. Hofmann, & A. Schweikard. Computer- and robot-assisted stereotaxy for high-precision small animal brain exploration. *Biomedizinische Technik. Biomedical engineering*, 54 (1):8--13, Feb. 2009. ISSN 0013-5585. doi: 10.1515/BMT.2009.002. URL http://www.ncbi.nlm.nih.gov/pubmed/19182868.

a. Raz, E. Vaadia, & H. Bergman. Firing patterns and correlations of spontaneous discharge of pallidal neurons in the normal and the tremulous 1-methyl-4-phenyl-1,2,3,6-tetrahydropyridine vervet model of parkinsonism. *The Journal of neuroscience : the official journal of the Society for Neuroscience*, 20(22):8559--71, Nov. 2000. ISSN 1529-2401. URL http://www.ncbi.nlm.nih.gov/pubmed/11069964.

R. R. Richardson, J. A. Miller, & W. M. Reichert. Polyimides as biomaterials: preliminary biocompatibility testing. *Biomaterials*, 14(8):627--35, July 1993. ISSN 0142-9612. URL http://www.ncbi.nlm.nih.gov/pubmed/8399958.

A. Richter, Y. Xie, A. Schumacher, S. Löffler, J. Al-Hasani, C. Kruse, A. Moser, S. Danner, & U. G. Hofmann. Easy adaptable implantation method for flexible deep brain stimulating electrodes to rat brains. *submitted to JoVE*, 2012.

D. Robinson. The electrical properties of metal microelectrodes. *Proceedings of the IEEE*, 56(6):1065--1071, 1968. ISSN 0018-9219. doi: 10.1109/PROC.1968.6458. URL http://ieeexplore.ieee.org/xpl/freeabs_all.jsp?arnumber=1448388.

T. Roitbak & E. Syková. Diffusion barriers evoked in the rat cortex by reactive astrogliosis. *Glia*, 28(1):40--8, Oct. 1999. ISSN 0894-1491. URL http://www.ncbi.nlm.nih.gov/pubmed/10498821.

T. L. Rose & L. S. Robblee. Electrical stimulation with Pt electrodes. VIII. Electrochemically safe charge injection limits with 0.2 ms pulses. *IEEE transactions on bio-medical engineering*, 37(11):1118--20, Nov. 1990. ISSN 0018-9294. doi: 10.1109/10.61038. URL http://www.ncbi.nlm.nih.gov/pubmed/2276759.

P. J. Rousche, D. S. Pellinen, D. P. Pivin, J. C. Williams, R. J. Vetter, & D. R. Kipke. Flexible polyimide-based intracortical electrode arrays with bioactive capability. *IEEE transactions on bio-medical engineering*, 48(3): 361--71, Mar. 2001. ISSN 0018-9294. doi: 10.1109/10.914800. URL http://www.ncbi.nlm.nih.gov/pubmed/11327505.

D. N. Ruskin, D. A. Bergstrom, J. R. Walters, Y. Kaneoke, B. N. Patel, & J. Twery. Multisecond oscillations in firing rate in the globus pallidus: synergistic modulation by D1 and D2 dopamine receptors. *J Neurophysiol*, 290(3):1493--501, Sept. 1999. ISSN 0022-3565. URL http://www.ncbi.nlm.nih.gov/pubmed/10454529.

D. N. Ruskin, D. A. Bergstrom, P. L. Tierney, & J. R. Walters. Correlated multisecond oscillations in firing rate in the basal ganglia: modulation by dopamine and the subthalamic nucleus. *Neuroscience*, 117(2):427--38, Jan. 2003. ISSN 0306-4522. URL http://www.ncbi.nlm.nih.gov/pubmed/12614683.

S. I. Ryu & K. V. Shenoy. Human cortical prostheses: lost in translation? *Neurosurgical focus*, 27(1):E5, July 2009. ISSN 1092-0684. doi: 10.3171/2009.4.FOCUS0987. URL http://www.ncbi.nlm.nih.gov/pubmed/19569893.

J. A. Saint-Cyr, L. L. Trepanier, R. Kumar, A. M. Lozano, A. E. Lang, J. A. Saint-cyr, L. L. Tre, & C. J. Saint-cyr. Neuropsychological consequences of chronic bilateral stimulation of the subthalamic nucleus in Parkinson's disease. *Brain*, 123:2091--2108, 2000.

M. Sakai, H. Sakai, & C. D. Woody. Sampling distribution of morphologically identified neurons of the coronalpericruciate cortex of awake cats following intracellular injection of HRP. *Brain research*, 152 (2):329--33, Aug. 1978. ISSN 0006-8993. URL http://www.ncbi.nlm.nih.gov/pubmed/679030.

H. Sauer & W. H. Oertel. Progressive Degeneration of Nigrostriatal Dopamine Neurons Following Intrastriatal Terminal Lesions with 6-Hydroxydopamine: A combined retrograde tracing and immunocytochemical study in the rat. *Neuroscience*, 59(2):401--415, 1994.

A. H. Schapira. Science, medicine, and the future: Parkinson's disease. *BMJ (Clinical research ed.)*, 318(7179):311--4, Jan. 1999. ISSN 0959-8138. URL `http://www.pubmedcentral.nih.gov/articlerender.fcgi?artid=1114782&tool=pmcentrez&rendertype=abstract`.

S. J. Schiff. Towards model-based control of Parkinson's disease. *Philosophical transactions. Series A, Mathematical, physical, and engineering sciences*, 368(1918):2269--308, May 2010. ISSN 1364-503X. doi: 10.1098/rsta.2010.0050. URL `http://www.pubmedcentral.nih.gov/articlerender.fcgi?artid=2944387&tool=pmcentrez&rendertype=abstract`.

R. L. Schultz & T. J. Willey. The ultrastructure of the sheath around chronically implanted electrodes in brain. *Journal of neurocytology*, 5(6):621--42, Dec. 1976. ISSN 0300-4864. URL `http://www.ncbi.nlm.nih.gov/pubmed/1003257`.

H. P. Schwan. Electrode polarization impedance and measurements in biological materials. *Annals of the New York Academy of Sciences*, 148(1):191--209, Feb. 1968. ISSN 0077-8923. URL `http://www.ncbi.nlm.nih.gov/pubmed/5237641`.

A. B. Schwartz, R. E. Kettner, & A. P. Georgopolous. Primate motor cortex and free arm movements to visual targets in three-dimensional space. I. Relations between single cell discharge and direction of movement. *Journal of Neuroscience*, 8(8):2913--2927, 1988.

I. Segev & W. Rall. Excitable dendrites and spines : earlier theoretical insights elucidate recent direct observations. *Trends in Neurosciences*, 21:453--460, 1998.

C. Seifried, L. Weise, R. Hartmann, T. Gasser, S. Baudrexel, A. Szelényi, S. van de Loo, H. Steinmetz, V. Seifert, J. Roeper, & R. Hilker. Intraoperative microelectrode recording for the delineation of subthalamic nucleus topography in Parkinson's disease. *Brain stimulation*, July 2011. ISSN 1935-861X. doi: 10.1016/j.brs.2011.06.002. URL `http://www.ncbi.nlm.nih.gov/pubmed/21782543`.

R. S. Shah, S.-Y. Chang, H.-K. Min, Z.-H. Cho, C. D. Blaha, & K. H. Lee. Deep Brain Stimulation: Technology at the Cutting Edge. *Journal of Clinical Neurology*, 6:167--182, 2010.

K. Z. Shen & S. W. Johnson. Presynaptic dopamine D2 and muscarine M3 receptors inhibit excitatory and inhibitory transmission to rat subthalamic neurones in vitro. *The Journal of physiology*, 525 Pt 2:

331--41, June 2000. ISSN 0022-3751. URL http://www.pubmedcentral.nih.gov/articlerender.fcgi?artid=2269945&tool=pmcentrez&rendertype=abstract.

K.-Z. Shen & S. W. Johnson. Regulation of polysynaptic subthalamonigral transmission by D2, D3 and D4 dopamine receptors in rat brain slices. *The Journal of physiology*, pages jphysiol.2011.225672--, Feb. 2012. ISSN 1469-7793. doi: 10.1113/jphysiol.2011.225672. URL http://jp.physoc.org/cgi/content/abstract/jphysiol.2011.225672v1.

M. Shin, J.-P. Lefaucheur, M. F. Penholate, P. Brugières, J.-M. Gurruchaga, & J.-P. Nguyen. Subthalamic nucleus stimulation in Parkinson's disease: postoperative CT-MRI fusion images confirm accuracy of electrode placement using intraoperative multi-unit recording. *Neurophysiologie clinique = Clinical neurophysiology*, 37(6):457--66, Dec. 2007. ISSN 0987-7053. doi: 10.1016/j.neucli.2007.09.005. URL http://www.ncbi.nlm.nih.gov/pubmed/18083502.

K. Sidiropoulou, E. K. Pissadaki, & P. Poirazi. Inside the brain of a neuron. *EMBO reports*, 7(9):886--92, Sept. 2006. ISSN 1469-221X. doi: 10.1038/sj.embor.7400789. URL http://www.pubmedcentral.nih.gov/articlerender.fcgi?artid=1559659&tool=pmcentrez&rendertype=abstract.

L. R. Silva, Y. Amitai, & B. W. Connors. Intrinsic oscillations of neocortex generated by layer 5 pyramidal neurons. *Science (New York, N.Y.)*, 251 (4992):432--5, Jan. 1991. ISSN 0036-8075. URL http://www.ncbi.nlm.nih.gov/pubmed/1824881.

R. A. Silver. Neuronal arithmetic. *Nature reviews. Neuroscience*, 11(7): 474--89, July 2010. ISSN 1471-0048. doi: 10.1038/nrn2864. URL http://www.ncbi.nlm.nih.gov/pubmed/20531421.

J. C. Skou. The influence of some cations on an adenosine triphosphatase from peripheral nerves. *Biochimica et biophysica acta*, 23(2):394--401, Feb. 1957. ISSN 0006-3002. URL http://www.ncbi.nlm.nih.gov/pubmed/13412736.

A. J. Smith, S. Owens, & I. D. Forsythe. Characterisation of inhibitory and excitatory postsynaptic currents of the rat medial superior olive. *The Journal of physiology*, 529(3):681--98, Dec. 2000. ISSN 0022-3751. URL http://www.pubmedcentral.nih.gov/articlerender.fcgi?artid=2270210&tool=pmcentrez&rendertype=abstract.

P. a. Starr, R. S. Turner, G. Rau, N. Lindsey, S. Heath, M. Volz, J. L. Ostrem, & W. J. Marks. Microelectrode-guided implantation of deep brain stimulators into the globus pallidus internus for dystonia: techniques, electrode locations, and outcomes. *Journal of neurosurgery*, 104(4): 488--501, Apr. 2006. ISSN 0022-3085. doi: 10.3171/jns.2006.104.4.488. URL http://www.ncbi.nlm.nih.gov/pubmed/16619651.

S. S. Stensaas & L. J. Stensaas. Histopathological evaluation of materials implanted in the cerebral cortex. *Acta neuropathologica*, 41(2):145--55, Feb. 1978. ISSN 0001-6322. URL http://www.ncbi.nlm.nih.gov/pubmed/636844.

D. Sterio, M. Zonenshayn, A. Y. Mogilner, A. R. Rezai, K. Kiprovski, P. J. Kelly, & A. Beric. Neurophysiological refinement of subthalamic nucleus targeting. *Neurosurgery*, 50(1):58--67; discussion 67--9, Jan. 2002. ISSN 0148-396X. URL http://www.ncbi.nlm.nih.gov/pubmed/11844235.

T. Stieglitz. Implantable microsystems for monitoring and neural rehabilitation, Part II. *Medical device technology*, 13(1):24--7, 2002. ISSN 1048-6690. URL http://www.ncbi.nlm.nih.gov/pubmed/11921778.

T. Stieglitz & J. U. Meyer. Implantable microsystems. Polyimide-based neuroprostheses for interfacing nerves. *Medical device technology*, 10(6): 28--30, 1999. ISSN 1048-6690. URL http://www.ncbi.nlm.nih.gov/pubmed/10623349.

S. S. D. Stone & J. T. Rutka. Utility of neuronavigation and neuromonitoring in epilepsy surgery. *Neurosurgical Focus*, 25(3):E17, Sept. 2008. ISSN 1092-0684. doi: 10.3171/FOC/2008/25/9/E17. URL http://www.ncbi.nlm.nih.gov/pubmed/18759618.

U. Strauss, F.-W. Zhou, J. Henning, A. Battefeld, A. Wree, R. Köhling, S. J.-P. Haas, R. Benecke, A. Rolfs, & U. Gimsa. Increasing extracellular potassium results in subthalamic neuron activity resembling that seen in a 6-hydroxydopamine lesion. *Journal of neurophysiology*, 99(6):2902--15, June 2008. ISSN 0022-3077. doi: 10.1152/jn.00402.2007. URL http://www.ncbi.nlm.nih.gov/pubmed/18385482.

J. Subbaroyan, D. C. Martin, & D. R. Kipke. A finite-element model of the mechanical effects of implantable microelectrodes in the cerebral cortex. *Journal of neural engineering*, 2(4):103--13, Dec. 2005. ISSN 1741-2560. doi: 10.1088/1741-2560/2/4/006. URL http://www.ncbi.nlm.nih.gov/pubmed/16317234.

S. Suner, M. R. Fellows, C. Vargas-Irwin, G. K. Nakata, & J. P. Donoghue. Reliability of signals from a chronically implanted, silicon-based electrode array in non-human primate primary motor cortex. *IEEE transactions on neural systems and rehabilitation engineering : a publication of the IEEE Engineering in Medicine and Biology Society*, 13(4): 524--41, Dec. 2005. ISSN 1534-4320. doi: 10.1109/TNSRE.2005.857687. URL http://www.ncbi.nlm.nih.gov/pubmed/16425835.

S. Takeuchi, T. Suzuki, K. Mabuchi, & H. Fujita. 3D flexible multichannel neural probe array. *Journal of Micromechanics and Microengineering*, 14 (1):104--107, Jan. 2004. ISSN 0960-1317. doi: 10.1088/0960-1317/14/1/014. URL http://stacks.iop.org/0960-1317/14/i=1/a=014?key=crossref.b72b8652900cda018fa71fd0a9c71f3e.

D. M. Taylor, S. I. H. Tillery, & A. B. Schwartz. Direct cortical control of 3D neuroprosthetic devices. *Science (New York, N.Y.)*, 296(5574):1829--32, June 2002. ISSN 1095-9203. doi: 10.1126/science.1070291. URL http://www.ncbi.nlm.nih.gov/pubmed/12052948.

Y. Temel, A. Kessels, S. Tan, A. Topdag, P. Boon, & V. Visser-Vandewalle. Behavioural changes after bilateral subthalamic stimulation in advanced Parkinson disease: a systematic review. *Parkinsonism & related disorders*, 12(5):265--72, June 2006. ISSN 1353-8020. doi: 10.1016/j.parkreldis.2006.01.004. URL http://www.ncbi.nlm.nih.gov/pubmed/16621661.

J. B. Troy, D. R. Cantrell, A. Taflove, & R. S. Ruoff. Modeling the electrode-electrolyte interface for recording and stimulating electrodes. *Conference proceedings : ... Annual International Conference of the IEEE Engineering in Medicine and Biology Society. IEEE Engineering in Medicine and Biology Society. Conference*, 1:879--81, Jan. 2006. ISSN 1557-170X. doi: 10.1109/IEMBS.2006.260112. URL http://www.ncbi.nlm.nih.gov/pubmed/17945606.

M.-L. Tsai & C.-T. Yen. A simple method for fabricating horizontal and vertical microwire arrays. *Journal of neuroscience methods*, 131(1-2): 107--10, Dec. 2003. ISSN 0165-0270. URL http://www.ncbi.nlm.nih.gov/pubmed/14659830.

V. Tsytsarev, M. Taketani, F. Schottler, S. Tanaka, & M. Hara. A new planar multielectrode array: recording from a rat auditory cortex. *Journal of neural engineering*, 3(4):293--8, Dec. 2006. ISSN 1741-2560. doi: 10.1088/1741-2560/3/4/006. URL http://www.ncbi.nlm.nih.gov/pubmed/17124333.

J. N. Turner, W. Shain, D. H. Szarowski, M. Andersen, S. Martins, M. Isaacson, & H. Craighead. Cerebral astrocyte response to micromachined silicon implants. *Experimental neurology*, 156(1):33--49, Mar. 1999. ISSN 0014-4886. doi: 10.1006/exnr.1998.6983. URL http://www.ncbi.nlm.nih.gov/pubmed/10192775.

U. Ungerstedt. 6-Hydroxy-dopamine induced degeneration of central monoamine neurons. *European journal of pharmacology*, 5(1):107--10, Dec. 1968. ISSN 0014-2999. URL http://www.ncbi.nlm.nih.gov/pubmed/5718510.

U. Ungerstedt. Adipsia and aphagia after 6-hydroxydopamine induced degeneration of the nigro-striatal dopamine system. *Acta physiologica Scandinavica. Supplementum*, 367:95--122, Jan. 1971. ISSN 0302-2994. URL http://www.ncbi.nlm.nih.gov/pubmed/4332694.

F. Urbano, E. Leznik, & R. Llinás. Cortical activation patterns evoked by afferent axons stimuli at different frequencies: an in vitro voltage-sensitive dye imaging study. *Thalamus and Related Systems*, 1:

371--378, Apr. 2002. ISSN 1472-9288. doi: 10.1017/S1472928802000092. URL http://www.journals.cambridge.org/abstract_S1472928802000092.

V. Vedam-Mai, E. Y. van Battum, W. Kamphuis, M. G. P. Feenstra, D. Denys, B. a. Reynolds, M. S. Okun, & E. M. Hol. Deep brain stimulation and the role of astrocytes. *Molecular psychiatry*, pages 1--8, May 2011. ISSN 1476-5578. doi: 10.1038/mp.2011.61. URL http://www.ncbi.nlm.nih.gov/pubmed/21625231.

J. L. Vitek. Mechanisms of Deep Brain Stimulation : Excitation or Inhibition. *Movement Disorders*, 17:69--72, 2002. doi: 10.1002/mds.10144.

J. Volkmann, J. Herzog, F. Kopper, & G. Deuschl. Introduction to the programming of deep brain stimulators. *Movement disorders : official journal of the Movement Disorder Society*, 17 Suppl 3:S181--7, Jan. 2002. ISSN 0885-3185. URL http://www.ncbi.nlm.nih.gov/pubmed/11948775.

F. M. Weaver, K. Follett, M. Stern, K. Hur, C. Harris, W. J. Marks, J. Rothlind, O. Sagher, D. Reda, C. S. Moy, R. Pahwa, K. Burchiel, P. Hogarth, E. C. Lai, J. E. Duda, K. Holloway, A. Samii, S. Horn, J. Bronstein, G. Stoner, J. Heemskerk, & G. D. Huang. Bilateral deep brain stimulation versus best medical therapy for patients with advanced Parkinson's disease. *JAMA*, 301(1):63--73, July 2009. ISSN 1534-6293. URL http://www.ncbi.nlm.nih.gov/pubmed/19515276.

X. F. Wei & W. M. Grill. Impedance characteristics of deep brain stimulation electrodes in vitro and in vivo. *Journal of neural engineering*, 6(4):046008, Aug. 2009. ISSN 1741-2552. doi: 10.1088/1741-2560/6/4/046008. URL http://www.pubmedcentral.nih.gov/articlerender.fcgi?artid=3066196&tool=pmcentrez&rendertype=abstract.

J. D. Weiland & D. J. Anderson. Chronic neural stimulation with thin-film, iridium oxide electrodes. *IEEE Transactions on Biomedical Engineering*, 47 (7):911--918, 2000. ISSN 00189294. doi: 10.1109/10.846685. URL http://www.ncbi.nlm.nih.gov/pubmed/10916262.

T. Wichmann & M. R. DeLong. Functional and pathophysiological models of the basal ganglia. *Current opinion in neurobiology*, 6(6):751--8, Dec. 1996. ISSN 0959-4388. URL http://www.ncbi.nlm.nih.gov/pubmed/9000030.

C. J. Wilson, B. Beverlin, & T. Netoff. Chaotic desynchronization as the therapeutic mechanism of deep brain stimulation. *Frontiers in Systems Neuroscience*, 5:50, Jan. 2011. ISSN 1662-5137. doi: 10.3389/fnsys.2011.00050. URL http://www.pubmedcentral.nih.gov/articlerender.fcgi?artid=3122072&tool=pmcentrez&rendertype=abstract.

F. Windels, N. Bruet, A. Poupard, C. Feuerstein, A. Bertrand, & M. Savasta. Influence of the Frequency Parameter on Extracellular Glutamate and gamma -Aminobutyric Acid in Substantia Nigra and Globus Pallidus During Electrical Stimulation of Subthalamic Franc. *Journal of Neuroscience Research*, 72:259 --267, 2003.

K. D. Wise, D. J. Anderson, J. F. Hetke, D. R. Kipke, & K. Najafi. Wireless Implantable Microsystems: High-Density Electronic Interfaces to the Nervous System. *Proceedings of the IEEE*, 92(1):76--97, 2004.

K. Xie, S. Wang, T. Z. Aziz, J. F. Stein, & X. Liu. The physiologically modulated electrode potentials at the depth electrode-brain interface in humans. *Neuroscience letters*, 402(3):238--43, July 2006. ISSN 0304-3940. doi: 10.1016/j.neulet.2006.04.015. URL `http://www.ncbi.nlm.nih.gov/pubmed/16697525`.

Y. Xie, T. Bonin, S. Loeffler, G. Huettmann, V. Tronnier, & U. G. Hofmann. Fiber spectral domain optical coherence tomography for in vivo rat brain imaging. In *Proceedings of SPIE*, page 77152F, 2010. doi: doi:10.1117/12.854798.

T. Yokoyama, K. Sugiyama, S. Nishizawa, T. Tanaka, N. Yokota, S. Ohta, & K. Uemura. Neural Activity of the Subthalamic Nucleus in Parkinson's Disease Patients. *Acta Neurochirurgica*, 140(12):1287--1291, Dec. 1998. ISSN 0001-6268. doi: 10.1007/s007010050251. URL `http://www.springerlink.com/openurl.asp?genre=article&id=doi:10.1007/s007010050251`.

N. Yousif & X. Liu. Investigating the depth electrode-brain interface in deep brain stimulation using finite element models with graded complexity in structure and solution. *Journal of neuroscience methods*, 184(1):142--51, Oct. 2009. ISSN 1872-678X. doi: 10.1016/j.jneumeth.2009.07.005. URL `http://www.pubmedcentral.nih.gov/articlerender.fcgi?artid=2754374&tool=pmcentrez&rendertype=abstract`.

N. Yousif, R. Bayford, P. G. Bain, & X. Liu. The peri-electrode space is a significant element of the electrode-brain interface in deep brain stimulation: a computational study. *Brain research bulletin*, 74(5):361--8, Oct. 2007. ISSN 0361-9230. doi: 10.1016/j.brainresbull.2007.07.007. URL `http://www.pubmedcentral.nih.gov/articlerender.fcgi?artid=2486401&tool=pmcentrez&rendertype=abstract`.

N. Yousif, R. Bayford, & X. Liu. The influence of reactivity of the electrode-brain interface on the crossing electric current in therapeutic deep brain stimulation. *Neuroscience*, 156(3):597--606, Oct. 2008. ISSN 0306-4522. doi: 10.1016/j.neuroscience.2008.07.051. URL `http://www.pubmedcentral.nih.gov/articlerender.fcgi?artid=2730055&tool=pmcentrez&rendertype=abstract`.

X.-Z. Yuan, C. Song, H. Wang, & J. Zhang. *Electrochemical Impedance Spectroscopy in PEM Fuel Cells Fundamentals and Applications*. Springer Verlag, London, 1st edition, 2010. ISBN 978-1-84882-845-2. doi: 10.1007.978-1-84882-846-9.

D. Zhang, A. Z. Snyder, M. D. Fox, M. W. Sansbury, J. S. Shimony, & M. E. Raichle. Intrinsic functional relations between human cerebral cortex and thalamus. *Journal of neurophysiology*, 100(4):1740--8, Oct. 2008. ISSN 0022-3077. doi: 10.1152/jn.90463.2008. URL `http://www.pubmedcentral.nih.gov/articlerender.fcgi?artid=2576214&tool=pmcentrez&rendertype=abstract`.

Z.-T. Zhu, K.-Z. Shen, & S. W. Johnson. Pharmacological identification of inward current evoked by dopamine in rat subthalamic neurons in vitro. *Neuropharmacology*, 42(6):772--81, May 2002. ISSN 0028-3908. URL `http://www.ncbi.nlm.nih.gov/pubmed/12015203`.

ACKNOWLEDGEMENTS

This work was funded by the "Bundesministerium für Bildung und Forschung" (BMBF) within the nanotechnology research project BiCIRTS. Further, I received generous funding from the "German Academic Exchange Service" (DAAD) and the Carl Benett AB (Sweden).

"If I have seen further, it is
by standing on the shoulders of Giants "
— Issac Newton

I wish to thank my supervisors Prof. Moser and Prof. Hofmann. Prof. Moser endured me with incredible patience. He guided me back on the path, when I had, again, completely lost it. His conviction and massive knowledge will be something I will look up to in my whole life. I thank Prof. Hofmann for his unimaginable creative energy, for seeing the good, when all I saw was largely mediocre, and for creating a truly inspiring and familiar atmosphere in his group. I will remember the "biosignal group" forever, and will always be proud to have been part of it.

My deeply felt gratitude to Prof. Agneta Richter Dahlfors, and the "Swedish Medical Nanoscience Center" for trusting and believing in me, and for making the last year such a rich experience. Many thanks to Prof. Mertins for welcoming me in his institute, and to Frau Ehlers for holding a firm grip on organization. Thanks to Prof. Tronnier for providing a bridge to the "real world" of clinics.

Further I want to thank our cooperation partners in the BiCIRTS project Dr. Peter Detemple and Dr. Jens Wüsten from the IMM in Mainz, Wolfgang Noack und Saschka Busch from the Inomed GmbH in Freiburg as well as Prof. Wolfgang Parak from the biophotonics research group at the Phillips Universität in Marburg for productive, interdisciplinary collaboration.

Beyond scientific supervision, I was lucky to have the "ladies from the liquorlab", guiding me through all the worldly matters. My heartily felt gratitude to Katharina Schnackenberg, for …just everything… I have no means of expressing it. Thanks to Gisa Brunk and Marie Luise Reher for being like mothers and sisters and for taking good care of me.

People say, that you are partly like the people you meet and the people you work with. I sincerely hope that this saying is true, since I had the chance to meet people that are plainly amazing, and I'm unspeakable grateful to call some of them friends. Thanks to Dr. Anja Hiller and Dr. Fatimunissa Quadri who got me started on neuroscience, and to Dr. Noel for good advice and helping me find the right way to deal with animal experiments. Thanks, David for pulling out the geek in me and showing me, that you can do anything, if you are just stubborn enough. Thanks Yijing, for amazing collaboration. You are the master in not showing off how great you are.

Thanks Kunal for your wise comments and for whiteboard sessions in the Biosig lab. Thanks Aritra. You are my model for just how much people can grow. Thanks Mehrnaz for being so ravishingly intelligent. Thanks Sofyan for brewing the most delicious tee in the middle of the night, and for staying calm when I got mad. Thanks, Simon for trying to make a difference. Thanks Olaf & Matthias for coffee and trying to explain things, I will never understand…and for the washing machine. Thanks to the crew of the "awesome office" for just making the office so …awesome. Thanks Kalle, It is an honour to build up on the work of a genius. Thanks Jorrit for not letting me be a lonely geek. You lead the way. Tack så mycket, världens bästa Karin! Nu ska vi snart sluta att kämpa!

There is another saying, that your friend believe in you, when you stop believing in yourself. In these last few years, it was your friendship that kept me going. Thank you Matthias, Charlotte & Romy for inviting me to sunday night dinner on skype. Thank you Michael, Luise & Jonathan for generously sharing your happiness and making me feel loved. Thanks, Arnika & Anette for all those good times. Thank you Albert for nerd talk, astra and long walks. Thanks to the best WG of the world! Thank you my old friend Carthago, I miss you so much. Thanks, Carina, for being my sister. Thanks, for never giving up on me and for never letting my excuses count! Thanks to my family for letting me go, and find my way back.

LIST OF FIGURES

1.1 The action potential . . . 2
1.2 Neuronal cells and synapses . . . 3
1.3 The *electrode-electrolyte interface* . . . 6
1.4 Impedance & Nyquist plot . . . 12
1.5 Bode Plot . . . 13
1.6 Neuronavigation to the *subthalamic nucleus* . . . 14
1.7 Rat Parkinson Model . . . 23

2.1 Linear Array Probe . . . 27
2.2 Flexible Array Probe . . . 28
2.3 Flexible Array Probe Layouts . . . 28
2.4 Flexible Array Probe Connections . . . 29
2.5 Stereotaxic Targets . . . 33
2.6 Stereotaxic Surgery . . . 34
2.7 Skull Reference Points . . . 34
2.8 Mounting the micropositioning stage. . . . 36
2.9 Insertion of Flexible Array Probes . . . 37
2.10 Procedure of step by step *Flexible Array Probe* insertion . . . 38
2.11 Chronic Implant . . . 38
2.12 Linear Array Probe Implantation . . . 40
2.13 Microinjection System . . . 41
2.14 Chronic Experiment Setup . . . 42
2.15 Chronic Experiment Schedule . . . 42
2.16 Timesweep Experiment . . . 44
2.17 Currentsweep Experiment . . . 44
2.18 Apomorphine Test . . . 45
2.19 Treatment Groups . . . 46
2.20 Wavetrain Data . . . 47
2.21 Stimulation Artefact . . . 48
2.22 Edge Detection . . . 48
2.23 Spike Detection . . . 49
2.24 Spike Event Analysis . . . 51

3.1 Frequency Responce of Linear Array Probes. . . . 54
3.2 Frequency response of Flexible Array Probes. . . . 55
3.3 Impedance Area Relationship . . . 57
3.4 Neuronavigation by Wavetrain Pattern . . . 59
3.5 Neuronavigation by Spike Shape . . . 60
3.6 Neuronavigation by Spike Shapes . . . 60
3.7 Root Mean Square Activity Profile . . . 62
3.8 Spectral Density Profile . . . 63

3.9 Spike Activity Profile 64
3.10 Entropy Profile 65
3.11 Activity Profile Turning Points 66
3.12 Voltage Response Curves 67
3.13 Maximum Electrode Potential 67
3.14 Time Constants of the Voltage Response 68
3.15 Basal Neuronal Activity 69
3.16 Apomorphine induced Rotational Response 70
3.17 Apomorphine Induced Ipsilateral Rotations 71
3.18 Rotational Response Induced by Subthalamic Microstimulation 71
3.19 Contralateral Rotations Induced by Subthalamic Microstimulation 72
3.20 Root Mean Square Response after *Linear Array Probe* Microstimulation 73
3.21 Root Mean Square Response after *Flexible Array Probe* Microstimulation 74
3.22 Mean Spectral Density Response after *Linear Array Probe* Microstimulation 75
3.23 Mean Spectral Density Response after *Flexible Array Probe* Microstimulation 76
3.24 Oscillatory Neuronal Response to *Linear Array Probe* Microstimulation 78
3.25 Oscillatory Neuronal Response to *Linear Array Probe* Microstimulation 79
3.26 Altered Spike Activity in Sham treated Animals due to *Linear Array Probe* Microstimulation 80
3.27 Altered Spike Activity in Lesioned Animals due to *Linear Array Probe* Microstimulation 81
3.28 Increased and decreased spike activity in sham-treated animals with implanted *Linear Array Probes* depending on current amplitude 83
3.29 Increased and decreased spike activity in lesioned animals with implanted *Linear Array Probes* depending on current amplitude 84
3.30 Spike activity in Sham treated and Lesioned Animals 85
3.31 Imbalances in Spiking Behaviour in Sham Treated Animals due to *Flexible Array Probe* microstimulation 85
3.32 Imbalances in Spiking Behaviour in Lesioned Animals due to *Flexible Array Probe* microstimulation 86
3.33 Stimulation amplitude dependent spiking activity in sham-treated and lesioned animals with implanted *Flexible Array Probes* 87

LIST OF TABLES

1.1 Save charge injection capacities 10
1.2 Parameters for *deep brain stimulation* 15
1.3 Neurostimulator output capability 18
1.4 Deep Brain Stimulation Leads 19

2.1 Charge densities at *Linear-* and *Flexible Array Probe* stimulation sites 30
2.2 Stereotaxic Coordinates 35
2.3 Target depths 37

3.1 Randles cell parameters 56
3.2 Fitted Randles cell Parameters 57
3.3 Characteristic Impedances and Phase angles 58
3.4 Root Mean Square Activity Profile Turning Points 61
3.5 Spectral Activity Profile Turning Points 63
3.6 Spike Activity Profile Turning Points 65
3.7 Entropy Profile Turning Points 66
3.8 Maximum Electrode Potential 68
3.9 Time Constants 69

LIST OF LISTINGS

B.1 LCR800_FREQSWEEP.m B-3
B.2 LCR800_COMMANDS.m B-5
B.3 LCR800_GOONLINE.m B-6
B.4 LCR800_GOOFFLINE.m B-6
B.5 LCR800_SETPARAMS.m B-6
B.6 LCR800_GETPARAMS.m B-7
B.7 LCR800_SETFREQ.m B-7
B.8 LCR800_START.m B-7
B.9 LCR800_READVAL.m B-8
B.10 LCR800_GETSECOVAL.m B-8
B.11 LCR800_GENOUTPUT.m B-8

C.1 defineVars.m C-3
C.2 exportTDTtoMat.m C-3
C.3 getTankParams.m C-5
C.4 saveChannel.m C-6

D.1 groupdict.py D-3
D.2 Main.py D-9
D.3 Utils.py D-9
D.4 getdata.py D-20

LIST OF ABBREVIATIONS

6OHDA	6-hydroxydopamine
AC	alternating current
AcbSh	accumbens nucleus shell
AMPA	2-amino-3-(5-methyl-3-oxo-1,2-oxazol-4-yl)propanoic acid
AP	anterior-posterior
B	bregma
BOLD	blood oxygen level dependent [effect]
CPu	caudate putamen
DC	direct current
DV	dorsal-ventral
FDA	food and drug association
FFC	flat flexible cable
fMRI	functinal magnetic resonance tomography
G	ground
GABA	γ-aminobutyric acid
IAP	inter aural point
MEMS	microelectronic and microelectromechanical systems
ML	medial-lateral
MPTP	1-metyl-4-fenyl-1,2,3,6-tetrahydropyridin
PCB	printed circuit board
SNc	substantia nigra pars compacta
STN	subthalmic nucleus

A

CURRICULUM VITAE

Susanne Löffler

November, 4th 1983 in Sonneberg, Germany

Address:	Sichelreuther Strasse 1, 96524 Neuhaus-Schierschnitz
Phone:	+49 36764 139560
Email:	susanne.loeffler@neuro.uni-luebeck.de

Education

Postgraduate Studies

since 10/2010	Swedish Medical Nanoscience Center, *Karolinska Institute, Sweden* **Project**: *Development and Biomedical Application of Organic Bioelectronic Devices*
12/2007 - 09/2010	**Project**: *Nano-functional Bioprobes with multiple Microelectrodes on an Flexible Polymer Basis for Chronic Implantation and Closed Loop Deep Brain Stimulation* **Courses**: *Laboratory Animal Science, Cat. B FELASA, certified by GV-SOLAS*

Master's Programme

10/2005 - 12/2007	Molecular Life Science, *University of Lübeck, Germany* **Master Thesis**: *Characterization of HFS induced GABA release in the corpus striatum of the rat in vivo* **Degree**: *M. Sc.* **Focus of Studies**: *Cell biology, Treatment strategies, Drug design, Structural Analysis, Biophysics, Bioinformatics* **Lab Courses**: *Biomedical optics, Molecular dynamics, In vitro differentiation of murine embryonic stem cells Cardiovascular tissue engineering - bioreactors for cell and tissue growth Radiation protection course* **Positions**: *Student Assistant, Institute for Neurology*

Bachelor's Programme

10/2005 - 12/2007	Molecular Life Science, *University of Lübeck, Germany* **Bachelor Thesis**: *High frequency stimulation of the caudate nucleus in vivo - Determination of GABA and glutamate neurotransmitter* **Degree**: *B. Sc.* **Focus of Studies**: *Fundamentals of Natural & Medical Sciences, Structural Analysis, Computer Science, Statistics* **Lab Courses**: *Statistical Analysis using the SAS, Plant Biotechnology (Institute for Botanics, Leibnitz University, Hannover, Germany)*

Qualification for Higher Education

08/1994 - 06/2002	A-levels, *1. Staatliches Gymnasium Sonneberg, Germany*

Skills & Competences

Language	**German**: *native* **English**: *fluent* **Swedish**
Computer Skills	**Operating systems**: *GNU/Linux, MacOS X, MS Windows* **Prog. Languages**: *Python, Shell Script, LaTeX, Java, Matlab, R* **Applications**: *Scientific Python, LabVIEW, GraphPad Prism SAS, SPSS, Comsol Multiphysics* **Office**: *OpenOffice, MS Office*
Academic Interests	*Basal ganglia circuit models, Deep brain stimulation, Microstimulation, Interface reactions at brain implants, Conductive Polymers, Organic Electrochemical Transistors, Transistor based Biosensors, Organic Bioelectronic Devices*
Personal Interests	*Long-distance running, Cross-country skiing, Swimming, Cycling, Horseback riding, Rock Climbing*

B

LCR METER

To measure the impedance and phase angle spectrum, a frequency sweep experiment was performed by calling the LCR800_FREQSWEEP function (see Listing B.1).

The LCR800_FREQSWEEP function sequentially calls several utility functions so that a *Frequency Sweep Experiment* is performed.

First, the command variables are loaded with the LCR800_COMMANDS function (see lst Listing B.2). To compile the hexadecimal command variables, a reference command list supplied by the vendor. The hexadecimal digits were written and read via the RS232 serial port.

The instrument is set to online mode by using the LCR800_GOOFFLINE and LCR800_GOOFFLINE functions (see Listing B.4 and Listing B.3). The measurement parameter variables are loaded by the LCR800_GETPARAMS function (see Listing B.6) and set with the LCR800_SETPARAMS function (see Listing B.5). To store the parameters, the instrument status was toggled between online and offline. The newly set parameters were read using the LCR800_GETPARAMS function (see Listing B.5) and wrote into the *params* variable.

A predefined list of frequencies is defined in the *freqs* variable. This list can be altered by adding hexadecimal codes for the frequency commands in LCR800_COMMANDS (see Listing B.2) and adjusting the *freqs* array in the LCR_FREQSWEEP function (see Listing B.1).

The instrument sweeps through the list of frequencies in the *freqs* variable and the impedance and phase angle are measured for each frequency. The frequency is set by the LCR800_SETFREQ function (see Listing B.7), and the measurement is started when the LCR800_START function (see Listing B.8) is called. The LCR800_START function calls LCR800_READVAL (see Listing B.9) to read the measured impedance Z and LCR800_GETSECOVAL (see Listing B.10) to read the measured phase angle Φ.

After the measurement, all parameters and raw data are formatted into a *.txt* file using the LCR800_GENOUTPUT function (see Listing B.11).

Listing B.1: LCR800_FREQSWEEP.m

```
function [] = LCR800_FREQSWEEP(n)

%check if n is given as input argument
if nargin ~= 1
    error('Wrong number of input arguments')
end

% TIMER
t1 = timer('TimerFcn',@mycallback, 'Period', 10);

%INITIALIZE SERIAL PORT
s = 'offline';
s = LCR800_INITSERIAL(s);

% Get the Command Strings for the LCR800
LCR800_COMMANDS;

% LCR800 GO ONLINE
LCR800_GOONLINE(s, t1, GOONLINE, ONLINE);
```

```
display('LCR800 is ONLINE');

% LCR800 SET PARAMETER
display('setting parameters...')
LCR800_PARAMS;
PARAMS = {SPEED, DISPLAY, MODE, CIRCUIT, VOLTAGE, TRIGGER, RANGEHOLD
    , CONSTVOLT, INTBIAS, EXTBIAS, NOMVAL, AVERAGE};
SET_PARAMS = {SET_SPEED, SET_DISPLAY, SET_MODE, SET_CIRCUIT,
    SET_VOLTAGE, SET_TRIGGER, SET_RANGEHOLD, SET_CONSTVOLT,
    SET_INTBIAS, SET_EXTBIAS, SET_NOMVAL, SET_AVERAGE};

for j=1:length(SET_PARAMS);
    SET_PARAM = SET_PARAMS{j};
    PARAM = PARAMS{j};
    LCR800_SETPARAMS(s, t1, SET_PARAM, PARAM);
end

%Switching it OFF and ON
LCR800_GOOFFLINE(s, t1, GOOFFLINE, OFFLINE);
LCR800_GOONLINE(s, t1, GOONLINE, ONLINE);

%create a string for writing params into outputfile
params = '';
% LCR800 GET PARAMETER
display('getting parameters...')
GET_PARAMS = {GET_SPEED, GET_DISPLAY, GET_MODE, GET_CIRCUIT,
    GET_VOLTAGE, GET_TRIGGER, GET_RANGEHOLD, GET_CONSTVOLT,
    GET_INTBIAS, GET_EXTBIAS, GET_NOMVAL, GET_AVERAGE};
PARAMS = {SPEED, DISPLAY, MODE, CIRCUIT, VOLTAGE, TRIGGER, RANGEHOLD
    , CONSTVOLT, INTBIAS, EXTBIAS, NOMVAL, AVERAGE};
for j=1:length(GET_PARAMS);
    GET_PARAM = GET_PARAMS{j};
    PARAM = PARAMS{j};
    param = LCR800_GETPARAMS(s, t1, GET_PARAM, PARAM);
    params = strcat(params, '#', param, '\n');
end

% FREQUENCIES
freqs = {Hz100000, Hz050000, Hz020000, Hz010000, Hz005000, Hz003000,
     Hz002000, Hz001000, Hz000500, Hz000300, Hz000200, Hz000100};

% CREATE DATA MATRIX
Z_matrix = zeros(length(freqs),n+1);
Phi_matrix = zeros(length(freqs),n+1);

for k=1:n
    % LOOP THROUGH FREQUENCIES
    display(strcat('Measurement n=', int2str(k), ' running...'));
    for j=1:length(freqs)
        % LCR800 SET FREQUENCY
        FREQ = freqs{j};
        freq = LCR800_SETFREQ(s, t1, MAINFREQ, FREQ, END, FREQUENCY)
            ;
        Z_matrix(j,1) = str2double(freq(10:length(freq)));
        Phi_matrix(j,1) = str2double(freq(10:length(freq)));

        %START MEASUREMENT
        [Z, phi] = LCR800_START(s, t1, START, IMPEDANCE, PHASE);
        if exist(phi(17)) == 1 && phi(17) == 'k';
            phix = str2double(phi(10:16));
            zx = str2double(Z(10:length(Z)));
        else
            phix = str2double(phi(10:16));
            zx = str2double(Z(10:length(Z)))/1000;
        end
        Z_matrix(j,k+1) = zx;
```

```
        Phi_matrix(j,k+1) = phix;
    end
end

% LCR800 GO OFFLINE
LCR800_GOOFFLINE(s, t1, GOOFFLINE, OFFLINE);
display('LCR800 is OFFLINE');

fclose(s);
delete(s);
clear('s');

% GENERATE OUTPUT
display('processing data output...')
LCR800_GENOUTPUT(params, Z_matrix, Phi_matrix);

clear;
```

Listing B.2: LCR800_COMMANDS.m

```
%COMMAND FILE

%Send
GOOFFLINE = ['43H'; '4FH'; '4DH'; '55H'; '3AH'; '4FH'; '46H'; '46H';↩
      '2eH'; '0AH'; '0DH'];
GOONLINE = ['43H'; '4FH'; '4DH'; '55H'; '3FH'; '0AH'; '0DH'];
START = ['4DH'; '41H'; '49H'; '4EH'; '3AH'; '53H'; '54H'; '41H'; '52↩
    H'; '0AH'; '0DH'];

%Command structure to set the frequency: MAINFREQ + FREQ + END
MAINFREQ = ['4DH'; '41H'; '49H'; '4EH'; '3AH'; '46H'; '52H'; '45H'; ↩
     '51H'; '20H'];
Hz100000 = ['31H'; '30H'; '30H'; '2EH'; '30H'; '30H'; '30H'];
Hz050000 = ['30H'; '35H'; '30H'; '2EH'; '30H'; '30H'; '30H'];
Hz020000 = ['30H'; '32H'; '30H'; '2EH'; '30H'; '30H'; '30H'];
Hz010000 = ['30H'; '31H'; '30H'; '2EH'; '30H'; '30H'; '30H'];
Hz005000 = ['30H'; '30H'; '35H'; '2EH'; '30H'; '30H'; '30H'];
Hz003000 = ['30H'; '30H'; '33H'; '2EH'; '30H'; '30H'; '30H'];
Hz002000 = ['30H'; '30H'; '32H'; '2EH'; '30H'; '30H'; '30H'];
Hz001000 = ['30H'; '30H'; '31H'; '2EH'; '30H'; '30H'; '30H'];
Hz000500 = ['30H'; '30H'; '30H'; '2EH'; '35H'; '30H'; '30H'];
Hz000300 = ['30H'; '30H'; '30H'; '2EH'; '33H'; '30H'; '30H'];
Hz000200 = ['30H'; '30H'; '30H'; '2EH'; '32H'; '30H'; '30H'];
Hz000100 = ['30H'; '30H'; '30H'; '2EH'; '31H'; '30H'; '30H'];
END = ['0AH'; '0DH'];

GET_SPEED =      ['4DH'; '41H'; '49H'; '4EH'; '3AH'; '53H'; '50H'; '↩
     45H'; '45H'; '3FH'; '0AH'; '0DH'];
GET_DISPLAY =    ['4DH'; '41H'; '49H'; '4EH'; '3AH'; '44H'; '49H'; '↩
     53H'; '50H'; '3FH'; '0AH'; '0DH'];
GET_MODE =       ['4DH'; '41H'; '49H'; '4EH'; '3AH'; '4DH'; '4FH'; '↩
     44H'; '45H'; '3FH'; '0AH'; '0DH'];
GET_CIRCUIT =    ['4DH'; '41H'; '49H'; '4EH'; '3AH'; '43H'; '49H'; '↩
     52H'; '43H'; '3FH'; '0AH'; '0DH'];
GET_VOLTAGE =    ['4DH'; '41H'; '49H'; '4EH'; '3AH'; '56H'; '4FH'; '4↩
    CH'; '54H'; '3FH'; '0AH'; '0DH'];
GET_TRIGGER =    ['4DH'; '41H'; '49H'; '4EH'; '3AH'; '54H'; '52H'; '↩
     49H'; '47H'; '3FH'; '0AH'; '0DH'];
GET_RANGEHOLD = ['4DH'; '41H'; '49H'; '4EH'; '3AH'; '52H'; '2EH'; '↩
     48H'; '2EH'; '3FH'; '0AH'; '0DH'];
GET_CONSTVOLT = ['4DH'; '41H'; '49H'; '4EH'; '3AH'; '43H'; '2EH'; '↩
     56H'; '2EH'; '3FH'; '0AH'; '0DH'];
GET_INTBIAS =    ['4DH'; '41H'; '49H'; '4EH'; '3AH'; '49H'; '4EH'; '↩
     54H'; '42H'; '3FH'; '0AH'; '0DH'];
```

```
GET_EXTBIAS =   ['4DH'; '41H'; '49H'; '4EH'; '3AH'; '45H'; '58H'; '↩
    54H'; '42H'; '3FH'; '0AH'; '0DH'];
GET_NOMVAL =    ['53H'; '4FH'; '52H'; '54H'; '3AH'; '4EH'; '4FH'; '4↩
    DH'; '56H'; '3FH'; '0AH'; '0DH'];
GET_AVERAGE =   ['53H'; '54H'; '45H'; '50H'; '3AH'; '41H'; '56H'; '↩
    45H'; '52H'; '3FH'; '0AH'; '0DH'];

%Receive
ONLINE = 'COMU:ON..';
OFFLINE = 'COMU:OFF.';
IMPEDANCE = 'MAIN:PRIM';
PHASE = 'MAIN:SECO';
FREQUENCY = 'MAIN:FREQ';

SPEED = 'MAIN:SPEE';
DISPLAY = 'MAIN:DISP';
MODE = 'MAIN:MODE';
CIRCUIT = 'MAIN:CIRC';
VOLTAGE = 'MAIN:VOLT';
TRIGGER = 'MAIN:TRIG';
RANGEHOLD = 'MAIN:R.H.';
CONSTVOLT = 'MAIN:C.V.';
INTBIAS = 'MAIN:INTB';
EXTBIAS = 'MAIN:EXTB';
NOMVAL = 'SORT:NOMV';
AVERAGE = 'STEP:AVER';
```

Listing B.3: LCR800_GOONLINE.m

```
function [] = LCR800_GOONLINE(s, t1, GOONLINE, ONLINE)

for i=1:length(GOONLINE);
    fwrite(s,int16(sscanf(GOONLINE(i,:),'%x')));
end
wait(t1);
idn = fscanf(s);

l = length(ONLINE);
if idn(1:l) == ONLINE(1:l);
else
    LCR800_GOONLINE(s, t1, GOONLINE, ONLINE);
end
```

Listing B.4: LCR800_GOOFFLINE.m

```
function [idn] = LCR800_GOOFFLINE(s, t1, GOOFFLINE, OFFLINE)
%GOOFFLINE = ['43H'; '4FH'; '4DH'; '55H'; '3AH'; '4FH'; '46H'; '46H↩
    '; '2EH'; '0AH'; '0DH'];
for i=1:length(GOOFFLINE);
    fwrite(s,int16(sscanf(GOOFFLINE(i,:),'%x')));
end
idn = fscanf(s);

l = 0;
if length(idn) == l;
else
    LCR800_GOOFFLINE(s, t1, GOOFFLINE, OFFLINE);
end
```

Listing B.5: LCR800_SETPARAMS.m

```
function [] = LCR800_SETPARAMS(s, t1, SET_PARAM, PARAM)

for i=1:length(SET_PARAM);
fwrite(s,int16(sscanf(SET_PARAM(i,:),'%x')));
end
wait(t1);
idn = fscanf(s);

l = length(PARAM);
if length(idn) >= l && sum(eq(idn(1:l),PARAM(1:l))) == l;
%display(idn);
else
display('trying to get a value');
LCR800_SETPARAMS(s, t1, SET_PARAM, PARAM)
end
```

Listing B.6: LCR800_GETPARAMS.m

```
function [param] = LCR800_GETPARAMS(s, t1, GET_PARAM, PARAM)

for i=1:length(GET_PARAM);
fwrite(s,int16(sscanf(GET_PARAM(i,:),'%x')));
end
wait(t1);
idn = fscanf(s);

l = length(PARAM);
if length(idn) >= l && sum(eq(idn(1:l),PARAM(1:l))) == l;
%display(idn);
else
param = LCR800_GETPARAMS(s, t1, GET_PARAM, PARAM);
end

param = idn;
```

Listing B.7: LCR800_SETFREQ.m

```
function [freq] = LCR800_SETFREQ(s, t1, MAINFREQ, FREQ, END, ↩
    FREQUENCY)

for i=1:length(MAINFREQ);
    fwrite(s,int16(sscanf(MAINFREQ(i,:),'%x')));
end
for i=1:length(FREQ);
    fwrite(s,int16(sscanf(FREQ(i,:),'%x')));
end
for i=1:length(END)-1;
    fwrite(s,int16(sscanf(END(i,:),'%x')));
end
wait(t1);
idn = fscanf(s);

l = length(FREQUENCY);
if length(idn) >= l && sum(eq(idn(1:l),FREQUENCY(1:l))) == l;
else
    LCR800_SETFREQ(s, t1, MAINFREQ, FREQ, END, FREQUENCY);
end

freq = idn;
```

Listing B.8: LCR800_START.m

```
function [Z, phi] = LCR800_START(s, t1, START, IMPEDANCE, PHASE)
%START = ['4DH'; '41H'; '49H'; '4EH'; '3AH'; '53H'; '54H'; '41H'; '52H'; '0AH'; '0DH'];
for i=1:length(START);
    fwrite(s,int16(sscanf(START(i,:),'%x')));
end

idn = LCR800_READVAL(s, t1);

l = length(IMPEDANCE);
if length(idn) >= l && sum(eq(idn(1:l),IMPEDANCE)) == l;
    Z = idn;
    %display('got impedance value');
    %display(idn)
    %display(PHASE)
    wait(t1);
    phi = LCR800_GETSECOVAL(s, t1, START, PHASE);

else
    [Z, phi] = LCR800_START(s, t1, START, IMPEDANCE, PHASE);
    %display('waiting for impedance value');
end
```

Listing B.9: LCR800_READVAL.m

```
function [idn] = LCR800_READVAL(s, t1)
    wait(t1);
    idn = fscanf(s);
```

Listing B.10: LCR800_GETSECOVAL.m

```
function [phi] = LCR800_GETSECOVAL(s, t1, START, PHASE)
wait(t1);
idn = fscanf(s);

l = length(PHASE);
if length(idn) >= l && sum(eq(idn(1:l),PHASE)) == l;
    phi = idn;
    %display('got phi value');
else
    %display('waiting for phi value');
    phi = LCR800_GETSECOVAL(s, t1, START, PHASE);

end
```

Listing B.11: LCR800_GENOUTPUT.m

```
function [] = LCR800_GENOUTPUT(params, Z_matrix, Phi_matrix)

time = datestr(clock);
timestamp = strcat(time(1:11), '_', time(12:14), time(16:17), time(19:20));
filename = strcat(pwd,'\LCR800_results\','LCR800_', timestamp,'.txt');
dirname = strcat(pwd,'\LCR800_results');

%check if results subfolder exists. If not, create it.
if exist(dirname) == 7;
```

```
else
    mkdir(dirname);
end

out = fopen(filename, 'w');
fprintf(out, '#Measurement parameter: \n');
fprintf(out, params);
fprintf(out, '\n#Measurement results: \n');
fprintf(out, ' #Frequencies, Impedance Z in kOhm \n');

for i=1:size(Z_matrix,1)
   line = Z_matrix(i,:);
   for a=1:length(line);
    fprintf(out, '%f', line(a));
    fprintf(out, ' ');
   end
   fprintf(out, '\n');
end

fprintf(out, '\n #Frequencies, Phase angle Phi in degree (n) \n');
for i=1:size(Phi_matrix,1)
    line = Phi_matrix(i,:);
    for a=1:length(line)
        fprintf(out, '%f', line(a));
        fprintf(out, ' ');
   end
   fprintf(out, '\n');
end

fclose(out);
```

C

TDT EXPORT

TDT Export only works on *Windows PCs* with ActiveX. The TDT Harware needs to be switched on. Then, the TTank Monitor from the Sys3 Software package must be used to open and the data tanks that are to be exported. The function *defineVars()* is used to set a bunch of variables (see Listing C.1). The *'stores'* variable sets the type of data that is exported. 'NoFi', specifying the unfiltered data was used for all experiments. From the MATLAB command line, *exportTDTtoMat(tankname, projectname)* (see Listing C.2) is called to export the unfiltered wavetrain data for each recorded block into a single *.mat file*, named like the block in the *DataTank*. The *exportTDTtoMat* function calls the function *getTankParams(tankname, projectname)* to find the names of all data *Blocks* (see Listing C.3). Also, the function *saveChannel(channel, TTX, store, filename)* is called, which saves each channel, recorded in a block into a *.mat* file (see Listing C.4). The file will contain a variable *'samplerate'*, as well as variables *'wavearray_ch1', ..., 'wavearray_chn'* which contain the recorded wavetrain data for all channels.

Listing C.1: defineVars.m

```
function [path, stores] = defineVars()

    path = 'E:\TDTprojects';
    stores = 'NoFi';
```

Listing C.2: exportTDTtoMat.m

```
function [] = exportTDTtoMat(tankname, projectname)[project, tank, ↩
    blocks, stores, matfilepath] = getTankParams(tankname, ↩
    projectname);
%create active X control object
    TTX = actxcontrol('TTank.X');

% Then connect to a server
    s1_connected = TTX.ConnectServer('Local', 'Me');
    if s1_connected == 1
        display('connected to local activeX Server')
    else
        display('connection to local activeX Server refused')
        return
    end

% open tank for reading
    s2_open = TTX.OpenTank(tank, 'R');

    if s2_open == 1
        display(['DataTank ' tank ' open'])
    else
        display(['DataTank ' tank ' not found'])
        return
    end

    if exist(matfilepath) == 0
        mkdir(matfilepath);
    else
        content = dir(matfilepath);
        size = 0;
        for c = 1:length(content)
            if content(c).bytes > 200
```

```
                size = size + 1;
            else
                size = size + 0;
            end
        end

        if size >= length(content)-2
            display(['DataTank ' tank ' has already been fully ↩
                exported'])
            return
        else
            display(['an error occured for DataTank ' tank ' trying ↩
                again'])
        end
    end

% Select the block to access
    for a = 1:length(cellstr(blocks))
        block = blocks(a,:);
        split = strfind(block, '\');
        split = split(end);
        block = block(split+1:end);

        s3_blockfound = TTX.SelectBlock(block);

        if s2_open == 1
        else
            display(['Block ' tank ' not found'])
            return
        end

        if length(cellstr(stores)) == 1
            store = stores;
            display(['exporting block: ' block ', event: ' store]);

            %filename
            filename = strcat(matfilepath, '\', block,'_',store,'.↩
                mat');

            %getting some waveform data to extract sampling ↩
                frequency
            Nrecs=TTX.ReadEventsV(1000,store,0,0,0,10,'ALL');

            %get sampling frequency
            samplerate = TTX.ParseEvInfoV(0, 0, 9);
            %get channel number
            channels = TTX.ParseEvInfoV(0, 0, 4);
            %save sample frequency to mat file
            save(filename, 'samplerate');

            for i = 1:channels
                channel = int2str(i);
                saveChannel(channel, TTX, store, filename)
            end
        else
            for b = 1:length(stores)
                %select the event to read
                store = stores(b,:);
                display(['exporting block: ' block ', event: ' store↩
                    ]);

                %specifiying the filename
                filename = strcat(matfilepath, '\', block,'_',store,↩
                    '.mat')
```

```
                %getting some waveform data to extract sampling ↩
                    frequency
                Nrecs=TTX.ReadEventsV(1000,store,0,0,0,10,'ALL');

                %get sampling frequency
                samplerate = TTX.ParseEvInfoV(0, 0, 9);
                channelnum = TTX.ParseEvInfo(0, 0, 4)

                %save sample frequency to mat file
                save(filename, 'samplerate');


                    for i = 1:channels
                        saveChannel(channel, TTX, store, filename)
                    end
            end
        end
     end

    TTX.CloseTank();
    TTX.ReleaseServer();
```

Listing C.3: getTankParams.m

```
function [project, tank, blocks, stores, matfilepath] = ↩
    getTankParams(tankname, projectname)

    [path, stores] = defineVars();

    projects = dir(path);
    for i=3:length(projects)
        if strcmp(char(projects(i).name), projectname) == 1

            project = projectname;
        end
    end

    if exist('project', 'var') == 0
        project = 'undefined';
    end

    datatanks = dir(strcat(path, '\', project, '\', 'DataTanks'));
    for i=3:length(datatanks)
        if strcmp(char(datatanks(i).name), tankname) == 1
            tank = tankname;
        end
    end

    if exist('tank', 'var') == 0
        tank = 'undefined';
    end

    blocks = [];
    blockdirs = dir(strcat(path, '\', project, '\', 'DataTanks', '\'↩
        , tank));
    for i=3:length(blockdirs)
        b = strcat(path, '\', project, '\', 'DataTanks', '\', tank, ↩
            '\', char(blockdirs(i).name));
        s = dir(b);
        if exist(b, 'dir') && length(s) > 2 && strcmp(char(s(3).name↩
            (end-3:end)), '.Tbk') == 1
            blocks = [blocks; b];
        end
    end
```

```
    matfilepath = strcat(path, '\', project, '\', 'Matfiles', '\', ↩
        tank);
```

Listing C.4: saveChannel.m

```
function [] = saveChannel(channel, TTX, store, filename)
        %select one channel after another for all channels recorded
        TTX.SetGlobals(strcat('Channel=', channel));

        %retrieves the data for current block and current event, but
        %maximal 32 MB (for this one channel), different variables ↩
            for
        %each channel to append to mat file

        if strcmp(channel, '1') == 1
            wavearray_ch1 = TTX.ReadWavesV(store);
            save(filename, '-append', 'wavearray_ch1');

        elseif strcmp(channel, '2') == 1
            wavearray_ch2 = TTX.ReadWavesV(store);
            save(filename, '-append', 'wavearray_ch2');

        elseif strcmp(channel, '3') == 1
            wavearray_ch3 = TTX.ReadWavesV(store);
            save(filename, '-append', 'wavearray_ch3');

        elseif strcmp(channel, '4') == 1
            wavearray_ch4 = TTX.ReadWavesV(store);
            save(filename, '-append', 'wavearray_ch4');

        elseif strcmp(channel, '5') == 1
            wavearray_ch5 = TTX.ReadWavesV(store);
            save(filename, '-append', 'wavearray_ch5');

        elseif strcmp(channel, '6') == 1
            wavearray_ch6 = TTX.ReadWavesV(store);
            save(filename, '-append', 'wavearray_ch6');

        elseif strcmp(channel, '7') == 1
            wavearray_ch7 = TTX.ReadWavesV(store);
            save(filename, '-append', 'wavearray_ch7');

        elseif strcmp(channel, '8') == 1
            wavearray_ch8 = TTX.ReadWavesV(store);
            save(filename, '-append', 'wavearray_ch8');

        elseif strcmp(channel, '9') == 1
            wavearray_ch9 = TTX.ReadWavesV(store);
            save(filename, '-append', 'wavearray_ch9');

        elseif strcmp(channel, '10') == 1
            wavearray_ch10 = TTX.ReadWavesV(store);
            save(filename, '-append', 'wavearray_ch10');
        elseif strcmp(channel, '11') == 1
            wavearray_ch11 = TTX.ReadWavesV(store);
            save(filename, '-append', 'wavearray_ch11');

        elseif strcmp(channel, '12') == 1
            wavearray_ch12 = TTX.ReadWavesV(store);
            save(filename, '-append', 'wavearray_ch12');

        elseif strcmp(channel, '13') == 1
            wavearray_ch13 = TTX.ReadWavesV(store);
            save(filename, '-append', 'wavearray_ch13');
```

```
elseif strcmp(channel, '14') == 1
    wavearray_ch14 = TTX.ReadWavesV(store);
    save(filename, '-append', 'wavearray_ch14');

elseif strcmp(channel, '15') == 1
    wavearray_ch15 = TTX.ReadWavesV(store);
    save(filename, '-append', 'wavearray_ch15');

elseif strcmp(channel, '16') == 1
    wavearray_ch16 = TTX.ReadWavesV(store);
    save(filename, '-append', 'wavearray_ch16');
end
```

D

DATA PROCESSING

Experiments were grouped into eight groups, with five subgroups each for *high frequency microstimulation* with current amplitudes of 0.0, 0.1, 0.2, 0.3 and 0.4 mA (see Listing D.1)

Listing D.1: groupdict.py

```
groupdict = {

'Stiff_Apo_Sham':
(('NiotrodeChronic240910d', (('01', '02', '03', '04', '05', '06', '↩
    07', '08', '09'))),
('NiotrodeChronic240910d', (('01', '02', '03', '04', '05', '06', '07↩
    ', '08', '09')))),

'Stiff_Apo_Lesioned':
(('NiotrodeChronic270910', (('01', '02', '03', '04', '05', '06', '07↩
    ', '08', '09'))),
('NiotrodeChronic240910c', (('01', '02', '03', '04', '05', '06', '07↩
    ', '08', '09')))),

'Flex_Apo_Sham':
(('NiotrodeChronic270910c', (('01', '02', '03', '04', '05', '06', '↩
    07', '08', '09'))),
('NiotrodeChronic270910c', (('01', '02', '03', '04', '05', '06', '07↩
    ', '08', '09')))),

'Flex_Apo_Lesioned':
(('NiotrodeChronic270910a', (('01', '02', '03', '04', '05', '06', '↩
    07', '08', '09'))),
('NiotrodeChronic270910b', (('01', '02', '03', '04', '05', '06', '07↩
    ', '08', '09'))),
('NiotrodeChronic270910d', (('01', '02', '03', '04', '05', '06', '07↩
    ', '08', '09')))),

'Stiff_Sham_NaCl_0.0mA':
(('NiotrodeChronic270810', (('03', '04', '05'), ('06', '07', '08'), ↩
    ('11', '12', '13'), ('18', '19', '20'), ('27', '28', '29'))),
('NiotrodeChronic020910a', (('03', '04', '05'), ('06', '07', '08'), ↩
    ('11', '12', '13'), ('18', '19', '20'), ('27', '28', '29'))),
('NiotrodeChronic300810', (('03', '04', '05'), ('06', '07', '08'), (↩
    '11', '12', '13'), ('18', '19', '20'), ('27', '28', '29'))),
('NiotrodeChronic210910a', (('02', '03', '04'), ('05', '06', '07')))↩
    ,
('NiotrodeChronic300810b' , (('02', '03', '04'), ('05', '06', '07'))↩
    ),
('NiotrodeChronic030910a', (('02', '03', '04'), ('05', '06', '07')))↩
    ),

'Flex_Sham_NaCl_0.0mA':
(('NiotrodeChronic080910a', (('03', '04', '05'), ('06', '07', '08'),↩
     ('11', '12', '13'), ('18', '19', '20'), ('27', '28', '29'))),
('NiotrodeChronic160910a', (('03', '04', '05'), ('06', '07', '08'), ↩
    ('11', '12', '13'), ('18', '19', '20'), ('27', '28', '29'))),
('NiotrodeChronic230910a', (('02', '03', '04'), ('05', '06', '07')))↩
    ,
('NiotrodeChronic170910', (('02', '03', '04'), ('05', '06', '07'))),
('NiotrodeChronic130910d', (('02', '03', '04'), ('05', '06', '07')))↩
    ),

'Stiff_Lesioned_NaCl_0.0mA':
(('NiotrodeChronic260810', (('03', '04', '05'), ('06', '07', '08'), ↩
    ('11', '12', '13'), ('18', '19', '20'), ('27', '28', '29'))),
('NiotrodeChronic210910b', (('02', '03', '04'), ('05', '06', '07')))↩
    ,
```

```
('NiotrodeChronic030910', (('02', '03', '04'), ('05', '06', '07'))),
('NiotrodeChronic020910', (('02', '03', '04'), ('05', '06', '07'))),
('NiotrodeChronic210910', (('02', '03', '04'), ('05', '06', '07'))),
('NiotrodeChronic270810c', (('02', '03', '04'), ('05', '06', '07')))
    ),

'Flex_Lesioned_NaCl_0.0mA':
(('NiotrodeChronic090910', (('03', '04', '05'), ('06', '07', '08'),
    ('11', '12', '13'), ('18', '19', '20'), ('27', '28', '29'))),
('NiotrodeChronic140910', (('03', '04', '05'), ('06', '07', '08'), (
    '11', '12', '13'), ('18', '19', '20'), ('27', '28', '29'))),
('NiotrodeChronic160910b', (('03', '04', '05'), ('06', '07', '08'),
    ('11', '12', '13'), ('18', '19', '20'), ('27', '28', '29'))),
('NiotrodeChronic210910c', (('02', '03', '04'), ('05', '06', '07')))
    ,
('NiotrodeChronic130910c', (('02', '03', '04'), ('05', '06', '07')))
    ,
('NiotrodeChronic230910', (('02', '03', '04'), ('05', '06', '07'))),
('NiotrodeChronic160910', (('02', '03', '04'), ('05', '06', '07'))),
('NiotrodeChronic230910b', (('02', '03', '04'), ('05', '06', '07')))
    ,
('NiotrodeChronic170910a', (('02', '03', '04'), ('05', '06', '07')))
    ),

'Stiff_Sham_QP_0.0mA':
(('NiotrodeChronic220910a', (('02', '03', '04'), ('05', '06', '07'))
    ),
('NiotrodeChronic020910d', (('02', '03', '04'), ('05', '06', '07')))
    ,
('NiotrodeChronic060910a', (('02', '03', '04'), ('05', '06', '07')))
    ),

'Flex_Sham_QP_0.0mA':
(('NiotrodeChronic240910a', (('02', '03', '04'), ('05', '06', '07'))
    ),
('NiotrodeChronic200910', (('02', '03', '04'), ('05', '06', '07'))),
('NiotrodeChronic140910c', (('02', '03', '04'), ('05', '06', '07')))
    ),

'Stiff_Lesioned_QP_0.0mA':
(('NiotrodeChronic220910b', (('02', '03', '04'), ('05', '06', '07'))
    ),
('NiotrodeChronic060910', (('02', '03', '04'), ('05', '06', '07'))),
('NiotrodeChronic220910', (('02', '03', '04'), ('05', '06', '07'))),
('NiotrodeChronic300810c', (('02', '03', '04'), ('05', '06', '07')))
    ),

'Flex_Lesioned_QP_0.0mA':
(('NiotrodeChronic220910c', (('02', '03', '04'), ('05', '06', '07'))
    ),
('NiotrodeChronic140910c', (('02', '03', '04'), ('05', '06', '07')))
    ,
('NiotrodeChronic240910', (('02', '03', '04'), ('05', '06', '07'))),
('NiotrodeChronic170910b', (('02', '03', '04'), ('05', '06', '07')))
    ,
('NiotrodeChronic240910b', (('02', '03', '04'), ('05', '06', '07')))
    ,
('NiotrodeChronic200910', (('02', '03', '04'), ('05', '06', '07'))))
    ,

'Stiff_Sham_NaCl_0.1mA':
(('NiotrodeChronic260810a', (('03', '04', '05'), ('06', '07', '08'),
     ('11', '12', '13'), ('18', '19', '20'), ('27', '28', '29'))),
('NiotrodeChronic300810', (('03', '04', '05'), ('06', '07', '08'), (
    '11', '12', '13'), ('18', '19', '20'), ('27', '28', '29'))),
('NiotrodeChronic210910a', (('11', '12', '13'))),
```

```
('NiotrodeChronic300810b', (('11', '12', '13'))),
('NiotrodeChronic030910a', (('11', '12', '13')))),

'Flex_Sham_NaCl_0.1mA':
(('NiotrodeChronic080910c', (('03', '04', '05'), ('06', '07', '08'),↩
     ('11', '12', '13'), ('18', '19', '20'), ('27', '28', '29'))),
('NiotrodeChronic230910a', (('11', '12', '13'))),
('NiotrodeChronic170910', (('11', '12', '13'))),
('NiotrodeChronic130910d', (('11', '12', '13')))),

'Stiff_Lesioned_NaCl_0.1mA':
(('NiotrodeChronic270810a', (('03', '04', '05'), ('06', '07', '08'),↩
     ('11', '12', '13'), ('18', '19', '20'), ('27', '28', '29'))),
('NiotrodeChronic250810', (('03', '04', '05'), ('06', '07', '08'), (↩
    '11', '12', '13'), ('18', '19', '20'), ('27', '28', '29'))),
('NiotrodeChronic210910b', (('11', '12', '13'))),
('NiotrodeChronic030910', (('11', '12', '13'))),
('NiotrodeChronic020910', (('11', '12', '13'))),
('NiotrodeChronic210910', (('11', '12', '13'))),
('NiotrodeChronic270810c', (('11', '12', '13')))),


'Flex_Lesioned_NaCl_0.1mA':
(('NiotrodeChronic070910', (('03', '04', '05'), ('06', '07', '08'), ↩
    ('11', '12', '13'), ('18', '19', '20'), ('27', '28', '29'))),
('NiotrodeChronic070910a', (('03', '04', '05'), ('06', '07', '08'), ↩
    ('11', '12', '13'), ('18', '19', '20'), ('27', '28', '29'))),
('NiotrodeChronic080910d', (('03', '04', '05'), ('06', '07', '08'), ↩
    ('11', '12', '13'), ('18', '19', '20'), ('27', '28', '29'))),
('NiotrodeChronic210910c', (('11', '12', '13'))),
('NiotrodeChronic130910c', (('11', '12', '13'))),
('NiotrodeChronic230910', (('11', '12', '13'))),
('NiotrodeChronic160910', (('11', '12', '13'))),
('NiotrodeChronic230910b', (('11', '12', '13'))),
('NiotrodeChronic170910a', (('11', '12', '13')))),

'Stiff_Sham_QP_0.1mA':
(('NiotrodeChronic220910a', (('11', '12', '13'))),
('NiotrodeChronic020910d', (('11', '12', '13'))),
('NiotrodeChronic060910a', (('11', '12', '13')))),

'Flex_Sham_QP_0.1mA':
(('NiotrodeChronic240910a', (('11', '12', '13'))),
('NiotrodeChronic200910', (('11', '12', '13'))),
('NiotrodeChronic140910c', (('11', '12', '13')))),

'Stiff_Lesioned_QP_0.1mA':
(('NiotrodeChronic220910b', (('11', '12', '13'))),
('NiotrodeChronic060910', (('11', '12', '13'))),
('NiotrodeChronic220910', (('11', '12', '13'))),
('NiotrodeChronic300810c', (('11', '12', '13')))),

'Flex_Lesioned_QP_0.1mA':
(('NiotrodeChronic220910c', (('11', '12', '13'))),
('NiotrodeChronic240910', (('11', '12', '13'))),
('NiotrodeChronic170910b', (('11', '12', '13'))),
('NiotrodeChronic240910b', (('11', '12', '13')))),
#('NiotrodeChronic140910c', (('11', '12', '13'))),
#('NiotrodeChronic200910', (('11', '12', '13')))),

'Stiff_Sham_NaCl_0.2mA':
(('NiotrodeChronic250810a', (('03', '04', '05'), ('06', '07', '08'),↩
     ('11', '12', '13'), ('18', '19', '20'), ('27', '28', '29'))),
('NiotrodeChronic270810b', (('03', '04', '05'), ('06', '07', '08'), ↩
    ('11', '12', '13'), ('18', '19', '20'), ('27', '28', '29'))),
('NiotrodeChronic210910a', (('17', '18', '19'))),
```

```
('NiotrodeChronic300810b', (('17', '18', '19'))),
('NiotrodeChronic030910a', (('17', '18', '19')))),

'Flex_Sham_NaCl_0.2mA':
(('NiotrodeChronic030910c', (('03', '04', '05'), ('06', '07', '08'),↩
     ('11', '12', '13'), ('18', '19', '20'), ('27', '28', '29'))),
('NiotrodeChronic230910a', (('17', '18', '19'))),
('NiotrodeChronic170910', (('17', '18', '19'))),
('NiotrodeChronic130910d', (('17', '18', '19')))),

'Stiff_Lesioned_NaCl_0.2mA':
(('NiotrodeChronic260810b', (('03', '04', '05'), ('06', '07', '08'),↩
     ('11', '12', '13'), ('18', '19', '20'), ('27', '28', '29'))),
('NiotrodeChronic240810', (('03', '04', '05'), ('06', '07', '08'), (↩
    '11', '12', '13'), ('18', '19', '20'), ('27', '28', '29'))),
('NiotrodeChronic210910b', (('17', '18', '19'))),
('NiotrodeChronic030910', (('17', '18', '19'))),
('NiotrodeChronic020910', (('17', '18', '19'))),
('NiotrodeChronic210910', (('17', '18', '19'))),
('NiotrodeChronic270810c', (('17', '18', '19')))),

'Flex_Lesioned_NaCl_0.2mA':
(('NiotrodeChronic030910d', (('03', '04', '05'), ('06', '07', '08'),↩
     ('11', '12', '13'), ('18', '19', '20'), ('27', '28', '29'))),
('NiotrodeChronic030910b', (('03', '04', '05'), ('06', '07', '08'), ↩
    ('11', '12', '13'), ('18', '19', '20'), ('27', '28', '29'))),
('NiotrodeChronic080910b', (('03', '04', '05'), ('06', '07', '08'), ↩
    ('11', '12', '13'), ('18', '19', '20'), ('27', '28', '29'))),
('NiotrodeChronic090910d', (('03', '04', '05'), ('06', '07', '08'), ↩
    ('11', '12', '13'), ('18', '19', '20'), ('27', '28', '29'))),
('NiotrodeChronic210910c', (('17', '18', '19'))),
('NiotrodeChronic130910c', (('17', '18', '19'))),
('NiotrodeChronic230910', (('17', '18', '19'))),
('NiotrodeChronic160910', (('17', '18', '19'))),
('NiotrodeChronic230910b', (('17', '18', '19'))),
('NiotrodeChronic170910a', (('17', '18', '19')))),


'Stiff_Sham_QP_0.2mA':
(('NiotrodeChronic220910a', (('17', '18', '19'))),
('NiotrodeChronic020910d', (('17', '18', '19'))),
('NiotrodeChronic060910a', (('17', '18', '19')))),

'Stiff_Lesioned_QP_0.2mA':
(('NiotrodeChronic220910b', (('17', '18', '19'))),
('NiotrodeChronic060910', (('17', '18', '19'))),
('NiotrodeChronic220910', (('17', '18', '19'))),
('NiotrodeChronic300810c', (('17', '18', '19')))),

'Flex_Sham_QP_0.2mA':
(('NiotrodeChronic240910a', (('17', '18', '19'))),
('NiotrodeChronic200910', (('17', '18', '19'))),
('NiotrodeChronic140910c', (('17', '18', '19')))),

'Flex_Lesioned_QP_0.2mA':
(('NiotrodeChronic220910c', (('17', '18', '19'))),
('NiotrodeChronic240910', (('17', '18', '19'))),
('NiotrodeChronic170910b', (('17', '18', '19'))),
('NiotrodeChronic240910b', (('17', '18', '19')))),
#('NiotrodeChronic140910c', (('17', '18', '19'))),
#('NiotrodeChronic200910', (('17', '18', '19')))),

'Stiff_Sham_NaCl_0.3mA':
(('NiotrodeChronic230810a', (('03', '04', '05'), ('06', '07', '08'),↩
     ('11', '12', '13'), ('18', '19', '20'), ('27', '28', '29'))),
```

```
('NiotrodeChronic260810c', (('03', '04', '05'), ('06', '07', '08'), ↩
    ('11', '12', '13'), ('18', '19', '20'), ('27', '28', '29'))),
('NiotrodeChronic210910a', (('23', '24', '25'))),
('NiotrodeChronic300810b', (('23', '24', '25'))),
('NiotrodeChronic030910a', (('23', '24', '25')))),

'Flex_Sham_NaCl_0.3mA':
(('NiotrodeChronic060910d', (('03', '04', '05'), ('06', '07', '08'),↩
     ('11', '12', '13'), ('18', '19', '20'), ('27', '28', '29'))),
('NiotrodeChronic130910a', (('03', '04', '05'), ('06', '07', '08'), ↩
    ('11', '12', '13'), ('18', '19', '20'), ('27', '28', '29'))),
('NiotrodeChronic230910a', (('23', '24', '25'))),
('NiotrodeChronic170910', (('23', '24', '25'))),
('NiotrodeChronic130910d', (('23', '24', '25')))),

'Stiff_Lesioned_NaCl_0.3mA':
(('NiotrodeChronic240810b', (('03', '04', '05'), ('06', '07', '08'),↩
     ('11', '12', '13'), ('18', '19', '20'), ('27', '28', '29'))),
('NiotrodeChronic220810', (('03', '04', '05'), ('06', '07', '08'), (↩
    '11', '12', '13'), ('18', '19', '20'), ('27', '28', '29'))),
('NiotrodeChronic210910b', (('23', '24', '25'))),
('NiotrodeChronic030910', (('23', '24', '25'))),
('NiotrodeChronic020910', (('23', '24', '25'))),
('NiotrodeChronic210910', (('23', '24', '25'))),
('NiotrodeChronic270810c', (('23', '24', '25')))),

'Flex_Lesioned_NaCl_0.3mA':
(('NiotrodeChronic060910b', (('03', '04', '05'), ('06', '07', '08'),↩
     ('11', '12', '13'), ('18', '19', '20'), ('27', '28', '29'))),
('NiotrodeChronic060910c', (('03', '04', '05'), ('06', '07', '08'), ↩
    ('11', '12', '13'), ('18', '19', '20'), ('27', '28', '29'))),
('NiotrodeChronic090910b', (('03', '04', '05'), ('06', '07', '08'), ↩
    ('11', '12', '13'), ('18', '19', '20'), ('27', '28', '29'))),
('NiotrodeChronic130910b', (('03', '04', '05'), ('06', '07', '08'), ↩
    ('11', '12', '13'), ('18', '19', '20'), ('27', '28', '29'))),
('NiotrodeChronic210910c', (('23', '24', '25'))),
('NiotrodeChronic130910c', (('23', '24', '25'))),
('NiotrodeChronic230910', (('23', '24', '25'))),
('NiotrodeChronic160910', (('23', '24', '25'))),
('NiotrodeChronic230910b', (('23', '24', '25'))),
('NiotrodeChronic170910a', (('23', '24', '25')))),

'Stiff_Sham_QP_0.3mA':
(('NiotrodeChronic220910a', (('23', '24', '25'))),
('NiotrodeChronic020910d', (('23', '24', '25'))),
('NiotrodeChronic060910a', (('23', '24', '25')))),

'Flex_Sham_QP_0.3mA':
(('NiotrodeChronic240910a', (('23', '24', '25'))),
('NiotrodeChronic200910', (('23', '24', '25'))),
('NiotrodeChronic140910c', (('23', '24', '25')))),

'Stiff_Lesioned_QP_0.3mA':
(('NiotrodeChronic220910b', (('23', '24', '25'))),
('NiotrodeChronic060910', (('23', '24', '25'))),
('NiotrodeChronic220910', (('23', '24', '25'))),
('NiotrodeChronic300810c', (('23', '24', '25')))),

'Flex_Lesioned_QP_0.3mA':
(('NiotrodeChronic220910c', (('23', '24', '25'))),
('NiotrodeChronic240910', (('23', '24', '25'))),
('NiotrodeChronic170910b', (('23', '24', '25'))),
('NiotrodeChronic240910b', (('23', '24', '25')))),
#('NiotrodeChronic140910c', (('23', '24', '25'))),
#('NiotrodeChronic200910', (('23', '24', '25')))),
```

```
'Stiff_Sham_NaCl_0.4mA':
(('NiotrodeChronic210910a', (('29', '30', '31'))),
('NiotrodeChronic300810b', (('29', '30', '31'))),
('NiotrodeChronic030910a', (('29', '30', '31')))),

'Flex_Sham_NaCl_0.4mA':
(('NiotrodeChronic140910a', (('03', '04', '05'), ('06', '07', '08'),↩
     ('11', '12', '13'), ('18', '19', '20'), ('27', '28', '29'))),
('NiotrodeChronic230910a', (('29', '30', '31'))),
('NiotrodeChronic170910', (('29', '30', '31'))),
('NiotrodeChronic130910d', (('29', '30', '31')))),

'Stiff_Lesioned_NaCl_0.4mA':
(('NiotrodeChronic250810b', (('03', '04', '05'), ('06', '07', '08'),↩
     ('11', '12', '13'), ('18', '19', '20'), ('27', '28', '29'))),
('NiotrodeChronic230810', (('03', '04', '05'), ('06', '07', '08'), (↩
    '11', '12', '13'), ('18', '19', '20'), ('27', '28', '29'))),
('NiotrodeChronic210910b', (('29', '30', '31'))),
('NiotrodeChronic030910', (('29', '30', '31'))),
('NiotrodeChronic020910', (('29', '30', '31'))),
('NiotrodeChronic210910', (('29', '30', '31'))),
('NiotrodeChronic270810c', (('29', '30', '31')))),

'Flex_Lesioned_NaCl_0.4mA':
(('NiotrodeChronic080910', (('03', '04', '05'), ('06', '07', '08'), ↩
    ('11', '12', '13'), ('18', '19', '20'), ('27', '28', '29'))),
('NiotrodeChronic130910', (('03', '04', '05'), ('06', '07', '08'), (↩
    '11', '12', '13'), ('18', '19', '20'), ('27', '28', '29'))),
('NiotrodeChronic140910b', (('03', '04', '05'), ('06', '07', '08'), ↩
    ('11', '12', '13'), ('18', '19', '20'), ('27', '28', '29'))),
('NiotrodeChronic210910c', (('29', '30', '31'))),
('NiotrodeChronic130910c', (('29', '30', '31'))),
('NiotrodeChronic230910', (('29', '30', '31'))),
('NiotrodeChronic160910', (('29', '30', '31'))),
('NiotrodeChronic230910b', (('29', '30', '31'))),
('NiotrodeChronic170910a', (('29', '30', '31')))),

'Stiff_Sham_QP_0.4mA':
(('NiotrodeChronic220910a', (('29', '30', '31'))),
('NiotrodeChronic020910d', (('29', '30', '31'))),
('NiotrodeChronic060910a', (('29', '30', '31')))),

'Flex_Sham_QP_0.4mA':
(('NiotrodeChronic240910a', (('29', '30', '31'))),
('NiotrodeChronic200910', (('29', '30', '31'))),
('NiotrodeChronic140910c', (('29', '30', '31')))),

 'Stiff_Lesioned_QP_0.4mA':
(('NiotrodeChronic220910b', (('29', '30', '31'))),
('NiotrodeChronic060910', (('29', '30', '31'))),
('NiotrodeChronic220910', (('29', '30', '31'))),
('NiotrodeChronic300810c', (('29', '30', '31')))),

  'Flex_Lesioned_QP_0.4mA':
(('NiotrodeChronic220910c', (('29', '30', '31'))),
('NiotrodeChronic240910', (('29', '30', '31'))),
('NiotrodeChronic170910b', (('29', '30', '31'))),
('NiotrodeChronic240910b', (('29', '30', '31')))),
#('NiotrodeChronic140910c', (('29', '30', '31')))),
#('NiotrodeChronic200910',  (('29', '30', '31')))),

}
```

The step wise procedure of data analysis is listed in Listing D.2). Wavetrain data were merged to receive continous *wavetrains* with data before, during

and after *high frequency microstimulation* (see functions getmergedwavetraindatafiles(path, groupdict, groupname) in Listing D.4). Then, the stimulation artefact was found using gradient based edge detection Listing D.3, edgedetection(data)), and removed from the unfiltered *wavetrain data*. Statistical parameters were calculated from the wavetrain signal. Also, spike detection and clustering was performed.

Listing D.2: Main.py

```
import getdata
import groupdict

path = '/media/BigBang/NeuroData/NeuroData2/↩
    NiotrodeChronicExperiments'
groupdict = groupdict.groupdict

groupnames = ('Stiff_Sham_NaCl_0.0mA', 'Stiff_Sham_NaCl_0.1mA', '↩
    Stiff_Sham_NaCl_0.2mA', 'Stiff_Sham_NaCl_0.3mA', '↩
    Stiff_Sham_NaCl_0.4mA',
'Stiff_Lesioned_NaCl_0.0mA', 'Stiff_Lesioned_NaCl_0.1mA', '↩
    Stiff_Lesioned_NaCl_0.2mA', 'Stiff_Lesioned_NaCl_0.3mA', '↩
    Stiff_Lesioned_NaCl_0.4mA',
'Stiff_Sham_QP_0.0mA', 'Stiff_Sham_QP_0.1mA', 'Stiff_Sham_QP_0.2mA',↩
     'Stiff_Sham_QP_0.3mA', 'Stiff_Sham_QP_0.4mA',
'Stiff_Lesioned_QP_0.0mA', 'Stiff_Lesioned_QP_0.1mA', '↩
    Stiff_Lesioned_QP_0.2mA', 'Stiff_Lesioned_QP_0.3mA', '↩
    Stiff_Lesioned_QP_0.4mA',
'Flex_Sham_NaCl_0.0mA', 'Flex_Sham_NaCl_0.1mA', 'Flex_Sham_NaCl_0.2↩
    mA', 'Flex_Sham_NaCl_0.3mA', 'Flex_Sham_NaCl_0.4mA',
'Flex_Lesioned_NaCl_0.0mA', 'Flex_Lesioned_NaCl_0.1mA', '↩
    Flex_Lesioned_NaCl_0.2mA', 'Flex_Lesioned_NaCl_0.3mA', '↩
    Flex_Lesioned_NaCl_0.4mA',
'Flex_Sham_QP_0.0mA', 'Flex_Sham_QP_0.1mA', 'Flex_Sham_QP_0.2mA', '↩
    Flex_Sham_QP_0.3mA', 'Flex_Sham_QP_0.4mA',
'Flex_Lesioned_QP_0.0mA', 'Flex_Lesioned_QP_0.1mA', '↩
    Flex_Lesioned_QP_0.2mA', 'Flex_Lesioned_QP_0.3mA', '↩
    Flex_Lesioned_QP_0.4mA')

for groupname in groupnames:
  print(groupname)

  getdata.getmergedwavetraindatafiles(path, groupdict, groupname)
  getdata.getalignedwavetraindata(path, groupdict, groupname)
  getdata.getstatspersecond(path, groupdict, groupname)
  getdata.groupstatsdata(path, groupdict, groupname)
  getdata.exportstatsgroup(path, groupname)
  getdata.getspikedataforgroup(path, groupdict, groupname)
  getdata.groupspikedata(path, groupdict, groupname)
  getdata.rasterplots(path, groupname)
  getdata.plotspikeshapes(path, groupname)
  getdata.getspikeinfo(path, groupname)
  getdata.plotisidistribution(path, groupname)
  getdata.groupspikeinfo(path, groupname)
  getdata.exportspikeinfo(path, groupname)
  getdata.exportspikedata(path, groupname)
```

Listing D.3: Utils.py

```
import numpy
import pylab
import string
```

```
import Pycluster
import scipy.io
import scipy.signal
import scipy.stats
import scipy.fftpack
import os
import glob
import matplotlib.mlab

class Utils():

  def __init__(self, diri):
    self.diri = diri
    self.numnum = 'only needed for neuronav'
    self.channelconfig = {'wavearray_ch1': 1,
    'wavearray_ch2': 2,
      'wavearray_ch3': 3,
      'wavearray_ch4': 4,
      'wavearray_ch5': 5,
      'wavearray_ch6': 6,
      'wavearray_ch7': 7}
    self.wavetraindata = 'wavetraindata'
    self.spikedata = 'spikedata'
    self.results = '/results'
    self.fsample = 24414
    self.cutoff_low = 4000
    self.cutoff_high = 400
    self.offset = 50

    if diri == '':
      pass
    else:
      self.resultpath = diri+self.results
      self.spikepath = self.resultpath+'/spikes'
      self.statspath = self.resultpath+'/statspersecond'
      self.stackedwavetraindatapath = self.resultpath+'/↩
          stackedwavetraindata'
      self.stackedandalignedwavetraindatapath = self.resultpath+'/↩
          stackedandalignedwavetraindata'

      if os.path.exists(self.spikepath) == False:
    os.makedirs(self.spikepath)
      else:
    pass
      if os.path.exists(self.statspath) == False:
    os.makedirs(self.statspath)
      else:
    pass
      if os.path.exists(self.stackedwavetraindatapath) == False:
    os.makedirs(self.stackedwavetraindatapath)
      else:
    pass
      if os.path.exists(self.stackedandalignedwavetraindatapath) == ↩
          False:
    os.makedirs(self.stackedandalignedwavetraindatapath)
      else:
    pass

    self.maxtime = 10000
    self.minspike = 10
    self.filtfactor_ar = 9
    self.filtfactor_sd = 5
    self.filtiv = 64
    self.windowwidth = 244140
    self.colors = ('blue', 'green', 'red', 'cyan', 'magenta', '↩
        purple', 'yellow', 'brown', 'grey', 'black', 'blue', 'green↩
```

```
        ', 'red', 'cyan', 'magenta', 'purple', 'yellow', 'brown', '↩
        grey', 'black')
    self.k = 10
    self.minspike = 10
    self.maxspike = 50000

  def bpfilt(self, data):
    #filter data by butterworth filter order 4
    #set fsample via SpikeUtils.fsample, lower cut off freq via ↩
        SpikeUtils.cutoff_low,
    #high cut off freuquency via SpikeUtils.off_high
    #data: 1D array
    wlowpass = self.cutoff_low/(self.fsample/2.0)
    whighpass = self.cutoff_high/(self.fsample/2.0)

    [b,a] = scipy.signal.butter(4, wlowpass, btype='low', analog=0, ↩
        output='ba')
    lowfiltsig = scipy.signal.filtfilt(b,a,data)

    [b,a] = scipy.signal.butter(4, whighpass, btype='high', analog↩
        =0, output='ba')
    bpfiltsig = scipy.signal.filtfilt(b,a,lowfiltsig)

    return(bpfiltsig)

  def downsample(self, data, cycles):
    #downsample data by factor 2 per cycle
    #data: 1D array
    #cycle: int
    #set fsample via SpikeUtils.fsample
    fsample = self.fsample
    for c in range(cycles):
      data = data[::2]
      fsample = fsample/2
    return(data, fsample)


  def artefactfilter(self, data):
    threshold = self.filtfactor_ar*numpy.median((numpy.abs(data)↩
        /0.6745))
    a = numpy.where(data > threshold)[0]
    b = numpy.where(data < -1*threshold)[0]

    artefacts = numpy.hstack((a,b))
    artefacts = numpy.unique(artefacts)

    if len(artefacts) > 0:
      extendedartefacts = []
      for i in artefacts:
        if i > self.filtiv and i < len(data)-self.filtiv:
          extension = numpy.arange(i-self.filtiv, i+self.filtiv, 1)
        elif i < self.filtiv:
          extension=numpy.arange(0, i+self.filtiv, 1)
        elif i > len(data)-self.filtiv:
          extension=numpy.arange(i+self.filtiv, len(data), 1)
        extendedartefacts.append(extension)
      extendedartefacts = numpy.hstack(extendedartefacts)
      extendedartefacts = numpy.unique(extendedartefacts)

      data[extendedartefacts] = 0

    return(data)

  def findcenter(self, data, center, counter):
    if data[center] == numpy.max(data[center-(self.filtiv/2):(center↩
        +self.filtiv/2)]):
```

```
      return center
    else:
      if counter < 10:
        return self.findcenter(data, center+1, counter + 1)
      else:
        return 'none'

  def spikedetection(self, data):
    t = len(data)/self.fsample
    timeinms = t*1000

    threshold = self.filtfactor_sd*numpy.median((numpy.abs(data)↩
        /0.6745))
    a = numpy.where(data > threshold)[0]
    b = numpy.where(data <  -1*threshold)[0]

    overthreshold = numpy.hstack((a,b))
    overthreshold = numpy.unique(overthreshold)

    spikes = []
    spiketimes = []

    if len(overthreshold) < t*500:
      centers = []
      for i in overthreshold:
    if i > (self.filtiv+10) and i < len(data)-(self.filtiv+10):
      newcenter = self.findcenter(data, i, 0)
      if newcenter == 'none':
        pass
      else:
        centers.append(newcenter)
    else:
      pass

      for center in centers:
    spike = data[(center-self.filtiv/2):center+(self.filtiv/2)]
    if numpy.shape(spike)[0] == 64:
      time = float(center)/float(self.fsample)*1000
      if time < timeinms:
        spikes.append(spike)
        spiketimes.append(time)
      else:
        pass
    else:
      pass

    #print(len(spikes), len(spiketimes), timeinms)
    return(spikes, spiketimes, timeinms)

  def kcluster(self, spikes):
    n = self.k
    print('clustering ' +str(len(spikes))+' spikes')
    try:
      clusterids, error, nfound = Pycluster.kcluster(spikes, n, ↩
          npass=10)
    except ValueError:
      print('ValueError')
      clusterids = [0]
    except TypeError:
      print('TypeError')
      clusterids = [0]

    return(clusterids, n)

  def getmfr(self, spiketimes):
    num = len(spiketimes)
```

```
    if num > 1:
      lastspike = spiketimes[-1]
      mfr = (num*1000.0)/lastspike
    else:
      mfr = 0
    return(mfr)

  def getisis(self, spiketimes):
    isis = []
    for i in range(len(spiketimes)-1):
      isi = spiketimes[i+1]-spiketimes[i]
      isis.append(isi)
    return(isis)

  def getspikeentropy(self, isis):

    X = scipy.linspace(1,100, num=100)
    ns, bins = numpy.histogram(isis, X, normed = 1)
    n = ns[numpy.where(ns>0)]
    h = numpy.divide(numpy.array(n, numpy.float), numpy.sum(n))
    H = -1*(numpy.sum(h*numpy.log2(h)))

    return(H)

  def getdatawindow(self, data):
    if numpy.mod(len(data), self.windowwidth) == 0:
      data = numpy.reshape(data, (-1, self.windowwidth))
    else:
      data = data[0:int(len(data)/float(self.windowwidth))*self.↩
          windowwidth]
      return self.getdatawindow(data)
    rms = numpy.sqrt(float(numpy.sum(numpy.power(data,2)))/float(len↩
        (data)))
    #print(data)
    medians = []
    rmss = []
    for i, row in enumerate(data):
      rms = numpy.sqrt(float(numpy.sum(numpy.power(row,2)))/float(↩
          len(row)))
      rmss.append(rms)
      median = numpy.median(row)
      medians.append(numpy.abs(median))
    median = numpy.min(medians)
    rms = numpy.min(rmss)*1e6
    #print(median)
    #print(rms)
    if rms < 10:
      data = data[numpy.where(medians == median)][0]
    else:
      data = numpy.zeros(self.windowwidth)
    return(data)

  def quickview(self, allchdata, name):
    fig = pylab.figure()
    ax = fig.add_subplot(1,1,1)

    offset = 50
    for i, data in enumerate(allchdata):
      time = numpy.arange(0, len(data)*(1.0/self.fsample), 1.0/self.↩
          fsample)
      ax.plot(time, 1e6*(numpy.array(data))+offset*i, color = 'blue'↩
          )
      ax.set_xlabel('time in s')
      ax.set_title(name)
      ax.set_ylabel('potential in 1e-6 V')
```

```
    fig.savefig(self.quickviewpath+'/'+name+'.png')
    pylab.close()

  def neuronav(self, matfiles, area, dp):
    for key in self.channelconfig.keys():
        if 'wavearray_' in key:
          fig = pylab.figure(figsize=(15,5))
          ax = fig.add_subplot(1,1,1)
          for i, matfile in enumerate(matfiles):
            num = string.split(matfile, '_')[self.numnum]
            matdata = scipy.io.loadmat(matfile)
            data = matdata[key][:, 0]
            data = self.bpfilt(data)
            data = self.artefactfilter(data)
            data = data[0:dp]
            data, fsample = self.downsample(data, 4)
            time = numpy.arange(0, len(data)*(1.0/fsample), 1.0/↩
                fsample)
            ax.plot(time, (1e6*(data))+(self.offset*i), color='blue'↩
                )
            ax.set_title(area)
            ax.set_xlabel('time in s')
            ax.set_ylabel('potential in 1e-6 V')

          if os.path.exists(self.resultpath+'/neuronav') == False:
            os.makedirs(self.resultpath+'/neuronav/')
          channel = self.channelconfig[key]
          channel = 'ch'+str(channel)
          pylab.savefig(self.resultpath+'/neuronav/'+area+'_'+↩
              channel+'.svg')

  def getrms(self, wavetraindata):
    rms = numpy.sqrt(float(numpy.sum(numpy.power(wavetraindata,2)))/↩
        float(len(wavetraindata)))
    rms = rms*1e6
    return(rms)

  def getpsd(self, wavetraindata):
    pxx, freqs = matplotlib.mlab.psd(wavetraindata, 512, self.↩
        fsample)
    pxx = numpy.mean(pxx)

    return(pxx)


  #def getsignalentropy(self, wavetraindata):
    #histogram, bins = numpy.histogram(wavetraindata, bins=100, ↩
        normed = 1)
    #histogram_length = numpy.sum(histogram)
    ##print(histogram_length, len(data))

    #h_is  = []
    #for h in histogram:
      #p_i = float(h) / histogram_length
      #if p_i != 0:
    #h_i = p_i*(numpy.log2(p_i))
    #h_is.append(h_i)
      #else:
    #pass

    #entropy = -1*numpy.sum(h_is)
    ##print(entropy)
    #return(entropy)

  def getsignalentropy(self, wavetraindata):
    num = len(wavetraindata)
```

```
    if num > 0:
      X = scipy.linspace(1,100, num=100)
      ns, bins = numpy.histogram(wavetraindata, X, normed = 1)
      n = ns[numpy.where(ns>0)]
      h = numpy.divide(numpy.array(n, numpy.float), numpy.sum(n))
      H = -1*(numpy.sum(h*numpy.log2(h)))
    else:
      H = 0
    return(H)

  def chunkdata(self, data, chunksizeinsec):
    dp = len(data)
    freq = self.fsample

    exess = numpy.mod(dp, (freq*chunksizeinsec))
    data = data[0:dp-exess]
    splitf = int(len(data)/(freq*chunksizeinsec))

    chunkeddata = numpy.reshape(data, (splitf, -1))

    return(chunkeddata)

  def getstats_persecond(self, matfile):
    matfileout = string.split(matfile, '/')[-1]
    matfileout = string.replace(matfileout, '↩
        stackedandalignedwavetraindata', 'statspersecond')

    if os.path.exists(self.statspath+'/'+matfileout):
      print('stats per second data already exists, skipping stats')
    else:
      print(matfile)
      matdata = scipy.io.loadmat(matfile)
      datadict = {}
      for key in self.channelconfig.keys():
      print(key)
      channel = string.split(key, '_')[-1]
      data = matdata[key][:,0]
      data = self.bpfilt(data)

      rms = []
      psd = []
      entropy = []
      chunkeddata = self.chunkdata(data, 1.0)
      for chunk in chunkeddata:
        rms.append(self.getrms(chunk))
        psd.append(self.getpsd(chunk))
        entropy.append(self.getsignalentropy(chunk))

      #print(len(rms), rms)
      #print(len(psd), psd)
      #print(len(entropy), entropy)
      datadict['rms_'+channel] = rms
      datadict['psd_'+channel] = psd
      datadict['entropy_'+channel] = entropy

      print('saving '+self.statspath+'/'+matfileout)
      scipy.io.savemat(self.statspath+'/'+matfileout, datadict)

  def mergewavetraindata(self, matfiles, group, nexp):
    matfile = matfiles[0]
    matfileout = string.split(string.split(matfile, '/')[-1], '_')
    matfileout = 'stackedwavetraindata_'+group+'_'+matfileout[0]+'_'↩
        +matfileout[1]+'_'+matfileout[2]+'_'+str(nexp)+'.mat'
    if os.path.exists(self.stackedwavetraindatapath+'/'+matfileout):
      print('merged wavetraindata already exist, skipping this step'↩
          )
```

```
    else:
      stackedwavetraindatadict = {}

      for key in self.channelconfig.keys():
    stackchdata = []
    for matfile in matfiles:
      matdata = scipy.io.loadmat(matfile)
      stackchdata.append(matdata[key])
    stackchdata = numpy.vstack(stackchdata)
    stackedwavetraindatadict[key] = stackchdata

      matfileout = string.split(string.split(matfile, '/')[-1], '_')
      matfileout = 'stackedwavetraindata_'+group+'_'+matfileout[0]+'↩
          _'+matfileout[1]+'_'+matfileout[2]+'_'+str(nexp)+'.mat'
      print('saving '+self.stackedwavetraindatapath+'/'+matfileout)
      scipy.io.savemat(self.stackedwavetraindatapath+'/'+matfileout,↩
           stackedwavetraindatadict)

  def removedoubles(self, spikes, spiketimes):
    newspiketimes = []
    newspikes = []
    prevtime = 0
    for i in range(len(spiketimes)):
      time = int(spiketimes[i])
      if prevtime == time:
    pass
      else:
    newspiketimes.append(spiketimes[i])
    newspikes.append(spikes[i])
    prevtime = time
    return( newspikes, newspiketimes)

  def rearrangespikedata(self, spikes, spiketimes, clusterids, ↩
      totaltime):
    newtime = numpy.arange(totaltime)
    newtime = numpy.array(newtime, 'float')
    newclus = numpy.zeros(len(newtime))
    newclus = numpy.array(newclus, 'float')

    newspikes = numpy.zeros((len(spikes), len(spikes[0])+2))

    for i in range(len(spikes)):
      t = spiketimes[i]
      c = clusterids[i]
      s = spikes[i]*1e6
      newspikes[i][0] = t
      newspikes[i][1] = c
      newspikes[i][2::] = s
    #print(newspikes)

    spiketimecounter = 0
    for i in range(len(newtime)):
      if spiketimecounter > len(spiketimes)-1:
    newtime[i] = numpy.nan
    newclus[i] = numpy.nan
      elif i == int(spiketimes[spiketimecounter]):
    newtime[i] = spiketimes[spiketimecounter]
    newclus[i] = clusterids[spiketimecounter]
    spiketimecounter = spiketimecounter + 1
      else:
    newtime[i] = numpy.nan
    newclus[i] = numpy.nan

    return(newspikes, newtime, newclus)

  def alignspikedata(self, spikes, spiketimes, clusterids):
```

```
    spikes = spikes
    spiketimes = numpy.array(spiketimes)
    clusterids = numpy.array(clusterids)

    if len(spikes) > 0:
      timesinspikes = spikes[:, 0]

      differences = numpy.setdiff1d(spiketimes, timesinspikes)
      differenceswithoutnan = differences[numpy.isfinite(differences↩
          )]
      for differencewithoutnan in differenceswithoutnan:
    indexestodelete = numpy.where(spiketimes == differencewithoutnan↩
        )[0]
    spiketimes[indexestodelete] = numpy.nan
    clusterids[indexestodelete] = numpy.nan

      differences = numpy.setdiff1d(timesinspikes, spiketimes)
      differenceswithoutnan = differences[numpy.isfinite(differences↩
          )]

      rowstodeletefromspikes = []
      for differencewithoutnan in differenceswithoutnan:
    rowstodeletefromspikes.append(numpy.where(timesinspikes == ↩
        differencewithoutnan)[0][0])
      spikes = numpy.delete(spikes, rowstodeletefromspikes, 0)
      timesinspikes = spikes[:, 0]

      if len(spikes) == len(spiketimes[numpy.isfinite(spiketimes)]) ↩
          == len(clusterids[numpy.isfinite(clusterids)]):
    pass
      else:
    print('Warning: spikeshapes and clusters do not match')

    else:
      spikes = []
      spiketimes = []
      clusterids = []


    return(spikes, spiketimes, clusterids)

  def filterspikes(self, spikes):
    #print(len(spikes))
    rows, cols = numpy.shape(spikes)
    rowstodeletefromspikes = []
    for row in range(rows):
      spike = spikes[row, 2::]
      toobig = numpy.where(numpy.abs(spike) > 150)[0]
      if  len(toobig) > 0:
    #print('too big')
    rowstodeletefromspikes.append(row)
      else:
    pass
      if numpy.max(spike) < 30:
    #print('too small')
    rowstodeletefromspikes.append(row)
      else:
    pass

    spikes = numpy.delete(spikes, rowstodeletefromspikes, 0)
    for clus in range(self.k):
      if len(spikes) > 0:
    spikeclusters = spikes[:, 1]
    spikesinclus = numpy.where(spikeclusters == clus)[0]
    #print(clus, len(spikeclusters), len(spikesinclus))
    if len(spikesinclus) < 120:
```

```
      spikes = numpy.delete(spikes, spikesinclus, 0)
    else:
      pass
      else:
    spikes = []
    return(spikes)

  def getspikesandclusters(self, matfile):
    matfileout = string.split(matfile, '/')[-1]
    matfileout = string.replace(matfileout, '↩
        stackedandalignedwavetraindata', 'spikes')
    #print(matfileout)
    if os.path.exists(self.spikepath+'/'+matfileout):
      newspikedict = {}
      spikedata = scipy.io.loadmat(self.spikepath+'/'+matfileout)
      for channel in self.channelconfig.keys():
    ch = string.split(channel, '_')[1]
    spikes = spikedata['spikes_'+ch]
    clusterids = spikedata['clusters_'+ch]
    spiketimes  = spikedata['spiketimes_'+ch]

    if len(spikes) == len(spiketimes) == len(clusterids) and len(↩
        spikes) > 0:
      spikes = self.filterspikes(spikes)
      spikes, spiketimes, clusterids = self.alignspikedata(spikes, ↩
          spiketimes, clusterids)
    else:
      spikes = []
      spiketimes = []
      clusterids = []
    newspikedict['spikes_'+ch]  = spikes
    newspikedict['spiketimes_'+ch]  = spiketimes
    newspikedict['clusters_'+ch]  = clusterids

    else:
      matdata = scipy.io.loadmat(matfile)
      datadict = {}
      for key in matdata.keys():
    if key in self.channelconfig.keys():
      shortkey = string.split(key, '_')[-1]
      data = matdata[key][:,0]
      data = self.bpfilt(data)

      spikes, spiketimes, timeinms = self.spikedetection(data)
      spikes, spiketimes = self.removedoubles(spikes, spiketimes)
      clusterids, n = self.kcluster(spikes)

      if len(spikes) == len(spiketimes) == len(clusterids):
        spikes, spiketimes, clusterids = self.rearrangespikedata(↩
            spikes, spiketimes, clusterids, timeinms)
        spikes = self.filterspikes(spikes)
        spikes, spiketimes, clusterids = self.alignspikedata(spikes,↩
             spiketimes, clusterids)
      else:
        spikes = []
        spiketimes = []
        clusterids = []

      datadict['spikes_'+shortkey] = spikes
      datadict['spiketimes_'+shortkey] = spiketimes
      datadict['clusters_'+shortkey] = clusterids
    else:
      pass
      scipy.io.savemat(self.spikepath+'/'+matfileout, datadict)

  def stripmatfile(self, matfile):
```

```
    matdata = scipy.io.loadmat(matfile)
    for key in matdata.keys():
      if 'wavearray_' in key:
    dp = int(len(matdata[key])/2)
    data = matdata[key]
    data = data[0:dp]
    matdata[key] = data
    scipy.io.savemat(matfile,  matdata)

  def align_wavetraindata(self, matfile):
    matfileout = string.split(matfile, '/')[-1]
    matfileout = string.replace(matfileout, 'stackedwavetraindata', ↩
        'stackedandalignedwavetraindata')
    if os.path.exists(self.stackedandalignedwavetraindatapath+'/'+↩
        matfileout):
      print('wavetraindata are already aligned, skipping that step')
    else:
      stackedandalignedwavetraindata = {}
      stackedwavetraindata = scipy.io.loadmat(matfile)

      lendata_actual = []
      for key in self.channelconfig.keys():
    data = stackedwavetraindata[key]
    data = data.flatten()
    data = self.edgedetection(data)
    stackedandalignedwavetraindata[key] = data
    lendata_actual.append(len(data))

      lendata_target = numpy.zeros(7)
      lendata_target[:] = self.fsample*60*2

      #print(lendata_actual, lendata_target)
      if numpy.array_equal(lendata_actual, lendata_target) == True:
    print('saving '+self.stackedandalignedwavetraindatapath+'/'+↩
        matfileout)
    scipy.io.savemat(self.stackedandalignedwavetraindatapath+'/'+↩
        matfileout, stackedandalignedwavetraindata)
      else:
    print('WARNING: edge detection didn\'t work. Not saving: '+self.↩
        stackedandalignedwavetraindatapath+'/'+matfileout)

  def edgedetection(self, data):
    gradient = numpy.gradient(data)
    threshold = numpy.abs(numpy.mean(data)*10)
    overthreshold = numpy.where(gradient > threshold)
    underthreshold = numpy.where(gradient < (-1*threshold))
    sixtyseconds = self.fsample*60

    if len(overthreshold[0]) > 0 and len(underthreshold[0]) > 0:
      thresholds = (overthreshold[0][0], overthreshold[0][-1], ↩
          underthreshold[0][0], underthreshold[0][-1])

      leftedge = numpy.min(thresholds)
      rightedge = numpy.max(thresholds)

      #print(leftedge, rightedge)

      if leftedge-sixtyseconds > 0 and rightedge-sixtyseconds > 0 ↩
          and rightedge-leftedge > self.fsample*40:
    newdata = numpy.hstack((data[leftedge-sixtyseconds:leftedge], ↩
        data[rightedge:rightedge+sixtyseconds]))
      elif leftedge-sixtyseconds > 0 and rightedge-sixtyseconds > 0 ↩
          and rightedge-leftedge < self.fsample*40:
    newdata = numpy.hstack((data[0:leftedge], data[rightedge::]))
    newdata = numpy.hstack((data[0:sixtyseconds], data[len(data)-↩
        sixtyseconds::]))
```

```
      else:
    newdata = numpy.hstack((data[0:sixtyseconds], data[len(data)-↩
        sixtyseconds::]))
    else:
      newdata = numpy.hstack((data[0:sixtyseconds], data[len(data)-↩
          sixtyseconds::]))

    #print(len(newdata))

    #edges = (leftedge, rightedge)
    #space = numpy.zeros(rightedge-leftedge)
    #newdata = numpy.hstack((data[0:leftedge], space, data[rightedge↩
        ::]))
    #pylab.plot(data[::10], lw = 3)
    #pylab.plot(newdata[::10])
    #pylab.show()

    return(newdata)

  def spikematrixtospikedict(self, spikematrix):
    spikedict = {}
    for spike in spikematrix:
      clus = spike[1]
      if clus in spikedict.keys():
    spikedict[clus].append(spike)
      else:
    spikedict[clus] = []
    spikedict[clus].append(spike)
    return(spikedict)

  def spikedicttospikematrix(self, spikedict):
    spikematrix = []
    for key in spikedict.keys():
      clus = key
      spikes = spikedict[key]
      for spike in spikes:
    spikematrix.append(spike)

    if len(spikematrix) > 0:
      spikematrix = numpy.vstack(spikematrix)
    else:
      pass
    #print(numpy.shape(spikematrix))
    return(spikematrix)

  def getinfofromspiketimes(self, spiketimes):
    n = float(len(spiketimes))
    isis = self.getisis(spiketimes)

    hist, bins = numpy.histogram(isis, bins = 50, normed = 1)
    entropy = self.getspikeentropy(isis)
    isimedian = numpy.median(isis)
    alphaparams = scipy.stats.alpha.fit(isis)
    gammafit_a, gammafit_loc, gammafit_scale = scipy.stats.gamma.fit↩
        (isis)
    gammacurve = scipy.stats.gamma.pdf(bins, gammafit_a, loc=↩
        gammafit_loc, scale = gammafit_scale)

    return(n, entropy, isimedian, (hist, bins), (gammafit_a, ↩
        gammafit_loc, gammafit_scale), gammacurve)
```

Listing D.4: getdata.py

```
from Utils import *
```

```
import glob
import shutil
import scipy.stats
import pickle

def getmergedwavetraindatafiles(path, groupdict, groupname):
  group = groupdict[groupname]
  for exp in group:
    diri = path+'/Experiments/'+exp[0]
    U = Utils(diri)
    if len(exp[1]) == 9:
      cyclefiles = []
      nexp = 1
      for fid in exp[1]:
    fname = glob.glob(diri+'/'+'wavetraindata'+'/'+'*_'+fid+'_*')[0]
    size = os.path.getsize(fname)
    if size < 70000000:
      cyclefiles.append(fname)
    else:
      print('warning: '+fname+' file size exeeds limit, file ↩
          stripped')
      U.stripmatfile(fname)
      cyclefiles.append(fname)
      U.mergewavetraindata(cyclefiles, groupname, nexp)

    elif len(exp[1]) > 3 or len(exp[1]) == 2:
      for n, cycle in enumerate(exp[1]):
    nexp = n+1
    cyclefiles = []
    for fid in cycle:
      fname = glob.glob(diri+'/'+'wavetraindata'+'/'+'*_'+fid+'_*')↩
          [0]
      size = os.path.getsize(fname)
      if size < 70000000:
        cyclefiles.append(fname)
      else:
        print('warning: '+fname+' file size exeeds limit, file ↩
            stripped')
        U.stripmatfile(fname)
        cyclefiles.append(fname)
    U.mergewavetraindata(cyclefiles, groupname, nexp)
    else:
      cycle = exp[1]
      nexp = 1
      cyclefiles = []
      for fid in cycle:
    fname = glob.glob(diri+'/'+'wavetraindata'+'/'+'*_'+fid+'_*')[0]
    size = os.path.getsize(fname)
    if size < 70000000:
      cyclefiles.append(fname)
    else:
      print('warning: file size exeeds limit, file stripped')
      U.stripmatfile(fname)
      cyclefiles.append(fname)
      U.mergewavetraindata(cyclefiles, groupname, nexp)

def getalignedwavetraindata(path, groupdict, groupname):
  group = groupdict[groupname]
  for exp in group:
    diri = path+'/Experiments/'+exp[0]
    U = Utils(diri)
    stackedwavetraindatafiles = glob.glob(diri+'/results/↩
        stackedwavetraindata/'+'stackedwavetraindata_'+groupname+'↩
        *.mat')
    for stackedwavetraindatafile in stackedwavetraindatafiles:
      U.align_wavetraindata(stackedwavetraindatafile)
```

```
def getstatspersecond(path, groupdict,  groupname):
  group = groupdict[groupname]
  for exp in group:
    diri = path+'/Experiments/'+exp[0]
    U = Utils(diri)
    stackedandalignedwavetraindatafiles = glob.glob(diri+'/results/↩
        stackedandalignedwavetraindata/'+'↩
        stackedandalignedwavetraindata_'+groupname+'*.mat')
    for stackedandalignedwavetraindatafile in ↩
        stackedandalignedwavetraindatafiles:
      U.getstats_persecond(stackedandalignedwavetraindatafile)

def getspikedataforgroup(path, groupdict,  groupname):
  group = groupdict[groupname]
  for exp in group:
    diri = path+'/Experiments/'+exp[0]
    U = Utils(diri)
    stackedandalignedwavetraindatafiles = glob.glob(diri+'/results/↩
        stackedandalignedwavetraindata/'+'↩
        stackedandalignedwavetraindata_'+groupname+'*.mat')
    for stackedandalignedwavetraindatafile in ↩
        stackedandalignedwavetraindatafiles:
      U.getspikesandclusters(stackedandalignedwavetraindatafile)

def groupstatsdata(path, groupdict, groupname):
  group = groupdict[groupname]
  grouppath = path+'/Groups/'+groupname
  if os.path.exists(grouppath+'/stats'):
    pass
  else:
    os.makedirs(grouppath+'/stats')

  statfilesstripped = glob.glob(path+'/Experiments/*/results/↩
      statspersecond/statspersecond_'+groupname+'*')
  for statfilestripped in statfilesstripped:
    shutil.copyfile(statfilestripped, grouppath+'/stats/'+string.↩
        split(statfilestripped, '/')[-1])

def groupspikedata(path, groupdict, groupname):
  group = groupdict[groupname]
  grouppath = path+'/Groups/'+groupname
  if os.path.exists(grouppath+'/spikes'):
    pass
  else:
    os.makedirs(grouppath+'/spikes')

  spikefilesstripped = glob.glob(path+'/Experiments/*/results/spikes↩
      /spikes_'+groupname+'*')
  for spikefilestripped in spikefilesstripped:
    shutil.copyfile(spikefilestripped, grouppath+'/spikes/'+string.↩
        split(spikefilestripped, '/')[-1])

def exportstatsgroup(path, groupname):
  colors = ('blue', 'green', 'red', 'cyan', 'magenta', 'purple', '↩
      yellow', 'brown', 'grey', 'black', 'blue', 'green', 'red', '↩
      cyan', 'magenta', 'purple', 'yellow', 'brown', 'grey', 'black↩
      ')
  channels = ('ch1', 'ch2', 'ch3', 'ch4', 'ch5', 'ch6', 'ch7', 'ch8'↩
      )
  results = ('rms', 'psd', 'entropy')
  grouppath = path+'/Groups/'+groupname

  statfiles_stripped = glob.glob(grouppath+'/'+'stats'+'/↩
      statspersecond_*')
```

```
  for result in results:
    for c, channel in enumerate(channels):
      targetkey = result+'_'+channel
      if os.path.exists(grouppath+'/stats/'+result) == False:
    os.makedirs(grouppath+'/stats/'+result)
      else:
    pass
      targetpath = grouppath+'/stats/'+result
      targetdata = []
      for statfile_stripped in statfiles_stripped:
    #print(statfile_stripped)
    statdata_stripped = scipy.io.loadmat(statfile_stripped)
    for key in statdata_stripped.keys():
      if key == targetkey:
        data = numpy.array(statdata_stripped[key]).flatten()
        #print(statfile_stripped, key, len(data))

        preHFSmedian = numpy.median(data[0:60])
        normdata = data/preHFSmedian
        #print(len(normdata))
        targetdata.append(normdata)
      else:
        pass

      if len(targetdata) > 1:
    targetdata = numpy.vstack(targetdata)
    numpy.savetxt(targetpath+'/'+result+'_'+groupname+'_'+channel+'.↩
        txt', numpy.transpose(targetdata), delimiter = ', ')
    foo = open(targetpath+'/'+result+'_'+groupname+'_'+channel+'.txt↩
        ', 'r')
    alldata =  foo.read()
    #alldata = string.replace(alldata, 'nan', '')
    #alldata = string.replace(alldata, 'inf', '')
    #alldata = string.replace(alldata, ',-,', ',,')
    foo.close()
    foo = open(targetpath+'/'+result+'_'+groupname+'_'+channel+'.txt↩
        ', 'w')
    foo.write(alldata)
    foo.close()
      else:
    pass

def rasterplots(path, groupname):
  U = Utils('')
  colors = ('blue', 'green', 'red', 'cyan', 'magenta', 'purple', '↩
      yellow', 'brown', 'grey', 'black', 'blue', 'green', 'red', '↩
      cyan', 'magenta', 'purple', 'yellow', 'brown', 'grey', 'black↩
      ')
  channels = ('ch1', 'ch2', 'ch3', 'ch4', 'ch5', 'ch6', 'ch7')
  grouppath = path+'/Groups/'+groupname

  if os.path.exists(grouppath+'/spikes/rasterplots') == False:
    os.makedirs(grouppath+'/spikes/rasterplots')
  else:
    pass

  targetpath = grouppath+'/spikes/rasterplots'
  spikefiles_stacked = glob.glob(grouppath+'/'+'spikes'+'/spikes_*')
  for spikefile_stacked in spikefiles_stacked:
    figname = string.split(spikefile_stacked, '/')[-1][0:-4]+'.svg'
    figfileout = targetpath+'/'+figname
    if os.path.exists(figfileout):
      print('spikeshapes exist, skipping this step')
    else:
      fig = pylab.figure()
      spikedata = scipy.io.loadmat(spikefile_stacked)
```

```
      allch = []
      for c, channel in enumerate(channels):
    ch  = int(string.strip(channel, 'ch'))
    clusterkey = 'clusters_'+channel
    time = numpy.linspace(0, 120000/1000, 120000)
    ax = fig.add_subplot(4,2,ch)
    ax.set_title(channel)
    ax.plot(time, numpy.zeros(len(time)), lw=0)

    clusterids = numpy.array(spikedata[clusterkey]).flatten()
    time = numpy.linspace(0, len(clusterids)/1000, len(clusterids))
    yticklabels = []
    for clus in range(U.k):
      yticklabels.append('clus'+str(clus+1))
      spikesincluster = numpy.where(clusterids == clus)[0]
      if len(spikesincluster) > 0:
        cluster = numpy.zeros(len(spikesincluster))
        cluster[:] = clus+1
        ax.plot(spikesincluster/1000, cluster, lw=0, marker = 'o', ↩
            mfc=colors[clus], mec=colors[clus])
      else:
        pass
    ax.bar(59, U.k+1, width = 2, color = 'grey')
    #ax.set_yticklabels(yticklabels)
    ax.set_ylim((0,11))
      fig.subplots_adjust(wspace = 0.2, hspace = 0.6)
      fig.savefig(figfileout)
      fig.clf()
      pylab.close()

def plotspikeshapes(path, groupname):
  U = Utils('')
  colors = ('blue', 'green', 'red', 'cyan', 'magenta', 'purple', '↩
      yellow', 'brown', 'grey', 'black', 'blue', 'green', 'red', '↩
      cyan', 'magenta', 'purple', 'yellow', 'brown', 'grey', 'black↩
      ')
  channels = ('ch1', 'ch2', 'ch3', 'ch4', 'ch5', 'ch6', 'ch7')
  grouppath = path+'/Groups/'+groupname

  if os.path.exists(grouppath+'/spikes/spikeshapes') == False:
    os.makedirs(grouppath+'/spikes/spikeshapes')
  else:
    pass

  targetpath = grouppath+'/spikes/spikeshapes'
  spikefiles_stacked = glob.glob(grouppath+'/'+'spikes'+'/spikes_*')
  for spikefile_stacked in spikefiles_stacked:
    figname = string.split(spikefile_stacked, '/')[-1][0:-4]+'.svg'
    figfileout = targetpath+'/'+figname
    if os.path.exists(figfileout):
      print('spikeshapes exist, skipping this step')
    else:
      fig = pylab.figure()
      spikedata = scipy.io.loadmat(spikefile_stacked)
      allch = []
      for c, channel in enumerate(channels):
    ch  = int(string.strip(channel, 'ch'))
    spikekey = 'spikes_'+channel
    ax = fig.add_subplot(4,2,ch)
    for key in spikedata.keys():
      if key == spikekey:
        spikes = spikedata[key]
        spikedict = U.spikematrixtospikedict(spikes)
        for key in spikedict.keys():
          clus = int(key)
          spikes = spikedict[key]
```

```
            for i in range(20):
            spike = spikes[i][2::]
            ax.plot(spike, lw=1, color = colors[clus])
            else:
          pass
            ax.set_title(channel)
            ax.set_ylim((-150, 150))
        else:
          pass
        fig.subplots_adjust(wspace = 0.2, hspace = 0.6)
        fig.savefig(figfileout)
        fig.clf()
        pylab.close()

def getspikeinfo(path, groupname):
  U = Utils('')
  channels = ('ch1', 'ch2', 'ch3', 'ch4', 'ch5', 'ch6', 'ch7')
  grouppath = path+'/Groups/'+groupname

  if os.path.exists(grouppath+'/spikes/spikeinfo') == False:
    os.makedirs(grouppath+'/spikes/spikeinfo')
  else:
    pass

  targetpath = grouppath+'/spikes/spikeinfo'
  spikefiles = glob.glob(grouppath+'/'+'spikes'+'/spikes_*')
  for spikefile in spikefiles:
    spikeinfodict = {}
    spikeinfoout = targetpath+'/spikeinfo_'+string.split(spikefile, ↩
        '/')[-1][0:-4]+'.pkl'
    if os.path.exists(spikeinfoout):
      print('spikeinfo exist, skipping this one')
    else:
      spikedata = scipy.io.loadmat(spikefile)
      for channel in channels:
    ch  = int(string.strip(channel, 'ch'))
    clusterkey = 'clusters_'+channel
    clusterids = spikedata[clusterkey]

    spikekey = 'spikes_'+channel
    spikeshapes = spikedata[spikekey]

    if len(clusterids) > 0 and  len(spikeshapes) > 0:
      clusterids = numpy.array(clusterids).flatten()
      spikeshapeclusterids = spikeshapes[:, 1]
      spiketimes = spikeshapes[:, 0]

      for clus in range(U.k):
        spikeshapesinclusterindexes = numpy.where(↩
            spikeshapeclusterids == clus)[0]
        spikeshapesincluster = spikeshapes[↩
            spikeshapesinclusterindexes, 2::]
        spiketimesincluster = spiketimes[spikeshapesinclusterindexes↩
            ]
        spikesincluster = numpy.where(clusterids == clus)[0]

        if len(spikesincluster) > 0:
          preHFSspikes = spikesincluster[numpy.where(spikesincluster↩
              <60000)]
          postHFSspikes = spikesincluster[numpy.where(↩
              spikesincluster>60000)]

          preHFSspikeshapes = spikeshapesincluster[numpy.where(↩
              spiketimesincluster<60000)]
          postHFSspikeshapes = spikeshapesincluster[numpy.where(↩
              spiketimesincluster>60000)]
```

```
            if len(preHFSspikes) > 2 and len(postHFSspikes) > 2:
            #return(n, entropy, isimedian, (hist, bins), (gammafit_a, ↩
                gammafit_loc, gammafit_scale), gammacurve)
            preHFSparams = U.getinfofromspiketimes(preHFSspikes)
            postHFSparams = U.getinfofromspiketimes(postHFSspikes)

            ns = preHFSparams[0], postHFSparams[0]
            entropys = preHFSparams[1], postHFSparams[1]
            isimedians = preHFSparams[2], postHFSparams[2]

            #print(ns)
            #print(len(preHFSspikeshapes), len(postHFSspikeshapes))

            isidistributions = preHFSparams[3][1], preHFSparams[3][0], ↩
                postHFSparams[3][1], postHFSparams[3][0]
            gamma_shapes = preHFSparams[4][0], postHFSparams[4][0]
            gamma_locs = preHFSparams[4][1], postHFSparams[4][1]
            gamma_scales = preHFSparams[4][2], postHFSparams[4][2]
            gammacurves = preHFSparams[5], postHFSparams[5]

            shapes = preHFSspikeshapes, postHFSspikeshapes

            spikeinfokey = 'spikeinfo_'+channel+'_clus'+str(clus)
            spikeshapekey = 'spikeshape_'+channel+'_clus'+str(clus)

            spikeinfodict[spikeinfokey] = [ns, isimedians, entropys, ↩
                isidistributions, gamma_shapes, gamma_locs, ↩
                gamma_scales, gammacurves]
            spikeinfodict[spikeshapekey] = shapes
              else:
              pass
        else:
          pass
          output = open(spikeinfoout, 'wb')
          pickle.dump(spikeinfodict, output)
          output.close()

def plotisidistribution(path, groupname):
  U = Utils('')
  colors = ('blue', 'green', 'red', 'cyan', 'magenta', 'purple', '↩
      yellow', 'brown', 'grey', 'black', 'blue', 'green', 'red', '↩
      cyan', 'magenta', 'purple', 'yellow', 'brown', 'grey', 'black↩
      ')
  channels = ('ch1', 'ch2', 'ch3', 'ch4', 'ch5', 'ch6', 'ch7')
  grouppath = path+'/Groups/'+groupname

  if os.path.exists(grouppath+'/spikes/isidistributionplots') == ↩
      False:
    os.makedirs(grouppath+'/spikes/isidistributionplots')
  else:
    pass

  targetpath = grouppath+'/spikes/isidistributionplots'
  spikefiles = glob.glob(grouppath+'/'+'spikes/spikeinfo/spikeinfo_*↩
      ')
  for spikefile in spikefiles:
    figname = 'isidistribution_'+string.split(spikefile, '/')↩
        [-1][0:-4]+'.svg'
    figfileout = targetpath+'/'+figname
    if os.path.exists(figfileout):
      print('isi distribution plots exist, skipping this step')
    else:
      pkl_file = open(spikefile, 'rb')
      spikedata = pickle.load(pkl_file)
      pkl_file.close()
```

```
  fig = pylab.figure()
  subplot_counter = 0
  for channel in channels:
for clus in range(U.k):
  color = colors[clus]
  subplot_counter = subplot_counter + 1
  ax = fig.add_subplot(len(channels), 2*U.k, subplot_counter)
  ax.set_xticklabels(())
  ax.set_yticklabels(())
  if subplot_counter in [1, 21, 41, 61, 81, 101, 121]:
    ax.set_ylabel(channel)
  else:
    pass
  if subplot_counter in [1, 3, 5, 7, 9, 11, 13, 15, 17, 19]:
    ax.set_title('       clus'+str(clus+1), fontsize = 12)
  else:
    pass
  subplot_counter = subplot_counter + 1
  bx = fig.add_subplot(len(channels), 2*U.k, subplot_counter)
  bx.set_xticklabels(())
  bx.set_yticklabels(())

  key = 'spikeinfo_'+channel+'_clus'+str(clus)
  if key in spikedata.keys():
    clusterinfo = spikedata[key]
    isidistributions = clusterinfo[3]
    gammacurves = clusterinfo[7]

    xlim = numpy.max((numpy.max(isidistributions[0]), numpy.max(↩
        isidistributions[2])))
    ylim = numpy.max((numpy.max(isidistributions[1]), numpy.max(↩
        isidistributions[3])))

    preHFSn = isidistributions[0][0:-1]
    preHFSn[numpy.where(preHFSn > xlim)] = xlim
    preHFShist = isidistributions[1]
    preHFShist[numpy.where(preHFShist > ylim)] = ylim
    preHFSgamma = gammacurves[0][0:-1]
    preHFSgamma[numpy.where(preHFSgamma > ylim)] = ylim

    postHFSn = isidistributions[2][0:-1]
    postHFSn[numpy.where(postHFSn > xlim)] = xlim
    postHFShist = isidistributions[3]
    postHFShist[numpy.where(postHFShist > ylim)] = ylim
    postHFSgamma = gammacurves[1][0:-1]
    postHFSgamma[numpy.where(postHFSgamma > ylim)] = ylim

    ax.bar(preHFSn, preHFShist, color = color, edgecolor = color↩
        )
    ax.plot(preHFSn, preHFSgamma, color = 'black', linestyle = '↩
        --', lw = 1)
    bx.bar(postHFSn, postHFShist , color = color, edgecolor = ↩
        color)
    bx.plot(postHFSn, postHFSgamma, color = 'black', linestyle =↩
         '--', lw = 1)

    ax.set_xlim((0, xlim))
    ax.set_ylim((0, ylim))
    bx.set_xlim((0, xlim))
    bx.set_ylim((0, ylim))
  else:
    pass
  fig.subplots_adjust(wspace = 0.2, hspace = 0.6)
  fig.savefig(figfileout)
  fig.clf()
```

```
def plotspikeparamquotients(path, groupname):
  U = Utils('')
  colors = ('blue', 'green', 'red', 'cyan', 'magenta', 'purple', '↩
      yellow', 'brown', 'grey', 'black', 'blue', 'green', 'red', '↩
      cyan', 'magenta', 'purple', 'yellow', 'brown', 'grey', 'black↩
      ')
  channels = ('ch1', 'ch2', 'ch3', 'ch4', 'ch5', 'ch6', 'ch7')
  grouppath = path+'/Groups/'+groupname

  if os.path.exists(grouppath+'/spikes/spikeparamquotientplots') == ↩
      False:
    os.makedirs(grouppath+'/spikes/spikeparamquotientplots')
  else:
    pass

  targetpath = grouppath+'/spikes/spikeparamquotientplots'
  spikefiles = glob.glob(grouppath+'/'+'spikes/spikeinfo/spikeinfo_*↩
      ')
  for spikefile in spikefiles:
    figname = 'spikeparamquotients_'+string.split(spikefile, '/')↩
        [-1][0:-4]+'.svg'
    figfileout = targetpath+'/'+figname
    if os.path.exists(figfileout):
      print('spike param quotients already plotted, skipping this ↩
          step')
    else:
      pkl_file = open(spikefile, 'rb')
      spikedata = pickle.load(pkl_file)
      pkl_file.close()
      fig = pylab.figure()
      subplot_counter = 0
      for channel in channels:
    for clus in range(U.k):
      color = colors[clus]
      subplot_counter = subplot_counter + 1
      ax = fig.add_subplot(len(channels), U.k, subplot_counter)
      ax.set_xticklabels(())
      ax.set_yticklabels(())

      if subplot_counter in [1, 11, 21, 31, 41, 51, 61]:
        ax.set_ylabel(channel)
      else:
          pass
      if subplot_counter in [1, 2, 3, 4, 5, 6, 7, 8, 9, 10]:
        ax.set_title(' clus'+str(clus+1), fontsize = 12)
      else:
        pass

      key = 'spikeinfo_'+channel+'_clus'+str(clus)
      if key in spikedata.keys():
        clusterinfo = spikedata[key]
        ns = clusterinfo[0]
        isimedians = clusterinfo[1]
        entropys = clusterinfo[2]
        gamma_shapes = clusterinfo[4]
        gamma_locs = clusterinfo[5]
        gamma_scales = clusterinfo[6]

        width = 0.75
        space = 0.25
        barcounter = 0
        maxheight = 10
        for q in (ns, isimedians, entropys, gamma_scales, gamma_locs↩
            , gamma_scales):
          barheight = q[1]/q[0]
          if barheight > 10:
```

```
            barheight = 10
              else:
            pass

              barloc = 0.5+(barcounter*width)+(barcounter*space)
              barcounter = barcounter + 1
              alpha = 1.0/6.0*barcounter
              ax.bar(barloc, barheight, width = width, color = color, ↩
                  edgecolor = color, alpha = alpha)
            ax.set_xlim((0, barloc+width+0.5))
            ax.set_ylim((0, 10))
          else:
            pass
          fig.subplots_adjust(wspace = 0.2, hspace = 0.6)
          fig.savefig(figfileout)
          fig.clf()

def groupspikeinfo(path, groupname):
  U = Utils('')
  channels = ('ch1', 'ch2', 'ch3', 'ch4', 'ch5', 'ch6', 'ch7')
  grouppath = path+'/Groups/'+groupname

  if os.path.exists(grouppath+'/spikes/exportparams') == False:
    os.makedirs(grouppath+'/spikes/exportparams')
  else:
    pass
  paramfileout_pkl = grouppath+'/spikes/exportparams/↩
      groupparams_spikeinfo_'+groupname+'.pkl'

  spikeinfofiles = glob.glob(grouppath+'/spikes/spikeinfo/spikeinfo_↩
      *.pkl')
  paramdict = {}

  tags = []

  preHFSspikeshapes = []
  postHFSspikeshapes = []

  preHFSns = []
  postHFSns = []

  preHFSisimedians = []
  postHFSisimedians = []

  preHFSentropys = []
  postHFSentropys = []

  preHFSgammashapes = []
  postHFSgammashapes  =[]

  preHFSgammalocs = []
  postHFSgammalocs = []

  preHFSgammascales = []
  postHFSgammascales = []

  for spikeinfofile in spikeinfofiles:
    pkl_file = open(spikeinfofile, 'rb')
    spikeinfo = pickle.load(pkl_file)
    pkl_file.close()
    for channel in channels:
      for clus in range(U.k):
    infokey = 'spikeinfo_'+channel+'_clus'+str(clus)
    shapekey = 'spikeshape_'+channel+'_clus'+str(clus)
    if infokey in spikeinfo.keys():
      clusterinfo = spikeinfo[infokey]
```

```
            shapeinfo = spikeinfo[shapekey]

            tags.append(string.split(spikeinfofile, '/')[-1][0:-4]+'_'+↩
                channel+'_clus'+str(clus))

            preHFSspikeshapes.append(shapeinfo[0])
            postHFSspikeshapes.append(shapeinfo[1])

            preHFSns.append(clusterinfo[0][0])
            postHFSns.append(clusterinfo[0][1])

            preHFSisimedians.append(clusterinfo[1][0])
            postHFSisimedians.append(clusterinfo[1][1])

            preHFSentropys.append(clusterinfo[2][0])
            postHFSentropys.append(clusterinfo[2][1])

            preHFSgammashapes.append(clusterinfo[4][0])
            postHFSgammashapes.append(clusterinfo[4][1])

            preHFSgammalocs.append(clusterinfo[5][0])
            postHFSgammalocs.append(clusterinfo[5][1])

            preHFSgammascales.append(clusterinfo[6][0])
            postHFSgammascales.append(clusterinfo[6][1])
        else:
            pass

    ns = numpy.vstack((preHFSns, postHFSns))
    isimedians = numpy.vstack((preHFSisimedians, postHFSisimedians))
    entropys = numpy.vstack((preHFSentropys, postHFSentropys))
    gammashapes = numpy.vstack((preHFSgammashapes, postHFSgammashapes)↩
        )
    gammalocs = numpy.vstack((preHFSgammalocs, postHFSgammalocs))
    gammascales = numpy.vstack((preHFSgammascales, postHFSgammascales)↩
        )

    #exportmatrix = numpy.vstack((ns, isimedians, entropys, ↩
        gammashapes, gammalocs, gammascales))

    shapes = preHFSspikeshapes, postHFSspikeshapes

    paramdict['ns'] = ns
    paramdict['isimedians'] = isimedians
    paramdict['entropys'] = entropys
    paramdict['gammashapes'] = gammashapes
    paramdict['gammalocs'] = gammalocs
    paramdict['gammascales'] = gammascales
    paramdict['spikeshapes'] = shapes
    paramdict['tags'] = tags

    numpy.savetxt(grouppath+'/spikes/exportparams/ns_spikeinfo_'+↩
        groupname+'.txt', numpy.transpose(ns))
    numpy.savetxt(grouppath+'/spikes/exportparams/↩
        isimedians_spikeinfo_'+groupname+'.txt', numpy.transpose(↩
        isimedians))
    numpy.savetxt(grouppath+'/spikes/exportparams/entropys_spikeinfo_'↩
        +groupname+'.txt', numpy.transpose(entropys))
    numpy.savetxt(grouppath+'/spikes/exportparams/↩
        gammashapes_spikeinfo_'+groupname+'.txt', numpy.transpose(↩
        gammashapes))
    numpy.savetxt(grouppath+'/spikes/exportparams/gammalocs_spikeinfo_↩
        '+groupname+'.txt', numpy.transpose(gammalocs))
    numpy.savetxt(grouppath+'/spikes/exportparams/↩
        gammascales_spikeinfo_'+groupname+'.txt', numpy.transpose(↩
        gammascales))
```

```
  output = open(paramfileout_pkl, 'wb')
  pickle.dump(paramdict, output)
  output.close()

def exportspikeinfo(path, groupname):
  U = Utils('')
  channels = ('ch1', 'ch2', 'ch3', 'ch4', 'ch5', 'ch6', 'ch7')
  grouppath = path+'/Groups/'+groupname

  spikeinfofile = grouppath+'/spikes/exportparams/↩
      groupparams_spikeinfo_'+groupname+'.pkl'
  spikeinfofileout = grouppath+'/spikes/exportparams/spikeinfo_'+↩
      groupname+'.mat'

  pkl_file = open(spikeinfofile, 'rb')
  spikeinfo = pickle.load(pkl_file)
  pkl_file.close()

  #print(spikeinfo.keys())
  #print(len(spikeinfo['tags']), len(spikeinfo['entropys']), len(↩
      spikeinfo['entropys'][1]))

  preHFSspikeshapes, postHFSspikeshapes = spikeinfo['spikeshapes']
  tags = spikeinfo['tags']
  ns = spikeinfo['ns']
  isimedians = spikeinfo['isimedians']
  entropys = spikeinfo['entropys']

  spikes = []
  deltans = []
  deltaisis = []
  deltahs = []
  for i in range(len(preHFSspikeshapes)):
    stack = numpy.vstack((preHFSspikeshapes[i], postHFSspikeshapes[i↩
        ]))
    stackmean = numpy.mean(stack, axis = 0)

    if len(numpy.where((ns[1][i], ns[0][i], isimedians[1][i], ↩
        isimedians[0][i], entropys[1][i], entropys[0][i]) < 0)[0]) ↩
        == 0:
      deltan = float(ns[1][i] - ns[0][i])/float(ns[1][i] + ns[0][i])
      deltaisi = float(isimedians[1][i] - isimedians[0][i])/float(↩
          isimedians[1][i] + isimedians[0][i])
      deltah = entropys[1][i] - entropys[0][i]
      #print(ns[1][i], ns[0][i], deltan)
      spikes.append(stackmean)
      deltans.append(deltan)
      deltaisis.append(deltaisi)
      deltahs.append(deltah)
  else:
    pass
    #print(len(numpy.where((ns[1][i], ns[0][i], isimedians[1][i], ↩
        isimedians[0][i], entropys[1][i], entropys[0][i]) < 0)))
    #print(numpy.where((ns[1][i], ns[0][i], isimedians[1][i], ↩
        isimedians[0][i], entropys[1][i], entropys[0][i]) < 0))
    #print(ns[1][i], ns[0][i], isimedians[1][i], isimedians[0][i], ↩
        entropys[1][i], entropys[0][i])

  flattenedspikes = []
  flattenedtags = []
  flattenedn = []
  flattenedisim = []
  flattenedentropie = []
  for i in range(len(spikes)):
    flattenedtags.append(tags[i])
```

```
    flattenedn.append(deltans[i])
    flattenedisim.append(deltaisis[i])
    flattenedentropie.append(deltahs[i])
    flattenedspikes.append(spikes[i])

  clusterids, n = U.kcluster(flattenedspikes)

  newdict = {}
  newdict['spikes'] = flattenedspikes
  newdict['tags'] = flattenedtags
  newdict['clusterids'] = clusterids
  newdict['ns'] = flattenedn
  newdict['isis'] = flattenedisim
  newdict['entropy'] = flattenedentropie

  scipy.io.savemat(spikeinfofileout, newdict)

def exportspikedata(path, groupname):
  U = Utils('')
  colors = ('#0000ff', '#ff0000', '#800080', '#ffff00', '#008000', '↩
      #00ff00', '#008080', '#00ffff', '#000080', '#ff00ff')
  currents = ('0.0mA', '0.1mA', '0.2mA', '0.3mA', '0.4mA')
  channels = ('ch1', 'ch2', 'ch3', 'ch4', 'ch5', 'ch6', 'ch7')
  grouppath = path+'/Groups/'+groupname

  if os.path.exists(grouppath+'/spikes/spikeexport') == False:
    os.makedirs(grouppath+'/spikes/spikeexport')
  else:
    pass

  datafile = glob.glob(path+'/Groups/'+groupname+'/spikes/↩
      exportparams/*.mat')[0]
  data = scipy.io.loadmat(datafile)

  spikes = data['spikes']
  tags = data['tags']
  clusterids  = data['clusterids']
  dn = data['ns']
  disi = data['isis']
  dh = data['entropy']

  sumsdn = []
  sumsdi = []
  sumsdh = []
  for clus in range(U.k):
    indexes = numpy.where(clusterids == clus)[0]

    if len(spikes) > 0 and len(indexes) > 0:
      spikesinclus = spikes[indexes]
      dninclus = dn[indexes]
      diinclus = disi[indexes]
      dhinclus = dh[indexes]
      sumsdn.append(float(numpy.sum(dninclus))/float(len(dninclus)))
      sumsdi.append(float(numpy.sum(diinclus))/float(len(dninclus)))
      sumsdh.append(float(numpy.sum(dhinclus))/float(len(dninclus)))

      numpy.savetxt(grouppath+'/spikes/spikeexport/'+groupname+'↩
          _spikeshapes_clus'+str(clus)+'.txt', numpy.transpose(↩
          spikesinclus))
      numpy.savetxt(grouppath+'/spikes/spikeexport/'+groupname+'↩
          _dn_clus'+str(clus)+'.txt', dninclus)
      numpy.savetxt(grouppath+'/spikes/spikeexport/'+groupname+'↩
          _di_clus'+str(clus)+'.txt', diinclus)
      numpy.savetxt(grouppath+'/spikes/spikeexport/'+groupname+'↩
          _dh_clus'+str(clus)+'.txt', dhinclus)
```

```
stringn = ''
for sumdn in sumsdn:
  stringn = stringn + str(sumdn) + ', '
fn = open(grouppath+'/spikes/spikeexport/'+groupname+'_sum_dn.txt'↩
    , 'w')
fn.write(stringn)
fn.close()

stringi = ''
for sumdi in sumsdi:
  stringi = stringi + str(sumdi) + ', '
fi = open(grouppath+'/spikes/spikeexport/'+groupname+'_sum_di.txt'↩
    , 'w')
fi.write(stringi)
fi.close()

stringh = ''
for sumdh in sumsdh:
  stringh = stringh + str(sumdh) + ', '
fh = open(grouppath+'/spikes/spikeexport/'+groupname+'_sum_dh.txt'↩
    , 'w')
fh.write(stringh)
fh.close()

#numpy.savetxt(grouppath+'/spikes/spikeexport/'+groupname+'_sum_dn↩
    .txt', sumsdn, delimiter = ', ')
#numpy.savetxt(grouppath+'/spikes/spikeexport/'+groupname+'_sum_di↩
    .txt', sumsdi, delimiter = ', ')
#numpy.savetxt(grouppath+'/spikes/spikeexport/'+groupname+'_sum_dh↩
    .txt', sumsdh, delimiter = ', ')
```

E

PROTOCOLS

Implantation Protocol for BiCIRTS chronic Experiments

expID:

projectID:

animal info:

weight:

Anaesthesia:

time	substance

Stereotaxy:

IA_L:
IA_R:
Δ_{IR}:

Bregma:

AP_B:
ML_B:
DV_B:

Lambda:

AP_{IAP}:
ML_{IAP}:
DV_{IAP}:

DV_B:
DV_{IAP}:
Δ_{DV}:

1st Stereotaxic Target (ventrolateral Cpu, right side)

$\mathbf{AP_{CPu} = AP_B + 0.02 =}$
$\mathbf{ML_{CPu} = ML_B - 0.30 =}$
$\mathbf{DV_{CPu} = DV_B - 0.45 =}$

2nd Stereotaxic Target (STN, right side)

$\mathbf{AP_{STN} = AP_{IAP} + 0.56 =}$
$\mathbf{ML_{STN} = ML_{IAP} - 0.26 =}$
$\mathbf{DV_{STN} = DV_{IAP} - 0.84 =}$

Fixation Screws

$\mathbf{= 0.30 - AP_{STN} + 0.30 =}$
$\mathbf{= 0.10 - ML_{STN} + 0.10 =}$

Ground Screw

$\mathbf{AP_G = AP_{IAP} + 0.25 =}$
$\mathbf{ML_G = ML_{IAP} + 0.25 =}$

Trepanation

Fixation & Ground Screws: 0.9 mm
Injection: 1.4 mm
Recording: 2.9 mm

Reference Injection Needle

AP_{B_S} :
ML_{B_S} :
DV_{B_S} :

Target (CPu) Injection Needle

$AP_{CPu\_S} = AP_{B\_s} + 0.02 =$
$ML_{CPu\_S} = ML_{B\_s} - 0.30 =$
$DV_{CPu\_S} = DV_{B\_S} - 0.45 =$

CPu Injection

load substance:
perfuse 10 min, 1µl/min
wait 5 min (in situ)

Reference Electrode (Support Needle)

AP_{IAP_E} :
ML_{IAP_E} :
DV_{IAP_E} :

Target (STN) Electrode

$AP_{STN\_E} = AP_{IAP\_E} + 0.56 =$
$ML_{STN\_E} = ML_{IAP\_E} - 0.26 =$
$DV_{STN\_E} = DV_{IAP\_E} - 0.84 =$

Electrode Insertion

place Fixation & Ground Screws
place Agar 0.75% (made with NaCl 0.9%)
place electrode and navigate to target

Schedule for chronic DBS/Multisite Recording experiments – time sweep

Animal ID: _____ Implant:_____
Electrode: _____

Multisite Recoding Settings:

- TDT Sys3
- Project: Niotrode.wsp
- Circuit: Niotrode.rcx
- Controller: controller_1.xpc
- **Data Tank: _____**

- TDT G&R shortcut
- signal ground
  - electrode shaft
  - skull screw
  - WPI Isostim A320 (+)
- signal ground connected to TDT G&R
- chronic plug provides 3 shortcut connector pins connected to electrode shaft (signal ground).
- electrode recording channels 1-7 correspond to TDT recording channels 1-7 channels
- TDT channels 8-10 connected to signal ground
- electrode channel 8 connected to WPI Isostim A320 (-)

Noise Level:

- **RMS filtered (BP 300/4000):_____**
- **RMS unfiltered: _____**

Preconditions:

- **Day after Implant:_____**
- **CPu Lesion:_____**
- **Injections prior to recording:_____**
- **Previous experiments:_____**
- **Current amplitude:_____**
- **Stimulator:_____**

DBS/Multisite Recording Scheme:

file name prefix:

time [min]	desc	name	num
1	rec		
2	rec		
3	rec		
4	DBS1	Current:_____ DBS Signal file:_____ Video file:_____	
5	rec1		
6	rec2		
7	DBS2	Current:_____ DBS Signal file:_____ Video file:_____	
8	rec1		
9	rec2		
10	rec3		
11	rec4		
12	DBS3	Current:_____ DBS Signal file:_____ Video file:_____	
13	rec1		
14	rec2		
15	rec3		
16	rec4		
17	rec5		
18	rec6		
19	DBS4	Current:_____ DBS Signal file:_____ Video file:_____	
20	rec1		
21	rec2		
22	rec3		
23	rec4		
24	rec5		
25	rec6		
26	rec7		
27	rec8		
28	DBS5	Current:_____ DBS Signal file:_____ Video file:_____	
29	rec1		
30	rec2		
Wait_____			
62	rec1		
63	rec2		

Schedule for chronic DBS /Multisite Recording experiments – current sweep

Animal ID: _____ **Implant:**_____
Electrode: _____

Multisite Recoding Settings:

- TDT Sys3
- Project: Niotrode.wsp
- Circuit: Niotrode.rcx
- Controller: controller_1.xpc
- **Data Tank:** _____

- TDT G&R shortcut
- signal ground
  - electrode shaft
  - skull screw
  - WPI Isostim A320 (+)
- signal ground connected to TDT G&R
- chronic plug provides 3 shortcut connector pins connected to electrode shaft (signal ground).
- electrode recording channels 1-7 correspond to TDT recording channels 1-7 channels
- TDT channels 8-10 connected to signal ground
- electrode channel 8 connected to WPI Isostim A320 (-)

Noise Level:

- **RMS filtered (BP 300/4000):**_____
- **RMS unfiltered:** _____

Preconditions:

- **Day after Implant:**_____
- **CPu Lesion:**_____
- **Injections prior to recording:**_____
- **Previous experiments:**_____
- **Current amplitude:**_____
- **Stimulator:**_____

file name prefix:

time	desc	name	num
1	rec1		
2	rec2		
3	rec3		
4	rec4		
5	rec5		
6	DBS1	**Current: 0.0 mA** DBS Signal file:_____ Video file:_____	
7	rec1		
8	rec2		
9	rec3		
10	rec4		
11	rec5		
12	DBS2	**Current: 0.1 mA** DBS Signal file:_____ Video file:_____	
13	rec1		
14	rec2		
15	rec3		
16	rec4		
17	rec5		
18	DBS3	**Current: 0.2 mA** DBS Signal file:_____ Video file:_____	
19	rec1		
20	rec2		
21	rec3		
22	rec4		
23	rec5		
24	DBS4	**Current: 0.3 mA** DBS Signal file:_____ Video file:_____	
25	rec1		
26	rec2		
27	rec3		
28	rec4		
29	rec5		
30	DBS5	**Current: 0.4 mA** DBS Signal file:_____ Video file:_____	
31	rec1		
32	rec2		
33	rec3		
34	rec4		
35	rec5		

Schedule for chronic DBS /Multisite Recording experiments – apomorphine test

Animal ID: _____ **Implant:**_____
Electrode: _____

Multisite Recoding Settings:

- TDT Sys3
- Project: Niotrode.wsp
- Circuit: Niotrode.rcx
- Controller: controller_1.xpc
- **Data Tank:** _____
- TDT G&R shortcut
- signal ground
  - electrode shaft
  - skull screw
- chronic plug provides 3 shortcut connector pins connected to electrode shaft (signal ground).
- electrode recording channels 1-7 correspond to TDT recording channels 1-7 channels
- TDT channels 8-10 connected to signal ground

Noise Level:

- **RMS filtered (BP 300/4000):**_____
- **RMS unfiltered:** _____

Preconditions:

- **Day after Implant:**_____
- **CPu Lesion:**_____
- **Previous experiments:**_____
- **Apomorphine:**_____

DBS/Multisite Recording Scheme:

file name prefix:

time [min]	desc	video	recording
1	preapo	Video file:_____	
2	**preapo**		
3	preapo		
4	**preapo**		
5	preapo		
6	**preapo**		
7	preapo		
8	**preapo**		
9	preapo		
10	preapo		
Apomorphine Injection: 200µl, 0.5mg/kg KG			
11	apo	Video file:_____	
12	apo		
13	apo		
14	apo		
15	**apo**		
16	apo		
17	apo		
18	apo		
19	apo		
20	**apo**		
21	apo		
22	apo		
23	apo		
24	apo		
25	**apo**		
26	apo		
27	apo		
28	apo		
29	apo		
30	**apo**		
31	apo		
32	apo		
33	apo		
34	apo		
35	**apo**		
36	apo		
37	apo		
38	apo		
39	apo		
40	apo		